382

MAXIMUM LIKELIHOOD ADJUSTMENT OF NUCLEAR ~~CROSS-SECTION~~ DATA FOR REACTOR TECHNOLOGY.

Maurice Maxwell Chestnutt

A thesis submitted for
the award of
Doctor of Philosophy

Nuclear Power Section
Department of Mechanical Engineering
Imperial College of Science and Technology

March 1979

Abstract

The reactor physics based methods of data adjustment have no general application for the optimisation of nuclear data sets for use in the deep penetration problems of radiation shielding. The deficiencies of the existing methods are examined and the requirements of a shielding adjustment philosophy propounded. A statistical model for the prediction of observables is proposed and a likelihood formalism based on maximising the support for the hypothesised parameter set on the measured data is developed. A multi-channel detector distribution is introduced as a convenient data reduction statistic and the truncation of the exact support for the hypothesised model parameters to a hybrid likelihood functional is shown to arise from a limitation to linear neutron transport perturbation theory. The hybrid method described has the following novel features:-

(i) the observables are used in the optimisation functional

(ii) the detector response data (including possible energy scale calibration errors) and the radiation source normalisation are included as optimisable parameters.

(iii) by decoupling the response and transmission adjustment evaluators, an exact second order solution for the response parameters is obtained.

(iv) an iterative solution scheme, utilising a statistically tested linear search, for the transmission data adjustments is advanced as the most rapidly convergent linear evaluator.

(v) the variance-covariance data and the cross-correlations between the optimised model parameters are derived using expectation theory.

The hybrid adjustment formalism is demonstrated by optimisation of the UKNDL DFN 908A nuclear data file using measurements taken from the ASPIS iron benchmark experiment, for which a reference calculation is described and a detailed examination of the instrumental response data is given. The optimised scalar cross-section data is compared with the more recent ENDF/B-IV iron evaluation and with the adjusted fast reactor data set FD5, and use of the à posteriori error correlation matrices is displayed with reference to two NEA theoretical shielding benchmarks.

Acknowledgements

The author wishes to thank the following people for their assistance with this work:-

Professor P J Grant and Dr A J H Goddard of Imperial College, University of London, for their supervision, encouragement and for financial support allowing the author to attend a specialists' meeting in Paris (1977) and the neutron physics conference at AERE Harwell (1978).

All members of the Winfrith Radiation Physics and Shielding Group for their generous and friendly assistance. In particular, Dr J Butler has given constant encouragement and support, Mr D E Bendall has given advice on computing and Messers M D Carter and A Packwood have assisted in the interpretation of the measured data. Special thanks are due to Mr A K McCracken who has given invaluable guidance on the philosophical aspects of the interpretation of the observations and on the principles of statistics.

Dr C G Campbell for the hospitality extended to the author during the performance of this work in the Reactor Physics Division at AEE Winfrith.

Mr K Greenhouse and Mr C J Dean for their assistance in running the GALAXY code and to Mr M J Grimstone for useful discussions related to the RADAK unfolding code and the ANISN and DOT-III transport codes.

Mr A F Avery for useful comments on many varied aspects of this work.

Mr J L Rowlands who provided the FD5 data adjustments.

Dr M Salvatores (CNEN) who made available the results of his consistent adjustment study prior to publication.

The work described has been performed at AEE Winfrith and AERE Harwell under the joint auspices of the United Kingdom Atomic Energy Authority and Imperial College, supported by a UKAEA EMR Contract (Number WH 35488).

CONTENTS

CHAPTER I. SOME ASPECTS OF SHIELDING DATA ADJUSTMENT

1.1 Introduction 21

1.2 A Brief Overview of this Report 23

CHAPTER II. AN INTRODUCTION TO THE CONCEPTS OF SENSITIVITY, UNCERTAINTY AND CONSISTENCY ANALYSIS

2.1 Introduction 26

2.2 Sensitivity Analysis 26

2.3 Uncertainty Analysis 27

2.4 Sources of Errors and Correlations in Nuclear Cross-Section Data

2.4.1 Point Data Errors 29
2.4.2 Correlations Between Point Data 30
2.4.3 Group Processing Errors 31

2.5 Methods of Performing Uncertainty Analysis 33

2.6 Target Accuracies on Integral Quantities 33

2.7 Examples of Uncertainty Analysis

2.7.1 The Biological Shield for JET 35
2.7.2 The PWR Theoretical Benchmark 35
2.7.3 The FBR Theoretical Benchmark 38

2.8 Consistency Analysis 38

2.9 Summary 48

CHAPTER III. A COMMENTARY ON INTEGRAL EXPERIMENTS AND NUCLEAR DATA ADJUSTMENT METHODS

3.1 Integral Experiments 50

3.2 Methods of Nuclear Data Adjustment

3.2.1 Introduction 57
3.2.2 Reactor Physics Data Adjustment Methods 57
3.2.3 The Method of Macdougall and Rowlands 59
3.2.4 The Method of Mitani and Kuroi 61
3.2.5 The Consistent Method 63

3.3 Requirements of a Shielding Data Adjustment Methodology 65

3.4 Summary 68

CHAPTER IV. MAXIMUM LIKELIHOOD DATA ADJUSTMENT USING A MULTI-CHANNEL DETECTOR DISTRIBUTION

4.1 Statistical Theory

4.1.1 Introduction 70
4.1.2 Likelihood and the Method of Support 71
4.1.3 Likelihood, Evaluates and Information 72

4.2 The Statistical Model

4.2.1 Detector Response 73
4.2.2 The Calibration Energy Scale Error for Proton Recoil Counters 75
4.2.3 Neutron Transmission Parameters 76
4.2.4 The Calculational Prediction of Observed Quantities 77

4.3 Derivation of the Likelihood Functional

4.3.1 The Experimental Support Function 78
4.3.2 The Prior Support Function - The Constraints 80

4.4 Specification of the Flux Perturbation in Terms of Transmission Cross-Section Variations 82

4.5 The Choice of Adjoint Source 85

4.6 Maximisation of the Support Functional

4.6.1 The Adjustments to the Partition Coefficients 90
4.6.2 The Adjustments to the Activation Detector Response Functions 92
4.6.3 The Adjustments to the Spectrometer Energy Scale Error Parameter 94
4.6.4 The Adjustment to the Source Power Normalisation 94
4.6.5 The Adjustments to the Transmission Cross-Section Data 95

4.7 The Extension of the Method to Include Error Correlation Matrices 97

4.7.1 Independent Transmission Cross-Section Correlation Matrices 98
4.7.2 Response Cross-Section Correlation Matrices 98

4.8 Summary 99

CHAPTER V. THE DERIVATION OF THE COVARIANCE RELATIONSHIPS FOR THE ADJUSTED DATA USING EXPECTATION THEORY

5.1 Introduction 102

5.2 Asymptotic Requirements of the Cross-Section Covariance Matrix 103

5.3 Specification of the Partial Cross-Section Covariance Matrix in Terms of Intermediate Variables

5.3.1 The Covariance Matrix for a Partial Cross-Section 105
5.3.2 The Covariance Between Partial Cross-Sections 106

5.4 The Multi-Channel Detector Reaction-Rate 107

5.5 The Transmission Cross-Section Sensitivities 110

5.6 The Covariance Matrix for the Partition Coefficients 112

5.7 The Correlation Between the Partition Coefficients and the Transmission Cross-Sections 114

5.8 Summary 116

CHAPTER VI. TRANSPORT CALCULATIONS FOR THE ASPIS IRON BENCHMARK EXPERIMENT

6.1 Introduction 118

6.2 The Geometrical Model

6.2.1 Description of the Experimental Facility 119
6.2.2 Description of the Converter Plate 119
6.2.3 The Source Distribution 123

6.3 The Calculational Method 130

6.4 Choice of Calculational Parameters for DOT-III

6.4.1 Spatial Mesh 131
6.4.2 The Energy Group Structure 132
6.4.3 The Order of Angular Quadrature 135
6.4.4 The Iterative Solution Algorithm 135
6.4.5 Choice of Convergence Test 139
6.4.6 Acceleration Techniques 140
6.4.7 Initial Flux Guess 141

6.5 Comparison of the Reference Calculation Predictions with Measurement 142

6.6 Transformation to 1-D

6.6.1 Methods of Transformation 143
6.6.2 The Iron-Concrete Interface 154

6.7 Summary 156

CHAPTER VII. AN EXAMINATION OF THE ASPIS IRON BENCHMARK EXPERIMENTAL MEASUREMENTS

7.1 Introduction 158

7.2 The Information Content of the Detectors 158

7.3 Proton Recoil Counter Line-Shapes

7.3.1 Hydrogen Proportional Counter Line-Shapes 160
7.3.2 Organic Scintillation Counter Line-Shapes 164

7.4 An Assessment of the Integral Detector Response Data Uncertainties

7.4.1 Integral Detector Response Cross-Section Uncertainty Analysis 169
7.4.2 Integral Detector Response-Rate Profiles 171

7.4.3 The Consistency of the SAND-II Error Data for the Response Cross-Sections 179

7.5 Measurement Errors

7.5.1 The Differential Approach 181
7.5.2 The Integral Approach 184
7.5.3 Measurement Uncertainties 186

7.6 Energy Scale Calibration Errors

7.6.1 Introduction 187
7.6.2 Calibration of the Gas Counters 188
7.6.3 Calibration Errors (Proportional Counters) 188
7.6.4 Calibration Errors (Electronics) 190
7.6.5 Calibration Errors (NE 213 Counter) 192

7.7 Detector Partition Coefficients 193

7.8 Unfolded Measurement Spectra 193

7.9 Summary 199

CHAPTER VIII. THE PLATO COMPUTER CODE SUITE

8.1 Introduction 201

8.2 Calculation of Adjoint Sources 201

8.3 Calculation of Response Data Adjustments 204

8.4 Cross-Section Adjustment 205

8.5 The Variance-Covariance Calculation 206

CHAPTER IX. THE APPLICATION OF THE PLATO ADJUSTMENT SUITE TO THE ASPIS IRON BENCHMARK

9.1 Introduction 209

9.2 Sensitivity Profiles 209

9.3 The Data for the Optimisation Code 219

9.4 The Transmission Cross-Section Adjustments 225

9.5 Adjustments to the Detector Response Data 231

9.6 Comparison of Calculated Flux Profile with Unfolded Measurement Spectrum 233

9.7 Comparison of Predicted and Observed Response-Rates 243

9.8 Variance-Covariance Data 245

9.9 Comparison of the Adjusted Data Set with Other Libraries 255

9.10 Interpretation of the Observed Adjustments 267

9.11 Summary 271

CHAPTER X. SUMMARY AND FURTHER DEVELOPMENTS

10.1 Summary 273

10.2 à Posteriori Uncertainty Analysis 274

10.3 Further Improvements and Extensions 276

APPENDIX A. THE DIAGNOSTIC FRACTIONAI ENERGY SHIFT EVALUATOR FOR NEUTRON SPECTROMETERS

A.1 Introduction 278

A.2 Calculation of the Response Function Adjustment in the Bulk Matrix 279

A.3 A Single Channel Detector Near Threshold 279

APPENDIX B. THE EVALUATES OF THE LINEAR SUPPORT FUNCTION 281

APPENDIX C. CONSIDERATION OF THE SECOND ORDER TERMS IN THE SUPPORT FUNCTION FCR TRANSMISSION CROSS-SECTION ADJUSTMENT EVALUATORS 283

APPENDIX D. AN ANALYSIS OF THE RENORMALISATION ACCELERATION TECHNIQUES IN DOT-III

D.1 Space Independent Scaling 285

D.2 Space Dependent Scaling 286

APPENDIX E. A REVIEW OF THE NUCLEAR DATA FOR THE THRESHOLD DOSIMETRY REACTIONS USED IN THE ASPIS IRON BENCHMARK EXPERIMENTAL ANALYSIS

E.1 Sulphur (n,p) 288

E.2 Indium (n,n') 289

E.3 Rhodium (n,n') 290

REFERENCES 292

INDEX TO FIGURES

Fig. 2.1	Sensitivity Profile of Oxygen Cross-Section Data for Prediction of Neutron Dose-Rate Outside JET Shield.	36
Fig. 2.2	Measurement Sensitivity Profile of Oxygen Cross-Section Data - Dose-Rate Outside JET Shield.	37
Fig. 2.3	Sensitivity of PWR Pressure Vessel Displacement-Rate to Iron, Oxygen and Hydrogen Cross-Section Data.	39
Fig. 2.4	Measurement Sensitivity of PWR Pressure Vessel Displacement-Rate to Oxygen and Iron Cross-Section Data.	40
Fig. 2.5	Sensitivity of FBR Sodium Capture-Rate in the Heat Exchanger to Iron and Sodium Cross-Section Data.	41
Fig. 2.6	Sensitivity of FBR Core Restraint Structure Displacement-Rate to Iron and Sodium Cross-Section Data.	42
Fig. 2.7	Measurement Sensitivity of FBR Core Restraint Displacement-Rate to Sodium and Iron Cross-Section Data.	43
Fig. 2.8(A)	Measurement Sensitivity of Sodium Partial Cross-Section Data for Secondary Sodium Activation.	44
Fig. 2.8(B)	Measurement Sensitivity of Iron Partial Cross-Section Data for Secondary Sodium Activation.	45
Fig. 3.1	Comparison of Calculated Flux Profile with RADAK Unfolded Spectrum Measurement at 76.2 cm Position.	53
Fig. 3.2	Measured Neutron Flux Profile Derived from a 14 MeV Source After Penetration through an Iron Cylinder (30 cm x 20 cm).	54
Fig. 3.3	Sensitivity Profile for Iron Cylinder Exposed to a 14 MeV Source.	55
Fig. 6.1	Equivalent Area View of the ASPIS Iron Benchmark Experiment	120
Fig. 6.2	R-Z Geometrical Model for Transport Calculation.	121
Fig. 6.3	Spatial Distribution of Fuel in Converter Plate.	124
Fig. 6.4	Planar Lattice Cell of the Converter Plate.	125
Fig. 6.5	Intermediate Model of Lattice Cell (Planar).	126
Fig. 6.6	Comparison of Calculated Flux Profiles with RADAK Unfolded Spectrum Measurement at 20.3 cm Position.	146
Fig. 6.7	Comparison of Calculated Flux Profiles with RADAK Unfolded Spectrum Measurement at 50.8 cm Position.	147
Fig. 6.8	Comparison of Calculated Flux Profiles with RADAK Unfolded Spectrum Measurement at 76.2 cm Position.	148

Fig. 6.9	Comparison of Calculated Flux Profiles with RADAK Unfolded Spectrum Measurement at 101.6 cm Position.	149
Fig. 6.10	Comparison of Measured and Calculated Integral Detector Reaction-Rate Penetration Profiles.	150
Fig. 7.1	Schematic Diagram of Theoretical and Measured Hydrogen Chamber Line-Shapes.	162
Fig. 7.2	Functional Fit of Light Function to Experimental Data.	166
Fig. 7.3	Comparison of Unfolded Cf-252 Fission Spectrum with NBS Standard.	170
Fig. 7.4	Variation in S(n,p) Reaction-Rate Profile as a Function of Penetration.	173
Fig. 7.5	Variation in In(n,n') Reaction-Rate Profile as a Function of Penetration.	174
Fig. 7.6	Variation in Rh(n,n') Reaction-Rate Profile as a Function of Penetration.	175
Fig. 7.7	Variation in Au(n,γ) Reaction-Rate Profile as a Function of Penetration.	176
Fig. 7.8	Comparison of In-115(n,n') Multi-Group Cross-Section Data from Different Sources.	178
Fig. 7.9	Comparison of Self-Shielded Au(n,γ) Multi-Group Cross-Section Data from Different Sources.	182
Fig. 7.10	Comparison of Calculated Flux Profile with RADAK Unfolded Spectrum Measurements at 50.8 cm Position.	196
Fig. 7.11	Comparison of RADAK Unfolded Flux Spectra with and without Energy Scale Calibration Errors.	197
Fig. 7.12	Comparison of RADAK Unfolded Flux Spectra with and without Energy Scale Calibration Errors.	198
Fig. 8.1	Control Flow Chart for the PLATO Code Suite	202
Fig. 8.2	Flow Diagram for the OPTOR Code.	203
Fig. 9.1	Spatial Dependence of Sulphur (n,p) Reaction-Rate Total Sensitivity Profile to Iron Cross-Section Data.	210
Fig. 9.2	Spatial Dependence of Indium (n,n') Reaction-Rate Total Sensitivity Profile to Iron Cross-Section Data.	211
Fig. 9.3	Spatial Dependence of Rhodium (n,n') Reaction-Rate Total Sensitivity Profile to Iron Cross-Section Data.	212
Fig. 9.4(A)	Sensitivity Profile for Multi-Position Multi-Channel Detector Reaction-Rate to Iron Cross-Section Data - (Total).	213

Fig. 9.4(B)	Sensitivity Profile for Multi-Position Multi-Channel Detector Reaction-Rate to Iron Cross-Section Data - (Inelastic).	214
Fig. 9.4(C)	Sensitivity Profile for Multi-Position Multi-Channel Detector Reaction-Rate to Iron Cross-Section Data. - (Absorption).	215
Fig. 9.5	Spatial Dependence of the Initial Multi-Channel Detector Distribution.	216
Fig. 9.6	Comparison of Initial and Cycle 4 Multi-Position Multi-Channel Detector Distribution Sensitivity Profiles.	218
Fig. 9.7	Partial Cross-Section Adjustment Factors at End of Cycle IV.	226
Fig. 9.8	Comparison of Cross-Section Adjustments with Multi-Group Cross-Section Profile.	228
Fig. 9.9	Convergence of Cross-Section Adjustments as a Function of Cyclic Iteration.	229
Fig. 9.10	Comparison of Single Position and Multi-Position Cross-Section Adjustment Profiles.	230
Fig. 9.11	Comparison of Calculated Flux Profiles with RADAK Unfolded Spectrum Measurement at 20.3 cm Position.	234
Fig. 9.12	Comparison of Calculated Flux Profiles with RADAK Unfolded Spectrum Measurement at 50.8 cm Position.	235
Fig. 9.13	Comparison of Calculated Flux Profiles with RADAK Unfolded Spectrum Measurement at 76.2 cm Position.	236
Fig. 9.14	Comparison of Calculated Flux Profiles with RADAK Unfolded Spectrum Measurement at 101.6 cm Position.	237
Fig. 9.15	Comparison of Calculated Flux Profiles with RADAK Unfolded Spectrum Measurement at 76.2 cm Position.	240
Fig. 9.16	Comparison of Measured and Calculated Integral Detector Reaction-Rate Penetration Profiles.	241
Fig. 9.17	Convergence of Flux Profiles at 76.2 cm Position as a Function of Multi-Position Iteration.	244
Fig. 9.18	Comparison of Calculated Response-Rates at 20.3 cm with Measurement.	246
Fig. 9.19	Comparison of Calculated Response-Rates at 22.8 cm with Measurement.	247
Fig. 9.20	Comparison of Calculated Response-Rates at 50.8 cm with Measurement.	248
Fig. 9.21	Comparison of Calculated Response-Rates at 76.2 cm with Measurement.	249

Fig. 9.22	Comparison of Calculated Response-Rates at 101.6 cm with Measurement.	250
Fig. 9.23	Comparison of ENDF/B-III Flux Profile with UKNDL DFN 908A Flux Profile at 76.2 cm Position.	256
Fig. 9.24	Comparison of Adjusted Flux Profile with ENDF/B-IV Library Prediction at 50.8 cm Position.	258
Fig. 9.25	Comparison of Adjusted Flux Profile with ENDF/B-IV Library Prediction at 76.2 cm Position.	259
Fig. 9.26	Comparison of Adjusted Flux Profile with ENDF/B-IV Library Prediction at 101.6 cm Position.	260
Fig. 9.27	Comparison of Multi-Group Cross-Section Profiles from UKNDL, ENDF/B-IV and PLATO(4).	261
Fig. 9.28	Comparison of Adjusted Flux Profile with FD5 Adjusted Data Set Prediction at 50.8 cm Position.	264
Fig. 9.29	Comparison of Adjusted Flux Profile with FD5 Adjusted Data Set Prediction at 101.6 cm Position.	265
Fig. 9.30	Comparison of Measured and Calculated Integral Detector Reaction-Rates for Different Libraries.	266
Fig. 9.31	Comparison of Multi-Group Cross-Section Profiles from UKNDL, FD5 and PLATO(4).	268
Fig. 9.32	Comparison of Multi-Group Total Cross-Sections Derived from ENDF/B-IV using AMPX at Different Laboratories.	270

LIST OF TABLES

Table 2.1	Comparison of Uncertainty Estimates (1σ) using Available Cross-Section Error Data.	46
Table 3.1	Comparison of Cross-Section Adjustments for ENDF/B-IV Sodium and Iron Predicted from a Subset of 7 Experiments with those Obtained from the Full 21 Configurations.	56
Table 6.1(A)	Zone Materials Densities for the ASPIS Iron Benchmark Model.	122
Table 6.1(B)	Composition of Modelled Converter Plate.	122
Table 6.2	U^{235} Fission-Rate Distribution for Fuel Element No. 5 at 3 KW NESTOR Reactor Power.	123
Table 6.3	Results of a Symmetry Inspection at 3 KW of NESTOR Reactor Power.	127
Table 6.4	Variation of Fission-Rate at the Centre of the Converter Plate with NESTOR Reactor Power.	128
Table 6.5	Radial Dependence of Fuel Plate Self-Absorption Factors.	129
Table 6.6(A)	Radial Mesh Structure.	133
Table 6.6(B)	Axial Mesh Structure.	133
Table 6.7	Comparison of Spatial Mesh Increments.	134
Table 6.8(A)	Comparison of Group Fluxes.	136
Table 6.8(B)	Comparison of Integral Parameters.	136
Table 6.9	Order of Quadrature Comparison.	136
Table 6.10	Comparison of Models of Convergence using DOT-III with Different Mesh Interval Sizes (after Salvatores).	138
Table 6.11	Comparison of EURATOM Calculation with the ASPIS Iron DATAM Experiment Reference Calculation.	142
Table 6.12	S(n,p) Reaction-Rate - Axial Profile.	144
Table 6.13	Rh(n,n') Reaction-Rate - Axial Profile.	144
Table 6.14	Au(n,γ) Reaction-Rate - Axial Profile.	145
Table 6.15	In(n,n') Reaction-Rate - Axial Profile.	145
Table 6.16	Bucklings Derived from Bessel Function Approximation of DOT-III Radial Profiles.	153
Table 6.17	Comparison of Buckled ANISN Prediction of Integral Parameters with DOT-III Calculation.	153

Table 6.18	Comparison of DOT and ANISN Reference Calculation Reaction-Rate Predictions at Various Penetrations.	153
Table 6.19	Ratios of Dimensional Transformation Coefficients with Absorption and Total Cross-Sections for the ASPIS Iron DATAM Experimental Shield.	155
Table 7.1	Detectors used in the ASPIS Iron Benchmark Experiment.	159
Table 7.2	Percentage Difference in Gradient for Calculated and Measured Line-Shapes.	161
Table 7.3	Fractional Error on Gas Proportional Counter Line-Shapes.	168
Table 7.4	Least Squares Fit to NE 213 Counter Light Function.	168
Table 7.5	Fractional Uncertainty Estimates on Activation Detector Cross-Sections.	172
Table 7.6	Upper and Lower Energy-Dependent Correlation Bounds for the Expected Fractional (%) Error on the Integral Response-Rate as a Function of Penetration.	172
Table 7.7	Ratio of Response-Rates Calculated using Different Data Libraries Compared with the Response-Rates Determined using the Recommended Response Data as a Function of Penetration in the ASPIS Iron Benchmark Experiment.	180
Table 7.8	Effect of Resolution Smoothing on Proton Recoil Counter Differential Data.	185
Table 7.9	Comparison of Repeated Runs with Statistical Variance Prediction.	186
Table 7.10	The Pressure Variation of the α-source Calibration Energy for SP2 Counters.	190
Table 7.11	Calibration Data for the NE 213 Counter as a Function of Time.	192
Table 7.12	Estimated Fractional Energy Scale Error for Proton Recoil Counter.	194
Table 7.13	Comparison of a Typical Energy Scale Error Estimate.	194
Table 7.14	Partition Coefficients and Standard Errors used in the ASPIS Iron Benchmark Experiment.	194
Table 9.1	Sensitivity of the Elemental Constituents of the Iron Shield to the Multi-Channel Detector Distribution at the 76.2 cm Position.	217
Table 9.2	Fractional Uncertainties on Multi-Group Iron Cross-Section Data.	220
Table 9.3	Correlation Matrix for Iron Absorption Cross-Section (after Gerstl et al.).	222

Table 9.4	Correlation Matrix for Iron Inelastic Cross-Section (after Gerstl et al.).	223
Table 9.5	Correlation Matrix for Iron Total Cross-Section (after Gerstl et al.).	224
Table 9.6	Linear Search Scaling Parameter λ and the Fractional Reduction in χ^2 as a Function of Outer Iteration for the Multi-Position Optimisation.	227
Table 9.7	Fractional Reduction in χ^2 as a Function of Outer Iteration for the Single Position (76.2 cm) Optimisation.	231
Table 9.8	The Adjustments to the Detector Response Parameters.	232
Table 9.9	Comparison of Activation Detector Reaction-Rates Derived from Different Libraries.	242
Table 9.10	Sample Submatrix of End of Cycle I Energy-Dependent Correlation Matrix for Non-Elastic Cross-Section.	252
Table 9.11	Sample Submatrix of End of Cycle I Energy-Dependent Correlation Matrix for Total Cross-Section.	253
Table 9.12	Sample Submatrix of End of Cycle I Energy-Dependent Cross-Correlation Between Total and Non-Elastic Cross-Sections.	254
Table 9.13	Characteristics Pertaining to the Derivation of the FD5 and PLATO(4) Adjusted Data Sets.	263
Table 9.14	Initial χ^2 Values per Degree of Freedom for Various Data Sets.	267
Table 10.1	Comparison of NEA Theoretical Benchmark Design Parameter Uncertainties Derived from the Use of à Priori and à Posteriori Error Correlation Matrices.	275

A GLOSSARY OF TERMS AND ABBREVIATIONS

ABBN	Abagyan, Bazazyants, Bondarenko, Nikolaev - see ref 29.
Appropriate Solution	is a solution which satisfies the matrix equation to within the uncertainties on the measurements.
at.	atmosphere (unit of pressure) 1 at. = 1.01×10^5 Nm^{-2}
CDFR	Comercial Demonstration Fast Reactor - proposed UK successor to PFR
CPU	Central Processor Unit
CTR	Controlled Thermo-nuclear Reactor
DATAM	Data and Methods testing benchmark
DFN	Data File Number
DS_n	Discrete Segment n - commonly used to designate the Method of Discrete Ordinates
ENDF/B-	Evaluated Nuclear Data File Version B-
Evaluate	best supported value of a parameter (Maximum Likelihood value)
FBR	Fast Breeder Reactor
ILRR	Inter-Laboratory Reaction-Rate Comparison
IKE	Institut fur Kernergetik, Universtät Stuttgart
Information	Matrix of the second derivatives of the Support, multiplied by -1 and evaluated at maximum likelihood
JAERI	Japanese Atomic Energy Research Institute
JET	Joint European Torus
Measurement	the value inferred from a detector reading for a parameter of interest - unfolded flux
NEA/OECD	Nuclear Energy Agency of the Organisation for Economic Co-operation and Development
NE 213	Nuclear Enterprises Counter Number 213
Observable	the value indicated on a detector or meter during an experiment - counts per second
PRC or prc	Proton Recoil Counter
PWR	Pressurised Water Reactor
Schmidt-type	Only cross-section variance data used in the first optimisation cycle - the independent group cross-section assumption
Scores Vector	Vector of the first derivatives of the Support Function
Support	Natural logarithm of the likelihood function
TSF	Tower Shielding Facility
UKNDL	United Kingdom Nuclear Data Library
WRENDA	World Request List for Evaluated Nuclear Data

GLOSSARY OF SYMBOLS

This glossary contains some of the symbols in common usage in the text of this work.

A	the response matrix for the detectors
a_{qij}	the element of A corresponding to the response function for the i^{th} channel of the q^{th} detector type for the group j neutron flux
a	proton recoil counter radius as in $R(E)/a$
$a(E_j)$	energy intercept for a proton recoil counter line-shape
b_i	the fractional standard deviation of the probable systematic error in the i^{th} integral measurement
$b_j(E)$	the proton density at energy E arising from unit group flux per unit lethargy in the j^{th} neutron group
$\hat{B}_{jkrr'}$	the Boltzmann transport operator relating the flux per unit lethargy at position r and neutron group j to the neutron source in group k and position r'
$\underline{B}(E,z)$	a pseudo-geometric buckling for energy E and axial mesh z
$\hat{\overline{B}}$	flux weighted mean buckling
b_T	total number of recoil protons in the counter
$b(E_j)$	gradient of proton recoil line-shape for neutron energy E_j
$\mathrm{cov}(x_j^p, x_k^p)$	the covariance of the j^{th} group cross-section with the k^{th} group cross-section for the partial cross-section process p
$C_{i,r}$	the calculated value of an observable for signal channel i at the r^{th} position
C_i	the evaluator of the adjustment to the predicted value of an observable in signal channel i. The spatial dependence is understood
$c(l)dl$	NE 213 counter light output distribution
c_l	counts in a counting channel of which one or more may comprise a signal channel count-rate M_i
d_i	fractional discrepancy in the estimate of the i^{th} integral measurement obtained using adjusted nuclear data
D_q	for concision denotes the denominator of the adjustment evaluator for the partition coefficient α_q viz:

$$\sum_{i \in q} \frac{C_i^2}{\sigma^2(M_i)\alpha_q} + \frac{1}{\sigma^2(\alpha_q)}$$

$\hat{E}[\,]$	the expectation operator
E_{th}	threshold energy
e_i	the fractional standard deviation of the normally distributed part of the i^{th} integral measurement
ΔE_i	the energy width of the i^{th} energy bin
δE	a small change in the energy of a group or channel boundary
E_γ	lower energy boundary of a proton recoil counter working range
E_{max}	upper energy boundary of a proton recoil counter working range
E_α	α-source peak energy
E_n	neutron source energy

Ep_i	proton recoil energy corresponding to the i^{th} signal channel boundary
f_k^p	fractional adjustment to the group k of the p^{th} partial cross-section
F	minimisation functional
G	number of groups in the multi-group calculational scheme
g_k^p	fractional standard deviation for the k^{th} group of the p^{th} partial cross-section
g_q	the evaluator of the fractional energy scale uncertainty for the q^{th} spectrometer type
H	a general hypothesis - a set of model parameters
H_j^+	the multi-channel detector distribution for the cross-section adjustment evaluator. The spatial dependence is understood.
h	the corresponding multi-channel detector distribution reaction-rate
i	a signal channel within a detector partition
I_q	the total number of useful signal channels in the counter type q
J_z	axial neutron current
J_r	radial neutron current
j,k	energy group indicies
$L(H\|\underline{M})$	the likelihood of the hypothesis H given that the data $\underline{M}$ has been observed as the outcome of an experiment, compared with the maximum possible likelihood
ln	the natural logarithm - $\log_e$
L_j^+	the multi-channel detector distribution for the covariance estimates for the updated cross-section evaluates
l	the corresponding multi-channel detector distribution reaction-rate.
l_i	light output corresponding to recoil proton energy Ep_i
Δl	pulse height channel width
$\underline{M}$	a set of observed data
M_i	the observation corresponding to signal channel i
(n,n)	elastic scattering reaction
(n,n')	inelastic scattering reaction
(n,x)	non-elastic scattering reaction
(n,γ)	radiative capture
(n,α)	neutron induced α-particle emission
(n,f)	neutron induced fission
N(R(E))dE	number of recoil protons with range between R(E) and R(E+dE)
P	closed set of partial scalar cross-sections which define the neutron transport process (e.g. absorption, non-elastic and total cross-sections)
p	any member of P

$P(\underline{M}\|H)$	the probability of obtaining $\underline{M}$ in an experiment as predicted by the hypothesis H and a statistical model
q_m	the m^{th} parameter of a nuclear model e.g. temperature T or α in E^{α}
q'_m	the perturbed value of q_m
q	a detector type; $i \epsilon q$ all signal channels i contained in q
Q	the total number of detector partitions (usually detectors)
R	any general integral response, usually a design parameter e.g. neutron dose-rate.
r	a positional index e.g. $C_{i,r}$
$\mathcal{R}$	the rate of convergence of the flux in a transport code.
r_o	equivalent critical radius to buckling B
R(E)	range of a recoil proton of energy E
R_{ij}	element of the response matrix for a proton recoil counter
R(E,E')	proton recoil counter response kernel
ΔR	energy resolution width of a spectrometer
$S(\underline{\theta})$	the support for the set of parameters $\underline{\theta}$
S	the source normalisation factor
δS	the evaluator of the systematic error in the source normalisation
$S_{k,r'}$	the neutron source in group k at position r'
$\hat{s}_{qq_f}$	projection operator = 1 if q represents a foil monitor $q \epsilon q_f$ = 0 otherwise
$\hat{s}_{qq_s}$	projection operator = 1 if q represents a spectrometer $q \epsilon q_s$ = 0 otherwise
$U_k^{p,R}$	the sensitivity of the integral response R to a unit fractional increase in the transmission partial cross-section x_k^p as furnished by SWANLAKE
Δu	the lethargy of an energy group
$var(x_k^p)$	the variance of the group k cross-section for the p^{th} partial cross-section
V^p	variance-covariance matrix for the p^{th} partial cross-section
V	the volume of the calculational model
v_{jk}^p	the jk^{th} group element of the inverse variance-covariance matrix for the p^{th} partial cross-section
w_p	the specific ionization of a proton
$x^p(E)$	the value of the partial cross-section type p at energy E
x_k^p	multi-group form of $x^p(E)$ averaged using some weighting function over the energy range which constitutes group k
$\underline{x}^A$	the multi-group absorption cross-section vector
$\underline{x}^N$	the multi-group elastic cross-section vector
$\underline{x}^{N'}$	the multi-group inelastic cross-section vector
$\underline{x}^x$	the multi-group non-elastic cross-section vector
$\underline{x}^T$	the multi-group total cross-section vector

x_j^r	the random component of a measurement of the cross-section x at E_j
x_k'	the perturbed value of x_k
$\underline{\hat{x}}^p$	the evaluate of the cross-section $\underline{x}^p$
$\underline{y}_q^+$	the multi-channel detector distribution for the partition coefficient's adjustment evaluator. The spatial dependence is understood
y_q	the corresponding multi-channel detector distribution reaction-rate
$\underline{\alpha}$	the partition coefficients for the detectors
$\delta\alpha_q$	the evaluator of the adjustment to the q^{th} detector partition coefficient
(α,β,γ)	scalar parameters - least squares fit to the NE 213 light function
$\Gamma_k^{p,R}$	the independent cross-section sensitivity for the response R to the multi-group partial cross-section x_k^p in which changes in the p^{th} partial cross-section are correlated only to the same change in the total cross-section
δ_k^p	some tolerance on the residual for the k^{th} group adjustment to the p^{th} partial cross-section
$\delta_{jj'}$	Kroenecker Delta = 1 for j = j' = 0 otherwise
ε_i	some tolerance on the residual for the i^{th} observable
ε_j^s	the systematic error component of a measurement at energy E_j of the cross-section $\underline{x}$
$\underline{\varepsilon}^p$	the adjustment to the fiducial cross-section data to obtain the cross-section evaluate
$\underline{\varepsilon}^\alpha$	the adjustment to the fiducial partition coefficient data to obtain the partition coefficient evaluate
λ	the linear search scaling parameter for the cross-section adjustment evaluator
λ_1	the dominant eigenvalue of the transport operator
μ_{1i}	a channel reaction-rate defined by: $\sum_j \Sigma_{qij}\phi_j \qquad q\varepsilon q_s$ and $i\varepsilon q$
$\underline{\theta}$	a general set of parameters
ρ_{kj}^p	the correlation coefficient between the k^{th} and j^{th} group cross-section for the p^{th} partial cross-section
$\sigma(x_k^p)$	the standard deviation on x_k^p
$\sigma(M_i)$	the standard deviation on the measurement M_i
$\sigma(S)$	the standard deviation of the normal distribution assigned to the source normalisation factor by the Central Limit Theorem
$\sigma^2(\underline{\Psi})$	the variance on the unfolded flux vector - usually obtained from the unfolding code e.g. RADAK

Σ^R	the flux-to-response conversion vector
$\Sigma^T(E)$	the macroscopic energy-dependent total cross-section
Σ^{gg}	the macroscopic within group scattering cross-section
$\Sigma_k^s(\underline{r})$	spatially dependent scattering cross-section for group k
$\Sigma_H(E)$	the macroscopic hydrogen scattering cross-section
τ_{kj}	a measured ratio of the value of the cross-section at energy E_k relative to an absolutely determined cross-section measurement at E_j
$\underline{\phi}$	the calculated flux per unit source normalisation
$\underline{\phi}^+$	the adjoint flux vector
$\underline{\phi}_p$	the perturbed flux vector
$\underline{\phi}_s$	the ordinate fluxes of the DS_n approximation
ϕ_r	the flux at position r or at the boundary of spatial mesh r
ϕ_R	the central flux of mesh r
$\phi_k^{(i)}$	the flux after the i^{th} iteration in group k
ζ_{qij}	a symbol used for concision in relating a_{qij} to g_q and defined in Appendix A
χ_m^2	the measurement chi-squared; sometimes the subscript is omitted
$\underline{\Psi}$	the flux vector obtained by unfolding from a measurement distribution
ψ	angular flux $\psi(\underline{r},\underline{\Omega},E,t)$ (Chapter VI)
$\Psi(E)$	neutron flux spectrum
$\sum_l$	summation over l (Distinct from Σ)
$\{\ \}$	the set of parameters or values
$\int_\tau d\tau$	integration over all phase space $\tau \equiv (\underline{r},\underline{\Omega},E)$
$\langle\ \rangle$	expectation value
$\underline{\varepsilon}^{(i)}$	the error vector for the i^{th} iterate flux
Δ_z^k	dimensional transformation coefficient for axial mesh z and group k
$i \epsilon q$	all channels i contained in q

CHAPTER I

SOME ASPECTS OF SHIELDING DATA ADJUSTMENT

1.1 Introduction

Nuclear data adjustment was born out of the requirement for reduced uncertainty margins on commercial reactor design parameters. In the reactor physics domain the discrepancies between calculational prediction and observation were derived both from inadequacies in the calculational method and from errors in the nuclear data. The assessment of the adequacy of rival methods and data sets was conducted through theoretical intercomparison exercises and by the performance of integral experiments. Initially the integral experiments were used simply to identify the best existing evaluated nuclear data file and to indicate areas of the evaluated cross-section data where better quality measurements were required. The guidance given by these integral experiments helped designers and reactor physicists to formulate some of the more important requests for accurate nuclear data; the mechanism for making such requests known to evaluators and measurers was, and still is, the WRENDA list[1].

In general, therefore, the feedback to the nuclear data from these technical assessment exercises was either non-existent, as in the case of the UKNDL, or only over the time-scale for a complete re-evaluation of the library, as was the case for the ENDF/B library[2]. Moreover requests for more accurate nuclear data measurements had to await the development of new detection systems and better neutron sources. The time constant for the satiation of nuclear data requests became so long that the direct feedback of the results of integral experiments into design calculations appeared to be the only expedient way of significantly reducing the uncertainties on reactor design parameters. It was at this stage that the adjustment of nuclear data, on the basis of some statistical prescription, to obtain consistency with experimental observations was first advocated and in order to assist in this process a special class of integral experiments, designated 'benchmarks', were identified.

The conduct of benchmark experiments and the adjustment of nuclear data for reactor core calculations became fairly widespread throughout Europe; the heterogencities of the reactor core in some sense mitigated the effects of poor data adjustment. The situation in shielding physics, where the penetration flux is approximately exponentially dependent on the cross-section data, was rather more demanding. Whilst the economic advantages of reducing shield design margins were obvious, the requirements of accurate and meaningful data adjustments delayed the carry over of the adjustment procedures from the reactor core situation, and no adjusted data sets for use in shield design calculations have thus far been

published.

The problem of adjusting shielding data has been of international interest and the activities of many laboratories have been co-ordinated through the NEA collaborative benchmark programme. Within the framework of this exercise, it was decided that benchmark experiments in pure iron should be performed in order to assess the feasibility and value of adjusting data for shielding. In the context of shielding physics a benchmark experiment was defined to be[3]:

> "..... a penetration (or migration) experiment in which the uncertainties involved with the theoretical treatment of the source and the geometry of the system are small compared with errors in the measurements at a given penetration distance in the shield."

The ASPIS iron benchmark experiment[4] has represented the U.K. contribution to the NEA collaborative programme. The experiment was conducted by staff at A.E.E. Winfrith during the period 1974-75 and a preliminary analysis of the experiment has been published by Grimstone et al[5] in which the data adjustment was confined to the total cross-section and was based on a least squares group flux comparison.

The objective of this work has been to propose an adjustment philosophy for optimising nuclear data matrices for reactor shield design on the basis of a comparison with a benchmark experiment which furnishes many channels of high quality signal information. The two tier hybrid optimisation scheme developed in response to this requirement has been coded and interfaced with the DS_n transport code ANISN and the related cross-section sensitivity code SWANLAKE to form the PLATO suite which has been used with the results of the ASPIS iron benchmark experiment to evaluate maximum likelihood adjustments for the UKNDL iron data file DFN 908A[6].

The primary reason for having to develop a new optimisation scheme has been that the existing methods in the fast reactor physics field are neither economic nor adequate to meet the more demanding requirements of the shielding community. The data requirements for iron are so diverse, as has been shown by examination of generic design problems, (some of which are cited in Chapter II), that the wide scale quality of the data can only be assessed by appeal to benchmark experiments. Moreover the multiplicity of the data requirements for iron on the WRENDA list has meant that the achievement of the required data accuracies by purely differential measurement is, in many cases, beyond the time scales set for CDFR shield design. Indeed in some cases the analysis of benchmarks can provide higher quality and more consistent information on cross-

section data than microscopic measurement.

The adjustment philosophy developed in this work has attempted to preserve the integrity of the measured data by treating the observables as a sample of uncorrupted data obtained by experiment; processing of the measured data has been reduced to a minimum and the calculation has been forced to model both the transmission and the detection processes. In this way account has been taken of both the inadequacies in the response data and the systematic errors in the detector responses. Moreover, energy scale calibration errors in the proton recoil counters have been identified as a possible source of discrepancies with calculation and their effects have been examined and included in the statistical model which forms the basis of the OPTOR adjustment code. The use of the RADAK unfolding code[7] in integral form has shown that the energy displacement of spectrum features associated with cross-section resonances and interference minima, which is normally ascribed to energy scale calibration error, may in fact be derived from an inadequacy inherent in conventional (differential) unfolding procedures. Errors in proton recoil response matrices other than those arising from the energy scale have also been assessed by examination of the measured gas counter line-shapes and in the case of the NE 213 organic scintillation counter, an error analysis of the light function has been performed in conjunction with an integral unfolding of a standard Cf^{252} spectrum measurement. Finally, the multichannel detector distribution is given as a method of combining the observed data into a compact form for use in adjoint calculations; whilst representing a considerable economy in computational effort, it is shown to lead to a reduction to first order for the solution of the support equations for the cross-section adjustment evaluators.

1.2 A Brief Overview of this Report

In Chapter II the concepts of sensitivity and uncertainty analysis are examined and some sources of errors in nuclear data are identified. The target accuracies for reactor design parameters are discussed and examples of generic design problems are given with a view to displaying the wide variation of data requirements for iron in the shielding environment. Consistency analysis is introduced as a possible route for meeting these requirements. A comparison of the shielding approach with that of core physics is given in Chapter III and a discussion of the different types of experiments mounted for shielding data adjustment is given. Various aspects of the reactor physics methodology are then examined before the requirements of a shielding data adjustment philosophy

are proposed.

The statistical model for the prediction of observables is developed in Chapter IV and the utility of a multi-channel detector distribution for large measurement ensembles is considered. The likelihood function for the calculational prediction on the observed data is then formulated and after the expansion of the flux perturbations in terms of a complete set of cross-section perturbations with coefficients derived from the multi-channel detector distribution, the adjustment evaluators for all the parameters of the statistical model are obtained. The use of expectation theory to provide an estimate of the updated variance-covariance matrix for the adjusted model parameters forms the subject of Chapter V.

The next two chapters are concerned with the calculational and experimental aspects of the ASPIS iron benchmark experiment. In Chapter VI the theoretical approximations made during the performance of the reference calculation are critically assessed with a view to error estimation. The transformation to 1-D is also considered. Chapter VII is devoted to an examination of the response data for the proton recoil counters and the threshold detectors. A discussion of the sources of energy scale calibration errors is given and an examination of the energy displacement of the resonance-anti-resonance pair between 24 and 28 keV in iron is conducted.

In Chapter VIII a short guide to the operation of the OPTOR adjustment code is given and the interfacing with the transport, perturbation and data processing modules in the PLATO suite is examined. The results derived from the use of the PLATO suite on the ASPIS iron benchmark measurements are given in Chapter IX where the cross-section adjustments are compared with the trends predicted from the more recent ENDF/B-IV evaluation and with the FD5 fast reactor core adjusted data set predictions. Finally, the conclusions of the present work and a discussion on future extensions to the adjustment scheme are presented in Chapter X.

CHAPTER II

AN INTRODUCTION TO THE CONCEPTS OF SENSITIVITY, UNCERTAINTY AND CONSISTENCY ANALYSIS

2.1 Introduction

Although in its infancy, sensitivity analysis is now established as the primary technique for the examination of nuclear data related effects in neutron transport. Its applications cover problems relating to uncertainty analysis, group scheme optimisation[8,9] and consistency analysis. The growth in the use of sensitivity analysis has been prompted by recognition of the fact that recent improvements in the techniques for solving the transport equation have reduced method errors to the level where they are comparable with uncertainties arising from nuclear data. In recent years much effort in the U.S.A. has been concerned with the development of 1-D and 2-D discrete ordinates codes[10,11] and generalised geometry Monte Carlo programs[12] for solving radiation transport problems. The increased accuracy of these tools has prompted an examination of the adequacy of the nuclear data used by these codes. In the following chapter the errors and correlations that can arise in nuclear data are examined and a discussion is given of the techniques of sensitivity, uncertainty and consistency analysis and the information they provide. The examples, which have been drawn from three different reactor types, will be useful in the discussion of the utility of optimised data sets conducted in a later chapter.

2.2 Sensitivity Analysis

The aim of sensitivity theory is to formalise the relationship between the solution of the transport equation and the quality of the nuclear interaction constants dictating the transport process. The sensitivity function commonly used in reactor physics is derived by the application of generalised perturbation theory[13,14,15] to the linear Boltzmann transport equation. The perturbation treatment is usually limited to the first order variation of the multi-group averaged neutron interaction parameters[16] (cross-sections, secondary angular and energy distributions etc) of the one-dimensional time independent equation, although higher order approximations[17,18] and extensions to 2-D[19] and 3-D[20] have been investigated. A derivation of the sensitivity functional using operator notation is given in Chapter IV.

The sensitivity profile, $U^{p,R}(E)$, obtained for an integral parameter R where:

$$R = R(x^p(E),.....) \qquad 2.2.1$$

is defined as the fractional change in the predicted response, R, per unit fractional change in some dependent nuclear parameter $x^p(E)$:

$$U^{p,R}_{(E)} = \frac{\delta \ln R}{\delta \ln x^p(E)} \qquad 2.2.2$$

or in discrete form:

$$U_k^{p,R} = \frac{\delta R/R}{\delta x_k^p / x_k^p} \qquad 2.2.3$$

where x_k^p is some group averaged neutron transport parameter. The sensitivity vector, $\{\underline{U}^{p,R}\}$, derived from the perturbation approach therefore reflects the degree of ill-conditioning of the transport operator. The limitation of first order theory can be a particularly serious one. In radiation shielding, for instance, resonances, thresholds and interference minima tend to dominate the sensitivity profiles in design situations and it is in these regions that non-linear behaviour can become apparent after only small cross-section perturbations. Goldstein[21] has plotted $\delta \ln R$ as a function of $\delta \ln x(E)$ for the total cross-section of sodium in the vicinity of the 300 keV minimum and shown the change in the response (group flux at 100 keV after 5 m) to be markedly different depending upon whether the cross-section is increased or decreased, and also to be grossly non-linear even after rather small perturbations (~2%). A similar behaviour has been noted by Germogenova et al[22] who found that the error in the sensitivity function for the fast neutron flux behind a laminated iron-water shield could be as high as 40% for variations in the total cross-section of 3-5% and in the scattering cross-section of 7-10%.

2.3 Uncertainty Analysis

Uncertainty analysis utilises the convolution of the sensitivity profile with the error correlation matrix for the cross-section data. The sensitivity profile reflects the fractional degree of instability of the transport operator for prediction of some response parameter R and the error correlation matrix furnishes some estimate of the condition of the transport operator. The convolution of the two functions can therefore allow a confidence interval, usually taken at the 68% level, to be determined for the prediction of the integral parameter R. The ensuing derivation of the fractional variance on the prediction of an integral response, R, follows that of Lympany et al[23].

Since equation 2.2.3 is not an exact differential, it may be rewritten as:

$$\frac{\delta R}{R} = \sum_{p=1}^{P} \sum_{k=1}^{S} U_k^{p,R} \frac{\delta x_k^p}{x_k^p} \qquad 2.3.1$$

where k is the multi-group index and p accounts for a closed set of nuclear data parameters upon which R is dependent. In the subsequent analysis only scalar cross-section data sensitivities are discussed; sensitivities to secondary angular and secondary energy distributions are

usually small enough to be ignored. Therefore since, for example, neutron transport can be described by a closed set of absorption, elastic and inelastic cross-sections, $\underline{x}^{A}$,$\underline{x}^{N}$ and $\underline{x}^{N'}$ respectively:

$$R = R(\underline{\Sigma}^{R}, \underline{x}^{A}, \underline{x}^{N}, \underline{x}^{N'}) \qquad 2.3.2$$

then for the transport process:

$$\frac{\delta R}{R} = \sum_{k=1}^{G} U_k^{A,R} \frac{\delta x_k^A}{x_k^A} + U_k^{N,R} \frac{\delta x_k^N}{x_k^N} + U_k^{N',R} \frac{\delta x_k^{N'}}{x_k^{N'}} \qquad 2.3.3$$

The elastic cross-section is usually a derived quantity which is positively correlated with the total cross-section, $\underline{x}^{T}$, and anti-correlated with the absorption and inelastic cross-sections. It is therefore convenient to restructure equation 2.3.3 in terms of observables - the independently measured cross-sections, $\underline{x}^{A}$, $\underline{x}^{N'}$ and $\underline{x}^{T}$, for example.

Since

$$x_k^T = x_k^A + x_k^{N'} + x_k^N \qquad 2.3.4$$

and

$$\delta x_k^T = \delta x_k^A + \delta x_k^{N'} + \delta x_k^N \qquad 2.3.5$$

then:

$$\frac{\delta R}{R} = \sum_{k=1}^{G} \left[\frac{U_k^{A,R}}{x_k^A} - \frac{U_k^{N,R}}{x_k^N}\right]\delta x_k^A + \left[\frac{U_k^{N',R}}{x_k^{N'}} - \frac{U_k^{N,R}}{x_k^N}\right]\delta x_k^{N'} + \frac{U_k^{N,R}}{x_k^N}\delta x_k^T \qquad 2.3.6$$

The partial cross-section sensitivity vectors, $\{ \underline{U}_k^{p,R} \}$ k = 1,G can be determined by use of a first order perturbation code, such as SWANLAKE[24], which utilises the regular and adjoint angular fluxes from the DS_n code with which R was determined. Equation 2.3.6 can be abbreviated giving:

$$\frac{\delta R}{R} = \sum_{k=1}^{G} \frac{\Gamma_k^{A,R}}{x_k^A}\delta x_k^A + \frac{\Gamma_k^{N',R}}{x_k^{N'}}\delta x_k^{N'} + \frac{\Gamma_k^{T,R}}{x_k^T}\delta x_k^T \qquad 2.3.7$$

which is an expression relating the fractional change in the predicted value of an integral response to given changes in the independently measured group cross-section data. The $\{ \underline{\Gamma}^{p,R} \}$ represent the set of independent partial cross-section sensitivity vectors.

The fractional variance associated with any prediction R can be

derived from equation 2.3.7 using expectation theory:

$$\frac{\mathrm{Var}(R)}{R^2} = \hat{E}\left[\left(\frac{\delta R}{R}\right)^2\right] \qquad 2.3.8$$

$$= \sum_{k=1}^{G}\sum_{j=1}^{G} \frac{\Gamma_k^{A,R}}{x_k^A}\frac{\Gamma_j^{A,R}}{x_j^A}\mathrm{Cov}(x_k^A, x_j^A) + \frac{\Gamma_k^{N',R}}{x_k^{N'}}\frac{\Gamma_j^{N',R}}{x_j^{N'}}\mathrm{Cov}(x_k^{N'}, x_j^{N'}) + \frac{\Gamma_k^{T,R}}{x_k^T}\frac{\Gamma_j^{T,R}}{x_j^T}\mathrm{Cov}(x_k^T, x_j^T) \qquad 2.3.9$$

$$= \sum_{k=1}^{G}\sum_{j=1}^{G}\sum_{P=1}^{P} \frac{\Gamma_k^{P,R}}{x_k^P}\frac{\Gamma_j^{P,R}}{x_j^P}\rho_{kj}^P\,\sigma(x_k^P)\,\sigma(x_j^P) \qquad 2.3.10$$

where ρ_{kj}^{p} is the correlation coefficient for the group cross-sections. Equation 2.3.10 represents the final form of the expression relating the fractional variance on a calculated prediction to uncertainties in the nuclear data. Although the requirement of the first order perturbation model is that the elements of the fractional cross-section covariance matrices be small, in general the spread in cross-section uncertainty estimates taken from different sources is so large that mathematical rigor can be relaxed; it is conceded that until cross-section error analysis becomes more sophisticated, uncertainty analysis can only furnish a rough estimate of the confidence to be placed on a calculated parameter.

2.4 Sources of Errors and Correlations in Nuclear Cross-Section Data

2.4.1 Point Data Errors

Measured nuclear data parameters are observables. The data given in a nuclear data file (the evaluated point data) represent single points extracted from a population of possible values. The uncertainties on the scalar cross-sections can arise either from uncertainties in the measurement of the cross-section itself or from uncertainties in the measurement of the composite cross-sections. For example:

$$\mathrm{Var}(\underline{x}^A) = \mathrm{Var}(\underline{x}^{(n,\alpha)}) + \mathrm{Var}(\underline{x}^{(n,p)}) + \mathrm{Var}(\underline{x}^{(n,\gamma)}) + \text{etc.} \qquad 2.4.1$$

Using the limited population of measured data and the associated quoted experimental errors, the evaluator can select using some statistical artifice the best estimate of the cross-section and place upper and lower confidence bounds or quote a standard error on the value. This practice has been adopted by evaluators for some data files in ENDF/B-IV (viz C^{12}, O^{16} and N^{14}) and for many more in ENDF/B-V[25]. In most cases the frequency distribution for the measurements is approximately normal and a

standard error can be assigned. In threshold regions, however, the frequency distribution is skew since cross-sections cannot be negative. In these cases, although the confidence bound approach would be more meaningful, the evaluators of ENDF/B have chosen, for reasons of consistency, to replace the skew distribution with a normal distribution with the same mean and approximately the same shape[26] so that an estimate of the standard error can be made.

Unfortunately for data libraries other than ENDF/B the evaluated point data are not always derived in a rigorous statistical way. Often evaluators draw an eye-guide through the measured data and extract the data from this line. Thus the error in the evaluated point data must include not only an estimate of the accuracy of the measured data but also the uncertainty in the fit of the evaluation curve.

2.4.2 Correlations Between Point Data

The simplest identifiable correlation is the partial correlation that exists between derived and measured cross-sections at the same energy. Until recently measurements of the elastic cross-section in all but the simplest nuclei have been fraught with difficulty, and evaluated data for elastic scattering have been inferred from measurements of the absorption, inelastic (or in some cases non-elastic) and total cross-sections. The elastic cross-section is therefore a redundent piece of information which is positively correlated with the total cross-section and negatively correlated with the other partial cross-sections.

Cross-section measurements are frequently conducted over a range of energies and this can lead naturally to the appearance of an energy-dependent correlation. In the simplest form it is inherent in the measurements by way of a systematic error common to all the measurements, such as the uncertainties in the source intensity of an accelerator or the detection efficiency of a counter. An energy-dependent correlation can also arise from the frequently used technique of measuring cross-sections over a range of energies relative to the cross-section at some fixed energy E_o and then subsequently normalising the data to an absolute measurement of the cross-section at E_o. Any later revision of the cross-section at E_o would cause the re-normalisation of the complete set of measurements. Another common experimental practice which leads to an energy-dependent correlation is the use of cross-section standards. In many cases accurate nuclear data can be obtained by measurement of a sample cross-section relative to that of some well-known standard such as $U^{235}(n,f)$, $B^{10}(n,\alpha)$ or $H(n,p)$. The energy-dependent correlation, in this

case also known as the materials correlation, arises in that any revision of the standard cross-section naturally leads to a revision of the sample cross-sections.

The energy-dependent correlation is not merely a trait of the measured data; it can also be introduced in the evaluation process. For instance in energy regions where the physics is well understood and suitable theories exist, nuclear models are often fitted to the measurements and the evaluated data calculated from the model. The uncertainties in the model parameters can introduce an energy-dependent correlation in the evaluated data. Models frequently used in the nuclear data evaluation include the optical potential, the Breit-Wigner resonance approximation, R-matrix theory and the Weiskopf evaporation model. The energy-dependent correlation is usually positive, although in fitting resonances positive or negative correlations can exist.

The evaluator not only uses nuclear theory to fit measured data in areas with good measurement coverage; it can also be used to interpolate data in sparsely measured energy regions and to extrapolate to energies above the measured data. For example there are very few neutron sources capable of providing sufficient flux in the energy range 8 to 14 MeV for cross-section determination; nuclear data in this region has often to be evaluated by nuclear model fitting or by graphical interpolation. If subsequently one of the end points of the fit is re-assessed, the intermediate data will be perturbed by an amount dependent upon the energy displacement from the end point.

2.4.3 Group Processing Errors

Nuclear data in an evaluated data file can only be used in transport calculations by sophisticated point energy Monte Carlo[27] and discrete ordinates codes[28]. For more routine methods of solution, group averaging of the data is necessary. The errors that arise in the processing of nuclear data into multi-group format derive either from the use of an inappropriate weighting function or the choice of an unsuitable fitting algorithm.

The appropriate weighting function for collapsing nuclear data is the point angular differential energy flux. Since this is the quantity desired from the solution of the transport equation, or at least some discrete representation of it, an approximation to the flux, usually called the weighting spectrum is required for group collapsing. The weighting spectrum is usually a simple function of energy, which is isotropic and spatially independent. Two common global weighting spectra are the Fermi slowing-

down spectrum (1/E), used for thin media, and the narrow resonance weighting function, used for deep penetration. The latter spectrum, which in heterogeneous media becomes the Bondarenko background cross-section averaging method[29], takes into account the anisotropic nature of the penetrating flux and the resonance self-shielding imposed on the flux. However these weighting spectra are only approximations and although in smooth regions of the cross-section the errors are small, for regions containing resonances, thresholds or interference minima the errors can be large, especially if the group width is not sufficiently small for either the group collapsing to be independent of the chosen spectrum or the selected global weighting spectrum to be a good approximation to the scalar flux. Moreover in materials such as stainless steel where the 28 keV resonance of nickel overlaps the 27 keV resonance and the 24 keV minimum of iron, the background cross-section method is no longer valid and can lead to erroneously averaged cross-section data. Thus for design calculations in which the number of groups would be of the order 50 or less, and in which the narrow resonance weighting function $1/E\,\Sigma^{T}(E)$ has been chosen to produce spatially independent cross-sections for optically thick shielding media, considerable uncertainties can be introduced into the multi-group nuclear data, particularly in structured regions of the cross-section. At present no suitable method appears to be available for quantifying the magnitude of the uncertainty introduced into the group cross-section data by the choice of an inappropriate weighting function.

In some multi-group data processing programs, for example the MC^2 code[30], a mathematical function is chosen and fitted to the library data prior to collapsing. Whilst the use of such algorithms has been demonstrated in the 'self-consistent' adjustment procedure[31], the fitting function can only be an approximation to the evaluated data in the library and as such must introduce errors into the group cross-sections subsequently produced.

In summary therefore, nuclear data errors can arise from a multiplicity of sources which include the process of measurement, the fitting of nuclear models or evaluators' eye-guides for the purposes of extrapolation or interpolation and from the multi-group averaging of the data so necessary for rapid solution of the transport equation. The measurement uncertainties and the correlations introduced both by nature of the experiment and by evaluation can in general be assessed in the strictest statistical sense, but the errors injected by data processing cannot, as yet, be suitably quantified.

2.5 Methods of Performing Uncertainty Analysis

Three methods of establishing data errors for calculating design uncertainties have recently evolved. For design studies where nuclear data error files are unavailable, a method based on direct re-computation for a fixed model using different (usually national) data bases can establish the magnitude of a 'typical error' due to data uncertainties. Such a method has been used in an NEA/OECD collaborative benchmark exercise[32,33,34] for determining whether Pressurised Water Reactor (PWR) and Fast Breeder Reactor (FBR) shield design target accuracies can be attained. The validity of this approach can be questioned as nearly all national data libraries are evaluated from the same measured data so that the differences produced often reflect the evaluator's credibility, and in some cases also the data processing errors, rather than the accuracy of the cross-section per se.

A more realistic approach requires the generation of problem dependent multi-group correlated error files from the experimental results of integral benchmarks which closely resemble the theoretical problem under consideration - the so-called method of consistency analysis. This method requires a knowledge of the independent multi-group cross-section vectors and their relative group-wise variances. The generation of such correlated error matrices appropriate to an adjusted data set has been sucessfully demonstrated by Campbell and Rowlands[35] for fast reactor core calculations but has yet to be demonstrated in shield design.

Finally, the optimum method for constructing error files is for evaluators to estimate the variances and correlations during the processing of new nuclear data files. A limited number of such error files have been made available with ENDF/B-IV and it is expected that a wider coverage will be included in ENDF/B-V. For those materials without evaluated error correlation matrices, diagonal matrices can be constructed using the compilation of Schmidt[36] for fast reactor materials or the assignments of Simmons and McElroy[37] for detector response functions. Indeed Orphan[38] has constructed multi-group covariance matrices for the partial cross-sections of some nuclei on the basis of conservative error assignments and by fitting correlating functions to the data. Such guessed error data can be very useful in uncertainty analysis despite lacking the statistical rigor of Perey's method[25] for error evaluation in ENDF/B and some examples of the use of these data are given in Section 2.7.

2.6 Target Accuracies on Integral Quantities

Uncertainties on integral responses depend not only upon the medium

interaction parameters dictating neutron transport but also on the response function at the point of interest. If the detector response can be assumed to be independent of the transport process, the fractional error on a calculated design parameter may be expressed as:

$$\frac{\delta R}{R} = \left[\left(\frac{\delta R}{R} \right)^{2}_{\text{TRANSPORT}} + \left(\frac{\delta R}{R} \right)^{2}_{\text{RESPONSE}} \right]^{1/2} \qquad 2.6.1$$

The extension to include response functions which are related to the medium transport parameters is immediate relying on a modification of the sensitivity function[39]. A target accuracy encompasses errors arising at all stages of a calculation - source definition, modelling, method, response data and cross-section data errors; Herrnberger has suggested that the required accuracy be specified at the 2σ level (95.5% confidence level for a normal distribution) and that nuclear data errors alone should contribute no more than one half of this required target accuracy. In cases other than solution by Monte Carlo, method error probability distributions are largely unknown and can be difficult to determine. The required target accuracies for some aspects of shield design have been drawn up independently by Avery et al[40] and by Herrnberger et al[41,42]. The target accuracy is an important quantity to the theoretician because:-

(i) in conjunction with sensitivity analysis, it can be used to interpret the requested data accuracies in WRENDA[1]. For instance, use can be made of the so-called 'measurement sensitivity' defined as the fractional reduction in the standard deviation on an integral response per unit fractional reduction in the standard deviation on a group cross-section.

(ii) For advocates of automated energy group boundary selection schemes, target accuracies provide an important starting point for optimising the calculational effort.

(iii) For a given target accuracy, preferred calculational routes can be recommended.

Clearly whereas uncertainty analysis alone can only identify areas of ill-defined data, a knowledge of the target accuracy can help determine the accuracy requirements for these data.

2.7 Examples of Uncertainty Analysis

Three examples of uncertainty analysis are discussed in this section. The first has been drawn from a recent examination of the data requirements for fusion experiments whilst the other two are NEA theoretical benchmarks. The fusion example is given as a clean source simple geometry problem

which can be easily interpreted in terms of the sensitivity profile and data requirements. The reactor generic design problems, on the other hand, are more complicated and display the situation dependence of the sensitivity profile and data requirements. Moreover they illustrate the differing types of problem to which the optimised data sets from integral benchmark experiments might be expected to apply. Error correlation data from different sources have in some cases been used so that an assessment could be made of the dependence of the response uncertainty on the status and the assumptions inherent in the cross-section error data used.

2.7.1 The Biological Shield for JET

The calculational and geometric details of this fusion experiment have been given elsewhere by the author[43,44] but essentially the problem comprises a 14 MeV isotropic neutron source surrounded by a 3 m thick concrete blockhouse. Sensitivity analysis determined that nearly half the total problem sensitivity arose from uncertainties in the cross-section data for oxygen and the total sensitivity profile (Figure 2.1) showed that cross-sections at the source energy and in the 2.35 MeV window dominate the neutron transport. The uncertainties on the predicted neutron dose-rate (Table 2.1) outside of the biological shield were determined using 42 group partial covariance matrices derived from the ENDF/B-IV oxygen data file[45] using the processing code MCOVE[46] and a set of 15 group error matrices for oxygen published by Weisbin et al[47]. The 15 group data was also derived from ENDF/B-IV using PUFF[48] and both matrices were collapsed using a 1/E spectrum.

The partial cross-section measurement sensitivity (Figure 2.2) defined in Section 2.6 (i) has the functional form:

$$\frac{\delta \ln(\sigma(R)/R)}{\delta \ln(\sigma(x_k^r)/x_k^r)} = \frac{R^2}{\sigma^2(R)} \sum_{j=1}^{G} \frac{\Gamma_k^{cR}}{x_k^r} \frac{\Gamma_j^{cR}}{x_j^r} \mathrm{cov}(x_j^r, x_k^r) \qquad 2.7.1$$

Figure 2.2 shows that using Schmidt data[36] with zero energy-dependent correlation 70% of the error arising from oxygen cross-section uncertainties is derived from the source group absorption cross-section. The ENDF/B-IV error data puts the proportion at 86% being due to the 14 MeV (n,α) cross-section.

2.7.2 The PWR Theoretical Benchmark

The specification of the NEA PWR theoretical benchmark exercise has

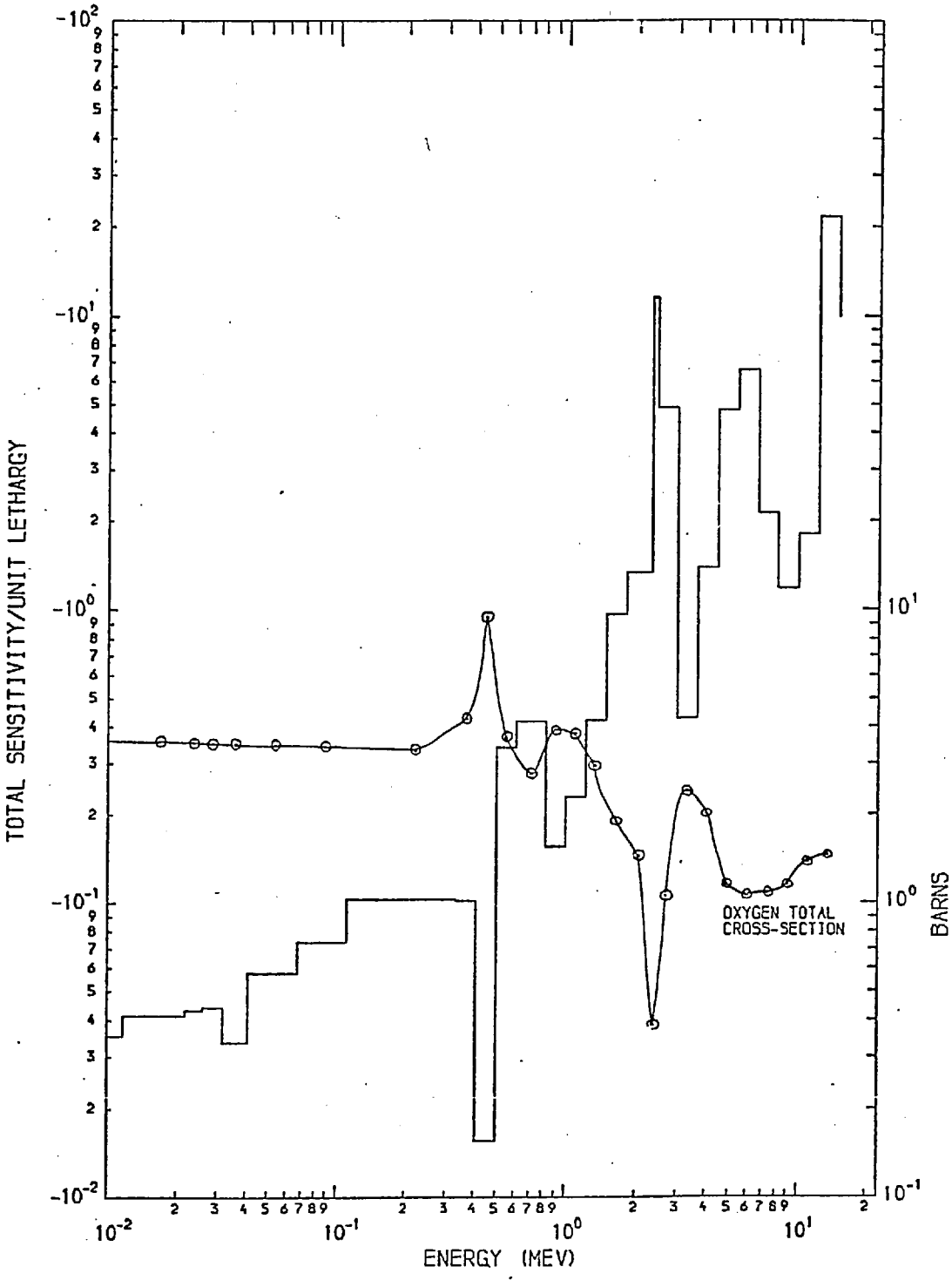


FIG. 2.1 SENSITIVITY PROFILE OF OXYGEN CROSS-SECTION DATA FOR PREDICTION OF NEUTRON DOSE-RATE OUTSIDE JET SHIELD.

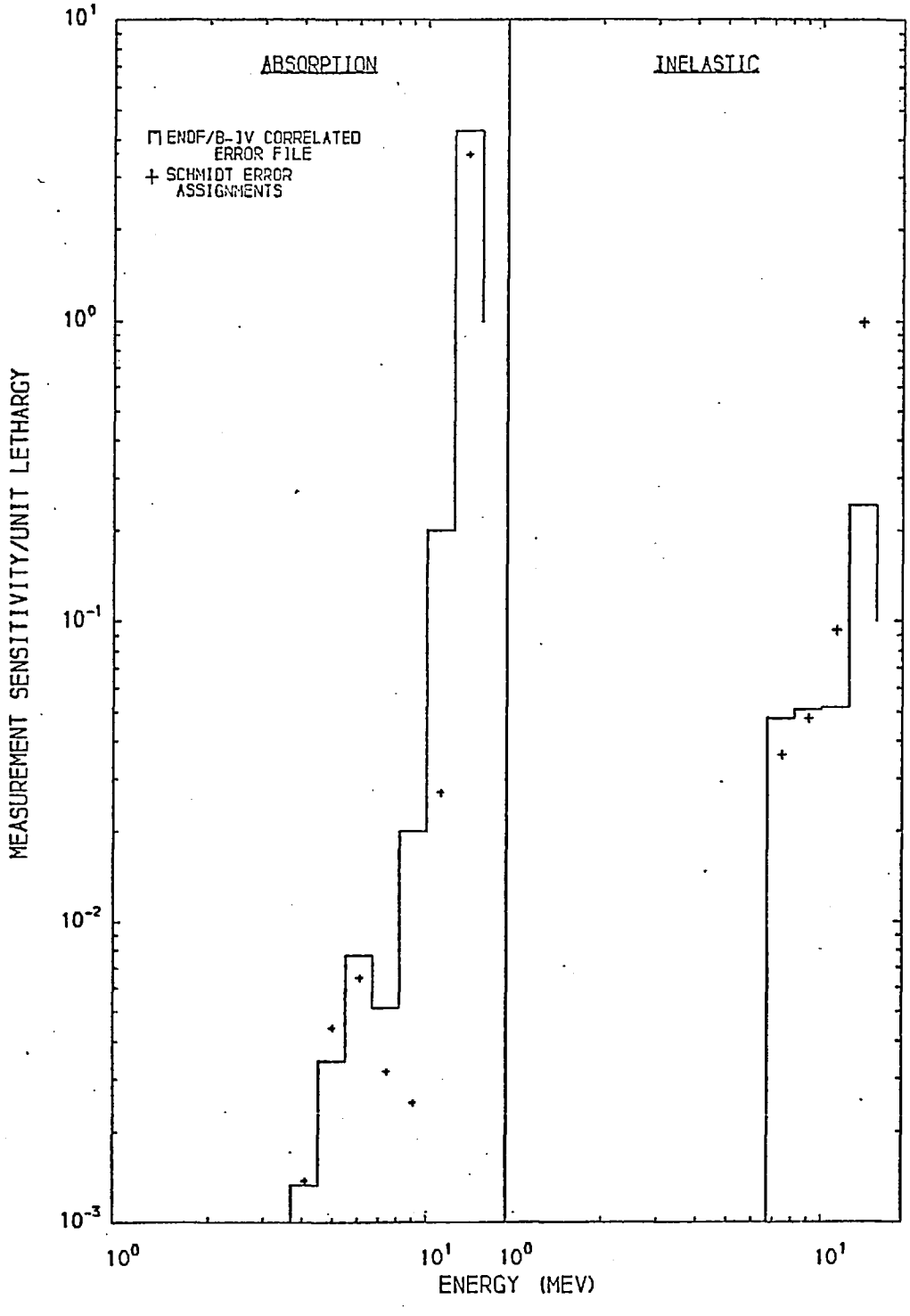


FIG. 2.2 MEASUREMENT SENSITIVITY PROFILE OF OXYGEN CROSS-SECTION DATA - DOSE-RATE OUTSIDE JET SHIELD.

been given by Hehn et al[49] and a discussion of the calculations and results is given by Lympany et al[50] and McCracken[51]. The sensitivity of the damage-rate in the pressure vessel (Figure 2.3) is dominated by the nuclear data for hydrogen (53%), oxygen (17.6%) and iron (15.9%). Since the cross-section for hydrogen is one of the best known (±2%), the uncertainties in the nuclear data for oxygen and iron dominate the expected error in the damage-rate prediction. The covariance matrices for oxygen were taken from Weisbin et al[47] and ENDF/B-IV[45]; for iron the error data of Weisbin et al have been compared with error estimates made by Orphan and published in the work by Gerstl et al[38]. Using the Schmidt[36] data, 92% of the uncertainties arising from iron cross-sections were derived from the inelastic cross-section; from Figure 2.4 it can be seen that group cross-section data in the energy range 5.5 to 10.0 MeV dominate the measurement sensitivity. For oxygen cross-sections the uncertainties derive from both the inelastic cross-section (47%) and the total cross-section (48.5%). The region of interest (Figure 2.4) for the inelastic cross-section (8.2-12.2MeV) is higher than that for the total cross-section (6.7-10.0 MeV).

2.7.3 The FBR Theoretical Benchmark

A general description of the problem has been given by Barré[52] and details of the calculations can be found in Lympany et al[23] and McCracken[51]. The sensitivity of the sodium (n,γ) activation-rate in the heat-exchanger and of the iron displacement-rate on the outside of the radial shield to the cross-section data for iron and sodium are given as Figures 2.5 and 2.6. In the uncertainty analysis, error data for sodium and iron were taken from Weisbin et al. The matrices of Orphan et al[38], which were derived for CTR calculations, only covered the energy range above 2 MeV and therefore could not be used. Using the data of Schmidt[36] the measurement sensitivity profile (Figure 2.7) showed that 96% of the uncertainty due to iron cross-sections and 97% of the uncertainty arising from sodium cross-sections for the prediction of the iron damage-rate in the core restraint structure was due to the respective elastic cross-sections in the vicinity of the 300 keV interference minimum. For the secondary sodium activation in the heat-exchanger, the elastic cross-section of iron around 300 keV was responsible for 95% of the error resulting from iron cross-sections whilst only 48.7% was due to the corresponding sodium cross-section (Figures 2.8(A) and (B)).

2.8 Consistency Analysis

Consistency analysis in the simplest form involves the comparison of

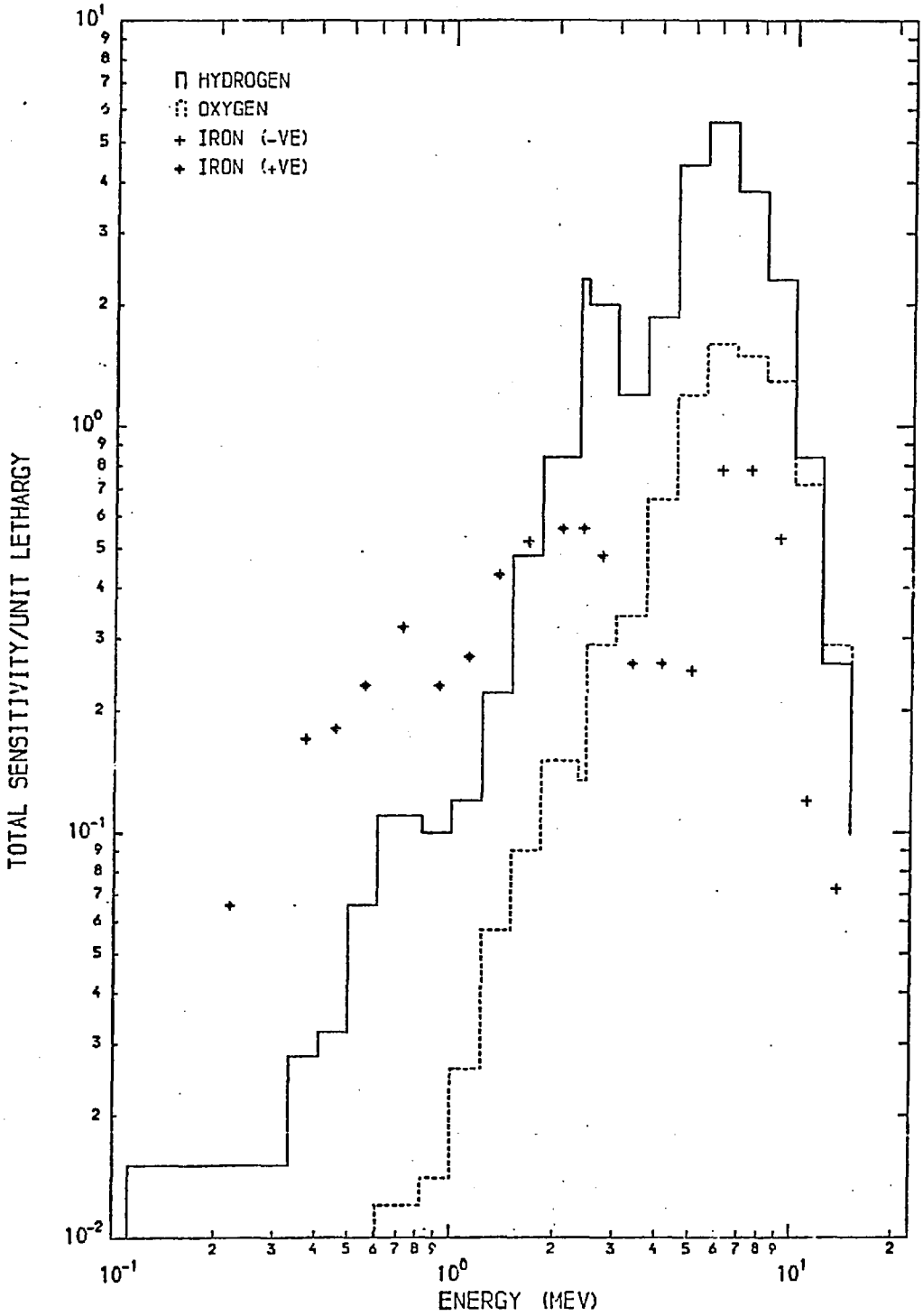


FIG. 2.3 SENSITIVITY OF PWR PRESSURE VESSEL DISPLACEMENT RATE TO IRON OXYGEN AND HYDROGEN CROSS-SECTION DATA.

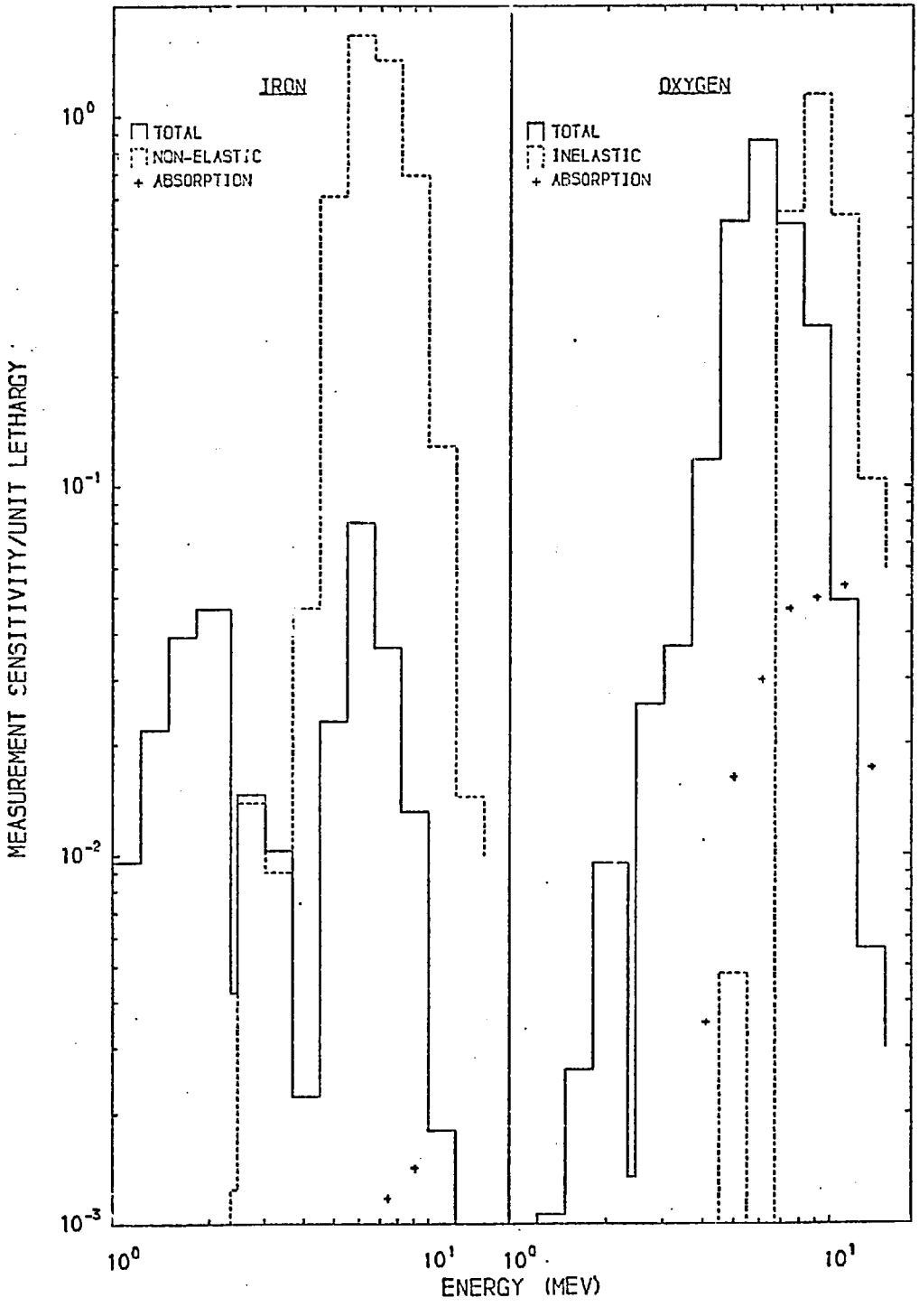


FIG. 2.4 MEASUREMENT SENSITIVITY OF PWR PRESSURE VESSEL DISPLACEMENT RATE TO OXYGEN AND IRON CROSS-SECTION DATA.

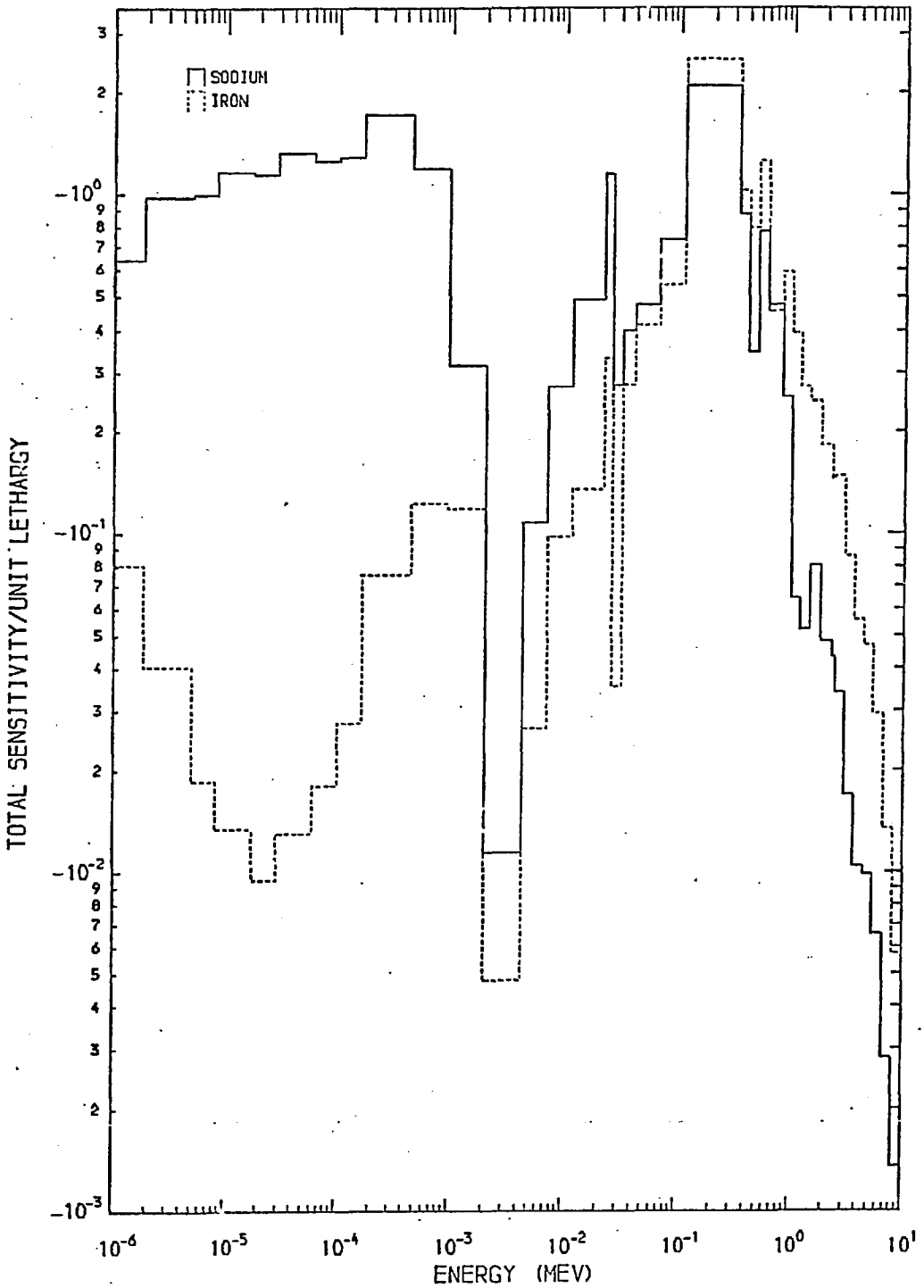


FIG. 2.5 SENSITIVITY OF FBR SODIUM CAPTURE-RATE IN THE HEAT EXCHANGER TO IRON AND SODIUM CROSS-SECTION DATA.

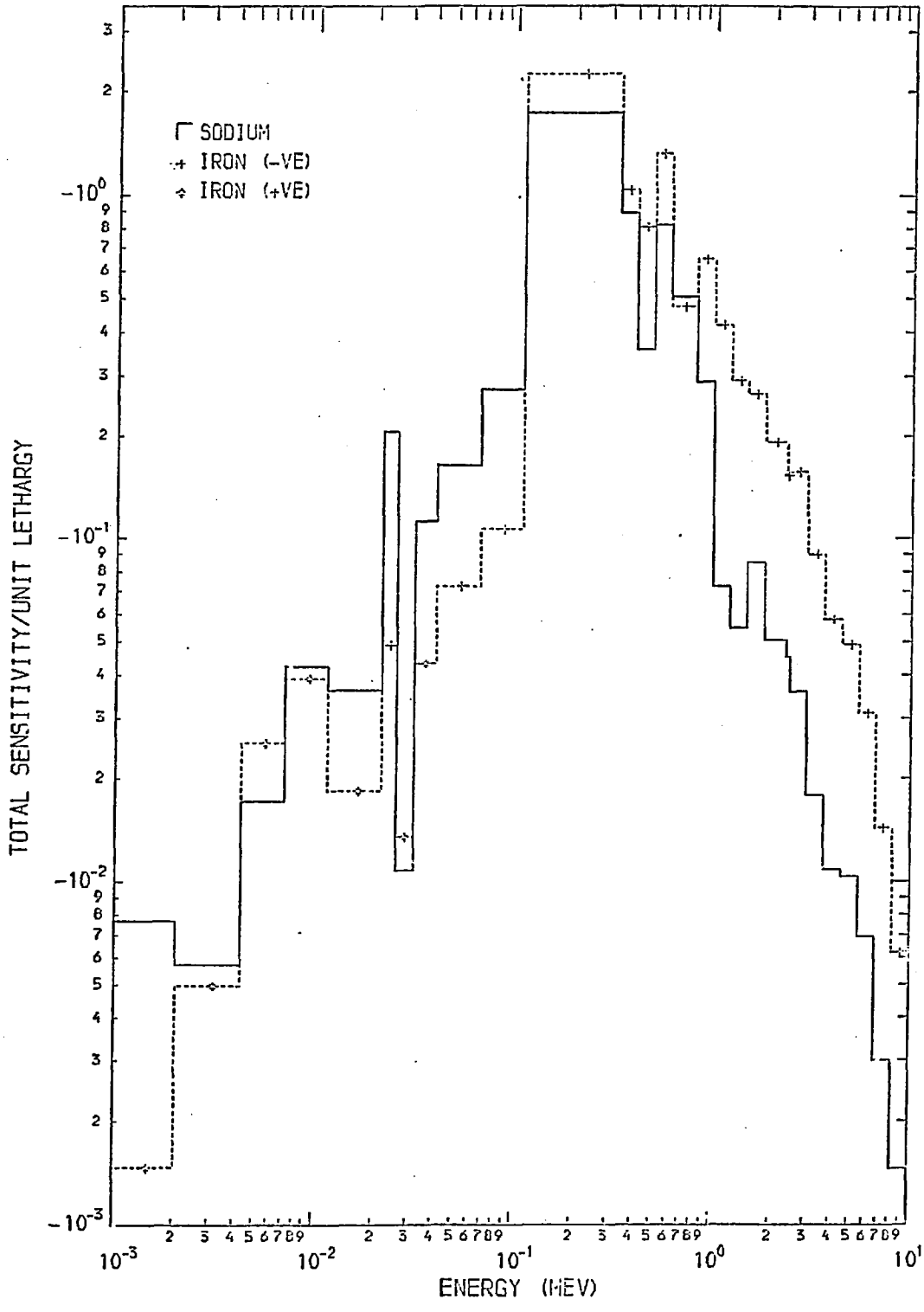


FIG. 2.6 SENSITIVITY OF FBR CORE RESTRAINT STRUCTURE DISPLACEMENT RATE TO IRON AND SODIUM CROSS-SECTION DATA.

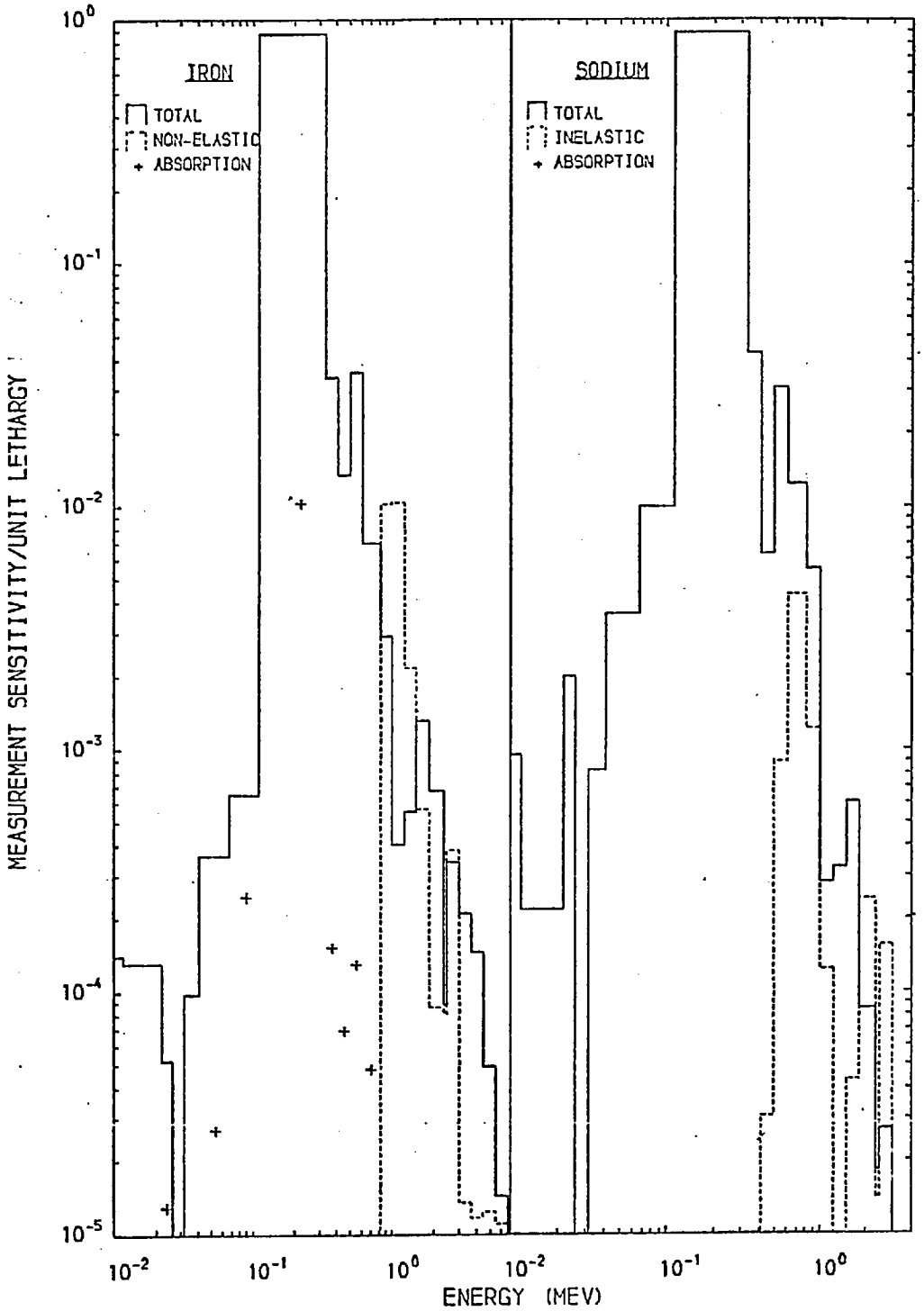


FIG. 2.7 MEASUREMENT SENSITIVITY OF FBR CORE RESTRAINT DISPLACEMENT RATE TO SODIUM AND IRON CROSS-SECTION DATA.

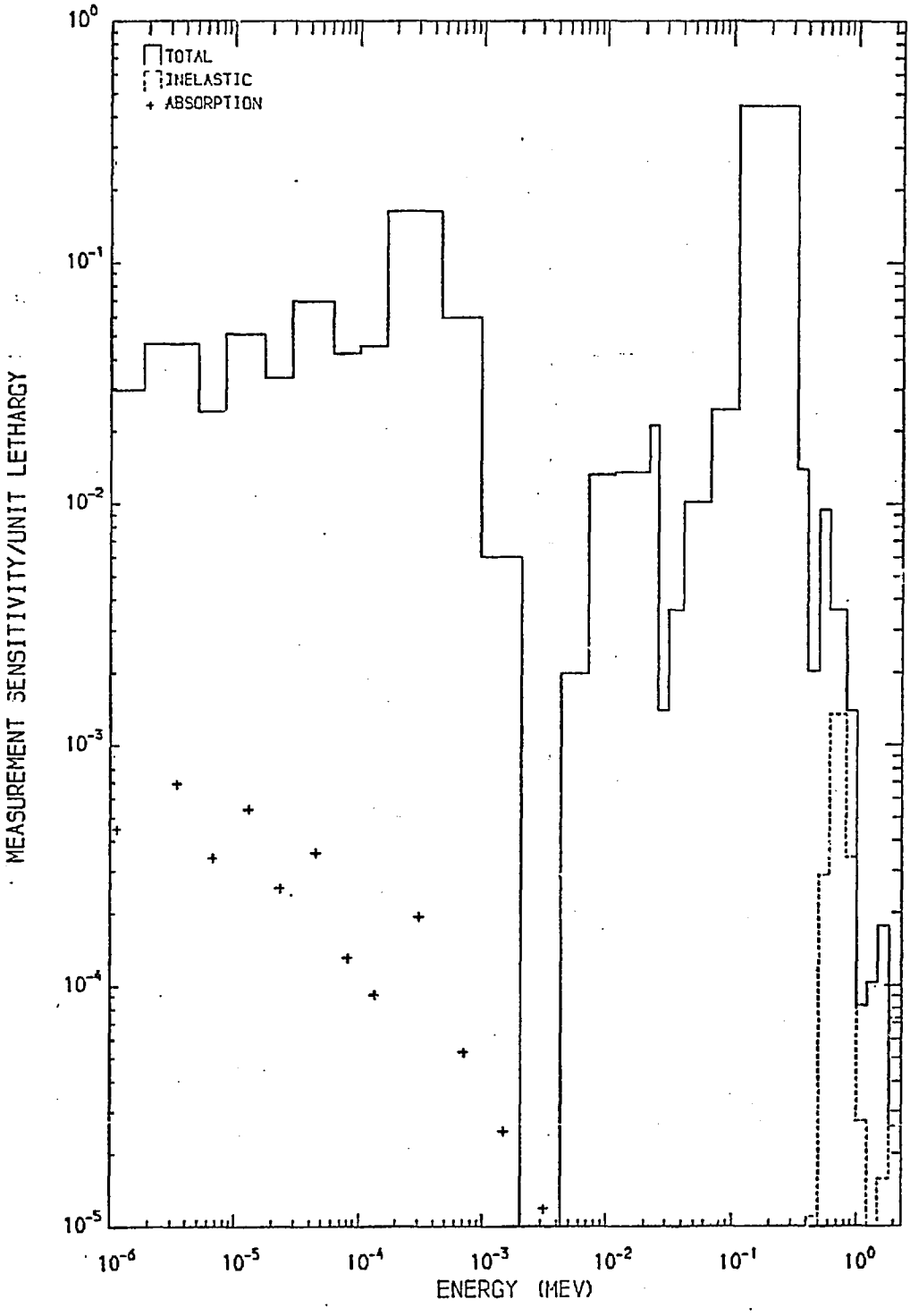


FIG. 2.8(A) MEASUREMENT SENSITIVITY OF SODIUM PARTIAL CROSS-SECTION DATA FOR SECONDARY SODIUM ACTIVATION.

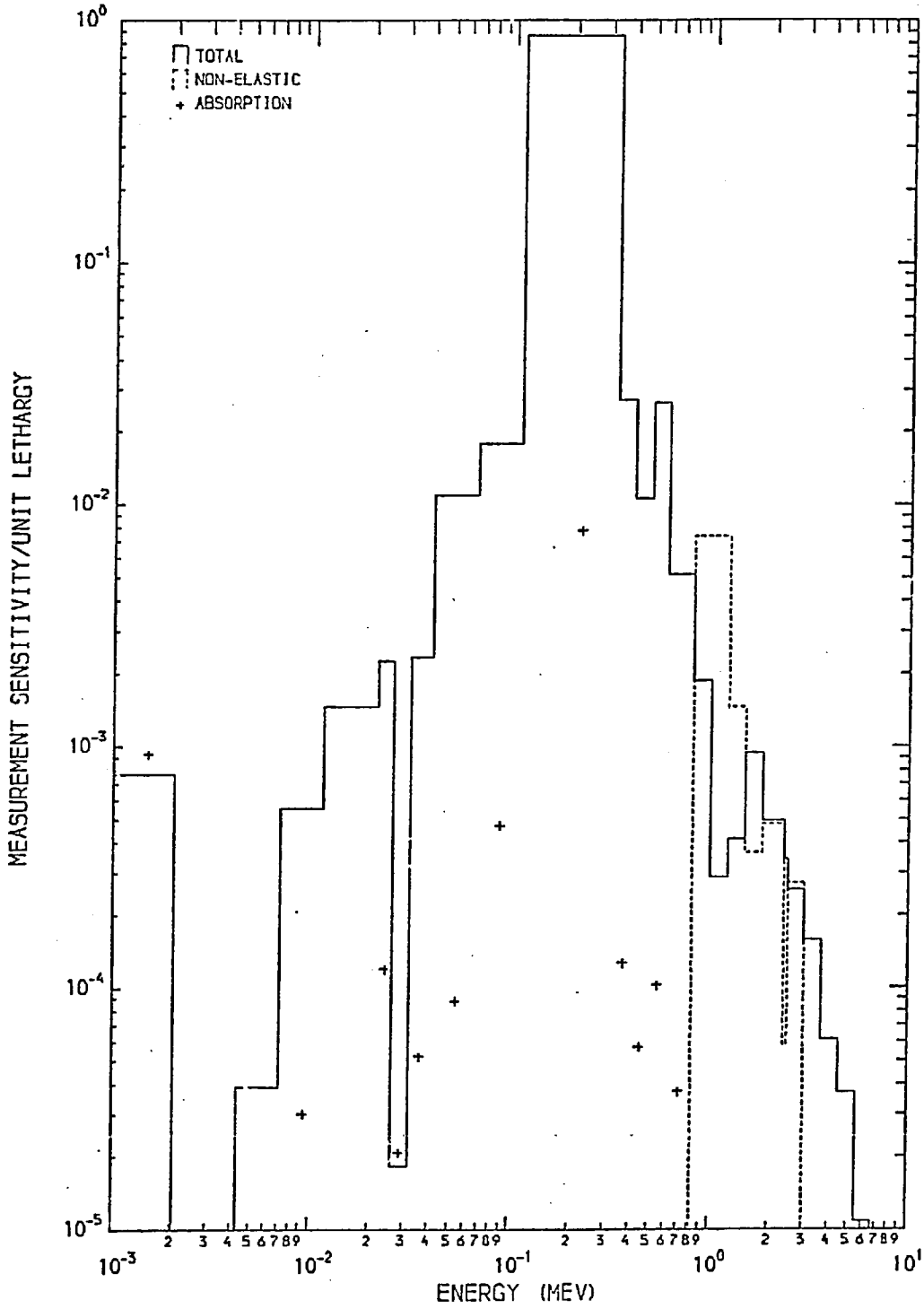


FIG. 2.8(B) MEASUREMENT SENSITIVITY OF IRON PARTIAL CROSS-SECTION DATA FOR SECONDARY SODIUM ACTIVATION.

Table 2.1

Comparison of Uncertainty Estimates (1σ) Using Available Cross-Section Error Data

Generic Design	Target Quantity	R.T.A.	Nuclide	Schmidt Upper Bound	ENDF/B Matrix	Weisbin Matrix	Gerstl Matrix
JFT	Personnel Exposure	50%	O	80%	51%	47%	-
FWR	P.V. Damage-Rate	20%	O	8.5%	2.7%	2.6%	-
			Fe	7.9%	-	9.5%	7.4%
FBR	R.S. Damage-Rate	20%	Na	14.6%	-	7.0%	-
			Fe	9.8%	-	2.8%	-
FBR	H.X. Activation-Rate	50%	Na	56.9%	-	40%	-
			Fe	22.5%	-	4.4%	-

In the above analysis, it has been assumed that fractional error matrices from the various sources are applicable to the data in the UKNDL; for small differences between libraries, the assumption is equivalent to the use of linear perturbation theory for the cross-section expansion.

calculated integral parameters with experimental measurements. In the forward problem, an uncertainty analysis is performed to assess the quality or the consistency of the cross-section error data used. If the predicted errors for a set of responses are in agreement with the observed deviations between calculation and measurement then the cross-section data and the associated error matrices can be described as "consistent". In contradistinction, if the errors predicted from the uncertainty analysis are not in accord with the discrepancies between theory and experiment even after the limitations of first order perturbation theory are considered, then various statistical principles can be applied (the method of χ^2 scaling can be used if à priori all the error data are equally likely) to obtain consistency. In this way error data can be obtained which is a more likely representation of the cross-section uncertainties than the initial data. In this form the method can also be used to "weigh" various different error evaluations on the same measured data.

The inverse problem of consistency analysis concerns itself not with adjusting the error data for a given mean (cross-section value) to gain consistency, but with, in the first instance adjusting the mean for a given error and statistical model. This form of the problem has been used by many workers in reactor physics (e.g. Campbell and Rowlands[35]) to produce "in-house" data sets optimised using integral experiments. This so-called adjustment aspect of consistency analysis is founded on the statistical proposition that ranges of χ^2 per degree of freedom (or any other test of model quality) exist in which dissatisfaction can be addressed towards both the mean and its expected standard error. The central philosophy of the method rests with the use of high quality integral measurements in conjunction with linear perturbation theory to displace the means to values which are more likely in terms of the statistical method adopted. The displacement of the cross-section values introduces mathematical correlations between the group cross-section data and if the adjustments are large, the injected correlations can swamp the original cross-section error data and in this case the resultant covariance matrix is described as being appropriate to the adjusted (and possibly optimised) cross-section data set. Moreover this method of finely tuning nuclear data for specific design situations removes uncertainties arising from group collapsing and in some cases neutron transport methods, and is thought by some workers to be superior to attempts by evaluators to identify all the important correlations underlying evaluated nuclear data.

2.9 Summary

Sensitivity analysis provides a rapid, if approximate, method for analysing the effects of data changes on the solution of the transport equation. These effects may be quantified in terms of a single number - the integral uncertainty - which is of use to the technologist or administrator who does not wish to concern himself with the details of differential cross-section uncertainties and correlations. Sources of uncertainty information for evaluated data have been cited and the effect of different error data on integral uncertainty prediction has been investigated.

The concept of uncertainty analysis may be still more of an art than a science in that it depends on a subjective assessment of the correlations in nuclear data, the ability of the evaluator to identify possible large correlations and his credibility in weighing differential measurements (the differences between which often greatly exceed the quoted errors) against each other. The dual roles of consistency analysis have been shown to increase the confidence that can be given to calculated predictions of integral uncertainties. In the forward mode, the method can be used to check the adequacy of the evaluated (or otherwise) error correlation matrices in a rigorously defined environment. Such a method allows the assessment of the performance of different sets of matrices possibly in a situation close to the design context where they will be of more value. On the other hand, the inverse problem of consistency analysis can furnish optimal data sets with appropriate error correlation matrices for use in similar problems. It is with this aspect of nuclear data analysis that the remaining chapters of this work are concerned.

CHAPTER III

A COMMENTARY ON INTEGRAL EXPERIMENTS AND NUCLEAR DATA ADJUSTMENT METHODS

3.1 Integral Experiments

In fast reactor physics the integral experiments mounted have been 'mock-up' versions of design study cores. Indeed the assembly is made to resemble as closely as possible the cold clean reactor core. During the conduct of the experiment fission-rates, leakage, critical sizes and k_{eff} are measured[53] and compared with calculations using design tools viz. diffusion theory. The cross-section data can then be adjusted according to some prescription in order to obtain closer agreement with experiment. It is often argued that the adjustments do not represent purely data related uncertainties (errors in the evaluated data and inappropriate group condensation), but also account for errors arising out of the inappropriate use of diffusion theory in quasi-heterogeneous systems. Since in the reactor core situation the measured responses are those desired by the designer, and the calculational method and data are simple and appropriate to design work, the adjustment of the cross-section data, for whatever reason, will produce a data set which is optimised for that type of reactor core. This type of pragmatic approach has been adopted by the reactor physics community as an expedient to better quality design calculations, whilst awaiting the arrival of high quality nuclear data and the emergence of more rapid techniques for the accurate solution of the neutron transport equation (e.g. better DS_n methods and developments in finite element techniques).

The situation in reactor shielding is very different. The design quantities of interest such as nuclear heating, biological dose-rates and material damage-rates cannot be measured in integral experiments; instead neutron spectra and/or foil activation measurements have to be made. Uncertainties are therefore injected into the calculation-to-measurement comparison through unfolding schemes, counting techniques and flux-to-response conversion factors. Moreover from the design viewpoint full scale reactor shield 'mock-ups', with the plethora of duct and instrumentation penetrations, are rarely possible so that the methods and data have to be tested in much simpler situations. These clean source, simple geometry single material experiments, which can be wholly unrelated to design situations, have sometimes been referred to as DATAM[54] experiments in that their purpose is to check data and methods. The data related effects are assessed using nominally exact methods of solution of the transport equation such as Monte Carlo or discrete ordinate techniques; the performance of simpler design oriented codes such as removal diffusion theory can be subsequently tested using

where possible the same nuclear data[50,55]. Since the DATAM experiments can rarely be extrapolated to provide bias factors for design calculations, the performance of the method and data must be accurately and independently assessed.

The method of consistency analysis can be used to optimise multi-group nuclear data sets in accordance with some statistical prescription. The adjustment factors can be interpreted in two ways. The adjustments can be considered to be order of magnitude estimates of the typical errors on the data contained in the original data set[56] and so used in an uncertainty analysis, or a new adjusted optimal data set can be constructed with an appropriate covariance matrix and this latter set used in design studies and related uncertainty analyses.

In either case for shielding studies it is important that the integral experiment, against which data and methods are being tested, should have a sensitivity profile closely resembling that of the shield design for which the results of the consistency analysis are to be used. If the integral benchmark experiment sensitivity profile has poor coverage in a particular energy region, it cannot be expected to pass sensible comment on the nuclear data in that energy range or on any method approximations particularly pertainent in that region. The nuclear data requirements for radiation shielding cover a wide range of energies and it is only recently through the conduct of uncertainty exercises on a few generic design problems that the extent of these needs are being identified. For example data at 14 MeV in iron is of importance in D-T fusion experiments[43], whereas in PWR pressure vessel shield design, data at 7 MeV are of more interest[50] and as seen in the last chapter, it is the intermediate energy nuclear data at around 300 and 500 keV in iron that is most sensitive in sodium cooled FBR design studies[23]. No integral benchmark experiment can be expected to be simultaneously sensitive to data over such a wide range of energy.

In tackling the problem of data testing benchmarks the shielding community have in general chosen either fission neutron sources (U^{235} and Cf^{252}) or an accelerator target neutron source making use of the D-T reaction. Experiments utilising reactor leakage spectra have also been devised but the difficulties of spectral characterisation of the source in a high γ-ray field have limited the usefulness of the measured data from such facilities[57]. The geometries of the experiments have, by necessity of modelling, been simple mainly comprising slabs, cylinders and spherical shells. The use of a fission source and optically thick

penetration depths (30 cm or more) allows an assessment of the quality of the data in the slowing-down region (1 keV - 1 MeV) and careful liquid scintillator spectrometry can extend the measurement range up to about 7 MeV. Above this energy the liquid scintillator becomes saturated by the high slowing-down flux and unless this is removed by the use of a light water filter, for example, no measurements at higher energies can be attempted using spectrometers. The use of water to filter a fission source spectrum (a high band filter) has been considered for the ASPIS facility[58] but difficulties arise from the requirement either to measure the angular leakage spectrum at the water-shield interface for use as the neutron source in the penetration calculation or to use the original fission source and allow for uncertainties in the oxygen cross-section (hydrogen is considered to be sufficiently well-known) as well as in the shield data when adjusting the nuclear cross-section parameters. Such measurements have indeed been performed on the ASPIS iron benchmark[59] but have not yet been interpreted. On facilities of higher power, for example EURACOS-II[60], high energy threshold detectors such as $Al^{27}(n,\alpha)$ and $Mg^{24}(n,p)$ ($E_{th} > 6$ MeV) can be irradiated to produce statistically meaningful measurements. Unfolded and calculated flux spectra for the ASPIS iron experiment are given in Figure 3.1.

From the viewpoint of testing the adequacy of the data for fusion reactor design and for the wider coverage implied, groups at IKE Stuttgart[61] and JAERI[62] have used 14 MeV neutrons from D-T sources for iron data studies. The leakage flux from an iron cylinder of 30 cm radius and 20 cm length is shown in Figure 3.2 and the sensitivity of the total scalar flux to the cross-section data is given as Figure 3.3.

It is obvious therefore that for the purpose of data testing in a particular energy region, consideration has to be given both to the choice of neutron source and to the sensitivity of the detector distribution to the nuclear data. Whilst the preceding discussion has been concerned with experiments in iron, it should be stated that several experiments have been conducted in sodium[63,64] and indeed two laboratories have been engaged in multi-layer integral experiments. The team at Cadarache have conducted a series of penetration experiments, on the reactors HARMONIE and TAPIRO, with mixtures of varying proportions of sodium and iron[65]. Unadjusted calculations have been carried out using a suite of design oriented codes designated PROPANE-0[66] and it is intended to optimise the nuclear data using the "formulary" PROPANE-1[67]. No results have yet been published. In contradistinction,

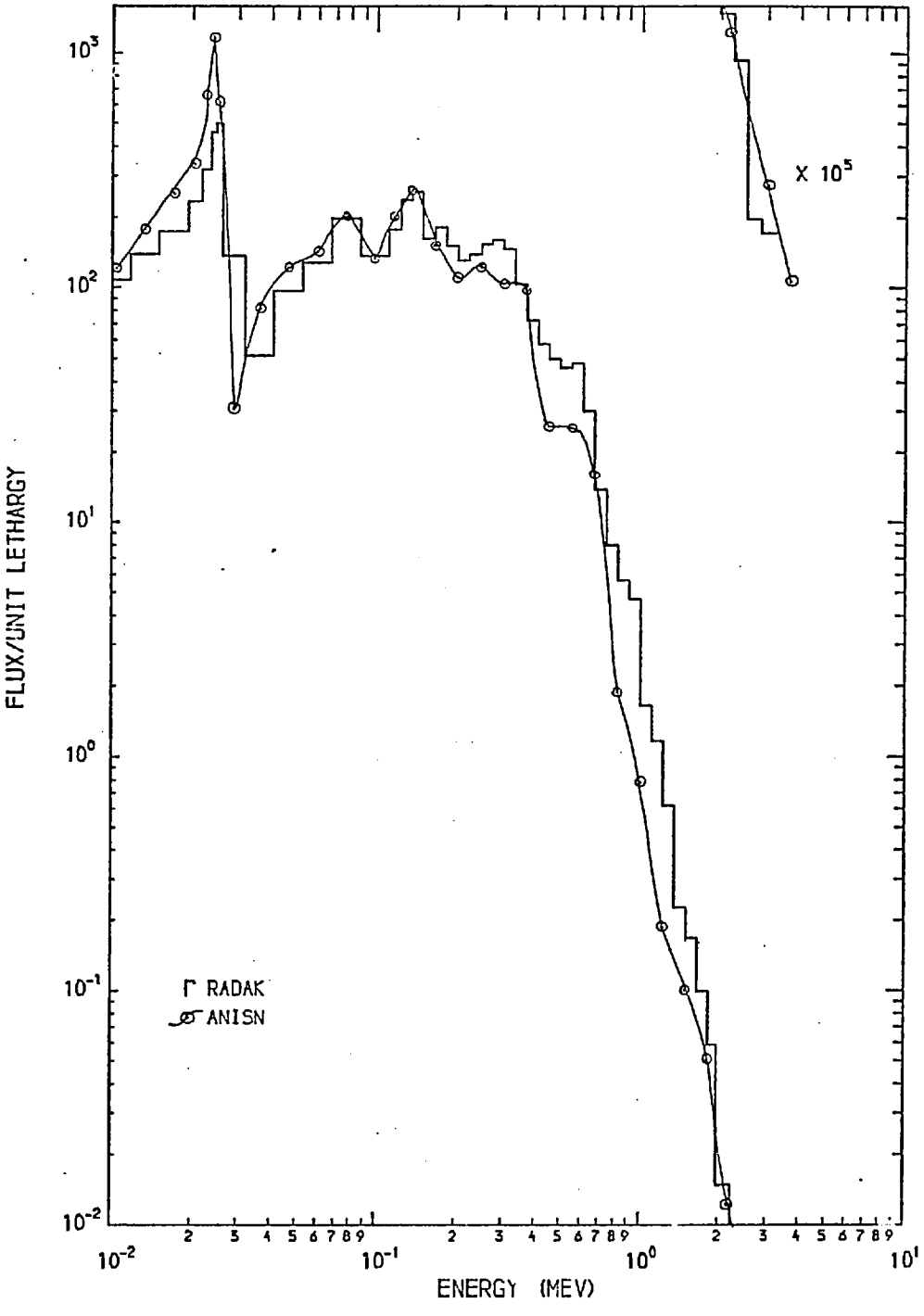


FIG. 3.1 COMPARISON OF CALCULATED FLUX PROFILE WITH RADAK UNFOLDED SPECTRUM MEASUREMENT AT 76.2CM POSITION.

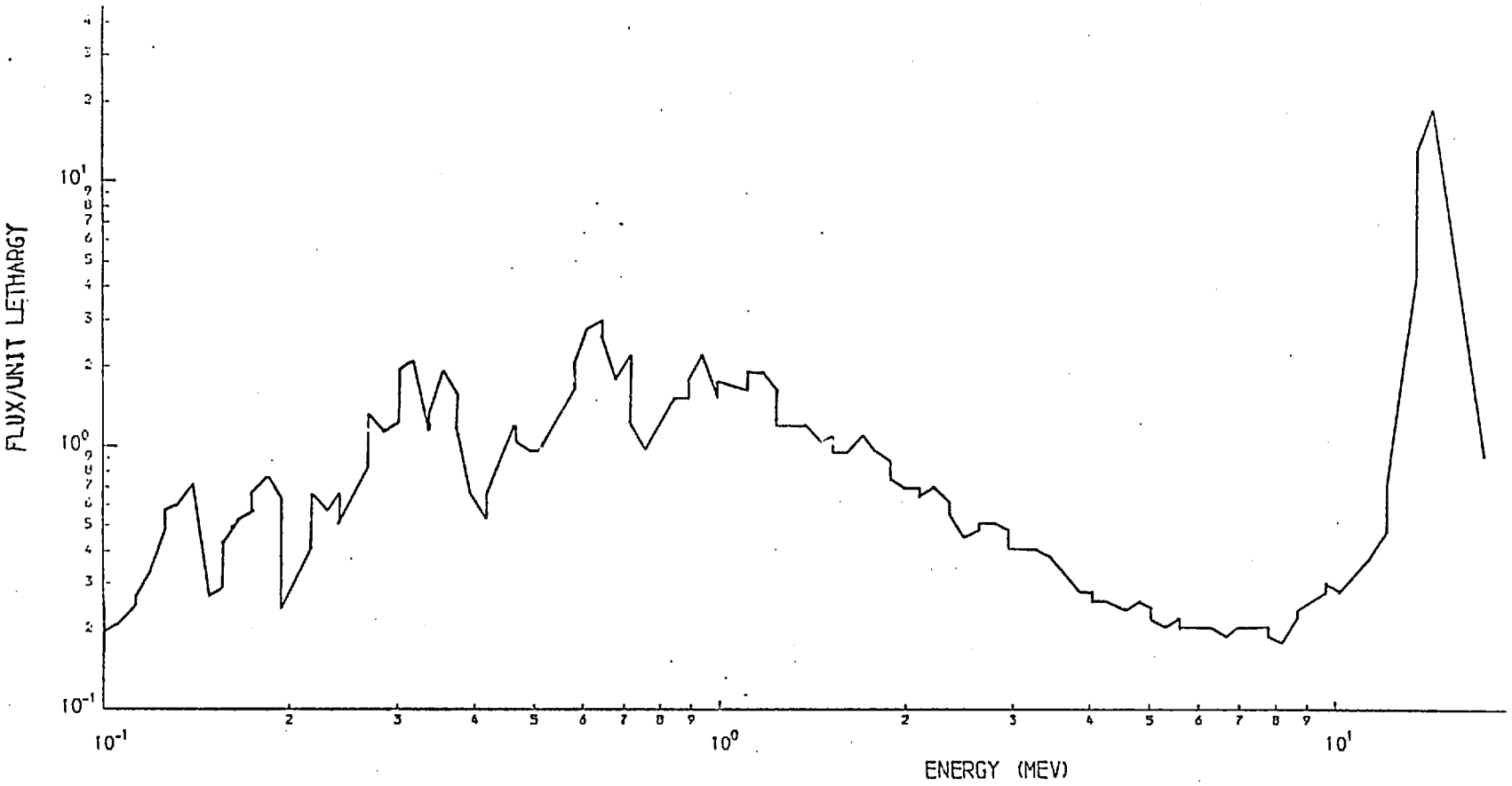


FIG 3.2 MEASURED NEUTRON FLUX PROFILE DERIVED FROM A 14 MEV SOURCE AFTER PENETRATION THROUGH AN IRON CYLINDER (30cm×20cm) (after (61)).

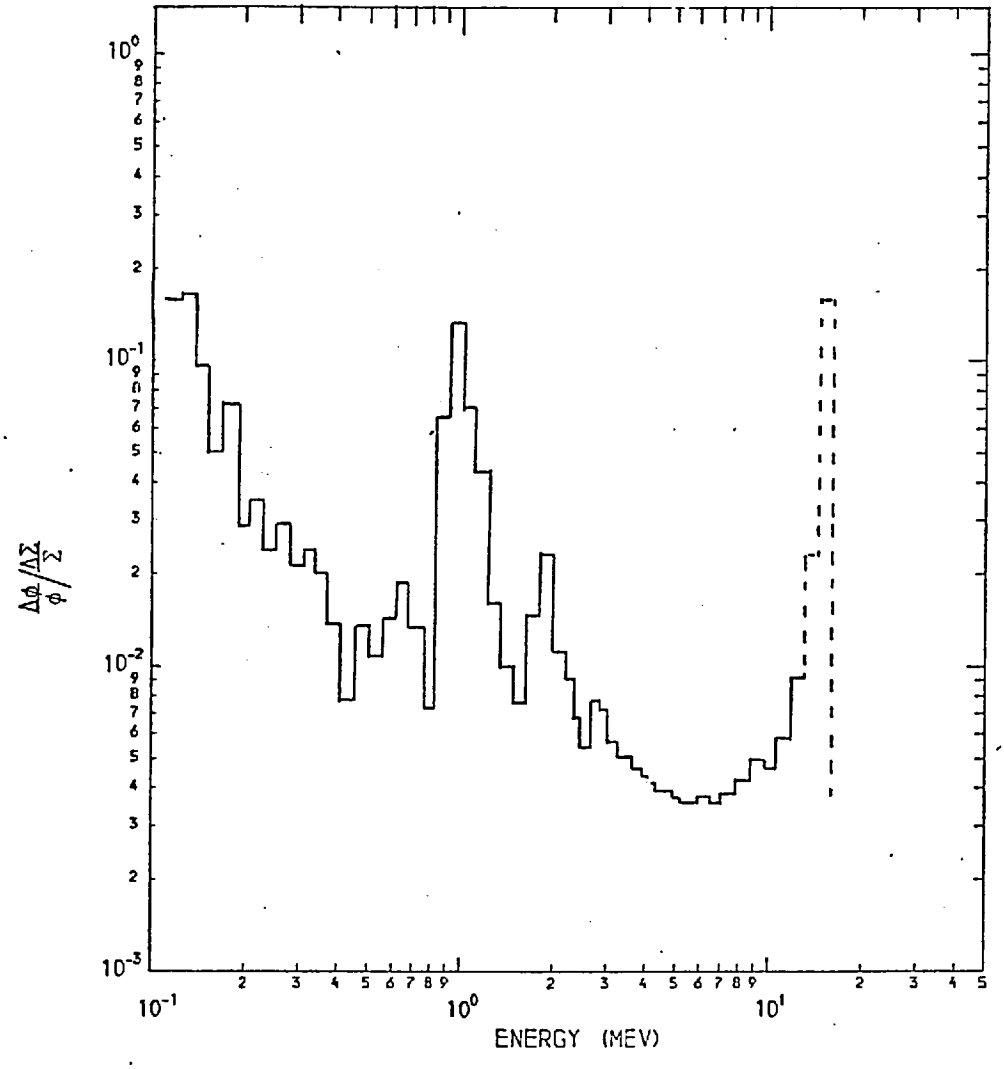


FIG 3.3 SENSITIVITY PROFILE FOR IRON CYLINDER EXPOSED TO A 14 MEV SOURCE (after (61)).

the results of an attempted adjustment for the multi-layer sodium, iron and stainless steel deep penetration experiments at TSF[68] have been given by Oblow and Weisbin[69,70]. The results of 21 different configurations were analysed and data adjustments were produced for sodium and iron using the FORSS[71] code system. In two seperate exercises subsets of 5 and 7 configurations, with similar sensitivity profiles to the complete set of 21 experiments, were used in the consistency analysis and the resultant adjusted data sets used in comparison calculations for the excluded configurations. The subset adjusted data sets failed "by a wide margin" to predict the responses of the other experiments. The major cross-section adjustments obtained with the subset of 7 experiments (reported at Vienna) and with the full 21 configurations (reported at Oak Ridge) are summarised in Table 3.1 and can be seen to be very different and in some cases inconsistent.

Table 3.1

Comparison of Cross-Section Adjustments for ENDF/B-IV Sodium and Iron Predicted from a Subset of 7 Experiments with those Obtained from the Full 21 Configurations

Cross-Section	Na(n,n)		Na(n,n')		Fe(n,n)		Fe(n,n')	
Configuration	21	7	21	7	21	7	21	7
< 1 keV	-8%	-3%	-	-	5%	-6%	-	-
1-250 keV	6%	-	-	-	-	-	-	-
300 keV	-13%	-5%	-	-	-	-	-	-
1-5 MeV	4%	-13%	-3%	-14%	-5%	3%	8%	-4%
5-15 MeV	5%		-3%		6%		-7%	

The group cross-section standard deviations are not given so that it is not possible to determine if the adjustments in Table 3.1 are significant. However the authors do indicate that the iron adjustments arose primarily in the stainless steel regions so that contributions from nickel, chromium and manganese are most likely included. This example clearly indicates the pitfalls that can arise in a heterogeneous shield arrangment where the neutron spectrum may never achieve an equilibrium distribution in the shield. Indeed the experiments can be likened to studies where filters are interposed between the reactor

source and the shield in order to alter the energy distribution of the source. The concept of a stainless steel benchmark will be considered in the conclusions of this work, but it is evident that in radiation shielding, the performance of single material benchmarks to check methods and adjustment procedures is an important pre-requisite to the examination of more complicated materials geometries, except in those cases where the experiment to be conducted essentially models all the relevant features (similar sensitivity profile) of the shield design for which the data set is to be used. It is for this reason that the very extensive analysis, which forms the bulk of this work, has been conducted on the ASPIS benchmark experiment on neutron penetration in iron.

3.2 Methods of Nuclear Data Adjustment

3.2.1 Introduction

It is appropriate at this stage to review some of the important concepts embodied in the methods of data adjustment which have emerged in core reactor physics over the past decade and to examine why the existing tools are unsuitable for use in shielding data optimisation. Particular attention will be given to the treatment of systematic errors in the integral data and a discussion will be conducted on the propriety, or otherwise, of linking adjustments in group interaction constants to the parameters of the nuclear models used, either in fitting algorithms for group condensation codes or for adjustment of the nuclear data library.

3.2.2 Reactor Physics Data Adjustment Methods

The history of the adjustment of multi-group neutron interaction parameters by fitting integral measurements stems in the U.K. from the work of Pendlebury et al[72,73] and later by Macdougall and Rowlands[74]. In parallel with this work has been the development of methods by Gandini[75], Barré et al[76], Pazy et al[77] and Mitani and Kuroi[78]. The methods basically disagree on the treatment of the energy-dependent correlation in the nuclear data and of the systematic errors in the cross-section data and the integral measurements. The algorithm used by Macdougall and Rowlands required a least squares fit to both the integral and nuclear data parameters:

$$\text{Min } F = \sum_{p=1}^{P} \sum_{k=1}^{g} \left\{ \frac{f_k^p}{g_k^p} \right\}^2 + \sum_{i=1}^{n} \left\{ \frac{d_i}{e_i} \right\}^2 \qquad 3.2.1$$

where:

f_k^p is the fractional group cross-section adjustment for the p^{th} partial cross-section

g_k^p is the fractional standard deviation of the differential cross-section which is assumed to be normally distributed

d_i is the residual fractional discrepancy in the estimate of the integral measurement obtained using the adjusted nuclear data

e_i is the fractional standard deviation of the normally distributed part of the integral measurement.

The method by which Macdougall and Rowlands represented correlations and systematic errors in the differential and integral data will be considered in detail below. Pendlebury[73] chose to allow for correlations in the cross-section data by a rather crude method of using a weight factor of G^{-1} (corresponding to the number of energy groups) on the cross-section adjustment penalty, viz:

$$\text{Min } F = \sum_{p=1}^{P} \sum_{k=1}^{G} \frac{1}{G} \left\{ \frac{f_k^p}{g_k^p} \right\}^2 + \sum_{i=1}^{n} \left\{ \frac{d_i}{e_i} \right\}^2 \qquad 3.2.2$$

In the treatment of systematic errors in the integral data, Cecchini et al[79] chose an equiprobable distribution for the integral measurements and the normal error distribution for the group cross-section data:

$$\text{Min } F = \sum_{p=1}^{P} \sum_{k=1}^{G} \left\{ \frac{f_k^p}{g_k^p} \right\}^2 \qquad \text{subject to } |d_i| < \epsilon_i \text{ for all } i \qquad 3.2.3$$

whilst Barré and his collaborators chose the reverse, adopting a square distribution for the cross-section data and allowing the integral measurements to be randomly distributed, viz:

$$\text{Min } F = \sum_{i=1}^{n} \left\{ \frac{d_i}{e_i} \right\}^2 \qquad \text{subject to } |f_k^p| < \delta_k^p \text{ for all k and p} \qquad 3.2.4$$

Pazy et al, however, constructed their adjustment method on the basis of a continuous energy formulation in which group adjustment parameters were defined by:

$$x'^p(E) = (1 + f_k^p)\, x^p(E) \qquad E_k \leqslant E \leqslant E_{k+1} \qquad 3.2.5$$

and the minimisation of the least squares integral reduced to the solution of a symmetric Fredholm equation with a degenerate kernel. No account was taken of nuclear data covariances other than the partial correlation between the total cross-section and its components. An excellant review of the prominent adjustment methods in use in fast reactor physics has been given by Gandini[80] and a discussion of the

development of the adjustment techniques has been given by Mitani and Kuroi[81].

3.2.3 The Method of Macdougall and Rowlands

The method is based on the general least square principle as expounded by Linnik[82] and is given as an example of a systematic attempt to perform consistency analysis in fast reactor physics. The fractional discrepancy, d_i, between the calculated value of an integral response, R_i, and the measurement, M_i, can be related to variations in the cross-section data by a Taylor expansion:

$$d_i = \frac{M_i - R_i'}{R_i} = \frac{M_i}{R_i} - 1 - \sum_{p=1}^{P}\sum_{k=1}^{G} U_k^{p,R_i} f_k^p \qquad 3.2.6$$

where R_i' is the computed response for a fractional change f_k^p in the k^{th} group of the reaction cross-section $\underline{x}^p$. U_k^{p,R_i} is the k^{th} element of the sensitivity vector (q.v.). The least square minimisation functional, F, is the discrete form of the expression derived by Pazy et al viz:

$$F = \sum_{p=1}^{P}\sum_{k=1}^{G}\left\{\frac{f_k^p}{g_k^p}\right\}^2 + \sum_{i=1}^{n}\left\{\frac{d_i}{e_i}\right\}^2 \qquad 3.2.7$$

where g_k^p and e_i are the standard deviations of the normal distributions of the populations from which x_k^p and M_i are independently selected.

The correlations in the integral measurements were assumed to arise largely from systematic errors and are included by redefining the variable d_i to include a discrepancy from this source. The correlation of systematic errors in integral measurements is relatively easy to identify as the same proton recoil counter, for example, may have been consistently used to measure the neutron spectrum in several assemblies of differing fuel composition. Thus:

$$d_i = \frac{M_i}{R_i} - 1 - \sum_{p=1}^{P}\sum_{k=1}^{G} U_k^{p,R_i} f_k^p - \sum_{l=1}^{L} \hat{T}_{il} h_l \qquad 3.2.8$$

where $\hat{T}_{il}h_l$ is the contribution to M_i from the systematic error h_l with fractional standard deviation b_l. The projection operator $\hat{T}_{il}$ can have values of zero or unity depending upon whether the systematic error h_l is thought to contribute to the discrepancy d_i. The systematic errors

were assumed to be independent of the random errors, and the values of h_l were obtained from the fit after minimisation of the modified functional:

$$\text{Min } F = \sum_{p=1}^{P} \sum_{k=1}^{G} \left\{ \frac{f_k^p}{g_k^p} \right\}^2 + \sum_{i=1}^{n} \left\{ \frac{d_i}{e_i} \right\}^2 + \sum_{l=1}^{L} \left\{ \frac{h_l}{b_l} \right\}^2 \qquad 3.2.9$$

In the minimisation of the functional, Macdougall and Rowlands assumed à priori a null vector for the systematic errors. Thus the effective fractional error on the integral data was increased to $e^2 + b^2$ which is equivalent to a reassessment of the original dispersion matrix.

The energy-dependent correlations in the cross-section data were deemed to be known à priori and were included by defining f_k^p in such a way that it is related to the adjustment of the adjacent lower energy group:

$$f_k^p = \tilde{f}_k^p + c_k^p f_{k+1}^p \qquad 3.2.10$$

In expression 3.2.10, the constant for the group, $\tilde{f}_k^p$, and the correlating term, $c_k^p f_{k+1}^p$, are assumed to be independent so that the error on f_k^p is derived from the joint distribution of $\tilde{f}_k^p$ and f_{k+1}^p such that:

$$(g_k^p)^2 = (\tilde{g}_k^p)^2 + (c_k^p g_{k+1}^p)^2 \qquad 3.2.11$$

and the modified sensitivity can be shown to be defined by:

$$\tilde{U}_k^{p,R_i} = U_k^{p,R_i} + c_{k-1}^p \tilde{U}_{k-1}^{p,R_i} \qquad 3.2.12$$

The quantities $\tilde{f}_k^p$, $\tilde{g}_k^p$ and $\tilde{U}_k^{p,R_i}$ are then used in the least square expression (3.2.9) with the observational constraint (3.2.8). This method relies essentially on correcting the integral measurements for systematic errors prior to adjustment and transforming the correlated cross-section variables to a mapping where they can be considered independent. The adjustments are determined by minimisation of the least square function (which can be performed by differentiation and matrix inversion or by numerical search techniques) the algebra of which can be found in Macdougall (loc. cit.). The method also allows the determination of the covariance matrix of the adjustment parameters through the use of expectation theory. Moreover the adjustment factors f_k^p can be shown to depend only upon the relative values of the assumed standard deviations e_i and g_k^p, whereas the covariance matrix of the adjusted data is depend-

ent upon the absolute values. To obtain an appropriate final matrix, a goodness-of-fit χ^2 test was performed and the final variances scaled indiscriminately à posteriori by χ^2/n. It is important that all the systematic errors in the integral measurements be identified and removed in the adjustment process otherwise the expected chi-squared per measurement degree of freedom would not be close to unity; this practice of à posteriori scaling has been criticised by Gandini[80], for example, who considers that the scaling factor applied by Macdougall and Rowlands may have arisen from inadequacies in the calculational methods (treatment of heterogeneity, group averaging etc) and from an improper account of the energy-dependent correlations in the nuclear data.

3.2.4 The Method of Mitani and Kuroi

A distinguishing feature of the work by Mitani and Kuroi[81] is the method by which they have attempted to quantify cross-section energy-dependent correlations and systematic errors in cross-section data. The uncertainties in 'absolutely' measured cross-section data have been assessed by fitting nuclear models (e.g. the optical potential and statistical models) to the experimental data and defining the errors in the group constants in terms of the standard deviations on the parameters of the fitted theory. Thus if $\hat{x}_k^p$ is the estimated value of the k^{th} group cross-section and $\hat{q}_m$ is the most likely value of the m^{th} parameter of the nuclear model, then for small changes:

$$\hat{x}_k^p - x_k^p = \sum_m \frac{\partial x_k^p}{\partial q_m} (\hat{q}_m - q_m) \qquad 3.2.13$$

and thus:

$$\mathrm{cov}(x_j^p, x_k^p) = \sum_m \sum_l \frac{\partial x_k^p}{\partial q_m} \cdot \frac{\partial x_j^p}{\partial q_l} \mathrm{cov}(q_m, q_l) \qquad 3.2.14$$

The values for the covariance matrix of the nuclear model parameters can be obtained by least squares fitting of the model to the individual point cross-section data. The uncertainties in relatively measured cross-sections were treated differently. For those cross-sections, $x^p(E)$ or x_k^p, whose values were inferred by measurement of the ratio r_{kj}^p with an 'absolutely' determined cross-section x_j^p, viz:

$$r_{kj}^p = \frac{x_k^p}{x_j^p} \qquad 3.2.15$$

Mitani and Kuroi established the simple relationships:

$$\mathrm{Var}(x_k^p) \quad = \quad (x_j^p)^2 \mathrm{Var}(\tau_{kj}^p) + (\tau_{kj}^p)^2 \mathrm{Var}(x_j^p) \qquad 3.2.16$$

and

$$\mathrm{Cov}(x_k^p, x_j^p) \quad = \quad \hat{E}\left[(\hat{x}_k^p - x_k^p)(\hat{x}_j^p - x_j^p)\right] \quad = \quad \tau_{kj}^p \mathrm{Var}(x_j^p) \qquad 3.2.17$$

on the assumption that the ratio τ_{kj}^p and the absolute value of the cross-section x_j^p were measured independently. An empirical approach to this aspect of cross-section evaluation has been given by Peelle[83]. In their consideration of the uncertainties in point cross-section measurements they assumed that ratio measurements had a normal random error distribution and that only 'absolute' cross-section measurements were affected by systematic error[78]. An absolutely determined cross-section measurement was therefore composed of a random component $(x_j^p)^r$ and an unknown systematic error $(\epsilon_j^p)^s$:

$$x_j^p \quad = \quad (x_j^p)^r + (\epsilon_j^p)^s \qquad 3.2.18$$

For a ratio measurement:

$$x_k^p \quad = \quad \tau_{kj}^p x_j^p \qquad 3.2.19$$

$$= \quad \tau_{kj}^p \left[(x_j^p)^r + (\epsilon_j^p)^s\right] \qquad 3.2.20$$

$$= \quad (x_k^p)^r + \tau_{kj}^p (\epsilon_j^p)^s \qquad 3.2.21$$

Thus provided the number of systematic errors $(\underline{\epsilon}^p)^s$ is less than the number (n) of integral experiments fitted, a method of the type proposed by Macdougall and Rowlands can be used to evaluate the fractional adjustments to the group cross-sections and the estimators of the systematic errors. Systematic errors in the extensive quantities cannot in general be treated simultaneously with the microscopic systematic uncertainties because of degeneracy (they can be considered to be largely equivalent).

Mitani and Kuroi[84] have published results of numerical experiments conducted with their correlation treatment which effectively show that the inclusion of the group-dependent correlation terms in the dispersion matrix for the fiduciary nuclear constants have only a small effect on

the adjustments to the data, but do increase the reliability of the adjusted set. They have also shown that the fitting of integral response data to the group cross-sections can allow determination of inconsistent or discrepant integral measurements and that after the removal of such poor extensive observations, the χ^2 test may be applied to the set of adjusted cross-sections in order to identify the presence or otherwise of systematic errors in the nuclear data.

The methods described by Mitani and Kuroi[81] and by Pearlstein[85] and others are representative of the techniques that can be adopted by theoreticians for obtaining error correlation data for use with adjustment procedures. They contrast sharply with the empirical approach proposed by Perey[86,25] and used in the evaluation of ENDF/B correlated error files. The effort required, however, still appears to be formidable, especially for the treatment of a medium heavy nucleus such as iron where individual resonances would require fitting, and these methods have not been adopted by the author for use in this work. A discussion of the nuclear data error estimates used in fitting the ASPIS iron benchmark integral measurements to the UKNDL iron data file is given in Chapter IX.

3.2.5 The Consistent Method

A limitation of the multi-group data adjustment approach is the dependence of the cross-section modification factors upon the selected group scheme and condensation weighting function. In an attempt to overcome this restriction Pazy et al[87] developed their continuous energy formalism and Gandini and Salvatores[88,89] proposed 'the consistent method'. In this latter approach the sensitivity of an integral response is related directly to the parameters of a nuclear model either as specified in the nuclear data file or as a fitting algorithm in a data file processing code[90]. Using the same notation as above, the Taylor expansion (3.2.6) may be written as:

$$R' - R = \sum_p \sum_k \frac{\partial R}{\partial x_k^p} \left(x_k^{p'} - x_k^p\right) \qquad 3.2.22$$

so that using expression (3.2.13):

$$\delta R = \sum_p \sum_k \frac{\partial R}{\partial x_k^p} \sum_m \frac{\partial x_k^p}{\partial q_m} \left(q_m' - q_m\right) \qquad 3.2.23$$

The derivative $\partial R/\partial x_k^p$ can be found by sensitivity analysis and the function $\partial x_k^p/\partial q_m$ can be determined analytically from the nuclear model. Thus using

the correlation matrix for the nuclear model parameters, a least square fit to the integral data can furnish estimates of correction factors to be applied directly to the nuclear model parameters. Examples of nuclear models to which the theory has been extended include the ABBN approach to resonance self-shielding, the Porter-Thomas distribution for unresolved resonances, the Breit-Wigner formalism for resolved resonances and the Weiskopf evaporation model. All these models are included in the MC^2 data processing code[90] and Salvatores et al[31] have demonstrated the consistent method using selected integral data from the ASPIS iron benchmark[4] and the HARMONIE sodium/stainless steel experiments to adjust the α, β and γ parameters of the Weiskopf evaporation model fitted by the MC^2 code to the secondary energy distribution data for iron tabulated in ENDF/B-IV.

$$P(E_m \rightarrow E') = \alpha_m E'^{\beta_m} e^{-E'/\gamma_m} \qquad 3.2.24$$

The method essentially removes part of the problem dependence of the data adjustment technique. Indeed it enables the adjustment of parameters such as the energy transfer cross-sections which it would be impractical to treat systematically in the multi-group form. Moreover the method allows for the evaluation of basic nuclear data parameters from the extensive measurements; in some cases this method can lead to a more accurate estimator of a nuclear parameter than can the corresponding differential microscopic measurement. The method, therefore, represents the opposite end of the spectrum as regards cross-section measurement techniques. Microscopic measurements are usually performed on the thinest material samples that the detector efficiency will allow, in order to mitigate the effect of multiple scattering. In a single material integral benchmark, on the other hand, it is the equilibrium distribution of a population of neutrons derived from a well defined source that is being modelled.

The concept of the direct adjustment of an evaluated library on the basis of the results of consistency analysis has represented a major philosophical problem in the domain of nuclear data quantification. In reactor physics it is generally appreciated that the allocation of data adjustments to particular nuclides is largely dependent upon the composition and degree of heterogeneity of the experimental assembly. In radiation shielding, on the other hand, where deep penetration single material benchmarks are modelled using transport theory, greater insight into the behaviour of the transmission data can be gleaned. However, as

illustrated in Chapter II, neutron transport in shields after a few mean free paths is frequently dominated by resonance maxima, interference minima and inelastic cross-section thresholds; it is in these rapidly varying regions of the cross-section that the group averaging technique is least accurate. An expression of the dichotomy that can exist in the mind of the shielding analyst might be thus: is it better to optimise the multi-group data set irrespective of the source of the errors in the group constants and use the adjusted data in the restricted design context for which it has been modified, or should some effort be made to quantify the accuracy of the group condensation mechanism in order to delve into and modify the contents of the evaluated nuclear data library itself and so generalise the applicability of the optimised data set? An example of the way in which data processing errors can affect reactor parameters has been made evident by the results of calculations contributed to the NEA theoretical fast reactor core benchmark, where three different laboratories using the same library (ENDF/B-IV) but different processing routes obtained answers which were unacceptably different[91]. The interpretation to be placed on the data adjustments and the uses to which the optimised data set should be put appear to be subjective decisions which are dependent upon the magnitude of the adjustments and the way in which they were generated; an attempt to give some enlightment in the case of the iron data adjustments derived from the ASPIS experiment will be given in a later chapter.

3.3 Requirements of a Shielding Data Adjustment Methodology

The requirement to optimise nuclear data sets, or at least to inspect the adequacy of existing nuclear data for radiation shield design, has posed new and different problems to those encountered in the domain of reactor core physics. In order to contrast the differences in the two fields, it is pertainent to summarize the aims of the reactor core physics methodology, which were to:

(i) Provide a data set and method which were consistent with the observed integral data.

(ii) Construct an error correlation matrix appropriate to the adjusted data set for use in power reactor performance parameter uncertainty analysis.

(iii) Identify from the predictions of the adjusted data set and covariance matrix, measured integral responses which were systematically inconsistent.

Each of these aspects of the reactor physics philosophy has been illus-

trated in the paper by Macdougall and Rowlands (loc. cit.). Moreover Campbell and Rowlands[35] have shown that the LSQ method is internally consistent and a comparison of LSQ with the method of Barré et al has been shown to result in close agreement for the final value of the U^{238} capture data in spite of starting from different libraries[92]. There are however some limitations apparent in the reactor physics approach which include:

(iv) The use of the diffusion approximation in a quasi-heterogeneous materials geometry results in problems in distinguishing between method and nuclear data errors.

(v) Since the method is in essence interpolative rather than extrapolative, a large number of 'mock-up' experiments covering all possible design configurations have to be performed.

(vi) Difficulties in the assignment of cross-section adjustments specifically to discrepancies in the nuclear data of one nuclide ensue from the use of multi-material geometries and cross-section smearing techniques. Rowlands[93] for example has commented that the iron data adjustments in the FD5 library may reflect uncertainties arising from inadequacies of the data for chromium and nickel.

(vii) The methods require a matrix inversion in order to determine the adjustments. Since for a well-posed problem the number of adjustment variables must be less than the number of integral measurements (including unfolded group flux spectra), the number of energy groups for adjustment is limited to that which can be conveniently handled on a computer. In the LSQ program, Rowlands et al used ten groups with three variables to be fitted for each group.

In contrast the requirement of radiation shielding physics is the production of an optimised data set for power reactor shield design. The integral experiments frequently cannot in any real sense model the complex reactor design conditions, and so data and methods testing are conducted on some idealised version of the shield. Moreover the quantities of interest in shielding physics cannot be measured outside of a power reactor so that integral activation foils and proton recoil spectrometers have to be relied upon to furnish an adequate estimate of the differential energy neutron flux over the range of interest. Some of the requirements of a radiation shielding adjustment methodology can be assessed as:

(viii) The number of energy groups in the calculational scheme should be large in order to mitigate the effects of a global weighting

spectrum used in preference to spatially dependent cross-section averaging.

(ix) Properly converged transport calculations should be used to minimise method errors in the reference solution.

(x) An iterative adjustment scheme should be selected which ensures that the adjustment factors at each cycle remain within the range of validity of first order perturbation theory..

(xi) The choice of a single material homogeneous shield results in a simple set of adjustment factors which are particular to that nuclide.

(xii) The wide range of data requirements for shielding as illustrated in Chapter II indicates that either a small number of measurements be made to cover the data important to one particular design study or that a very large number of integral responses be measured with a view to data assessment for a multiplicity of shielding problems. In this latter case of "global data testing benchmarks", the number of energy groups and the plethora of measurement data may lead to a requirement for a very large matrix inversion. Consequently an iterative solution technique without matrix inversion would be desirable.

(xiii) In shielding benchmark experiments measurements are frequently made at different positions using the same detectors at each position. The integral data at the different positions are therefore strongly correlated being subject to the same systematic errors, and since it is not generally possible to measure response-rates using different and independent techniques, identification of these systematic errors à priori is exceedingly difficult. Coarse checks on consistency are possible by comparing unfolded spectra with activation detector response-rates but systematic errors in the integral data can only be assessed through the optimisation prescription.

(xiv) In some cases measurements of the differential energy spectrum in conjunction with good quality integral activation detector (category I) response-rates can furnish useful information about the response function data of a less well known (category II) activation detector. By seeking adjustments to the response data which give consistency with other integral data, especially if performed simultaneously with measurements at all positions (representing a small variation in neutron flux spectrum) valuable insight into response data discrepancies can be obtained.

(xv) The method must have the ability to calculate the error correlation matrix appropriate to the adjusted parameter set. It has been noted in the reactor physics domain[74,84] that whilst the standard deviations on the adjusted cross-section data may not change by very much, the correlations injected by the optimisation process can increase considerably the reliability of the integral responses calculated with the modified data set. This reflects a general 'stiffening' of the error surface.

(xvi) The identification of discrepant integral data by fitting the adjusted cross-section data to the measurements is an important pre-requisite of the final data adjustment cycle.

None of the methods of reactor physics are able to satisfy all the requirements of the deep penetration benchmark analysis programme and it has therefore been necessary to develop a new formalism for the optimisation of transmission and response data for radiation shielding. The formal derivation of this method is the subject of the next two chapters.

3.4 Summary

A review of the techniques for data adjustment in the reactor physics domain has been given and a comparison of the philosophies of data optimisation for core and shield performance assessment examined. Some of the experiments utilised in the NEA collaborative benchmark exercise have been studied with a view to the information that can be obtained and the problems of multi-layer heterogeneous shields have been noted. The adjustment methods of reactor physics have been examined with particular reference to the treatment of systematic errors in the integral and nuclear data and a theoretical method for deriving error correlation matrices for cross-section data based on work by Mitani and Kuroi has been indicated. The extension of the multi-group method to 'the consistent approach' for modifying basic nuclear data or optimising nuclear model parameters has been described and an example of the use of the method to adjust the inelastic scattering energy distribution for iron has been cited. Finally the requirements of a method of data adjustment for radiation shielding physics have been examined.

CHAPTER IV

MAXIMUM LIKELIHOOD DATA ADJUSTMENT USING A MULTI-CHANNEL DETECTOR DISTRIBUTION

4.1 Statistical Theory

4.1.1 Introduction

The theory of parameter evaluation is built on a framework comprising the concepts of a "statistical hypothesis", the "statistical model" and the "observed data". The statistical model is the mathematical formalism assumed to represent the physical processes under examination; the model is taken to be acceptable and is not the subject of investigation. On the other hand the assignment of values to the parameters of the model is known as the "statistical hypothesis". The distinction between the "model" and the "hypothesis" is not however clearly defined, as can be illustrated by the dual rôle of DATAM experiments in the physics of radiation shielding. In the standard data-testing function, the model is taken to be the representation of the transport operator and the method by which fluxes are converted to integral responses, whilst the hypothesis is the attribution of optimal (in some statistical sense) cross-section values to the transport operator. In the methods-testing property of integral benchmark experiments, however, the allocation of parameter values to the model may represent the relative comparison of the adequacy of rival models as with the evaluation of the values of coefficients preceding the diffusion and transport terms in the Boltzmann operator. In this latter case, it is the character of the model which is in dispute and the subject of examination.

Whilst no general distinction can be drawn between the "statistical model" and the "statistical hypothesis", the convolution of the two concepts yields a powerful predictive theory by which the probability of the measured data taking a particular form can be estimated à priori within the limitations of the model. Reactor design calculations and the subsequent use of uncertainty analysis fall within this context. Probability theory, however, becomes meaningless once an experiment has been conducted. The particular form of the data is now known and it is the purpose of statistical theory to compare rival hypotheses on the basis that of all the possible outcomes of the experiment, one, the observed data, has occurred. The integral data along with any prior measurements relating to the hypothesis are used to select the most likely hypothesis which is consistent with all the measured information. This is a statistical statement of the data adjustment philosophy.

The theory defined, it is now appropriate to address the problem of how to select in a rigorous statistical sense the optimal parameter set, given a model and sets of observations. The method most generally accepted

by the scientific community revolves around the concept of likelihood as first propounded by Fisher[94]. Whilst fulfilling many of the requirements of Laplace's "inverse probability"[95] it represents the relative assessment of the adequacy of rival hypotheses, rather than an "absolute measure of belief" in a particular hypothesis, as deduced from the frequencies of events. Indeed whereas the probability of an experiment yielding the data $\underline{M}$ based on a given hypothesis H may be specified absolutely by $P(\underline{M}|H)$, the likelihood of a hypothesis H given the data $\underline{M}$, $L(H|\underline{M})$ has no meaning unless there is a comparison of two distinct hypotheses H1 and H2. It is only the likelihood ratio:

$$L(H1,H2|\underline{M}) = \frac{L(H1|\underline{M})}{L(H2|\underline{M})} \qquad 4.1.1$$

that has any meaning and is a relative measure of the adequacy of rival hypotheses H1 and H2 in describing, through the given statistical model, the experimental data $\underline{M}$. By convention the likelihood ratio is usually quoted against that hypothesis whose likelihood ratio is a maximum; if the maximum value is equated to unity, the likelihood ratio can be truncated to $L(H|\underline{M})$.

4.1.2 Likelihood and the Method of Support

The use of the likelihood ratio as a method of hypothesis testing and parameter attribution in scientific inference has its philosophical roots in the likelihood axiom which states that within the framework of a statistical model, all the information which the data provide concerning the relative merits of two hypotheses is contained in the likelihood ratio of those hypotheses on the data and the likelihood ratio is to be interpreted as the degree to which the data support the one hypothesis against the other.

The definition of likelihood is usually given in terms of the relationship with the theory of probability such that the likelihood, $L(H|\underline{M})$, of a hypothesis H given the data $\underline{M}$ and a specific model, is proportional to $P(\underline{M}|H)$, the constant of proportionality being arbitrary. This constant of proportionality disappears when likelihood ratios are formed. The relative support for a hypothesis given a set of measured data is defined to be the natural logarithm of the likelihood ratio[96] and has the following properties:

(i) Transistivity. If H1 is supported better than H2 and H2 better than H3 then H1 must be supported better than H3.

(ii) Additivity. Relative support for two hypotheses adduced from a set of data can be combined additively with the relative

support from other independent data.

(iii) Invariance. The support function is invariant under conformal transformations of the data and in the case of continuous parameters is independent of transformations of the parameters.

In estimation theory, in which the most probable values of parameters are deduced from the frequency of outcomes derived by repeated sampling, the Principle of Maximum Likelihood[97] can be used to derive estimators which have the properties of consistency and efficiency (minimum variance). Thus the likelihood framework will also allow the adjustment of data in situations where the integral experiments are repeated a number of times so that the axioms of probability theory can be applied.

4.1.3 Likelihood, Evaluates and Information

The best-supported value of a parameter, called 'the evaluate', is determined by maximising the likelihood or support functions; the method of maximum likelihood therefore allows determination of the evaluates by taking the first derivative of the support function, known as 'the scores vector', and solving the set of equations for zero scores vector. Using Taylor's theorem the support function for a set of parameters $\underline{\theta}$ can be expanded to second order as:

$$S(\underline{\theta}+\delta\underline{\theta}) = S(\underline{\theta}) + \delta\underline{\theta}^T\left\{\frac{\partial S}{\partial \underline{\theta}}\right\} + \frac{1}{2}\delta\underline{\theta}^T\left\{\frac{\partial^2 S}{\partial\underline{\theta}\partial\underline{\theta}}\right\}\delta\underline{\theta} \qquad 4.1.2$$

and if $\underline{\theta}$ is the best-supported value, then for small perturbations from the evaluate, the support can be specified as:

$$S(\underline{\theta}+\delta\underline{\theta}) = S(\underline{\theta}) + \frac{1}{2}\delta\underline{\theta}^T\left\{\frac{\partial^2 S}{\partial\underline{\theta}\,\partial\underline{\theta}}\right\}\delta\underline{\theta} \qquad 4.1.3$$

This equation defines the behaviour of the curve around the maximum and the curvature defined by the inverse of the second differential furnishes information about how well the maximum of the support surface is defined. It is for this reason that the second derivative of the support function multiplied by minus one and taken at the evaluate is known as 'the observed information'. This definition of information in the likelihood framework is very different from that of "information theory" as proposed by Shannon[98] but can be shown to be analogous to the concept of the covariance of a set of parameters estimated by repeated measurement. Thus the information matrix can be interpreted as a measure of the confidence to be placed on the value of a parameter evaluated by maximising the

likelihood for a particular hypothesis on some observed data. The problem of characterising the shape of the joint likelihood surface for the fiducial and observed data is the subject of the next chapter; the concern of this chapter will be the description of the statistical model and the method by which the evaluation of parameter values can be performed.

4.2 The Statistical Model

The model chosen to represent the propagation of neutrons in a deep penetration experiment and their subsequent detection by the effect which they have on a neutron monitor should reflect all the detailed knowledge that is known about the average behaviour of an ensemble of neutrons. It is not the physics of neutron propagation and detection which is in dispute; it is the attribution of values to the parameters describing the physical processes which is being investigated. The usefulness of the optimised parameters is therefore wholly dependent upon the acceptability of the statistical model.

4.2.1 Detector Response.

In shielding benchmark experiments the response-rates of a multitude of detectors can form the observed data. The measured reaction-rates, $\{M_i\}$, have associated with them estimated standard deviations, $\{\sigma(M_i)\}$, which are assumed to characterise the normal distribution from which the $\{M_i\}$ have been drawn at random. The measured reaction-rate is therefore considered to be an estimate of the true measured response-rate and is subject only to random error.

For the optimisation procedure, the calculational method is expected to model, as nearly as posible, all the physics required to explain how the measurements $\{M_i\}$ came to be observed. A set of parameters which can be used to characterise the predicted response-rates are the source normalisation factor, S, the partition coefficients, $\underline{\alpha}$, the response matrix, A, and the flux per unit source normalisation, $\underline{\phi}$. The calculated prediction for the reaction-rate in channel i of a detector type q, at position r, can be expressed as:

$$C_{i,r} = S\alpha_q \sum_j a_{qij}\phi_{j,r} \qquad 4.2.1$$

The signal channel index i is used because neutron spectrometers, (the counter-type denoted by $q \varepsilon q_s$) can furnish many independent channels of information; in the case of activation detectors, however, only one signal channel is present so that i and q are synonymous.

The neutron source normalisation factor, S, is included since for any one set of simultaneous measurements the source normalisation can be subject to systematic and random errors. In the case of a fission converter plate driven by thermal column leakage, the source reactor power determines the fission-rate in the converter; the power monitor for the reactor can be systematically in error and moreover can only be set to within a certain tolerance. The combined effect of this uncertainty (random and systematic) can be evaluated only in the case of a set of measurements made at the same time. In an extensive benchmark programme, however, measurements are made at different penetrations over a long period of time and between measurements the reactor may be reduced in power or even shut down. The random error therefore reflects itself as a small time-dependent inconsistency between sets of measured data and this can be accommodated by attributing a slightly larger standard deviation to the observed data. On the other hand, the systematic error is a consistent error common to all the data and can be evaluated in the optimisation process. The systematic error is expected to be composed of many individual components all governed by different probability distributions. The reason for this inference is that if the uncertainty were dominated by one or possibly two sources of systematic error, then identification of these sources could be attempted and a correction could be made for their presence when conducting the experiment or performing the calculations. The fact that the error sources cannot be identified and also that their magnitude is in general small suggests that they can be considered to be a combination of a number of different sources with unspecified probability distribution. Under such circumstances it is reasonable to apply the Central Limit Theorem[99] which states that the summands need not be normally distributed in order for the sum to be approximated by a normal distribution. Thus if the source normalisation factor is specified initially as unity, the average systematic error δS representing the departure from unity (and therefore our prior knowledge) will have a Gaussian distribution and can be characterised by an estimated standard deviation $\sigma(S)$.

The partition coefficient, α_q, represents a multiplication factor affecting all the signal information derived from a particular counter type. A deviation of α_q from unity reflects the existance of a systematic error affecting the normalisation of the response surface for that particular counter at all measurement positions. The parameter incorporates uncertainties in the absolute value of the counter efficiency calibration which may arise, for example, from an ill-defined hydrogen atom content

in a proton recoil spectrometer, errors in the thickness of a resonance foil or uncertainty in the branching ratio of the decay scheme monitored in foil activation detectors. It can also account for any systematic errors in the counting or count processing routines which can be modelled as a fractional shift in the counter response-rate. In common with the source power normalisation adjustment parameter, the counter systematic error evaluators, $\underline{\delta\alpha}$, have been assumed to include uncertainties from many seperate and independent sources, since if any one systematic error were to dominate the response its presence could be established and either included in the response matrix or removed. Thus by the Central Limit Theorem $\delta\alpha_q$ can be represented by a normal error distribution.

4.2.2 The Calibration Energy Scale Error for Proton Recoil Counters

For activation detectors the meaning of the term δa_{qij} is clear - it is a small perturbation to the response cross-section in neutron group j for the activation foil designated by the q^{th} partition. The energy dependence of the foil response cross-section has a status similar to that of the transmission cross-sections and may require optimisation due to uncertainties in the basic data or in the group condensation process. However in the case of neutron spectrometers the situation is more complex. The response surface of a proton recoil spectrometer is derived from theory and adjusted to agree with experiment through the use of correction factors. The measurements derived from the counter are numbers of recoil protons in specified energy bins; the energy group structure of the proton recoil response matrix is taken to be the same as the energies assigned to the boundaries of these bins. This energy scheme is assigned through a calibration energy marker and has an uncertainty associated with it.

Thus if a_{qij} represents the total number of protons contained in the channel covering the energy range E_i to E_{i+1} then:

$$a_{qij} = \frac{[\,b_j(E_{i+1}) + b_j(E_i)\,]}{2}(E_{i+1} - E_i) \qquad 4.2.2$$

where $b_j(E)$ is the proton density at energy E per unit group flux per unit lethargy in group j[7]. Thus:

$$\delta a_{qij} = \frac{[\,\delta b_j(E_{i+1}) + \delta b_j(E_i)\,]}{2}(E_{i+1} - E_i) + \frac{a_{qij}}{\Delta E_i}(\delta E_{i+1} - \delta E_i) \qquad 4.2.3$$

If it is assumed that the uncertainty in the energy scale is a fractional

error so that:

$$g_q = \frac{\delta E}{E} \qquad 4.2.4$$

is a characteristic of the counter q then it can be shown (Appendix A) that:

$$\delta a_{qij} = \mathfrak{z}_{qij}\, g_q \qquad 4.2.5$$

where $\mathfrak{z}_{qij}$ is a function of a_{qi-1j}, a_{qij} and a_{qi+1j}. In the derivation of $\mathfrak{z}_{qij}$ it has been assumed, as will be shown in Chapter VII, that the error in $b_j(E)$ and therefore in a_{qij} arises largely from the uncertainty of the assigned proton energy scale rather than uncertainties in the response surface itself. This treatment of the energy scale error for neutron spectrometers is to some extent an approximation (as pointed out in Appendix A), and other, possibly second order, expansions in g_q may need to be used near the line-shape threshold. However the intention here is simply to use g_q as a diagnostic indicator; if unacceptably large values of g_q are evaluated by the optimisation process then this model of the benchmark experiment is no longer valid and it is questionable whether such erroneous data can or should be used for data adjustment in deep penetration experiments where the effects of energy scale shift and low quality transmission data can be indistinguishable.

4.2.3 Neutron Transmission Parameters

The neutron transmission process is only crudely represented in the statistical model by the multi-group absorption, non-elastic and total scalar cross-sections. The choice of these parameters as the evaluates of the hypothesised parameter set furnishes no detailed information about the precise source of any discrepancies found in the penetration medium nuclear interaction constants. For example, even assuming the group averaging invokes no unacceptable errors, an adjustment to the group absorption cross-section may in reality be due to errors in calculating the leakage for the transformed 1-D model rather than any deficiency in the capture data. Moreover neither the secondary energy nor the secondary angular distributions of neutron scattering are investigated; uncertainties in these distributions can be expected to manifest themselves as adjustments to the non-elastic and total group cross-sections. In order for these "second level" parameters to be investigated, however, either:

(i) a data processing code which uses a parametric functional form to represent the secondary energy distribution of neutron

inelastic scatter

or (ii) a knowledge of the individual sensitivities to the energy transfer cross-sections

is required. In the multi-group data processing code MC^{2}[90] the inelastic scattering secondary energy distribution is represented by the Weiskopf evaporation model and using the "consistent method" the temperature could be adjusted to increase the support of the hypothesised inelastic data. The individual energy transfer cross-section sensitivities on the other hand can be obtained from the SWANLAKE code[24], but without prior physical insight the number of parameters to be fitted to the model becomes unacceptably large. This situation may in future be considerably simplified by the use of the recently developed spatial channel theory of Engle and Williams[100], which allows identification of the importance of various transport mechanisms, with a consequent reduction in the number of variables to be optimised. Since however neither of these tools were available to the author, the nuclear data optimisation has been carried out on the basis that the errors in the transmission data can be attributed solely to the absorption, non-elastic and total cross-sections.

4.2.4 The Calculational Prediction of Observed Quantities

The representation of the ASPIS neutron propagation experiment has been founded on a simple statistical model in which the detectors have been modelled using a source power normalisation factor, S, a partition coefficient, α_q, and a multi-group response function, $\underline{a}_{qi}$. These parameters serve to characterise the uncertainties inherent in the calculation of a detector response for a given flux and furnish detailed information about the source of any discrepancy found as a result of multi-detector optimisation with good 'coverage' (for example the situation where the neutron flux in a particular energy region is monitored by several independent detectors whose response functions overlap). The representation of the neutron transport, however, is the minmimum which is consistent with the transmission process. The model as posed therefore represents the predicted value of an observable in terms of the Boltzmann transport operator $\hat{B}_{jkrr'}$ and the fixed group source $\underline{\chi}$ so that:

$$C_{i,r} = C_{i,r}(\alpha_q, a_{qi}, S, \underline{x}^n, \underline{x}^x, \underline{x}^T) \qquad 4.2.6$$

$$= \alpha_q S \sum_j a_{qij} \sum_{r'} \sum_k \hat{B}^{-1}_{jkrr'} \chi_{kr'} \qquad 4.2.7$$

and whereas the adjustments to $\underline{\alpha}$, A and S are physically interpretable, the adjustments to the closed set of partial cross-sections, $\{\underline{x}^p\}$, may have a multiplicity of sources. The adjustments to these parameters and the resulting change in the values of the evaluators arising from the joint optimisation for the ASPIS iron benchmark experiment will be examined in Chapter IX. The approximations and assumptions in the model and the ensuing development have been made with regard to the measurement techniques and calculational methods applied in the analysis of the ASPIS iron benchmark experiment and should therefore be critically assessed before the method is applied to the analysis of other experiments.

4.3 Derivation of the Likelihood Functional

4.3.1 The Experimental Support Function

For variates which obey the normal probability distribution, the likelihood function can be related, through the support function, to the constrained χ^2 function for the measured data:

$$\ln L(\underline{C}|\underline{M}) = -\frac{\chi^2_m}{2} + \text{constants} = -\sum_{q=1}^{Q}\sum_{i\in q}^{I_q}\left[\frac{C_i - M_i + \delta C_i}{2\sigma(M_i)}\right]^2 + \text{constants} \qquad 4.3.1$$

where

$$C_i = C_i(\alpha_q, S, a_{qi1} \ldots\ldots a_{qiG}, x^r_1 \ldots\ldots x^r_G) \qquad 4.3.2$$

and δC_i is to be chosen so as to minimise the χ^2_m, i.e. maximise the likelihood of the set $\underline{C}$ given the data $\underline{M}$. The measurement M_i is the signal strength detected in the i^{th} channel of a particular counter type q. The summation is therefore over all the channels, I_q, within a counter partition and over all the Q counter types. In the case of a multi-channel pulse height analyser connected to a proton recoil counter, I_q might typically represent 20 counting groups. The calculated prediction of an integral parameter is derived à priori from the neutron transport flux calculation and the fiducial data for the detector response using the relationship:

$$C_i = S\alpha_q \sum_j a_{qij}\,\phi_j(\{x^r_k\}) \qquad 4.3.3$$

The group fluxes $\{\phi_j\}$ are determined from the best transport calculation available which in the case of the ASPIS iron DATAM experiment is represented by a pseudo 2-D P_3S_8 ANISN calculation. The elements of the multi-

group response function, a_{qij}, for any neutron group j, appropriate to the i^{th} channel of the q^{th} spectrometer type are derived either from a basic nuclear data library using, for example, the GALAXY multi-group cross-section processing code[101] in the case of activation detectors or when q represents a neutron spectrometer the PRCM code[102] for generating proton recoil matrices can be used; a discussion of the accuracy assignments for these data will be given in Chapter VII. Thus using Taylor's theorem to second order of small changes, the maximum likelihood evaluator of δC_i may be expanded as:

$$\delta C_i = \left[\frac{\delta\alpha_q}{\alpha_q} + \frac{\delta S\,\delta\alpha_q}{S\,\alpha_q} + \frac{\delta S}{S}\right] C_i + S\alpha_q \sum_j (\delta a_{qij}\,\hat{s}_{qq_f} + \zeta_{qij}\,g_q\,\hat{s}_{qq_s})\,\delta\phi_j$$

$$+ \left[S\alpha_q + S\delta\alpha_q + \delta S\alpha_q\right]\left[\sum_j (\delta a_{qij}\,\hat{s}_{qq_f} + \zeta_{qij}\,g_q\,\hat{s}_{qq_s})\,\phi_j + a_{qij}\,\delta\phi_j\right] \qquad \ldots\ldots\ldots\ldots 4.3.4$$

where $\hat{s}_{qq_f}$ and $\hat{s}_{qq_s}$ are projection operators whose values are zero or unity depending upon whether the counter type q is an activation foil (single channel detector) or a proton recoil spectrometer (multi-channel detector) respectively. The expansion to second order is necessitated by the requirement of consistency with the constraints. Substitution of this relation into the log-likelihood or support function gives:

$$\ln L(\underline{c}|\underline{m}) = -\sum_q \sum_{i\epsilon q} \frac{1}{2\sigma^2(m_i)} \left\{ c_i - m_i + \left[\frac{\delta\alpha_q}{\alpha_q} + \frac{\delta S\,\delta\alpha_q}{S\alpha_q} + \frac{\delta S}{S}\right] C_i + S\alpha_q \sum_j (\delta a_{qij}\,\hat{s}_{qq_f} + \right.$$

$$\left. \zeta_{qij}\,g_q\,\hat{s}_{qq_s})\delta\phi_j + \left[S\alpha_q + S\delta\alpha_q + \delta S\alpha_q\right]\left[\sum_j (\delta a_{qij}\,\hat{s}_{qq_f} + \zeta_{qij}\,g_q\,\hat{s}_{qq_s})\,\phi_j + a_{qij}\,\delta\phi_j\right]\right\}^2$$

$$- \text{ constraints.} \qquad 4.3.5$$

Rewriting:

$$\ln L(\underline{c}|\underline{m}) = -\sum_q \sum_{i\epsilon q} \frac{1}{2\sigma^2(m_i)} \left\{ (c_i - m_i)^2 + 2(c_i - m_i)\left[\left(\frac{\delta\alpha_q}{\alpha_q} + \frac{\delta S\,\delta\alpha_q}{S\alpha_q} + \frac{\delta S}{S}\right) C_i \right.\right.$$

$$+ (S\alpha_q + S\delta\alpha_q + \delta S\alpha_q)\left(\sum_j \delta a_{qij}\,\hat{s}_{qq_f}\phi_j + \zeta_{qij}\,g_q\,\hat{s}_{qq_s}\phi_j + a_{qij}\,\delta\phi_j\right) + S\alpha_q \sum_j \left(\delta a_{qij}\,\hat{s}_{qq_f}\right.$$

$$\left.\left. + \zeta_{qij}\,g_q\,\hat{s}_{qq_s}\right)\delta\phi_j\right] + \left[\left(\frac{\delta\alpha_q}{\alpha_q} + \frac{\delta S\,\delta\alpha_q}{S\alpha_q} + \frac{\delta S}{S}\right) C_i + S\alpha_q \sum_j \left(\delta a_{qij}\,\hat{s}_{qq_f} + \zeta_{qij}\,g_q\,\hat{s}_{qq_s}\right)\delta\phi_j\right.$$

$$+ \left(S\alpha_q + S\delta\alpha_q + \delta S\alpha_q\right)\left(\sum_j \delta a_{qij}\hat{S}_{qq_f}\phi_j + \zeta_{qij}g_q\hat{S}_{qq_s}\phi_j + a_{qij}\delta\phi_j\right)\Bigg]^2\Bigg\} - \text{Constraints}$$

.....4.3.6

4.3.2 The Prior Support Function - The Constraints

The constraints represent the penalty incurred for evaluating non-zero adjustments to the partition coefficients, the counter response function, the source normalisation, the energy scale calibration indicator and the bulk medium nuclear interaction constants which were all individually at maximum likelihood given the measurements made to evaluate them. To be more specific, the set of calculations $\underline{C}$ will be initially at maximum likelihood with the differential cross-section data assuming that the predicted neutron phase space distribution is independent of the calculational group structure for sensible group structures. Thus $L(\underline{C}\,|\,\{\underline{x}^p\},\underline{\alpha},A,\underline{g}\&S)$ will be a maximum. The purpose of an integral benchmark is to allow the joint likelihood function of the calculation vector to be maximised given both a set of differential cross-section data, counter parameters etc., and some new integral measurement information. Thus the requirement is that $L(\underline{C}\,|\,\{\underline{x}^p\},\underline{\alpha},A,\underline{g},S\&\underline{M})$ be at maximum likelihood. In performing this optimisation the constraints are represented by the à priori information, namely that $L(\underline{C}\,|\,\{\underline{x}^p\},\underline{\alpha},A,\underline{g}\&S)$ is a maximum and any change in $\{\underline{x}^p\}$, $\underline{\alpha}$, A, $\underline{g}$ or S incurs the penalty that this à priori information is no longer the most probable set. Thus the maximisation process will produce evaluators of the parameters which will be at maximum likelihood with respect to the total information available, but will not except in degenerate cases be at maximum likelihood with the seperate differential or integral sets of information. It is the orthogonal nature of the measurements vector that forbids degeneracy of the information and indeed it is the global insight into the consistency of the cross-section data over a wide range of energy that is the hallmark of a good integral benchmark.

For the remainder of this work the partition coefficients for the different counters have been assumed to be independent. This simplifying assumption does not affect the generality of the results to be discussed, but only reduces the algebraic content of the work. Indeed in the ASPIS iron benchmark it is not a true statement of fact, but serves as a very good approximation since the off-diagonal elements of the covariance matrix are small compared with the detector partition coefficient variances.

The arguments concerning the independence of the proton recoil counter partition coefficients will be set out in Chapter VII. In the case of the activation foils the following example will serve to illustrate what is meant. The partition factors do not include any possible correlation between detector reaction cross-sections; such 'materials correlations' will be explicitly included in the variance-covariance matrices for the activation foil response functions.

The sources of error common to the α_q's will be detector positioning errors in the shield and day-to-day variations in NESTOR reactor power output. These errors amount to less than $\pm 3\%$[4]. However the $S^{32}(n,p)$ reaction-rate, for example, is measured by counting the P^{32} β^- emission; the calibration of the burning technique and the $4\pi\beta$ counter efficiency is systematically uncertain to $\pm 8\%$. Similarly the $In^{115}(n,n')$ reaction-rate is determined by counting the 335 keV γ-ray emission of In^{115m}; the detection efficiency of the NaI(Tl) γ-ray spectrometer is systematically uncertain to $\pm 5\%$. Therefore although the detector partition coefficients $\underline{\alpha}$ are systematically correlated by up to 3%, the independent uncertainties of the activation monitors dominate the uncertainties on the partition coefficients and so it appears reasonable to consider the $\delta\alpha_q$ quantities to be predominantly independent.

In this exposition on the method it will be assumed, for simplicity, that only the cross-section variances are known. The extension of the method to encompass the more general situation where the energy-dependent correlations are quantified is reserved for a later section of this chapter. The scenario to be discussed is therefore relevant to the present day situation where no recommended covariance data are available for either iron or the dosimetry cross-sections used in the analysis of the ASPIS iron experiment. The data that are available comprise the Schmidt estimates[36] of the accuracy of the measured cross-section data for iron over various energy ranges and similar range-wise estimates by McElroy et al[37] and the author (Chapter VII) for the dosimetry cross-sections.

According to Schmidt the independently measured cross-sections for iron are the absorption, non-elastic and total cross-sections. The elastic and inelastic cross-sections used in the transport equation for predicting the neutron flux are 'redundant' quantities. The identification of the parameters to be evaluated by maximisation of the support function allows the form of the constraints to be deduced. Thus an exact second order support function for a Schmidt-type analysis may be expressed as:

$$\ln L(\underline{c}|\underline{m},\{\underline{x}^r\},\underline{\alpha},A,\underline{g}\&S) = -\sum_q \sum_{i\epsilon q} \frac{1}{2\sigma^2(m_i)} \left\{ (c_i-m_i)^2 + 2(c_i-m_i)\left[\left(\frac{\delta\alpha_q}{\alpha_q}\right.\right.\right.$$

$$\left. + \frac{\delta S\,\delta\alpha_q}{S\,\alpha_q} + \frac{\delta S}{S}\right) c_i + \left(S\alpha_q + S\delta\alpha_q + \delta S\alpha_q\right)\left(\sum_j \delta a_{qij}\hat{S}_{qq_f}\phi_j + \sum_{qij} g_q \hat{S}_{qq_s}\phi_j + a_{qij}\delta\phi_j\right)$$

$$+ S\alpha_q \sum_j \left(\delta a_{qij}\hat{S}_{qq_f} + \sum_{qij} g_q \hat{S}_{qq_s}\right)\delta\phi_j \Bigg] + \left[\left(\frac{\delta\alpha_q}{\alpha_q} + \frac{\delta S\,\delta\alpha_q}{S\alpha_q} + \frac{\delta S}{S}\right) c_i + \left(S\alpha_q + S\delta\alpha_q\right.\right.$$

$$\left.\left. + \delta S\alpha_q\right)\left(\sum_j \delta a_{qij}\hat{S}_{qq_f}\phi_j + \sum_{qij} g_q \hat{S}_{qq_s}\phi_j + a_{qij}\delta\phi_j\right) + S\alpha_q \sum_j \left(\delta a_{qij}\hat{S}_{qq_f} + \sum_{qij} g_q \hat{S}_{qq_s}\right)\delta\phi_j \Bigg]^2 \Bigg\}$$

$$- \frac{1}{2}\sum_q \left\{\frac{\delta\alpha_q}{\sigma(\alpha_q)}\right\}^2 - \frac{1}{2}\sum_k \left[\left\{\frac{\delta x_k^A}{\sigma(x_k^A)}\right\}^2 + \left\{\frac{\delta x_k^x}{\sigma(x_k^x)}\right\}^2 + \left\{\frac{\delta x_k^T}{\sigma(x_k^T)}\right\}^2\right] - \frac{1}{2}\sum_{q\epsilon q_s}\left\{\frac{g_q}{\sigma(g_q)}\right\}^2$$

$$- \frac{1}{2}\sum_{q\epsilon q_f}\sum_{i\epsilon q}\sum_l \left\{\frac{\delta a_{qil}}{\sigma(a_{qil})}\right\}^2 - \frac{1}{2}\left\{\frac{\delta S}{\sigma(S)}\right\}^2 \qquad 4.3.7$$

4.4 Specification of the Flux Perturbation in terms of Transmission Cross-Section Variations.

Apart from in the constraints, the cross-section adjustment evaluators do not appear explicitly anywhere else in the support function. Instead, they are implied through the perturbed flux vector $\underline{\delta\phi}$. The nature of the relationship between the flux perturbations and changes in the transmission cross-sections can be established through the use of perturbation theory. Second order perturbation theory when applied to the Boltzmann transport equation would produce a relationship between the $\underline{\delta\phi}$ and the cross-section perturbations with the same order of precision as the support function itself. However a second order neutron transport perturbation capability is not generally available if indeed it has even been developed and for this reason linear perturbation theory has been adopted. The use of this approximation in order to render the support functional soluble is at a cost; it can be argued that if the cross-section perturbations are kept small, as might be achieved by use of an iterative solution procedure, then no significant loss of accuracy accrues. The sacrifice in using linear theory goes far beyond the requirement of "small" changes, it leaves the transmission cross-sections unscaled. In other words the

concept "small" is not defined within the model.

The approximations made by linear perturbation theory can best be explored by writing the Boltzmann transport equation in the operator formalism:

$$\hat{B}\underline{\phi} = \underline{S} \qquad 4.4.1$$

where the transport operator $\hat{B}$ relates the flux $\underline{\phi}$ at a certain point in function space to the neutron source $\underline{S}$. Correspondingly the adjoint problem can be defined whereby the adjoint transport operator $\hat{B}^+$ allows determination of the importance[103] of neutrons at various points on the function space in contributing to the removal-rate at the sink $\underline{S}^+$:

$$\hat{B}^+\underline{\phi}^+ = \underline{S}^+ \qquad 4.4.2$$

Moreover a perturbed problem can be defined such that the perturbed regular flux $\underline{\phi}_p$ and importance $\underline{\phi}_p^+$ resulting from the perturbed forward and adjoint transport operators $\hat{B}_p$ and $\hat{B}_p^+$, respectively, satisfy the following equations:

$$\hat{B}_p\underline{\phi}_p = \underline{S} \qquad 4.4.3$$

$$\hat{B}_p^+\underline{\phi}_p^+ = \underline{S}^+ \qquad 4.4.4$$

where $\hat{B}_p = \hat{B} + \delta\hat{B}$, and $\underline{\phi}_p = \underline{\phi} + \underline{\delta\phi}$ with similar relations for the adjoint case. The connection between the forward and adjoint representations of the problem can be made through the definition of the adjoint operator, namely that:

$$\int_\tau \underline{\phi}^+\hat{B}\underline{\phi}\, d\tau = \int_\tau \underline{\phi}\hat{B}^+\underline{\phi}^+\, d\tau \qquad 4.4.5$$

for a suitable choice of boundary conditions. Applying this definition to equations 4.4.1 and 4.4.2 gives:

$$\int_\tau \underline{\phi}^+\underline{S}\, d\tau = \int_\tau \underline{\phi}\underline{S}^+\, d\tau \qquad 4.4.6$$

The term $\int \underline{\phi}^+\underline{S}\, d\tau$ is the contribution of source neutrons to the loss-rate at the neutron sink $\underline{S}^+$; $\underline{S}^+$ is therefore the response function relating the neutron flux at the neutron sink to the loss-rate. Thus:

$$\underline{S}^+ = \underline{\Sigma}^R \qquad 4.4.7$$

and equation 4.4.6 is just the alternative ways of expressing a reaction-rate R. For the unperturbed problem, the reaction-rate for a particular response may be expressed as:

$$R = \int \underline{\phi}\,\underline{\Sigma}^{R}\,d\tau = \int \underline{\phi}\hat{B}^{+}\underline{\phi}^{+}\,d\tau \qquad 4.4.8$$

Similarly for the perturbed problem:

$$R^{p} = \int \underline{\phi}_{p}\hat{B}^{+}_{p}\underline{\phi}^{+}_{p}\,d\tau \qquad 4.4.9$$

$$= \int \underline{\phi}\hat{B}^{+}_{p}\underline{\phi}^{+}_{p}\,d\tau + \int \underline{\delta\phi}\hat{B}^{+}_{p}\underline{\phi}^{+}_{p}\,d\tau \qquad 4.4.10$$

$$= \int \underline{\phi}\hat{B}^{+}_{p}\underline{\phi}^{+}_{p}\,d\tau + \int \underline{\delta\phi}\hat{B}^{+}_{p}\underline{\phi}^{+}\,d\tau + \int \underline{\delta\phi}\hat{B}^{+}_{p}\underline{\delta\phi}^{+}\,d\tau \qquad \text{.....4.4.11}$$

Clearly from equations 4.4.2 and 4.4.4:

$$\hat{B}^{+}_{p}\underline{\phi}^{+}_{p} = \hat{B}^{+}\underline{\phi}^{+} \qquad 4.4.12$$

so that:

$$R^{p} = \int \underline{\phi}\hat{B}^{+}\underline{\phi}^{+}\,d\tau + \int \underline{\delta\phi}\hat{B}^{+}_{p}\underline{\phi}^{+}\,d\tau + \int \underline{\delta\phi}\hat{B}^{+}_{p}\underline{\delta\phi}^{+}\,d\tau \qquad \text{.....4.4.13}$$

Assuming first order theory only and using equation 4.4.8:

$$\delta R = (R^{p} - R) = \int \underline{\delta\phi}\hat{B}^{+}_{p}\underline{\phi}^{+}\,d\tau \qquad 4.4.14$$

$$= \int \underline{\phi}^{+}\hat{B}_{p}\underline{\delta\phi}\,d\tau \qquad \text{(by 4.4.5)} \qquad 4.4.15$$

By definition of the perturbed operator and equating equations 4.4.1 and 4.4.3:

$$\hat{B}_{p}\underline{\phi}_{p} = \hat{B}_{p}(\underline{\phi} + \underline{\delta\phi}) = \hat{B}\underline{\phi} \qquad 4.4.16$$

$$\therefore (\hat{B}_{p} - \hat{B})\underline{\phi} = -\hat{B}_{p}\underline{\delta\phi} \qquad 4.4.17$$

$$\therefore \delta\hat{B}\underline{\phi} = -\hat{B}_{p}\underline{\delta\phi} \qquad 4.4.18$$

Substituting into equation 4.4.15:

$$\delta R = -\int \underline{\phi}^{+}\delta\hat{B}\underline{\phi}\,d\tau \qquad 4.4.19$$

and thus for a constant response cross-section, i.e. the transmission processes and the response are independent:

$$\frac{\delta R}{R} = \frac{\int \underline{\delta\phi}\,\underline{\Sigma}^{R}\,d\tau}{\int \underline{\phi}\,\underline{\Sigma}^{R}\,d\tau} = -\frac{\int \underline{\phi}^{+}\delta\hat{B}\,\underline{\phi}\,d\tau}{\int \underline{\phi}^{+}\hat{B}\,\underline{\phi}\,d\tau} \qquad 4.4.20$$

It is the right-hand side of equation 4.4.20 that is computed by the cross-section sensitivity code SWANLAKE where the operator perturbation,

$\delta\hat{B}$ is assumed to be a 1% change in the transmission cross-sections. Recalling from Chapter II, the sensitivity of the reaction-rate R to the partial cross-section p in group k, as determined by the code, is defined to be:

$$U_k^{p,R} = \frac{\delta \ln R}{\delta \ln x_k^p} \qquad 4.4.21$$

then:

$$\int \underline{\delta\phi}\, \underline{\Sigma}^{r}\, d\tau = R \sum_{p} \sum_{k} U_k^{p,R} \frac{\delta x_k^p}{x_k^p} \qquad 4.4.22$$

This is the relationship which expresses the change in the flux vector $\underline{\phi}$ arising from perturbations to the partial transmission cross-sections:

$$\underline{\delta\phi} = \underline{\Phi} \sum_{p} \sum_{k} U_k^{p,\phi} \frac{\delta x_k^p}{x_k^p} \qquad 4.4.23$$

4.5 The Choice of Adjoint Source

In this section the term of interest is the first order term in $\underline{\delta\phi}$. Since it is proposed to use linear perturbation theory, in which the higher order flux terms are neglected, to replace this term by an expansion of the kind contained in equation 4.4.23, then to be consistent all the terms in $(\underline{\delta\phi})^2$ in the support functional must be neglected. A typical component of the coefficient of the $\underline{\delta\phi}$ term viz:

$$\sum_{q} \sum_{i \in q} \frac{(c_i - m_i)}{\sigma^2(m_i)} S\alpha_q \sum_{j} a_{qij}\, \delta\phi_j \qquad 4.5.1$$

shows that three different adjoint source types can be chosen. Using conventional sensitivity theory the response function $\underline{a}_{qi}$ could be chosen as the adjoint source for the perturbation calculation. For the ASPIS iron benchmark experiment, such a choice would require one adjoint and one sensitivity calculation for each signal channel - a forbidding 500 calculations at about 100 Harwell CPU work units (about 12 mins.) each. An alternative, though no less formidable, choice of adjointing from each individual flux group in turn, corresponding to:

$$S_j^{+} = \delta_{jj'} \qquad 4.5.2$$

would reduce the number of calculations to the number of groups in the calculational scheme - namely 100 calculations for each measurement position in the ASPIS experiment. The third and only feasible choice is to use a collective 'Multi-Channel Detector Distribution' where:

$$S_j^+ = \sum_q \sum_{i \epsilon q} \frac{(c_i - m_i)\alpha_q}{\sigma^2(m_i)} S\, a_{qij} \qquad 4.5.3$$

In this way only one adjoint transport and sensitivity calculation need be performed. The considerable cost benefit associated with the use of this detector distribution is to some extent off-set by the dominance in the problem sensitivity profile of that region containing the greatest concentration of high quality measurements. This detector distribution is an extension of an earlier adjoint source suggested by McCracken and Grimstone[5] which was based on the comparison of a calculated flux vector $\underline{\phi}$ with a flux vector $\underline{\Psi}$ obtained by unfolding the measurement vector $\underline{M}$:

$$S_j^+ = \frac{(\phi_j - \psi_j)}{\sigma^2(\psi_j)} \qquad 4.5.4$$

where

$$A\underline{\Psi} = \underline{M} + \underline{\epsilon} \qquad 4.5.5$$

and $\underline{\Psi}$ was chosen as a maximum likelihood solution of 4.5.5[104]. The reason for rejecting this type of detector distribution (4.5.4) will be discussed in a later chapter in the context of measurement flux unfolding, but may be summarised as follows:

(i) The conditioning of equation 4.5.5 is such that no unique solution exists and therefore $\underline{\Psi}$ can be drawn from a wide distribution of admissable solutions. Statistical criteria are often used to select a solution, called the appropriate solution, from this distribution. In the unfolding code RADAK, the Principle of Maximum Likelihood is used to select the 'appropriate solution' and an estimate of the covariance on this solution is obtained by Monte Carlo sampling.

(ii) The computational solution of the equation may inject spurious noise and unwanted correlations into the unfolded measurement flux vector chosen in accordance with (i) above.

(iii) The estimation of $\sigma^2(\psi_j)$ or more rigorously $\langle \psi_j \psi_{j'} \rangle$ suffers from many approximations in the RADAK code so that although

the flavour of the errors and correlations in the flux solution is given, the method may not be sufficiently precise for use in the interpretation of benchmark experiments.

The choice of the Multi-Channel Detector Distribution overcomes all these difficulties by using the maximum amount of information available and maintaining its quality. Discussions on this choice of detector distribution have been given elsewhere by McCracken[105] and McCracken and Chestnutt[106] and a recent review of this work has been given by Matthes[107]. With a view to the use of an iterative scheme of solution of the scores equations in which $\underline{\delta\alpha}$, $\underline{g}$, $\underline{\delta a_{qi}}$, and δS are determined seperately from $\underline{\delta x}^p$, all terms in $\underline{\delta\phi}$ may be collected into a 'Multi-Channel Detector Distribution' denoted by H_j^+:

$$H_j^+ = \sum_q \sum_{i\epsilon q} \frac{1}{\sigma^2(m_i)} \Bigg\{ (c_i - m_i)\Big[(S\alpha_q + S\delta\alpha_q + \delta S\alpha_q)a_{qij} + S\alpha_q(\delta a_{qij}\hat{S}_{qq_f} + \underset{\sim}{\zeta}_{qij} g_q \hat{S}_{qq_s})\Big]$$

$$+ \left(\sum_k (\delta a_{qik}\hat{S}_{qq_f} + \underset{\sim}{\zeta}_{qik} g_q \hat{S}_{qq_s})\phi_k\right)\Big[(S\alpha_q + S\delta\alpha_q + \delta S\alpha_q)^2 a_{qij} + (S\alpha_q + S\delta\alpha_q + \delta S\alpha_q)$$

$$S\alpha_q(\delta a_{qij}\hat{S}_{qq_f} + \underset{\sim}{\zeta}_{qij} g_q \hat{S}_{qq_s})\Big] + \left(\frac{\delta\alpha_q}{\alpha_q} + \frac{\delta S}{S}\right) c_i \Big[(S\alpha_q + S\delta\alpha_q + \delta S\alpha_q)a_{qij}$$

$$+ S\alpha_q(\delta a_{qij}\hat{S}_{qq_f} + \underset{\sim}{\zeta}_{qij} g_q \hat{S}_{qq_s})\Big]\Bigg\} \qquad 4.5.6$$

This represents a formidable expression for the adjoint source and in practice it is not used. Instead an alternative, though essentially similar approach is adopted. The use of first order perturbation theory in establishing the relationship between flux perturbations and transmission cross-section variations demands the use of an iterative solution scheme for maximising the support function, in which the flux and cross-section perturbations are kept small enough in each cycle for terms of order $(\underline{\delta\phi})^2$ to be negligible. This cyclic method lends itself to a two tier solution method in which the adjustments to the detector responses are obtained first and then after updating the predicted value of the response, C_i', with these adjustments, the evaluates of the transmission cross-sections are sought. Thus if:

$$C_i' = (S+\delta S)(\alpha_q + \delta\alpha_q)\sum_j (a_{qij} + \delta a_{qij})\phi_j \qquad 4.5.7$$

represents the updated predictions then:

$$H_j^+ = \sum_q \sum_{i \epsilon q} \frac{(S+\delta S)(\alpha_q + \delta\alpha_q)(c_i' - m_i)(a_{qij} + \delta a_{qij})}{\sigma^2(m_i)} \qquad 4.5.8$$

essentially represents the same 'Multi-Channel Detector Distribution' as specified in equation 4.5.6. If the reaction-rate for this detector distribution is defined to be:

$$\sum_j H_j^+ \phi_j = h \qquad 4.5.9$$

then in accordance with equation 4.4.22:

$$\sum_j H_j^+ \delta\phi_j = h \sum_k \left\{ \frac{U_k^{A,h}}{x_k^A} \delta x_k^A + \frac{U_k^{N',h}}{x_k^{N'}} \delta x_k^{N'} + \frac{U_k^{N,h}}{x_k^N} \delta x_k^N \right\} \qquad 4.5.10$$

Rewriting this equation in terms of the independent sensitivity vectors established in Chapter II:

$$\sum_j H_j^+ \delta\phi_j = h \sum_k \left\{ \Gamma_k^{A,h} \frac{\delta x_k^A}{x_k^A} + \Gamma_k^{X,h} \frac{\delta x_k^X}{x_k^X} + \Gamma_k^{T,h} \frac{\delta x_k^T}{x_k^T} \right\} \qquad 4.5.11$$

and substituting into the support function 4.3.7:

$$\begin{aligned} \ln L(\underline{c}|\underline{m}, \{\underline{x}^e\}, \underline{\alpha}, A, S \,\&\, \underline{g}) = & -\sum_q \sum_{i \epsilon q} \frac{1}{2\sigma^2(m_i)} \left\{ (c_i - m_i)^2 + 2(c_i - m_i) \right. \\ & \left[\left(\frac{\delta\alpha_q}{\alpha_q} + \frac{\delta S \delta\alpha_q}{S\alpha_q} + \frac{\delta S}{S} \right) c_i + (S\alpha_q + S\delta\alpha_q + \delta S\alpha_q) \left(\sum_j \left(\delta a_{qij} \hat{S}_{qq_f} + \{_{qij} g_q \hat{S}_{qq_s} \right) \phi_j \right) \right] \\ & \left. + \left[\left(\frac{\delta\alpha_q}{\alpha_q} + \frac{\delta S \delta\alpha_q}{S\alpha_q} + \frac{\delta S}{S} \right) c_i + (S\alpha_q + S\delta\alpha_q + \delta S\alpha_q) \left(\sum_j \left(\delta a_{qij} \hat{S}_{qq_f} + \{_{qij} g_q \hat{S}_{qq_s} \right) \phi_j \right) \right]^2 \right\} \\ & - \frac{1}{2} \sum_q \sum_{i \epsilon q} \sum_m \left\{ \frac{\delta a_{qim}}{\sigma(a_{qim})} \right\}^2 - \frac{1}{2} \left\{ \frac{\delta S}{\sigma(S)} \right\}^2 - h \sum_K \left[\Gamma_K^{A,h} \frac{\delta x_K^A}{x_K^A} + \Gamma_K^{X,h} \frac{\delta x_K^X}{x_K^X} + \Gamma_K^{T,h} \frac{\delta x_K^T}{x_K^T} \right] \\ & - \frac{1}{2} \sum_{q \epsilon q_s} \left\{ \frac{g_q}{\sigma(g_q)} \right\}^2 - \frac{1}{2} \sum_q \left\{ \frac{\delta\alpha_q}{\sigma(\alpha_q)} \right\}^2 - \frac{1}{2} \sum_k \left[\left\{ \frac{\delta x_k^A}{\sigma(x_k^A)} \right\}^2 + \left\{ \frac{\delta x_k^X}{\sigma(x_k^X)} \right\}^2 + \left\{ \frac{\delta x_k^T}{\sigma(x_k^T)} \right\}^2 \right] \end{aligned} \qquad \ldots\ldots\ldots\ldots 4.5.12$$

Equation 4.5.12 represents the final form of the support function; it is second order with respect to the evaluation of $\underline{\delta\alpha}$, δS, $\underline{g}$ and $\underline{\delta a_{qi}}$, but is only first order with respect to $\{\underline{\delta x^p}\}$ and so will henceforth be referred to as the 'hybrid support functional' for the hypothesised parameter set.

In summary therefore it may be said that through the requirement that the second order flux perturbation be negligible, the direct solution of the scores equations by matrix inversion is no longer possible. Moreover, for the cross-section adjustments, the omission of the second order flux terms leads to arbitrary adjustments in the sense that the inherent normalisation scaling of the adjustments is lost. Recourse has therefore to be made to an iterative method of solution in which the adjustments at the end of each cycle are forced to lie within the realm of linear theory and before the beginning of the next cycle, all the parameters to be evaluated are updated with the derived adjustments. The functional at the end of each cycle will be randomly distributed as χ^2, (assuming a normal distribution of the measured data) and if the iterative procedure is well-conditioned, χ^2 should be a monotonically decreasing function with each cycle and ideally distributed as n degrees of freedom near the functional maximum (minimum χ^2).

At the beginning of each cycle a new adjoint transport and sensitivity calculation will have to be performed using the updated values of C_i, α_q, S, a_{qij}, g_q and $\{\underline{x}^p\}$. Initially the sensitivity of the 'Multi-Channel Detector Distribution' will be dominated by the region containing the greatest density of high quality discrepant measurements, but as the cyclic procedures continues, the discrepancies in this region will be the fastest to disappear, and the informative range of the sensitivity profile (the region over which the optimisation functional is usefully testing the data) will expand into those regions containing a lower density of benchmark quality measurements. Near the stationary point of the functional where $|(C_i - M_i)| \sim \sigma(M_i)$, the adjoint source may be rapidly changing at each cycle and the optimisation of the data may become oscillatory due to instabilities in the adjoint source.

4.6 Maximisation of the Support Functional

In this section the support equation for each type of adjustment evaluator is derived. Some simplification of the system of equations is necessary, usually on the basis of a reduction to first order in the adjustment evaluates, so that the coupling of the equations can be reduced (a set of linear simultaneous equations can be obtained) and also to minimise the number of adjoint transport and sensitivity calcula-

tions that would be required. The solution of the maximisation equations for zero score as derived from a linear support function, the hybrid two tier support function and a simplification of the second order support function are compared; the evaluates of the linear theory (developed in Appendix B) are shown to be unnormalised, whilst the solutions of the hybrid support equation are shown to be special iterative solutions of the simplified second order scores vector equations.

4.6.1 The Adjustments to the Partition Coefficients

The evaluates for the adjustments to the partition coefficients are derived by equating the scores vector for the partition coefficients to zero;

$$\frac{\partial}{\partial \delta\alpha_q} \ln L(\underline{c}|\underline{m},\underline{\alpha}, A, \underline{g}, S \& \{\underline{x}^p\}) = 0 \qquad q=1,Q \qquad 4.6.1$$

For the hybrid support function (equation 4.5.12) this corresponds to:

$$\frac{\delta\alpha_q}{\sigma^2(\alpha_q)} + \sum_{i\epsilon q} \frac{1}{\sigma^2(m_i)} \left\{ \left[\frac{c_i}{\alpha_q} + \frac{\delta S\, c_i}{S\alpha_q} + S \sum_j \left(\delta a_{qij} \hat{S}_{qq_f} + \zeta_{qij} g_q \hat{S}_{qq_s} \right) \phi_j \right] \right.$$
$$\left. \left[c_i - m_i + \left(\frac{\delta S}{S} + \frac{\delta\alpha_q \delta S}{\alpha_q S} + \frac{\delta\alpha_q}{\alpha_q} \right) c_i + (S\alpha_q + S\delta\alpha_q + \delta S\alpha_q) \left(\sum_j \left(\delta a_{qij} \hat{S}_{qq_f} + \zeta_{qij} g_q \hat{S}_{qq_s} \right) \phi_j \right) \right] \right\} = 0$$

.....4.6.2

Neglecting all the second order terms in the adjustment evaluators, the solution of the hybrid support equation may be expressed to first order in the adjustment evaluates as:

$$\left[\sum_{i\epsilon q} \frac{c_i^2}{\sigma^2(m_i)\alpha_q^2} + \frac{1}{\sigma^2(\alpha_q)} \right] \delta\alpha_q + \left[\sum_{i\epsilon q} \frac{(2c_i - m_i)c_i}{\sigma^2(m_i)\alpha_q S} \right] \delta S$$
$$+ \left[\sum_{i\epsilon q} \frac{(2c_i - m_i)S}{\sigma^2(m_i)} \sum_j \left(\delta a_{qij} \hat{S}_{qq_f} + \zeta_{qij} g_q \hat{S}_{qq_s} \right) \phi_j \right] = - \sum_{i\epsilon q} \frac{(c_i - m_i)c_i}{\sigma^2(m_i)\alpha_q}$$

.....4.6.3

Equation 4.6.3 represents a series of Q simultaneous equations in which the solution for $\underline{\delta\alpha}$ is coupled to the adjustment evaluates of δS, $\underline{\delta a}_{qi}$ and $\underline{g}$. The corresponding linearised score equation for the exact second order support function is:

$$\left[\sum_{i\in q}\frac{c_i^2}{\sigma^2(m_i)\alpha_q^2}+\frac{1}{\sigma^2(\alpha_q)}\right]\delta\alpha_q+\left[\sum_{i\in q}\frac{(2c_i-m_i)c_i}{\sigma^2(m_i)\alpha_q S}\right]\delta S+\left[\sum_{i\in q}\frac{(2c_i-m_i)S}{\sigma^2(m_i)}\sum_j a_{qij}\delta\phi_j\right]$$

$$+\left[\sum_{i\in q}\frac{(2c_i-m_i)S}{\sigma^2(m_i)}\sum_j\left(\delta a_{qij}\hat{S}_{qq_f}+\zeta_{qij}\,g_q\hat{S}_{qq_s}\right)\phi_j\right]=-\sum_{i\in q}\frac{(c_i-m_i)c_i}{\sigma^2(m_i)\alpha_q}$$

.....4.6.4

This equation serves as a reminder that the hybrid two tier scores equations represent the decoupling of the detector response data from the medium neutron transport data in the sense that the two tier scores equations can be represented by the partial derivatives:

$$\frac{\partial \ln L(\underline{c}|\underline{m},\underline{\alpha},A,S,\underline{g}\,\&\,\{\underline{x}^p\})}{\partial\delta\underline{\Theta}}\bigg|_{\{\underline{x}^p\}}=0 \qquad 4.6.5$$

and

$$\frac{\partial \ln L(\underline{c}|\underline{m},\underline{\alpha},A,S,\underline{g}\,\&\,\{\underline{x}^p\})}{\partial\delta\underline{x}^p}\bigg|_{\underline{\theta}}=0 \qquad 4.6.6$$

where $\underline{\theta}$ designates the set of prior evaluates (prior to optimisation or prior to a new cycle):

$$\underline{\theta}=\{\underline{\alpha},A,\underline{g},S\} \qquad 4.6.7$$

The two tier system can be envisaged as the maximisation of the likelihood of the parameter set by moving the adjustment evaluators over the support surface, first along lines of constant $\underline{\theta}$ and then along contours of constant $\{\underline{x}^p\}$. The second order support equations can be solved, should they be required for speed and accuracy, by selecting the coefficient of $\delta\underline{\phi}$ as a multi-channel detector distribution in analogy with equation 4.5.6 so that the term may be expanded in a complete linear set of cross-section adjustment evaluators. This would require the performance of Q adjoint/sensitivity calculations at each cycle.

The above scores equations for $\delta\alpha_q$ (4.6.3 and 4.6.4) may be compared with the adjustment evaluate for $\delta\alpha_q$ as derived in Appendix B using pure linear theory:

$$\delta\alpha_q=-\sum_{i\in q}\frac{c_i(c_i-m_i)\sigma^2(\alpha_q)}{\sigma^2(m_i)\alpha_q} \qquad 4.6.8$$

It is obvious that this solution for the adjustment evaluate is wholly dependent upon the number of signal channels for the counter q included in the experimental support for the model parameters. The adjustment evaluate is unnormalised and for detectors with a systematic bias leading to consistent under-prediction, for example, the first order adjustment evaluate is unbounded, i.e.

$$\delta\alpha_q \to \infty \qquad \text{as } i \to \infty \text{ for } i \epsilon q \qquad 4.6.9$$

In contradistinction the adjustment evaluator $\delta\alpha_q$ derived from the hybrid support function is a well-behaved function and in the simple case where the constraints are such that null adjustments are found for the parameters $\underline{\delta a}_{qi}$, g_q and δS (corresponding to zero variance on these parameters) then from equation 4.6.3:

$$\delta\alpha_q = - \frac{\sum_{i \epsilon q} \frac{(c_i - m_i)c_i}{\sigma^2(m_i)\alpha_q}}{\sum_{i \epsilon q} \frac{c_i^2}{\sigma^2(m_i)\alpha_q^2} + \frac{1}{\sigma^2(\alpha_q)}} \qquad 4.6.10$$

In the case where α_q has to be evaluated without any prior information (i.e. $\sigma^2(\alpha_q) \to \infty$) from a single information channel, equation 4.6.10 furnishes the physically reasonable value of:

$$\frac{\delta\alpha_q}{\alpha_q} = \frac{(m-c)}{c} \qquad 4.6.11$$

The first order theory evaluator, however, being proportional to the variance on the parameter is in this situation unbounded for non-zero discrepancies.

The detailed comparison that has been drawn here between the first order and pseudo-second order theories is important, because it serves to high-light the difficulties that will be encountered when recourse is made to first order theory to evaluate the adjustments to the transmission cross-section parameters; the adjustments will be unnormalised and no meaningful insight will accrue from the use of asymptotic theory.

4.6.2 Adjustments to the Activation Detector Response Functions

The evaluates for the adjustments to the activation detector response functions can be derived by solution of the support equation:

$$\frac{\partial \ln L(\underline{c} | \underline{m}, \underline{\alpha}, A, S, \underline{g} \& \{\underline{x}^p\})}{\partial \delta a_{qij}} = 0 \qquad q \epsilon q_f,\ i \epsilon q,\ j=1,G \qquad 4.6.12$$

On taking the derivative of the hybrid support function and neglecting second order terms in the adjustment evaluators, the following set of linear simultaneous equations can be derived:

$$\sum_{K}\left[\frac{S^2\alpha_q^2\phi_K}{\sigma^2(m)}+\frac{\delta_{Kj}}{\sigma^2(a_{qj})\phi_j}\right]\delta a_{qK}+\frac{(2c-m)(S\delta\alpha_q+\alpha_q\delta S)}{\sigma^2(m)}=\frac{(m-c)S\alpha_q}{\sigma^2(m)}\quad j=1,g \qquad 4.6.13$$

The corresponding set of equations derived using the pseudo-second order theory are:

$$\sum_{K}\left[\frac{S^2\alpha_q^2\phi_K}{\sigma^2(m)}+\frac{\delta_{Kj}}{\sigma^2(a_{qj})\phi_j}\right]\delta a_{qK}+\frac{(2c-m)(S\delta\alpha_q+\alpha_q\delta S)}{\sigma^2(m)}+S\alpha_q\frac{(c-m)}{\sigma^2(m)}\delta\phi_j$$

$$+\frac{S^2\alpha_q^2}{\sigma^2(m)}\sum_{l}a_{ql}\delta\phi_l=\frac{(m-c)S\alpha_q}{\sigma^2(m)}\quad j=1,g \qquad 4.6.14$$

The transformation of the flux perturbations by a linear expansion in terms of the transmission cross-section adjustments requires the performance of G adjoint transport/sensitivity calculations to find the expansion coefficients (less calculations are required if the activation response function set does not cover the entire energy range). It is in this kind of situation that the two tier iterative hybrid support function (equation 4.5.12) displays its economic advantages.

The comparison with first order theory is again of interest. The evaluate for activation detector response function adjustment, derived in Appendix B using linear theory, viz:

$$\delta a_{qj}=\left[\frac{(m-c)S\alpha_q\phi_j}{\sigma^2(m)}\right]\sigma^2(a_{qj}) \qquad 4.6.15$$

is unscaled and simply relates the size of the adjustments to the magnitudes of the group flux and the variance on the group response cross-section. The hybrid support function, on the other hand, allows for feedback arising from adjustments to the other cross-sections in the channel response function. Moreover in the case where an interference minimum in the penetration medium cross-section data causes flux peaking in the transmission spectrum (for example around 24 keV in pure iron), the first order solution predicts the adjustment to the response cross-section in the corresponding group to be proportional to the magnitude of the group flux, such that:

$$\delta c_i\Big|_{\alpha_q,\underline{\phi},S} \simeq S\alpha_q \delta a_{qj}\phi_j \propto \phi_j^2 \quad \text{for } \phi_j \gg \phi_k, \text{ for all } k\neq j \qquad 4.6.16$$

On the same basis the hybrid theory predicts:

$$\delta c_i\Big|_{\alpha_q,\underline{\phi},S} \simeq S\alpha_q \delta a_{qj}\phi_j = (m-c) \quad \text{for } \phi_j \gg \phi_k, \text{ for all } k\neq j \qquad 4.6.17$$

so that the perturbation to the calculated value of an integral parameter is independent of the magnitude of the flux in the regime where a single group flux dominates the response-rate.

4.6.3 The Adjustments to the Spectrometer Energy Scale Error Parameter

The adjustments to the neutron spectrometer energy calibration can be derived by maximising the hybrid support functional in the $\underline{g}$ vector space, that is by solution of:

$$\frac{\partial}{\partial \underline{g}} \ln L(\underline{c}|\underline{m},\underline{\alpha},A,S,\underline{g}\,\&\,\{\underline{x}^r\}) = 0 \qquad 4.6.18$$

which for the hybrid support function leads to the set of scores vector equations:

$$\left[S^2\alpha_q^2 \sum_{i\in q}\frac{\mu_{qi}^2}{\sigma^2(m_i)} + \frac{1}{\sigma^2(g_q)}\right] g_q + \left[\sum_{i\in q}\frac{(2c_i-m_i)\mu_{qi}}{\sigma^2(m_i)}\right](S\delta\alpha_q + \delta S\alpha_q) = S\alpha_q \sum_{i\in q}\frac{(m_i-c_i)}{\sigma^2(m_i)}\mu_{qi}$$

.....4.6.19

where for concision the reaction-rate μ_{qi} has been defined to be:

$$\mu_{qi} = \sum_j \}_{qij}\phi_j \qquad \text{for } q\in q_s \text{ and } i\in q \qquad 4.6.20$$

If large values of g_q are found (say $> \sigma(g_q)/5$ where $\sigma(g_q)$ will be assessed in Chapter VII), then they can only serve as a diagnostic indicator of poor quality data. If meaningful adjustments are required, some extension of the simple energy scale model, described in Appendix A, would be required and the results would have to be used to calculate proton recoil spectrometer response matrices in the new hypothesised group scheme before calculations in the next iterative cycle could be performed.

4.6.4 The Adjustments to the Source Power Normalisation

Differentiating the hybrid support function with respect to the source power normalisation adjustment evaluator will give the following equation for the evaluate δS:

$$\left[\sum_{q}\sum_{i\epsilon q}\frac{C_i^2}{\sigma^2(m_i)S^2}+\frac{1}{\sigma^2(S)}\right]\delta S+\left[\sum_{q}\sum_{i\epsilon q}\frac{C_i^2}{\sigma^2(m_i)S\alpha_q}\right]\delta\alpha_q$$

$$+\sum_{q}\sum_{i\epsilon q}\frac{(2C_i-m_i)\alpha_q}{\sigma^2(m_i)}\left[\sum_{j}\left(\delta a_{qij}S_{qq_f}+\sum_{q}\gamma_{qij}q_qS_{qq_s}\right)\phi_j\right]=\sum_{q}\sum_{i\epsilon q}\frac{(m_i-C_i)C_i}{\sigma^2(m_i)S}$$

4.6.21

Equation 4.6.21 therefore completes the derivation of the $(2Q+1)+(G-1)q_f$ equations necessary to derive the adjustments to the detector responses as represented by the statistical model. The simultaneous solution of this set of equations comprises tier I of the hybrid two tier maximum likelihood data optimisation scheme.

4.6.5 The Adjustments to the Transmission Cross-Section Data

The second tier of the hybrid iterative optimisation scheme comprises the updating of the support function with the adjustments to the detector response parameters and the subsequent solution of the support equation for the adjustments to the transmission cross-section data. For this solution method, the adjustment evaluate δx_k^p, determined from equation 4.5.12 can be expressed as:

$$\delta x_k^p = \frac{-h\,\Gamma_k^{p,h}\,\sigma^2(x_k^p)}{x_k^p} \qquad 4.6.22$$

The evaluate is unscaled owing to the neglect of second order terms in $\underline{\delta\phi}$ and the behaviour is analogous to that of the adjustment evaluate for the partition coefficient, $\delta\alpha_q$, when only first order terms were considered in the expansion for δC_i. Indeed the magnitude of the cross-section adjustments is entirely dependent upon the number of channels of information included in the multi-channel detector distribution since:

$$h = \sum_{q}\sum_{i\epsilon q}\frac{(C_i-m_i)C_i}{\sigma^2(m_i)} \qquad 4.6.23$$

whereas the sensitivity $\Gamma_k^{p,h}$ is only the fractional quantity:

$$\Gamma_k^{p,h} = \frac{\delta h/h}{\delta x_k^p/x_k^p} \qquad 4.6.24$$

Although the fractional cross-section adjustments are unscaled so that

they have no absolute value, relatively they should be in the correct proportions, being dependent upon the fractional group cross-section variance modulated by the sensitivity profile. Moreover using asymptotic theory on the ratio of any general fractional cross-section adjustment shows that physically meaningful ratios can be expected; indeed if the fractional uncertainties for two group cross-sections are the same, then the posterior ratio will be selected entirely on the basis of the relative values of the group sensitivities. Therefore if some mathematical or statistical criterion is chosen to limit the value of the largest fractional adjustment, then the set of adjustments obtained will be relatively correct and by iterating over many cycles (unspecified because of problem dependence) convergence to the correct magnitude should ensue. The rigorous mathematical criterion can be chosen on the basis that for adjustments greater than some magnitude the second order terms in $\underline{\delta\phi}$ start to become important and/or the nature of the multi-channel detector distribution is changing so rapidly that:

$$\frac{\partial \Gamma_k^{p,h}}{\partial x_k^p} \neq 0 \qquad 4.6.25$$

Owing to the lack of suitable user codes, the extraction of the necessary information to decide whether the mathematical criterion is satisfied would be cumbersome and time-consuming. Instead for the optimisation of the ASPIS iron benchmark the statistical criterion has been used; in this a linear search is performed to determine the maximum value of a multiplier λ such that for the end of each cycle, the adjusted data set when scaled by λ produces a local minimum of χ_λ^2 for the model, i.e.

$$\chi^2_{\lambda-\epsilon} > \chi^2_\lambda < \chi^2_{\lambda+\epsilon} \quad \text{for all } \epsilon \qquad 4.6.26$$

and

$$\delta x_k^p = -\lambda h \Gamma_k^{p,h} \frac{\sigma^2(x_k^p)}{x_k^p} \qquad 4.6.27$$

Since the χ^2 for the system falls at the end of each cycle, the support for the adjusted data set will be greater than that for the original set. Moreover a reduction in χ^2 necessarily implies a reduction in h so that eventually a stage is reached in the iteration scheme whereby, in the absence of large systematic error, λ becomes redundant and h is small

enough to predict meaningfully scaled adjustments.

A feature of the optimisation scheme to be discussed in the next chapter is the updating of the variance-covariance matrix for the adjusted data. If λ is chosen as described above, then for group cross-sections with small sensitivities, $\Gamma_k^{p,h}$, the predicted adjustments will be negligible. This corresponds to one of two situations; either the integral benchmark data contains no quality information about these cross-sections, in which case the prior values need not be modified, or the benchmark lends experimental support for the adequacy of the prior values and their error data. In cases where significant cross-section adjustments are made, the experimental data does not support the prior value and a posterior value has to be chosen with reference to the prior value, its error data and the experimental support for the hypothesis. Therefore not only are adjustments made to the transmission cross-section data during each iterative cycle, but the variance-covariance matrix also evolves during the optimisation process.

In Appendix C, the pseudo-second order theory solution has been derived on the basis that the prior response data were fully supported corresponding to null adjustments:

$$\sum_l \left[\left(\sum_q \sum_{i \in q} \frac{c_i^2 \Gamma_j^{p,c_i}}{\sigma^2(m_i)\, x_j^p} \right) \frac{\Gamma_l^{p,c_i}}{x_l^p} + \frac{\delta_{lj}}{\sigma^2(x_j^p)} \right] \delta x_l^p = \frac{-h\, \Gamma_j^{p,h}}{x_j^p} \qquad 4.6.28$$

The adjustments predicted from the solution of this system of equations are meaningfully scaled and for a one group, one measurement situation with no prior information, the predicted group cross-section adjustment is just that to be expected from sensitivity theory:

$$\frac{\delta x^p}{x^p} = -\frac{(c-m)}{c} \frac{1}{\Gamma^{p,c}} \qquad 4.6.29$$

and is independent of the magnitude of C. Moreover it can be seen from equation 4.6.28 that the dependence on $\sigma^2(x_j^p)$ for the pseudo-second order equation becomes weaker the more relevant high quality information channels are considered. This is an extremely important feature to have in an optimisation scheme where the error data on the transmission cross-sections may be either sparse or largely guessed.

4.7 The Extension of the Method to Include Error Correlation Matrices

Error correlation matrices for nuclear data can be divided into two

types, those that are deduced by statistical theory and those that are inferred on heuristic arguments. Whereas the former are objective and shall be called "expected error correlation matrices", the latter in reality are subjective and only have the status of a guess; for this reason they will be designated as "assessed error correlation matrices". In Chapter II, examples of the use of error correlation information in uncertainty analysis were given. In the field of benchmark data optimisation the use of covariant constraints represents a starting point of higher information content and as such should enhance the posterior support for the derived cross-section evaluates.

4.7.1 Independent Transmission Cross-Section Correlation Matrices

The extension of the method to include a full matrix of error data rather than a diagonal variance matrix (represented by Schmidt error data) involves only the modification of the constraints or prior support for the adjustment evaluators, viz:

$$\text{Prior Support} = -\sum_{p}\sum_{j}\sum_{k} \delta x_j^p \, V_{jk}^p \, \delta x_k^p = -(\underline{\delta x}^p)^T (V^p)^{-1} (\underline{\delta x}^p) \qquad \ldots\ldots\ldots 4.7.1$$

where V_{jk}^p represents the $(jk)^{th}$ element of the inverse variance-covariance matrix for the partial cross-section type p. The adjustment evaluator therefore becomes:

$$\delta x_k^p = -h \sum_{j} V_{kj}^p \frac{\Gamma_j^{p,h}}{x_j^p} \qquad 4.7.2$$

4.7.2 Response Cross-Section Correlation Matrices

Expected error correlation matrices for response cross-section data are unlikely to be available for some time to come because of their lack of direct technological interest. Reliance will therefore have to be put on the assessments of evaluators or on the assessments of calculators. This latter class of information addresses the question "What effect will correlation information have on the answer?", or more generally "Are the correlations important?". With a view to answering this type of question the calculator might inject a few almost random data group correlating functions and examine the consequences. An example of such functions might be:

$$\varrho(x_j, x_k) = 1 - \frac{|j-k|}{n} \quad \text{for } |j-k| \leq n \qquad 4.7.3$$

for a correlation range over n groups, or

$$\rho(x_j, x_k) = \begin{cases} e^{-|\bar{E}_j - \bar{E}_k|/\bar{E}_k} & \text{for } \bar{E}_j/\bar{E}_k \leq 3 \\ 0 & \text{otherwise} \end{cases} \qquad 4.7.4$$

where $\bar{E}_j$ and $\bar{E}_k$ represent the mean energies of groups j and k respectively. For variance-covariance data of any type the modified form of the equations is:

$$\left[\sum_k \left(\frac{S^2 \alpha_q^2 \phi_k}{\sigma^2(m)} + \frac{(V_q^{-1})_{jk}}{\phi_j}\right)\delta a_{qk}\right] + \frac{(2c-m)}{\sigma^2(m)}(S\delta\alpha_q + \delta S\alpha_q) = \frac{(m-c)}{\sigma^2(m)} S\alpha_q \quad j = 1,g$$

.....4.7.5

4.8 Summary

The method described in this chapter, based on the Likelihood Axiom, is an attempt to optimise a nuclear data matrix using the results of a deep penetration integral benchmark experiment where many high quality measurements are available and the reference calculation has been conducted in a large number of energy groups in order to reduce the effect of the energy-dependent weighting function on the group cross-sections and to obviate the requirement for spatially dependent group cross-sections. In such cases where both the neutron energy group index ($j \sim 100$) and the number of measurements ($i \sim 500$) are large, it is not possible from the viewpoint of computational efficiency to adjoint either from the group scheme (using a unit detector source for each group at each measurement position in turn) or from each response function. The method devised has the ability to treat such systems with great computational velocity and with the use of a second order perturbation capability, can produce properly conditioned adjustments - scaled in such a way that the cycle step is the largest possible within the second order regime and thus minimising the number of iterative cycles necessary for optimal solution.

The disadvantages of the method are only apparent when, as in the case of the analysis of the ASPIS iron benchmark experiment, no second order perturbation capability exists. Under the first order and truncated second order (hybrid) regimes it has been shown that the evaluates of the transmission cross-section adjustments are completely unnormalised requiring the imposition of some ad hoc restriction in order to satisfy the criteria of first order perturbation theory and of physical reality. Moreover the evaluators of the cross-section adjustments predicted using such approximations can be shown to be strongly dependent upon the prior

cross-section information matrix which, lacking an ENDF/B-V correlated error file, is subject to a high degree of personal bias. In contradistinction the second order method can be largely independent of the assumed error data provided sufficient high quality measurement information relating to the region of interest is available. Nevertheless the hybrid method represents an efficient technique for combining microscopic and integral data to produce, using the Likelihood Axiom, a data set which is consistent with the prior and observed information.

CHAPTER V

THE DERIVATION OF THE COVARIANCE RELATIONSHIPS FOR THE ADJUSTED DATA USING EXPECTATION THEORY

5.1 Introduction

The use of signal information from an integral benchmark experiment to optimise the parameters of the calculational model for consistency with the experimental data allows not only the determination of the best-supported values of these parameters but also an updating of the information matrix associated with the vector of evaluates. In fact in the region of the maximum of a quadratic support function, the support surface can be characterised by the vector of evaluates and its corresponding information matrix, since by Taylor's theorem:

$$S(\underline{\hat{\theta}}+\underline{\delta\theta}) = S(\underline{\hat{\theta}}) + \frac{1}{2}\underline{\delta\theta}^{T}\left\{\frac{\partial^{2}S}{\partial\underline{\theta}\,\partial\underline{\theta}}\right\}\Bigg|_{\hat{\theta}}\underline{\delta\theta} \qquad 5.1.1$$

where $S(\underline{\hat{\theta}} + \underline{\delta\theta})$ is the value of the support function at some general value of $\underline{\theta}$ and the scores vector evaluated at $\underline{\hat{\theta}}$ has been equated to zero. In such a case, the evaluate $\underline{\hat{\theta}}$ and the information matrix are said to be sufficient statistics.

Although the Maximum Likelihood evaluates may not necessarily be unbiased, there is an important class of evaluates, called unbiased sufficient evaluators, for which a likelihood theorem established by Cramér[108] allows the covariance matrix of the evaluates to be identified with the inverse of the expected information matrix:

$$\mathrm{cov}(\theta_i, \theta_j) = -\left[\left(\frac{\partial^{2}S(\theta)}{\partial\theta_i\,\partial\theta_j}\right)\Bigg|_{\underline{\hat{\theta}}}\right]^{-1} \qquad 5.1.2$$

For the ASPIS iron benchmark the requirement of unbiased evaluators is satisfied by the linear search iterative solution method in which, at the end of each cycle, χ^2 is inspected and shown to be a minimum. However from equation 5.1.2 it is clear that the information matrix can only be accurately determined for support functions which are correct to second order in the adjustment evaluators. In the case of a linearised support function, such as the hybrid support function derived in the previous chapter, Cramér's theorem cannot be used. Indeed it can be seen that, arising from the use of linear perturbation theory to relate flux variations to the transmission cross-section adjustment evaluators in the hybrid support function, the 'observed information' is zero and therefore the à posteriori information matrix for the transmission cross-sections is the same as the à priori information. Clearly information is contained in the experimental measurements about the shape of

the support surface for the model parameters; it is only that it cannot be represented by the hybrid support function. It is for this reason that recourse has to be made to expectation theory in order to quantify the updated error data for the adjusted parameters.

5.2 Asymptotic Requirements of the Cross-Section Covariance Matrix

The updating of the prior covariance matrix with the information extracted from an integral benchmark experiment can be expected to display the following properties:

(i) If a prior cross-section is largely unknown (in the sense of being ill-defined), implying a very large covariance vector, then the best-supported value of the cross-section will be dictated by the integral benchmark data (representing a measurement of the cross-section) and the variance-covariance of the cross-section will depend strongly on the variance, and if necessary covariance, data of the integral measurements. In other words, the quality of the integral measurements and the sensitivity of the measurements to the cross-section of interest will define the 'span' of the support surface of which $\hat{\underline{x}}$ is the evaluate.

(ii) If a cross-section, ab initio, is well defined (the associated prior support surface having a narrow span) and the integral measurement data is of poor quality (represented by large variances), then the adjustment to the cross-section will be small, if any, and the covariance vector will be defined largely by the prior error data on the differential nuclear data.

(iii) Between these limiting cases the cross-section adjustments and the à posteriori variance-covariance data will be dependent upon both the prior differential measurement error data and the integral measurement uncertainties. The benchmark data will represent new information about the cross-sections which, if consistent with the prior nuclear data, will result in a narrowing of the support surface about the new optimised evaluate $\hat{\underline{x}}$.

(iv) In the last section it was shown that the covariance matrix can be likened to the inverse information matrix. However whilst the use of the information from an integral benchmark, to optimise model parameters, can lead to a reduction in the fractional span of the likelihood surface and therefore a corresponding reduction in the fractional variance on the parameters, it is apparent that, in the inverse mode of

consistency analysis, the integral benchmark data cannot pass useful comment on the appropriateness of the prior covariance matrix, since the updating process assumes the prior matrix as a basis on which to build up the correlations between parameters which arise from the adjustment process. Indeed if only small adjustments are made to the cross-section data, then the injected mathematical correlations will be correspondingly small and the dispersion matrix will be largely unchanged. The appropriateness of the prior error matrix has therefore not been checked other than in the scalar sense that the constraints are not so rigid as to produce unacceptable answers to excellence tests (e.g. χ^2 per degree of freedom ~ 1) at maximum likelihood. On the other hand, if the adjustments are everywhere large, then the mathematical correlations arising from the optimisation process may dominate the covariance matrix) and the dispersion matrix will be the one 'appropriate' to the adjusted data set. It would be wholly fallacious to compare this matrix with the matrix of differential measurement errors given in a nuclear data library. Expected error correlation matrices, such as those contained in ENDF/B-IV and B-V, represent measurement errors; the dispersion matrix evaluated by a data optimisation process, in which the mathematical correlations are dominant, represents uncertainties in the integro-differential data. Such a matrix can be technologically very useful in those situations where errors in the nuclear data are swamped by a systematic error in the group processing mechanism.

5.3 Specification of the Partial Cross-Section Covariance Matrix in Terms of Intermediate Variables

For any independently measured cross-section, an adjustment parameter $\underline{\epsilon}^p$ can be evaluated such as to maximise the support for that cross-section with respect to the available information. Thus:

$$\underline{\hat{x}}^p = \underline{x}^p + \underline{\epsilon}^p \qquad 5.3.1$$

and for small variations

$$\underline{\delta\hat{x}}^p = \underline{\delta x}^p + \underline{\delta\epsilon}^p \qquad 5.3.2$$

which allows the general expected covariance to be defined by:

$$\langle \delta\hat{x}_k^p \delta\hat{x}_l^{p'} \rangle = \langle \delta x_k^p \delta x_l^{p'} \rangle + \langle \delta x_k^p \delta\epsilon_l^{p'} \rangle + \langle \delta\epsilon_k^p \delta x_l^{p'} \rangle + \langle \delta\epsilon_k^p \delta\epsilon_l^{p'} \rangle \qquad 5.3.3$$

where $\langle \delta x_k^p \, \delta x_l^{p'} \rangle$ is the prior covariance between the group k cross-section for a neutron interaction process p and the l^{th} group cross-section for a neutron interaction event p'.

5.3.1 The Covariance Matrix for a Partial Cross-Section

In Chapter IV (Section 4.6.5) the adjustment evaluator for a general group cross-section was derived as:

$$\epsilon_k^p = -h \frac{\Gamma_k^{p,h}}{x_k^p} \sigma^2(x_k^p) \qquad 5.3.4$$

so that:

$$\delta\epsilon_k^p = \frac{\delta h}{h} \epsilon_k^p - h\,\delta\left(\frac{\Gamma_k^{p,h}}{x_k^p}\right) \sigma^2(x_k^p) \qquad 5.3.5$$

and using the formalism of expectation theory, the covariance matrix of the adjustment evaluators can be defined as:

$$\langle \delta\epsilon_k^p \delta\epsilon_l^{p'} \rangle = \frac{\langle \delta h^2 \rangle}{h^2} \epsilon_k^p \epsilon_l^{p'} + h^2 \left\langle \delta\left(\frac{\Gamma_k^{p,h}}{x_k^p}\right) \delta\left(\frac{\Gamma_l^{p,h}}{x_l^{p'}}\right) \right\rangle \sigma^2(x_k^p)\, \sigma^2(x_l^{p'})$$

$$- \epsilon_k^p \left\langle \delta h\, \delta\left(\frac{\Gamma_l^{p,h}}{x_l^{p'}}\right) \right\rangle \sigma^2(x_l^{p'}) - \sigma^2(x_k^p) \left\langle \delta\left(\frac{\Gamma_k^{p,h}}{x_k^p}\right) \delta h \right\rangle \epsilon_l^{p'}$$

.....5.3.6

This expression for the covariance, in analogy with the iterative adjustment evaluates, is unscaled; the value of h is to some extent arbitrary. In evaluating the adjustments to the partial cross-sections, the value of h has been determined by a linear search procedure, to be the largest value which minimises χ^2 at the end of the iterative cycle. It is therefore this scaled value of h, denoted by h' (= λh), which must be used in the determination of the expected covariance matrix of the optimised cross-section vector.

$$\langle \delta\hat{x}_k^p \delta\hat{x}_l^{p'} \rangle = \langle \delta x_k^p \delta x_l^{p'} \rangle + \frac{\epsilon_l^{p'}}{h'} \langle \delta x_k^p \delta h' \rangle - h' \sigma^2(x_l^{p'}) \left\langle \delta x_k^p\, \delta\left(\frac{\Gamma_l^{p,h}}{x_l^{p'}}\right) \right\rangle$$

$$+ \frac{\epsilon_k^p}{h'} \langle \delta h' \delta x_l^{p'} \rangle - h' \sigma^2(x_k^p) \left\langle \delta\left(\frac{\Gamma_k^{p,h}}{x_k^p}\right) \delta x_l^{p'} \right\rangle + \frac{\langle \delta h'^2 \rangle}{h'^2} \epsilon_k^p \epsilon_l^{p'}$$

$$- \epsilon_k^p \sigma^2(x_l^{p'}) \left\langle \delta h' \delta\left(\frac{\Gamma_l^{p,h}}{x_l^{p'}}\right) \right\rangle - \epsilon_l^{p'} \sigma^2(x_k^p) \left\langle \delta h' \delta\left(\frac{\Gamma_k^{p,h}}{x_k^p}\right) \right\rangle + h'^2 \left\langle \delta\left(\frac{\Gamma_k^{p,h}}{x_k^p}\right) \delta\left(\frac{\Gamma_l^{p,h}}{x_l^{p'}}\right) \right\rangle \sigma^2(x_k^p) \sigma^2(x_l^{p'})$$

.....5.3.7

The expression for the updated covariance matrix is seen to have the required asymptotic values in that for cases where only small adjustments are made, the matrix is dominated by the prior matrix, whilst for situations where the adjustments are relatively large, the matrix becomes swamped by the injected mathematical correlations.

5.3.2 The Covariance Between Partial Cross-Sections

The procedure of evaluating all the adjustment parameters from the same set of measurement data, $\underline{M}$, imposes a constraint on the evaluates so that even though the prior support function may be orthogonal (as is the case with Schmidt type data), correlations are injected by the optimisation method which cover all the evaluates. These correlations between different independently measured cross-section parameters have no physical interpretation from the viewpoint of the microscopic nuclear data file; they are purely an abstract contrivance of the optimisation model. In analogy with equation 5.3.7 an expression for this covariance between partial cross-sections can be shown to have the form:

$$\langle \delta\hat{x}_k^{\rho} \delta\hat{x}_l^{\rho'} \rangle = \langle \delta x_k^{\rho} \delta x_l^{\rho'} \rangle + \frac{\epsilon_l^{\rho'}}{h'} \langle \delta h' \delta x_k^{\rho} \rangle - h' \sigma^2(x_l^{\rho'}) \left\langle \delta x_k^{\rho} \delta \left(\frac{\Gamma_l^{\rho,h}}{x_l^{\rho'}} \right) \right\rangle$$

$$+ \frac{\epsilon_k^{\rho}}{h'} \langle \delta h' \delta x_l^{\rho'} \rangle - h' \sigma^2(x_k^{\rho}) \left\langle \delta \left(\frac{\Gamma_k^{\rho,h}}{x_k^{\rho}} \right) \delta x_l^{\rho'} \right\rangle + \frac{\langle \delta h^2 \rangle}{h^2} \epsilon_k^{\rho} \epsilon_l^{\rho'}$$

$$- \epsilon_k^{\rho} \sigma^2(x_l^{\rho'}) \left\langle \delta h' \delta \left(\frac{\Gamma_l^{\rho,h}}{x_l^{\rho'}} \right) \right\rangle - \epsilon_l^{\rho'} \sigma^2(x_k^{\rho}) \left\langle \delta h' \delta \left(\frac{\Gamma_k^{\rho,h}}{x_k^{\rho}} \right) \right\rangle + h'^2 \left\langle \delta \left(\frac{\Gamma_k^{\rho,h}}{x_k^{\rho}} \right) \delta \left(\frac{\Gamma_l^{\rho,h}}{x_l^{\rho'}} \right) \right\rangle \sigma^2(x_k^{\rho}) \sigma^2(x_l^{\rho'})$$

.....5.3.8

Although the injected cross-correlations between the adjusted parameters are purely mathematical in nature, being dependent upon the statistical model and the nature of the discrepancies vector, $(\underline{C} - \underline{M})$, they can be beneficial in reducing the expected fractional standard deviation on an integral parameter calculated with the optimised data set and its appropriate covariance matrix. Campbell and Rowlands[35] have demonstrated that optimised data covariance matrices can be used to reduce the uncertainty margins on fast reactor core parameter prediction and a discussion on this property of the covariance matrices derived from the ASPIS iron benchmark measurements using the two tier hybrid optimisation scheme can be found in Chapter X. Moreover from the viewpoint of the two tier

hybrid optimisation scheme, the updated parameter covariance and correlation matrices are important because together with the best-supported parameter set they define the starting data for the next cycle. This point will be reviewed again in a later chapter.

5.4 The Multi-Channel Detector Reaction-Rate

In this section the stochastic parameter $\delta h'$ is analysed and reduced to an expansion in terms of the adjustment evaluators. The effect of the multiplicative scaling constant resulting from the linear search in the cross-section adjustment stage will be neglected until the final results are derived. The reaction-rate h, corresponding to the multi-channel detector distribution H_j^+, is for small response parameter adjustments essentially:

$$h = \sum_q \sum_{i \epsilon q} \frac{(c_i - m_i)\, c_i}{\sigma^2(m_i)} \qquad 5.4.1$$

For first order of small changes:

$$\delta h = \sum_q \sum_{i \epsilon q} \frac{(2c_i \delta c_i - m_i \delta c_i - c_i \delta m_i)}{\sigma^2(m_i)} \qquad 5.4.2$$

and substituting for δC_i (equation 4.3.4)

$$\delta h = \sum_q \sum_{i \epsilon q} \left\{ \frac{(2c_i - m_i)}{\sigma^2(m_i)} \left[\left(\frac{\delta \alpha_q}{\alpha_q} + \frac{\delta S \delta \alpha_q}{S \alpha_q} + \frac{\delta S}{S} \right) c_i + S\alpha_q \sum_j \delta a_{qij} \delta \phi_j \right. \right.$$
$$\left. \left. + (S\alpha_q + \delta S \alpha_q + S \delta \alpha_q) \left(\sum_j \delta a_{qij} \phi_j + a_{qij} \delta \phi_j \right) \right] - \frac{c_i \delta m_i}{\sigma^2(m_i)} \right\} \qquad 5.4.3$$

where the calibration energy scale parameter is included implicitly in δa_{qij} for $q \epsilon q_s$. This expression is analogous to the support function for the hypothesised model parameters and therefore the coefficient of the term in $\underline{\delta \phi}$, with the variables set equal to their evaluates, may be used to specify a multi-channel detector distribution, viz:

$$L_j^+ = \sum_q \sum_{i \epsilon q} \frac{(2c_i - m_i)}{\sigma^2(m_i)} \left[(S\alpha_q + \delta S \alpha_q + S \delta \alpha_q) a_{qij} + S\alpha_q \delta a_{qij} \right] \qquad 5.4.4$$

with a corresponding reaction-rate:

$$\ell = \sum_j L_j^+ \phi_j \qquad 5.4.5$$

such that:

$$\sum_j L_j^+ \delta\phi_j = \ell \sum_K \frac{\Gamma_K^{A,\ell}}{x_K^A} \delta x_K^A + \frac{\Gamma_K^{x,\ell}}{x_K^x} \delta x_K^x + \frac{\Gamma_K^{\tau,\ell}}{x_K^\tau} \delta x_K^\tau \qquad 5.4.6$$

Substituting this into the expression for δh gives:

$$\delta h = \sum_q \sum_{i \in q} \left\{ \frac{(2C_i - m_i)}{\sigma^2(m_i)} \left[\left(\frac{\delta\alpha_q}{\alpha_q} + \frac{\delta S}{S} \delta\alpha_q + \frac{\delta S}{S} \right) C_i + (S\alpha_q + \delta S \alpha_q + S \delta\alpha_q) \sum_j \delta a_{qij} \phi_j \right] - \frac{C_i \delta m_i}{\sigma^2(m_i)} \right\} + \ell \sum_K \frac{\Gamma_K^{A,\ell}}{x_K^A} \delta x_K^A + \frac{\Gamma_K^{x,\ell}}{x_K^x} \delta x_K^x + \frac{\Gamma_K^{\tau,\ell}}{x_K^\tau} \delta x_K^\tau \qquad 5.4.7$$

Since the expected evaluates of the support surface are normally distributed variables, the third moment of which is zero, a reduction to first order in the evaluators can be performed with little loss of accuracy. The final expression for the stochastic variable δh is:

$$\delta h = \sum_q \sum_{i \in q} \left\{ \frac{(2C_i - m_i)}{\sigma^2(m_i)} \left[\left(\frac{\delta\alpha_q}{\alpha_q} + \frac{\delta S}{S} \right) C_i + S\alpha_q \sum_j \delta a_{qij} \phi_j \right] - \frac{C_i \delta m_i}{\sigma^2(m_i)} \right\} + \ell \sum_K \frac{\Gamma_K^{A,\ell}}{x_K^A} \delta x_K^A + \frac{\Gamma_K^{x,\ell}}{x_K^x} \delta x_K^x + \frac{\Gamma_K^{\tau,\ell}}{x_K^\tau} \delta x_K^\tau \qquad 5.4.8$$

This expression can be used to calculate the variance on the multi-channel detector distribution reaction-rate, a quantity that is required for determination of the adjusted cross-section covariance matrices.

$$\langle \delta h^2 \rangle = \left\langle \left\{ \sum_q \sum_{i \in q} \frac{(2C_i - m_i)}{\sigma^2(m_i)} \left[\left(\frac{\delta\alpha_q}{\alpha_q} + \frac{\delta S}{S} \right) C_i + S\alpha_q \sum_j \delta a_{qij} \phi_j \right] - \frac{C_i \delta m_i}{\sigma^2(m_i)} \right\} \left\{ \sum_{q'} \sum_{i' \in q'} \frac{(2C_{i'} - m_{i'})}{\sigma^2(m_{i'})} \left[\left(\frac{\delta\alpha_{q'}}{\alpha_{q'}} + \frac{\delta S}{S} \right) C_{i'} + S\alpha_{q'} \sum_{j'} \delta a_{q'i'j'} \phi_{j'} \right] - \frac{C_{i'} \delta m_{i'}}{\sigma^2(m_{i'})} \right\} \right\rangle$$
$$+ 2\ell \left\langle \sum_q \sum_{i \in q} \frac{(2C_i - m_i)}{\sigma^2(m_i)} \left[\left(\frac{\delta\alpha_q}{\alpha_q} + \frac{\delta S}{S} \right) C_i + S\alpha_q \sum_{j'} \delta a_{qij'} \phi_{j'} \right] - \frac{C_i \delta m_i}{\sigma^2(m_i)} \right\} \sum_\rho \sum_K \frac{\Gamma_K^{\rho,\ell}}{x_K^\rho} \delta x_K^\rho \Bigg\rangle + \ell^2 \sum_\rho \sum_{\rho'} \sum_K \sum_{K'} \frac{\Gamma_K^{\rho,\ell}}{x_K^\rho} \frac{\Gamma_{K'}^{\rho',\ell}}{x_{K'}^{\rho'}} \langle \delta x_K^\rho \delta x_{K'}^{\rho'} \rangle \qquad 5.4.9$$

For the first cycle, based on the Schmidt type start, the only expectation values that exist are those for the parameters with themselves; initially the parameters α_q, a_{qij}, S and x_k^p are assumed to be independent.

$$\langle \delta\alpha_q \, \delta\alpha_{q'} \rangle = \sigma^2(\alpha_q) \, \delta_{qq'} \qquad 5.4.10$$

$$\langle \delta a_{qij} \, \delta a_{q'i'j'} \rangle = \sigma^2(a_{qij}) \, \delta_{qq'} \delta_{ii'} \delta_{jj'} \qquad 5.4.11$$

$$\langle \delta x_k^p \, \delta x_{k'}^{p'} \rangle = \sigma^2(x_k^p) \, \delta_{pp'} \delta_{kk'} \qquad 5.4.12$$

Thus the full expression for the variance on h reduces to:

$$\begin{aligned}\langle \delta h^2 \rangle = & \sum_q \sum_{i \epsilon q} \sum_{i' \epsilon q} \frac{(2c_i - m_i)}{\sigma^2(m_i)} \frac{(2c_{i'} - m_{i'})}{\sigma^2(m_{i'})} c_i \, c_{i'} \left[\frac{\sigma^2(\alpha_q)}{\alpha_q^2} + \frac{\sigma^2(S)}{S^2} \right] \\ & + \sum_q \sum_{i \epsilon q} \frac{c_i^2}{\sigma^2(m_i)} + \sum_q \sum_{i \epsilon q} \sum_j \left[\frac{(2c_i - m_i) S \alpha_q \phi_j}{\sigma^2(m_i)} \right]^2 \sigma^2(a_{qij}) \\ & + l^2 \sum_K \left\{ \frac{\Gamma_K^{A,l}}{x_K^A} \right\}^2 \sigma^2(x_K^A) + \left\{ \frac{\Gamma_K^{X,l}}{x_K^X} \right\}^2 \sigma^2(x_K^X) + \left\{ \frac{\Gamma_K^{T,l}}{x_K^T} \right\}^2 \sigma^2(x_K^T)\end{aligned}$$

.....5.4.13

Similarly the expression for the covariance between the multi-channel detector distribution reaction-rate and a partial cross-section can be shown to be:

$$\langle \delta x_K^p \, \delta h \rangle = \frac{l \, \Gamma_K^{p,l}}{x_K^p} \sigma^2(x_K^p) \qquad 5.4.14$$

In deriving these expressions two sets of simplifying assumptions have been implicit in the analysis. The first set are those appropriate to the first adjustment cycle and can be shown, with reference to the measurement data (Chapter VII), to be largely true. These assumptions are:

(i) The partition coefficients for the different detectors are independent of each other.

(ii) The measurements are independent quantities.

(iii) The independently measured scalar cross-section parameters are known.

(iv) The responses for the threshold activation detectors and for the resonance sandwich foils are independent.

A further set of assumptions which have been made are dependent upon the use of Schmidt type data in the prior support function. They are:

(v) The grouped response function data for all the activation foils are uncorrelated in energy.

(vi) The variance-covariance matrices for the independently measured transmission cross-sections are diagonal.

These assumptions can only be justified on the basis that either no relevant energy-dependent correlation information about the transmission cross-sections and detector response functions is available or that the widths of the energy groups used in the calculational model are so large that the correlations within the groups are large and the covariances between the group cross-sections are negligible. The generalisation of the method to include energy-dependent correlation matrices is immediate. The extension to include the linear search scaling factor λ of Chapter IV is trivially performed by multiplication of the expressions for $\langle \delta h \ \delta x_k^p \rangle$ by λ. The term $\sigma^2(h)/h^2$ is independent of λ.

5.5 The Transmission Cross-Section Sensitivities

Following the previous discussion, it will be assumed that the absorption, non-elastic and total scalar cross-sections represent independently measured parameters. It will be clear though that this choice in no way limits the generality of the issues to be discussed and that a corresponding analysis can be performed for any known combination of measured cross-section parameters. Recalling the definitions of the independent cross-section sensitivities $\Gamma_k^{p,R}$ given in Chapter II:

$$\frac{\Gamma_K^{A,h}}{x_K^A} = \left\{ \frac{U_K^{A,h}}{x_K^A} - \frac{U_K^{N',h}}{x_K^{N'}} \right\} \qquad 5.5.1$$

$$\frac{\Gamma_K^{X,h}}{x_K^X} = \left\{ \frac{U_K^{N',h}}{x_K^{N'}} - \frac{U_K^{N,h}}{x_K^N} \right\} \qquad 5.5.2$$

and

$$\frac{\Gamma_K^{T,h}}{x_K^T} = \left\{ \frac{U_K^{N,h}}{x_K^N} \right\} \qquad 5.5.3$$

Considering small changes in the fractional absorption sensitivity:

$$\delta\left(\frac{\Gamma_K^{A,h}}{x_K^A}\right) = \frac{\delta U_K^{A,h}}{x_K^A} - \frac{U_K^{A,h}}{x_K^{A^2}} \delta x_K^A - \frac{\delta U_K^{N',h}}{x_K^{N'}} + \frac{U_K^{N',h}}{x_K^{N'^2}} \delta x_K^{N'} \qquad 5.5.4$$

where

$$\delta U_K^{B,h} = \frac{dU_K^{B,h}}{dx_K^f} \delta x_K^f \qquad 5.5.5$$

Since the optimisation functional is firmly posed in the realm of first order theory and the cross-section adjustments to be derived from the iterative procedure will be required to satisfy linear theory, the second order term of 5.5.5 can be set to zero. Therefore:

$$\delta\left(\frac{\Gamma_K^{A,h}}{x_K^A}\right) = -\left\{\frac{U_K^{A,h}}{x_K^{A^2}} + \frac{U_K^{N',h}}{x_K^{N'^2}}\right\}\delta x_K^A + \frac{U_K^{N',h}}{x_K^{N'^2}}\delta x_K^x \qquad 5.5.6$$

The corresponding results for the fractional non-elastic and total sensitivities are:

$$\delta\left(\frac{\Gamma_K^{x,h}}{x_K^x}\right) = \frac{U_K^{N',h}}{x_K^{N'^2}}\delta x_K^A - \left\{\frac{U_K^{N',h}}{x_K^{N'^2}} + \frac{U_K^{N,h}}{x_K^{N^2}}\right\}\delta x_K^x + \frac{U_K^{N,h}}{x_K^{N^2}}\delta x_K^T \qquad 5.5.7$$

and $$\delta\left(\frac{\Gamma_K^{T,h}}{x_K^T}\right) = -\frac{U_K^{N,h}}{x_K^{N^2}}\left(\delta x_K^T - \delta x_K^x\right) \qquad 5.5.8$$

Utilising these expressions, the terms $\left\langle \delta x_k^\rho\, \delta\left(\frac{\Gamma_{k'}^{\rho',h}}{x_{k'}^{\rho'}}\right)\right\rangle$, $\left\langle \delta h'\, \delta\left(\frac{\Gamma_k^{\rho,h}}{x_k^\rho}\right)\right\rangle$ and $\left\langle \delta\left(\frac{\Gamma_K^{\rho,h}}{x_K^\rho}\right)\delta\left(\frac{\Gamma_{K'}^{\rho',h}}{x_{K'}^{\rho'}}\right)\right\rangle$ contained in the covariance expansion (equation 5.3.8) can be reduced to quantities directly dependent upon the measured cross-section standard deviations. Thus taking the absorption cross-section as an example:

$$\left\langle \delta x_K^A\, \delta\left(\frac{\Gamma_{K'}^{A,h}}{x_{K'}^A}\right)\right\rangle = -\left\{\frac{U_K^{A,h}}{x_K^{A^2}} + \frac{U_K^{N',h}}{x_K^{N'^2}}\right\}\sigma^2(x_K^A)\,\delta_{KK'} \qquad 5.5.9$$

$$\left\langle \delta h\, \delta\left(\frac{\Gamma_K^{A,h}}{x_K^A}\right)\right\rangle = -l\,\frac{\Gamma_K^{A,l}}{x_K^A}\left\{\frac{U_K^{A,h}}{x_K^{A^2}} + \frac{U_K^{N',h}}{x_K^{N'^2}}\right\}\sigma^2(x_K^A) + l\,\frac{\Gamma_k^{x,h}\,U_K^{N',h}}{x_k^x\, x_K^{N'^2}}\sigma^2(x_K^x) \qquad 5.5.10$$

and $$\left\langle \delta\left(\frac{\Gamma_K^{A,h}}{x_K^A}\right)\delta\left(\frac{\Gamma_{K'}^{A,h}}{x_{K'}^A}\right)\right\rangle = \left[\left\{\frac{U_K^{A,h}}{x_K^{A^2}} + \frac{U_K^{N',h}}{x_K^{N'^2}}\right\}^2\sigma^2(x_K^A) + \left\{\frac{U_K^{N',h}}{x_K^{N'^2}}\right\}^2\sigma^2(x_K^x)\right]\delta_{KK'}$$

.....5.5.11

In deriving the connection between the intermediate expansion terms δh, $\delta\left(\frac{\Gamma_K^{\rho,h}}{x_K^\rho}\right)$ and the standard deviations on the measured data (cross-sections, reaction-rates etc.), the major approximation made is that linear perturbation theory is sufficient at each cycle in the iterative optimisation scheme. The analysis has been developed on the basis of the availability

of Schmidt type cross-section error data and although this considerably simplifies the arguments, allowing the underlying physics and the requisite mathematical approximations to be exposed, in no way does it represent a limitation. It is, to be sure, only an example of a special case of the more general analysis; the changes in the algorithms generating the covariance matrix for cases where a complete set of error data is available are immediate. The other restriction on the theory thus far is the requirement that the response parameters of each counter either be independent or predominantly irdependent. The latter case is distinguished by the associated strongly diagonal covariance matrix.

5.6 The Covariance Matrix for the Partition Coefficients

The previous section was concerned with a method for updating the cross-section covariance matrices at the end of the first iterative cycle. A procedure for calculating the covariance matrices appropriate to the new evaluators of the partition coefficients inferred at the end of the first cycle will now be presented and afterwards a discussion of the merit of its use will be given. In common with the cross-section adjustments, the partition coefficient $\hat{\alpha}_q$ at the end of the first cycle will be:

$$\hat{\alpha}_q = \alpha_q + \epsilon_q^{\alpha} \qquad 5.6.1$$

and the appropriate expected covariance will be:

$$\langle \delta\hat{\alpha}_q \, \delta\hat{\alpha}_{q'} \rangle = \langle \delta\alpha_q \, \delta\alpha_{q'} \rangle + \langle \delta\alpha_q \, \delta\epsilon_{q'}^{\alpha} \rangle + \langle \delta\epsilon_q^{\alpha} \, \delta\alpha_{q'} \rangle + \langle \delta\epsilon_q^{\alpha} \, \delta\epsilon_{q'}^{\alpha} \rangle \qquad 5.6.2$$

where ϵ_q^{α} is determined by solution of the set of coupled response adjustment equations given in Chapter IV. However a considerable reduction in the algebra can be afforded if it is assumed that the response functions are defined quantities, or that the adjustments to the response cross-sections are negligible. Moreover, for concision, the evaluator for corrections to the source normalisation will also be omitted. The extension to include these evaluates in the analysis, though tedious, is trivial and no new physical insight accrues from their inclusion. Thus for the remainder of this and the next section, the adjustment to the q^{th} partition coefficient will be considered to be:

$$\epsilon_q^{\alpha} = - \frac{\sum_{i \in q} \frac{(c_i - m_i) c_i}{\sigma^2(m_i) \alpha_q}}{\left[\sum_{i \in q} \frac{c_i^2}{\sigma^2(m_i) \alpha_q^2} + \frac{1}{\sigma^2(\alpha_q)} \right]} = - \frac{1}{D_q} \sum_{i \in q} \frac{(c_i - m_i) c_i}{\sigma^2(m_i) \alpha_q} \qquad 5.6.3$$

Thus for small changes:

$$\delta\epsilon_q^{\alpha} = -\frac{1}{D_q^2}\left[D_q \left\{ \sum_{i\epsilon q} \frac{\delta c_i (c_i - m_i)}{\sigma^2(m_i)\alpha_q} + \frac{c_i(\delta c_i - \delta m_i)}{\sigma^2(m_i)\alpha_q} - \frac{c_i(c_i-m_i)\delta\alpha_q}{\sigma^2(m_i)\alpha_q^2} \right\} + D_q \epsilon_q^{\alpha} \sum_{i\epsilon q} \left\{ \frac{2c_i \delta c_i}{\sigma^2(m_i)\alpha_q^2} - \frac{2c_i^2 \delta\alpha_q}{\sigma^2(m_i)\alpha_q^3} \right\} \right] \qquad 5.6.4$$

Consistent with the assumption of negligible changes to the detector response functions and to the source normalisation, the change in the calculated predictions reduces to:

$$\delta c_i = \frac{\delta\alpha_q}{\alpha_q} c_i + S(\alpha_q + \delta\alpha_q) \sum_j a_{qij}\, \delta\phi_j \qquad 5.6.5$$

Substitution of this expression into equation 5.6.4 ultimately leads to:

$$\delta\epsilon_q^{\alpha} = -\frac{1}{D_q}\left[\sum_{i\epsilon q} \left(\frac{c_i^2 \delta\alpha_q}{\sigma^2(m_i)\alpha_q^2} - \frac{c_i \delta m_i}{\sigma^2(m_i)\alpha_q} + \left\{ \left(1 + \frac{\delta\alpha_q}{\alpha_q}\right) \left(\frac{2c_i + 2c_i(\epsilon_q^{\alpha}/\alpha_q) - m_i}{\sigma^2(m_i)} \right) S \sum_i a_{qij} \delta\phi_j \right\} \right) \right] \qquad \ldots\ldots\ldots 5.6.6$$

The constant part of the coefficient of the $\delta\phi$ term can be selected as a multi-channel detector distribution:

$$Y_{q,j}^{+} = S \sum_{i\epsilon q} \frac{(2c_i + 2c_i(\epsilon_q^{\alpha}/\alpha_q) - m_i)\, a_{qij}}{\sigma^2(m_i)} \qquad 5.6.7$$

with reaction-rate:

$$y_q = \sum_j Y_{q,j}^{+} \phi_j \qquad 5.6.8$$

Using this expression to rewrite equation 5.6.6:

$$\delta\epsilon_q^{\alpha} = -\frac{1}{D_q}\left[\left\{ \sum_{i\epsilon q} \frac{c_i^2 \delta\alpha_q}{\sigma^2(m_i)\alpha_q^2} - \frac{c_i \delta m_i}{\sigma^2(m_i)\alpha_q} \right\} + \left(1 + \frac{\delta\alpha_q}{\alpha_q}\right) y_q \left\{ \sum_K \Gamma_K^{A,y_q} \frac{\delta x_K^A}{x_K^A} + \Gamma_K^{x,y_q} \frac{\delta x_K^x}{x_K^x} + \Gamma_K^{\tau,y_q} \frac{\delta x_K^{\tau}}{x_K^{\tau}} \right\} \right] \qquad 5.6.9$$

and the updated variance appropriate to the evaluate $\hat{\alpha}_q$ can be shown to be:

$$\sigma^2(\hat{\alpha}_q) = \sigma^2(\alpha_q) - \frac{2}{D_q}\sum_{i\in q}\frac{C_i^2\,\sigma^2(\alpha_q)}{\sigma^2(m_i)\,\alpha_q^2} + \frac{1}{D_q^2}\sum_{i\in q}\frac{C_i^2}{\sigma^2(m_i)\alpha_q^2} + \frac{1}{D_q^2}\sum_{i\in q}\sum_{i'\in q}\frac{C_i^2 C_{i'}^2\,\sigma^2(\alpha_q)}{\sigma^2(m_i)\sigma^2(m_{i'})\alpha_q^4}$$
$$+\left[1+\frac{\sigma^2(\alpha_q)}{\alpha_q^2}\right]y_q^2\left[\sum_K\left\{\frac{\Gamma_K^{A,\gamma_q}}{x_K^A}\right\}^2\sigma^2(x_K^A)+\left\{\frac{\Gamma_K^{X,\gamma_q}}{x_K^X}\right\}^2\sigma^2(x_K^X)+\left\{\frac{\Gamma_K^{T,\gamma_q}}{x_K^T}\right\}^2\sigma^2(x_K^T)\right]$$
.....5.6.10

and the corresponding covariance is:

$$\mathrm{cov}(\alpha_q,\alpha_{q'}) = y_q y_{q'}\left[\sum_K\frac{\Gamma_K^{A,\gamma_q}\Gamma_K^{A,\gamma_{q'}}}{x_K^{A\,2}}\sigma^2(x_K^A)+\frac{\Gamma_K^{X,\gamma_q}\Gamma_K^{X,\gamma_{q'}}}{x_K^{X\,2}}\sigma^2(x_K^X)+\frac{\Gamma_K^{T,\gamma_q}\Gamma_K^{T,\gamma_{q'}}}{x_K^{T\,2}}\sigma^2(x_K^T)\right]$$
.....5.6.11

where the prior partition coefficients and cross-sections are assumed to be independently distributed quantities:

$$\langle\delta\alpha_q\,\delta\alpha_q\,\delta x_K^\rho\rangle = \sigma^2(\alpha_q)\,\langle\delta x_K^\rho\rangle = 0 \qquad 5.6.12$$

and
$$\langle\delta\alpha_q\,\delta x_K^\rho\,\delta x_K^\rho\rangle = \langle\delta\alpha_q\rangle\,\sigma^2(x_K^\rho) = 0 \qquad 5.6.13$$

In this section a method has been suggested for deriving the magnitude and range of the correlations between the adjusted partition coefficients for the various counters. These correlations have no physical significance but arise from the nature of the statistical model used to describe the neutron transport and subsequent detection. The results have been derived on the basis that the source normalisation and response function uncertainties are negligible, as should be the case in a shielding benchmark experiment, but comparable expressions can be derived with their inclusion. The effort required to generate the covariance matrix for the partition coefficients is dominated by the performance of Q adjoint/sensitivity calculations.

5.7 The Correlation Between the Partition Coefficients and the Transmission Cross-Sections

Inspection of the expression for small changes in the partition coefficient adjustment evaluate (equation 5.6.9) shows that a correlation is injected between the transmission cross-sections and the partition coefficients as a result of the joint optimisation process. The expected covariance matrix can be established to be:

$$\langle\delta\hat{\alpha}_q\,\delta\hat{x}_K^\rho\rangle = \langle\delta\alpha_q\,\delta x_K^\rho\rangle + \langle\delta\epsilon_q^\alpha\,\delta x_K^\rho\rangle + \langle\delta\alpha_q\,\delta\epsilon_K^\rho\rangle + \langle\delta\epsilon_q^\alpha\,\delta\epsilon_K^\rho\rangle \qquad 5.7.1$$

where for the first cycle the prior covariance $\mathrm{cov}(\alpha_q, x_k^p)$ will be zero. Recalling that:

$$\delta\epsilon_k^p = \frac{\delta h}{h}\epsilon_k^p - h\sigma^2(x_k^p)\,\delta\left(\frac{\Gamma_k^{p,h}}{x_k^p}\right) \qquad 5.7.2$$

and

$$\delta\epsilon_q^\alpha = -\frac{1}{D_q}\left[\sum_{i\in q}\left\{\frac{c_i^2\,\delta\alpha_q}{\sigma^2(m_i)\alpha_q^2} - \frac{c_i\delta m_i}{\sigma^2(m_i)\alpha_q}\right\} + \left(1+\frac{\delta\alpha_q}{\alpha_q}\right)y_q\left\{\sum_K \Gamma_K^{A,y_q}\frac{\delta x_K^A}{x_K^A} + \Gamma_K^{x,y_q}\frac{\delta x_K^x}{x_K^x} + \Gamma_K^{T,y_q}\frac{\delta x_K^T}{x_K^T}\right\}\right] \qquad \ldots\ldots\ldots 5.7.3$$

Considering the absorption cross-section as an example, equation 5.7.2 can be written in more fundamental quantities:

$$\delta\epsilon_K^A = \frac{\epsilon_K^A}{h}\left[\sum_q\sum_{i\in q}\left\{\frac{(2c_i-m_i)c_i\,\delta\alpha_q}{\sigma^2(m_i)\alpha_q} - \frac{c_i\delta m_i}{\sigma^2(m_i)}\right\}\right] - h\sigma^2(x_K^A)\left[\frac{U_K^{N',h}}{x_K^{N'^2}}\delta x_K^x - \left\{\frac{U_K^{A,h}}{x_K^{A^2}} + \frac{U_K^{N',h}}{x_K^{N'^2}}\right\}\delta x_K^A + \frac{\epsilon_K^A l}{h}\left[\left\{\sum_L \Gamma_L^{A,l}\frac{\delta x_L^A}{x_L^A} + \Gamma_L^{x,l}\frac{\delta x_L^x}{x_L^x} + \Gamma_L^{T,l}\frac{\delta x_L^T}{x_L^T}\right\}\right]\right] \qquad \ldots\ldots\ldots 5.7.4$$

Considering the situation for the first cycle only and that à priori the adjustment evaluators are independent:

$$\langle\delta\alpha_q\,\delta\epsilon_K^A\rangle = \frac{\epsilon_K^A}{h}\sum_{i\in q}\frac{(2c_i-m_i)c_i\,\sigma^2(\alpha_q)}{\sigma^2(m_i)\alpha_q} \qquad 5.7.5$$

$$\langle\delta\epsilon_q^\alpha\,\delta x_K^A\rangle = -\frac{y_q}{D_q}\frac{\Gamma_K^{A,y_q}}{x_K^A}\sigma^2(x_K^A) \qquad 5.7.6$$

$$\langle\delta\epsilon_q^\alpha\,\delta\epsilon_K^A\rangle = -\frac{\epsilon_K^A}{D_q h}\left[\sum_{i\in q}\left\{\sum_{i'\in q}\left(\frac{c_i^2(2c_{i'}-m_{i'})c_{i'}\sigma^2(\alpha_q)}{\sigma^2(m_i)\;\sigma^2(m_{i'})\;\alpha_q^3}\right) + \frac{c_i^2}{\sigma^2(m_i)\alpha_q}\right\} + 2l\,y_q\sum_{K'}\Gamma_{K'}^{A,y_q}\Gamma_{K'}^{A,l}\frac{\sigma^2(x_{K'}^A)}{x_{K'}^{A^2}} + \Gamma_{K'}^{x,y_q}\Gamma_{K'}^{x,l}\frac{\sigma^2(x_{K'}^x)}{x_{K'}^{x^2}} + \Gamma_{K'}^{T,y_q}\Gamma_{K'}^{T,l}\frac{\sigma^2(x_{K'}^T)}{x_{K'}^{T^2}}\right] - \frac{h\,y_q}{D_q}\sigma^2(x_K^A)\left[\frac{U_K^{N',h}}{x_K^{N'^2}}\frac{\Gamma_K^{x,y_q}}{x_K^x}\sigma^2(x_K^x) - \left\{\frac{U_K^{A,h}}{x_K^{A^2}} + \frac{U_K^{N',h}}{x_K^{N'^2}}\right\}\frac{\Gamma_K^{A,y_q}}{x_K^A}\sigma^2(x_K^A)\right] \qquad 5.7.7$$

Using these terms in equation 5.7.1 the first cycle correlation coefficient relating changes in the partition coefficients to changes in the transmission cross-sections may be obtained. For subsequent cycles the situation is more complex since none of the adjustment evaluators are independent; the generalised matrix for the correlation between the partition coefficients

and the transmission cross-sections may be obtained by a similar approach to that established above but since the correlations between the parameters should be weak and have no physical significance, the appropriateness and desirability of calculating such a matrix are questionable. Certainly if necessary similar relationships can be established for the cross-correlations between other evaluators, $\langle \delta g_q \delta \alpha_{q'} \rangle$, $\langle \delta \alpha_q \delta a_{q'ij} \rangle$, $\langle \delta g_q \delta a_{q'ij} \rangle$, $\langle \delta x_k^p \delta S \rangle$ etc.

5.8 Summary

A method has been described for both establishing the updated variance-covariance matrices for the individual parameter types and for the cross-correlations injected between different parameters by the process of optimisation. The algebra has been developed only for the situation at the end of the first cycle for evaluators which prior to optimisation were known to be independent. The situation for subsequent cycles can be formulated, although the requirement of including these data tends to defeat the purpose of the two tier hybrid method in which the response data are assumed to be close to total maximum likelihood. If the adjustments to the response data are small, the cross-correlations between the detector data and the neutron transmission data are expected to be weak and so can be ignored. The evaluation of adjustments to the response data is considered only to represent the fine tuning of the statistical model and if large adjustments are found they serve as an indicator of either inconsistent detector data or erroneous integral measurements. Thus only the updating of the correlation matrix of the transmission cross-section data is considered to be of any useful interest in that large cross-section adjustments may be obtained and the correlation matrix at the end of one cycle represents the constraint for the following cycle.

It should be mentioned though that the joint optimisation of the response and transmission data is to some extent possible under the following regime. The response functions for a few individual detectors may be capable of optimisation provided the information they contain about the transmission data is weak - corresponding to the assignment of large response cross-section uncertainties. In this case the detector data will be optimised for consistency with the rest of the response data provided there is sufficient detector coverage in the sensitive region of the uncertain response function. Moreover, since the optimisation theory for the detector responses has been expanded to second order in all variables except the flux perturbation, a single cycle should be adequate to optimise the response data and obtain mutual consistency.

CHAPTER VI

TRANSPORT CALCULATIONS FOR THE ASPIS IRON BENCHMARK EXPERIMENT

6.1 Introduction

"The adjustment of the nuclear parameters of a medium on the basis of an intercomparison with a single material benchmark necessitates the use of a reference calculation containing no unacceptable error arising from the discretization of the analytic treatment of the interaction phenomena". This statement represents the 'predictive' criterion for benchmark consistent data adjustment, by which any discrepancy in the reaction data can be related wholly to the analytic behaviour imposed upon that phenomenon, be it by deduction from the models of nuclear theory or inference from the measurements of nuclear physics.

A less rigorous (engineering orientated) principle might demand that the representation and solution of the problem in spatial phase space introduce no unacceptable error, thus introducing a degree of freedom whereby the treatment of velocity space may be quite arbitrary. Adoption of this principle and the associated lack of resolution can destroy any pathway back to the basic measurements and models of nuclear physics, resulting in the loss of the predictive nature of the benchmark study. The adjustment procedure then becomes purely a self-consistent exercise for the determination of the errors and correlations in the group constants introduced as a result of the coarse discretization of the velocity space.

The reference calculation should seek to demonstrate that even under the most accurate conditions of geometric modelling of the problem and solution of the linearized transport equation, there exist discrepancies between the prediction of observables deduced from calculation and the values ascribed to them from measurement; these discrepancies can only then be attributed to the neutron interaction data, the errors arising from either shortcomings in the data itself or from uncertainties introduced by the code processing the data for the solution method. The magnitude of these discrepancies affords determination of the original χ^2 for the statistical model prior to data adjustment and indicates, that provided χ^2 is greater than the number of degrees of freedom of the system, that data adjustment and an associated reduction of χ^2 are at least possible in principle.

The reference calculation for the ASPIS iron benchmark experiment is described in this chapter and an attempt is made to satisfy the 'predictive' principle of data adjustment. The adjustment of nuclear parameters on the strength of comparison with benchmark experiments is still in its infancy and it is therefore important not only to derive

the adjusted data set with the appropriate covariance matrix, but also to demonstrate that such adjustments necessarily result from a lack of accuracy of the basic nuclear data - irrespective of the source.

The reference calculation also serves to provide dimensional transformation coefficients allowing reduction from the 2-D reference situation to a 1-D working model with no loss of generality or significant change of χ^2. It is propitious to reduce the dimensionality of the problem for two reasons. Firstly, from the economic viewpoint, multi-dimensional adjoint calculations are prohibitively expensive in other than the simplest of cases and secondly a two dimensional sensitivity code was unavailable for use in this work. The ASPIS iron benchmark was therefore essentially a 1-D study for which only on-axis observables were measured. Details of the derivation of the energy-dependent dimensional transformation coefficients are presented in a later section.

6.2 The Geometrical Model

6.2.1 Description of the Experimental Facility

A schematic diagram of the experimental arrangement is shown in Figure 6.1 in which the various component regions are named with their relevant equivalent area dimensions. A discussion pertaining to the ASPIS shielding facility and the iron benchmark shield can be found in reference (4). The actual model used for the DOT-III transport calculation, in r-z cylindrical geometry, is illustrated in Figure 6.2. The effect of neutron backscatter from the lead γ-ray shield in the source reactor, NESTOR, was shown, through importance calculations, to be negligible at the measurement positions and was therefore omitted. Many of the region boundaries were radially stretched to allow co-incidence with the outer radius of the converter plate (r = 66.5 cm) thus achieving a considerable reduction in the geometry specification for the transport code with no significant loss of accuracy. The air spaces on either side of the source fission plate were retained with no penalty in computational efficiency, whereas the inter-shield plate air gaps were smeared. The retention of all axial dimensions as true allowed conservation of geometrical disposition and mean free path, thus providing a precise treatment for both geometrical and material attenuation.

6.2.2 Description of the Converter Plate

The converter plate comprised ten aluminium clad fuel elements carried in an aluminium support plate. Each fuel element could contain a maximum of 46 natural uranium fuel coupons. The spatial distribution

ALL DIMENSIONS IN cm.

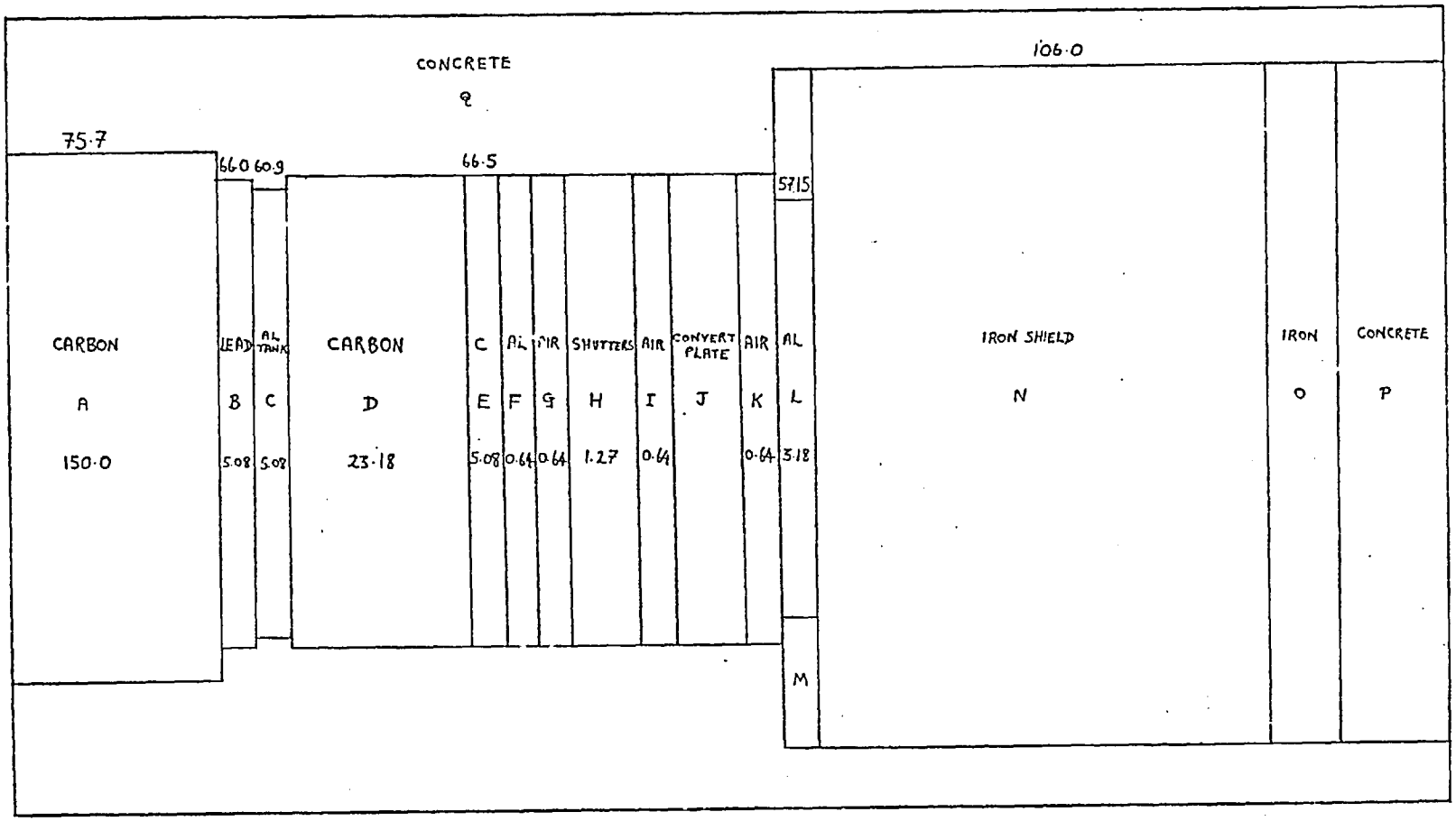


FIG. 6.1 EQUIVALENT AREA VIEW OF THE ASPIS IRON BENCHMARK EXPERIMENT.

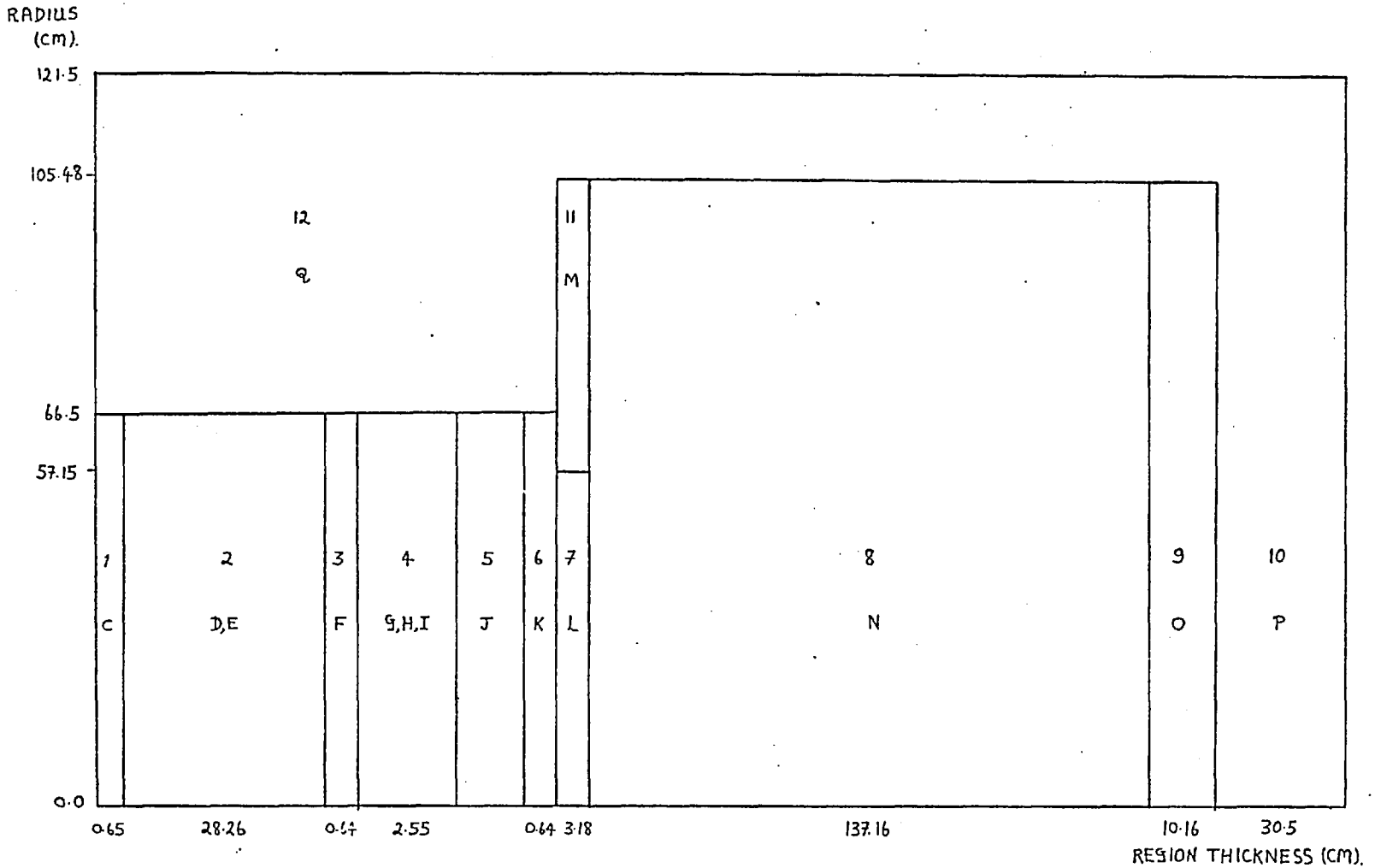


FIG. 6.2 R-Z GEOMETRICAL MODEL FOR TRANSPORT CALCULATION

Table 6.1(A)

Zone Materials Densities for the ASPIS Iron Benchmark Model

Zone No.	Material		Atomic Density atoms $b^{-1}cm^{-1}$.
1	Aluminium		6.024 -2
2	Carbon		8.534 -2
3	Aluminium		6.024 -2
4	Air	N	5.550 -5
5	Converter Plate		-
6	Air	N	5.550 -5
7	Aluminium		6.024 -2
8	Mild Steel	H	2.071 -5
		C	7.996 -4
		Fe	7.404 -2
		Mn	5.660 -4
9,11	Mild Steel	H	2.330 -5
		C	8.996 -4
		Fe	8.330 -2
		Mn	6.370 -4
10,12	Concrete	H	1.128 -2
		C	8.270 -3
		Al	6.610 -4
		Mn	2.130 -4
		Fe	4.990 -2
		O	1.482 -2
		Si	4.760 -3
		Ca	3.690 -3

Table 6.1(B)

Composition of Modelled Converter Plate

Material		Thickness cm.	Atomic Density atoms $b^{-1}cm^{-1}$
Aluminium (Reactor Side)		8.554 -1	4.808 -2
Mild Steel	H	3.640 -1	1.858 -5
	C		7.174 -4
	Mn		5.080 -4
	Fe		6.643 -2
Natural Uranium	U^{235}	3.988 -1	2.719 -4
	U^{238}		3.746 -2
Mild Steel		3.640 -1	Same as above
Aluminium (Shield Side)		8.930 -1	Same as above

of the fuel in the plate was chosen to represent a disc source, as shown in Figure 6.3, with mild steel dummy coupons inserted in positions not containing fuel. The inner region of the plate was modelled as a disc source of solid natural uranium and the outer region as an annulus of mild steel. The details of the smearing calculations have been given elsewhere[109] and are summarised in a unit cell of the plate in Figure 6.4. The intermediate stage model of the unit cell is illustrated in Figure 6.5 and the densities and thicknesses of the materials after volume smearing over the air gaps in the unit cell are displayed in Table 6.1.

6.2.3 The Source Distribution

The spatial distribution of the fission-rate on the reactor side of the converter plate, measured by Packwood and Carter[110], with 0.05 mm thick natural uranium foils calibrated in a thermal spectrum against an absolutely calibrated fission chamber, is given in Table 6.2. The relative flux profile across the converter plate was simultaneously monitored with manganese activation foils so that the ratio of the U^{235} fission-rate to the normalised manganese activities establishes a set of values for the fission-rate at the centre of the plate on the reactor side.

Table 6.2

U^{235} Fission-rate Distribution for Fuel Element No. 5 at 3 kW NESTOR Reactor Power

Plate Position No.	U^{235} Fission-rate		Normalised Manganese Activities	Ratio U/Mn	
	Run 1	Run 2		Run 1	Run 2
12	1.20 -13	1.24 -13	1.000	1.20 -13	1.24 -13
15	1.08 -13	-	0.890	1.21 -13	-
17	9.17 -14	9.63 -14	0.753	1.22 -13	1.28 -13
19	7.40 -14	-	0.590	1.25 -13	-
21	4.99 -14	5.02 -14	0.400	1.25 -13	1.25 -13
22	3.61 -14	-	0.305	1.18 -13	-
23	2.31 -14	-	0.202	1.05 -13	-

The average fission-rate, ignoring the least value of 1.05 -13 is $1.23 \pm 0.01 \times 10^{-13}$ fission s^{-1}/atom of U^{235} at 3 kW of NESTOR reactor power. The normalised manganese activities, compounded by azimuthal averaging from the seperately established angular dependent profiles

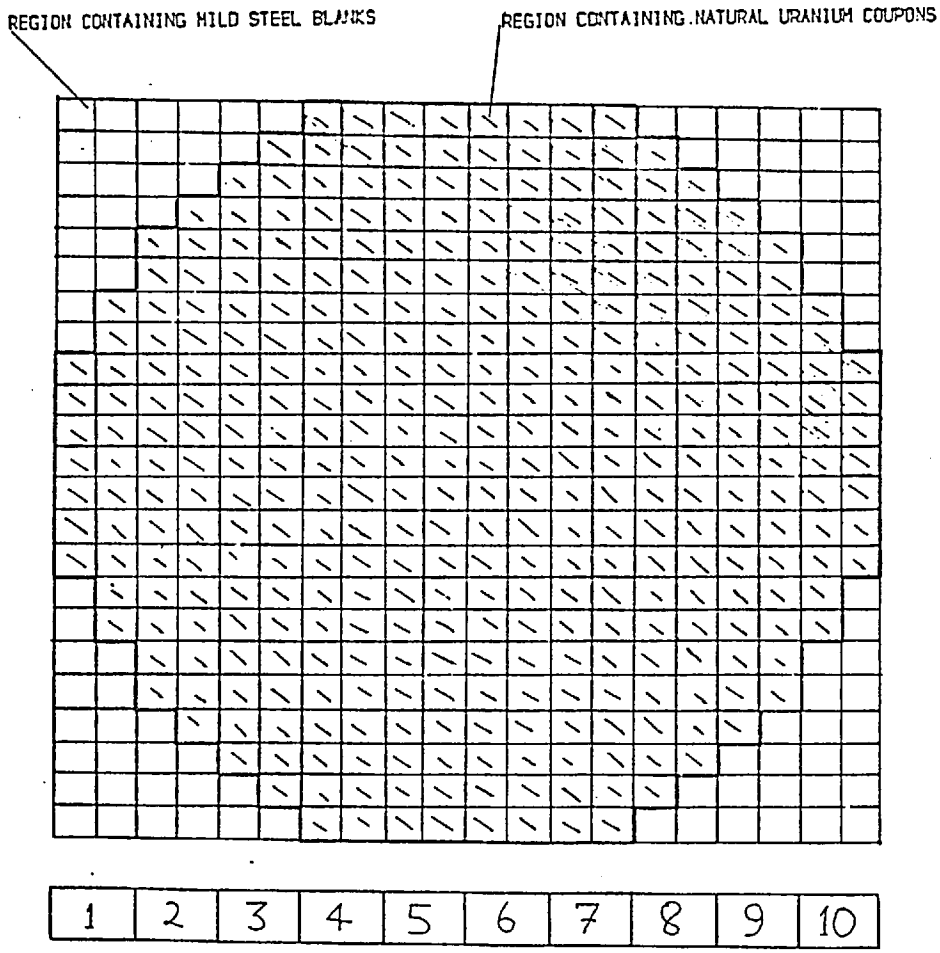


FIG. 6.3 SPATIAL DISTRIBUTION OF FUEL IN CONVERTER PLATE.

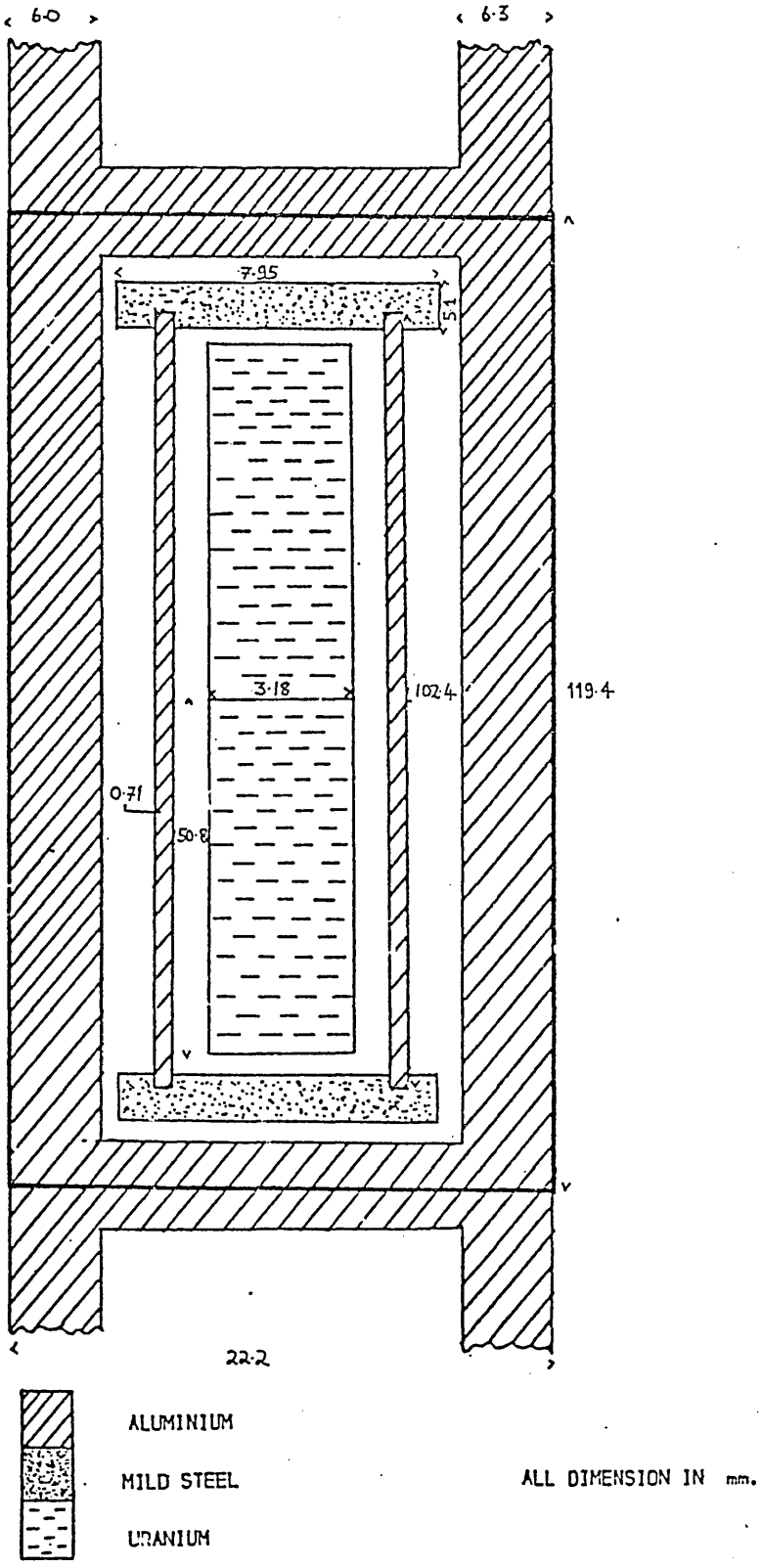


FIG. 6.4 PLANAR LATTICE CELL OF THE CONVERTER PLATE

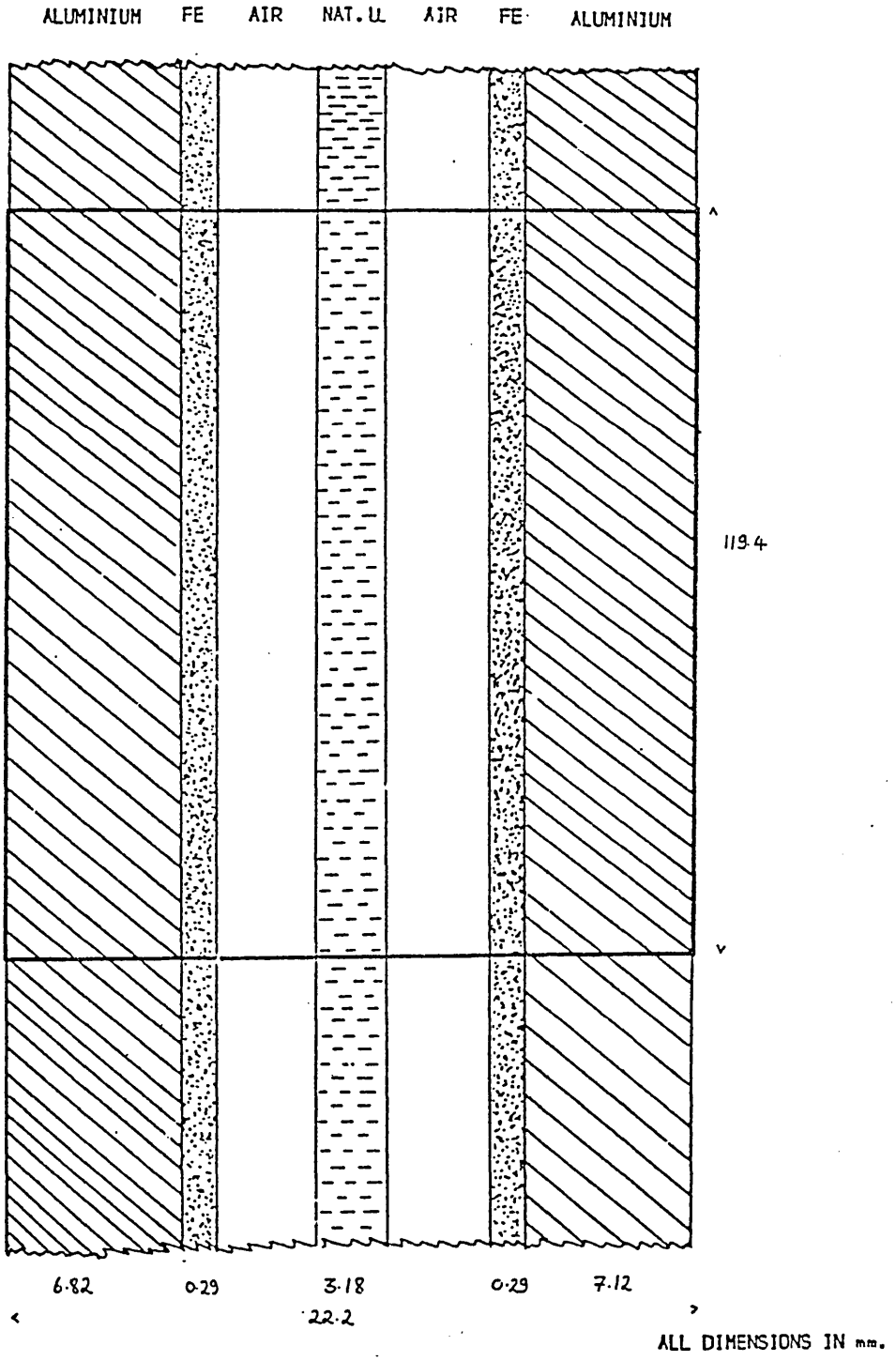


FIG. 6.5 INTERMEDIATE MODEL OF LATTICE CELL (PLANAR).

Table 6.3

Results of a Symmetry Inspection at 3 KW of NESTOR Reactor Power

Radius cm	$\theta=0^{\circ}\uparrow$	$\theta=90^{\circ}\rightarrow$	$\theta=180^{\circ}\downarrow$	$\theta=270^{\circ}\leftarrow$	Average	Cosine Fit	$\frac{\text{Fit}}{\text{Av}}-1\%$	$\frac{\sigma(\text{Av})}{\text{Av}}\%$
0	1.000	1.000	1.000	1.000	1.000	1.000	0.0	0.0
5	0.993	0.997	1.000	0.984	0.994	0.994	0.0	0.7
10	0.951	0.984	0.988	0.951	0.969	0.976	0.7	2.1
15	0.900	0.960	0.960	0.910	0.933	0.946	1.4	3.4
20	0.832	0.927	0.906	0.861	0.882	0.905	2.6	4.9
25	0.758	0.881	0.848	0.807	0.824	0.853	3.5	6.5
30	0.684	0.824	0.774	0.745	0.757	0.790	4.4	7.7
35	0.601	0.766	0.692	0.680	0.685	0.718	4.8	9.9
40	0.511	0.692	0.601	0.605	0.602	0.638	6.0	12.3
45	0.420	0.610	0.507	0.523	0.515	0.549	6.6	15.1
50	0.321	0.527	0.400	0.445	0.423	0.454	7.3	20.4
55	0.222	0.432	0.305	0.358	0.329	0.354	7.6	26.9
60	0.124	0.329	0.198	0.268	0.230	0.249	8.3	38.5

shown in Table 6.3, can be fitted by the least square technique to a cosinusoidal distribution of the form:

$$\frac{\phi(r)}{A} = \cos\left\{\frac{\pi . r}{142.9}\right\} \qquad 6.2.1$$

Although the fit is not the best possible, the error in the cosinusoidal representation is very much less than the deviation about the experimental mean. Moreover, the evidence of Table 6.3 appears to suggest that an asymmetry existed in the fission neutron distribution across the surface of the plate. The asymmetry cannot be included in the 2-D DOT-III and ANISN calculations; however since the distortion is small, the effect on axial measurements in the shield region should be negligible.

A non-linearity in the variation of flux output from the converter plate with change in NESTOR reactor power was observed during the experimental programme and since the relative error between fission foils is small, it may be inferred from Table 6.4 that there was an apparent loss of 2.15% of neutron flux at 3 kw compared with all other powers.

Table 6.4

Variation of Fission-rate at the Centre of the Converter Plate with NESTOR Reactor Power

NESTOR Reactor Power	10 kw	3 kw	1 kw	500 w	100 w
U^{235} Fission-rate s^{-1} $atom^{-1}$	4.13 -13	1.21 -13	4.10 -14	2.05 -14	4.17 -15

Although the majority of the iron benchmark experimental results were measured for reactor powers of either 10 kw or below 1 kw, the converter plate was normalised using fission foils at 3 kw. A non-linearity factor of 1.0215 has therefore been introduced into the source normalisation to obtain agreement with all other powers.

The source strength of the converter plate was established on the reactor face of the assembly for the reasons that the flux/power ratio was higher on the reactor side and background effects were smaller in comparison. However, for transport calculations some average source in the fuel is required and by utilising special fuel plates, the attenuation of the U^{235} fission-rate axially through the fuel has been measured for

a number of radial positions, the results being summarised in Table 6.5.

Table 6.5

Radial Dependence of Fuel Plate Self-Absorption Factors

Radial Position Coupon No.	Relative Attenuation through Fuel		
	Reactor Side	Middle	Shield Side
22	1.00	0.869	0.795
15	1.00	0.871	0.799
12	1.00	0.864	0.798
9	1.00	0.862	0.795
2	1.00	0.858	0.793
Average	-	0.865 ± 1%	0.796

Since it can be seen that the effect is neither simply exponential, nor linear, the value chosen is the experimental figure, which represents the best estimate, and the source distribution for the reactor side must be renormalised by the factor 0.865 to obtain the source strength for the centre of the fuel. The normalisation of the converter plate for the transport calculations must include the modelling factor 0.851 introduced in the smearing calculations[109]; the 'modelled' radial source profile may then be expressed as:

$$\phi(\tau) = 3.085 \times 10^{-17}\ \bar{\nu}_{235}\ \cos\left\{\frac{\pi\tau}{142.9}\right\} \quad \text{per NESTOR watt } U^{235} \text{ atoms}^{-1} \qquad 6.2.2$$

The adequacy of this representation of the converter plate source profile has been examined by comparison of the predicted total fission plate power with that obtained by radial integration of the manganese activation foil reaction-rates[109] and although the result indicates that the model prediction is 6% too high with respect to the experimental value, the discrepancy lies well within the error bounds on the source normalisation and experimental measurements, which are compounded from:

(i) experimental errors on the U^{235} fission foil reaction-rates

(ii) experimental errors on the manganese reaction-rates arising from counting statistics and calibration

(iii) uncertainties in the calibration of the U^{235} fission foils

(iv) truncation error in using Simpson's rule to determine the average manganese activity for the plate as a whole.

6.3 The Calculational Method

The most general formulation of the Boltzmann transport equation[111] describes the behaviour of the neutron flux ψ as a function of the independent variables of position $\underline{r}$, direction $\underline{\Omega}$, energy E and time t. The solution of the equation[112,113] by the method of discrete ordinates involves the use of a mechnical quadrature to replace the continuous angular flux $\psi(\underline{r},\underline{\Omega},E,t)$ by a finite set of δ functions of weight $\phi_s(\underline{r},E,t)$, s=1,n which are independent of direction.

$$\int_{\Omega} \psi(\underline{r},\underline{\Omega},E,t)\,\delta(\underline{\Omega}-\underline{\Omega}')\,d\underline{\Omega} = \phi(\underline{r},\underline{\Omega}',E,t) = \phi_s(\underline{r},E,t) \qquad 6.3.1$$

The strength of the δ functions, ϕ_s, represent the ordinates of the quadrature and the order of quadrature, n, specifies the precision. The method essentially transforms the integro-differential equation in the angular flux $\psi(\underline{r},\underline{\Omega},E,t)$ to a set of n simultaneous differential equations in the ordinate fluxes $\phi_s(\underline{r},E,t)$. Discretization of the spatial and energy variables, necessary for a numerical solution is usually performed by the application of a finite-difference operator[114]. The resultant discrete ordinates equations are an exact analogue of the analytic transport equation, obeying the required conservation laws[115] and in the limit of the phase space mesh volume tending to zero, the exact form is reconstructed provided the existance theorem for finite and bounded differentials is obeyed[116,117]. The method errors inherent in a discrete ordinates solution of the neutron transport problem result from the finite size of the phase space mesh and the truncation of the Legendre expansion representing the angular dependence of the scattered neutron. In a benchmark study it is necessary to evaluate these errors or to demonstrate that the error arising from a particular source is negligible in comparison with other uncertainties; perturbation of the phase space mesh represents the optimum method of assessment of the precision of the method and is discussed in the next section along with the choice of method parameters.

The major limitation of all discrete ordinates codes available for use in deep penetration problems is the restriction to orthogonal curvilinear and plane geometries. The introduction into discrete ordinates codes of the generalised geometry modules available to Monte Carlo programmes is beyond the storage capability of most modern computers. The modelling of the ASPIS iron DATAM experiment in cylindrical (r-z) geometry for the DOT-III[11] code has been considered in Section 6.2 and the errors arising from approximation of the geometry in this fashion are considered

to be negligible (< 5%). Although a Monte Carlo shielding code such as MORSE-CG[12] with a generalised geometry capability could have been used to model the geometry with greater precision and to solve the Boltzmann transport equation, nominally without incurring method errors, the reduction of the statistics on the differential flux to an acceptable level (<5%) would have represented a formidable and possibly even prohibitive computing penalty. Moreover diffusion theory is not applicable to the problem owing to the anisotropic nature of the scattering at high energies and the dominance of the forward-peaked flux in the within-group scattering, the latter resulting in part from the fine resolution chosen for the energy group structure. Thus any 2-D description of the experimental assembly must be a compromise between accuracy, computational expense and realistic description of the geometry.

6.4 Choice of Calculational Parameters for DOT-III

The cost and CPU time associated with two-dimensional DS_n problems dictates prudent usuage. The number of unknowns, and hence the core storage requirement is directly proportional to the product of the number of energy groups, spatial mesh cells and directions used. The resolution of each of these variables as well as the order of scattering integral expansion, P_l, represent quantities to be optimised. The procedure adopted for setting up the DOT-III reference calculation consisted of an independent systematic reduction in the input variables using the 1-D DS_n code ANISN[10] to determine the minimum resolution which would give the required precision in the calculated quantity of interest. Use of restart flux input substantially reduced the cost of the multiple runs necessary for the parametric assessment.

6.4.1 Spatial Mesh

The use of an adequate spatial mesh in all discrete ordinates programs is mandatory to obtaining an accurate flux solution. The literature cites many guide-lines for suitable choice of axial and radial mesh structure[118,119]. The strongest criterion suitable for benchmark calculations should be that the scalar flux must not vary by more than a factor two between contiguous spatial intervals. The choice of such a constraint should eliminate the negative fluxes and numerical instability causing oscillation which at the very least increase the CPU time by invoking negative flux fix-up procedures and at the very worst produce distortions in the angular flux leading to the anomolous evaluation of the scattering integral. However, such a criterion cannot be generally applicable for the spatial mesh structure would be defined by the group

containing the largest resonance maximum - shortest mean free path. Since in deep penetration problems resonances are self-shielded, the adoption of such a procedure would be unnecessarily restrictive. For the purpose of this reference calculation, the spatial mesh structure was chosen to be the average mean free path over all the energy groups. The radial and axial increments chosen for each material zone are given in Table 6.6. The adequacy of this mesh was inspected by comparison of integral and differential parameters predicted by ANISN calculations performed using double and half the axial mesh; Table 6.7 demonstrates that there is little gain to be achieved by further increasing the spatial resolution.

6.4.2 The Energy Group Structure

The DOT-III code cannot accept the point energy model of neutron kinematics and recourse has to be made to a multi-group energy representation with the associated cross-section group transition probability matrices. The group structure was chosen on the basis of the following two criteria. The energy resolution must be sufficient to adequately represent all the discrete characteristics of the iron cross-section, and the effect of the weighting function used to collapse the point cross-section data into multi-group format must be sufficiently small such as to incur no unacceptable error (<5%). The group boundaries of the EURLIB-100 energy group scheme[120], which has been adopted for use in this reference calculation, were chosen by the NEA/EURATOM collaborative benchmark committee with specific reference to the iron benchmark programme and to the structure of the iron cross-section. The adequacy of the group structure, the effect of the weighting function and the order of truncation of the Legendre polynomial expansion of the scattering cross-section were all investigated in a parametric survey using ANISN.

The energy range from 110 keV to 7 keV was considered to be the most demanding of the group structure. The penetration of a 1/E spectrum through 70 cm of iron was investigated for this energy region using the 14 groups of the EURLIB-100 energy group structure spanning this region and a pseudo 1000 group scheme obtained by dividing the original 14 groups by ten to obtain 140 groups. The pseudo 1000 group calculations were carried out using both a P_3 and P_5 cross-section expansion. The simulated EURLIB calculation used only a P_3 truncation. The predictions of the assessment calculations for integral responses and differential flux are compared in Table 6.8 and it can be seen that the relative error using the EURLIB-100 group scheme with a P_3 expansion compared with a 1000 group P_5 calculation is no greater than $\sim$5% for important (high

Table 6.6(A)

Radial Mesh Structure

Inner Radius cm	Outer Radius cm	Number of Intervals	Interval Width
0.0	57.5	10	5.75
57.5	59.3	1	1.80
59.3	66.5	3	2.40
66.5	106.0	13	3.04
106.0	121.5	6	2.58

Table 6.6(B)

Axial Mesh Structure

Material	Boundary 1 cm	Boundary 2 cm	Thickness cm	Mean Free Path cm	Mesh Interval
Al	0.0	0.650	0.650	1.53	0.650
C	0.650	28.910	28.260	2.50	2.570
Al	28.910	29.550	0.640	1.53	0.640
Air	29.550	32.100	2.550	-	2.550
Al	32.100	32.9554	0.8554	1.53	0.8554
Fe	32.9554	33.3194	0.3640	~1.00	0.3640
U	33.3194	33.7182	0.3988	-	0.3988
Fe	33.7182	34.0822	0.3640	~1.00	0.3640
Al	34.0822	34.9752	0.8930	1.53	0.8930
Air	34.9752	35.615	0.640	-	0.640
Al	35.615	38.795	3.180	1.53	1.590
Iron Shield	38.795	175.955	137.160	~1.13	1.414
Iron	175.955	186.115	10.160	~1.00	1.4514
Concrete	186.115	205.000	18.889	-	2.100

Table 6.7

Comparison of Spatial Mesh Increments

Position (Mesh No)		Increment Δz cm			% Deviations from 1	
		1 1.414	2 2.800	3 0.91	2/1	3/1
		Sulphur Reaction-Rate (High Energy)				
1	(50)	7.01 -1	6.84 -1	7.10 -1	2.4	1.3
2	(80)	1.39 -3	1.27 -3	1.39 -3	8.6	0.0
3	(100)	2.26 -5	1.97 -5	2.32 -5	12.8	2.7
4	(120)	3.68 -7	3.01 -7	3.83 -7	18.2	4.1
		Gold Reaction-Rate (Epithermal and Thermal)				
1	(50)	9.98 +4	8.77 +4	9.98 +4	12.2	0.0
4	(120)	6.46 +3	6.46 +3	6.46 +3	0.0	0.0
		Flux in Group 59 (27 keV Resonance Maximum)				
1	(50)	9.51 +1	9.51 +1	9.52 +1	0.0	0.0
4	(120)	1.43 +0	1.43 +0	1.44 +0	0.0	0.0
		Group 61 Flux (24 keV Interference Minimum)				
1	(50)	7.48 +2	7.47 +2	7.48 +2	0.0	0.0
4	(120)	3.56 +1	3.56 +1	3.56 +1	0.0	0.0
		Flux in Typical High Energy Group (25)				
1	(50)	2.65 +0	2.60 +0	2.67 +0	1.9	0.8
4	(120)	2.79 -6	2.30 -6	2.90 -6	17.6	3.9

* Reaction-Rates given as saturated disintegrations s^{-1} $atom^{-1}$ $barn^{-1}$ NESTOR $watt^{-1}$

flux) groups after 60 cm of pure iron.

As a direct result of the fine energy resolution afforded by the EURLIB-100 group scheme, the within group scattering angular distribution will be very forward peaked, thus demanding greater angular resolution. Although the core requirement increases in proportion to the number of groups, the rate of group convergence depends on Σ^{gg}/Σ^{T}, the dominance ratio of the transport matrix of the solution algorithm equations. If for a particular group structure the lethargy width, Δu, is small, then Σ^{gg} is small and $\Sigma^{gg}/\Sigma^{T} \ll 1$, giving rapid convergence. Thus the penalty for having fine energy resolution may not be large and a many group calculation can be more efficient than the corresponding few group problem with higher dominance ratio.

6.4.3 The Order of Angular Quadrature

The requirements of the quadrature set are that the integration of the angular flux evaluate the scalar flux accurately and that the scattering integral, involving the integration of Legendre polynomials, be calculated with a high degree of precision. These criteria were investigated using S_4 and S_8 quadrature in ANISN and comparing results. The assumption that the dependence on quadrature sets in the 1-D code ANISN is analogous to their behaviour in the 2-D DOT-III code may not be entirely satisfactory, but can be used as a guide-line. The dependence of the 1-D results on the order of quadrature was less than 2% (Table 6.9) in all cases and although the literature[121] suggests that the order of quadrature, n, be twice as large as the Legendre cross-section expansion, l, for accurate integration of the scattering integral, from the pragmatic viewpoint, the completely symmetric even moment S_4 quadrature set for cylindrical geometry appeared to be satisfactory.

6.4.4 The Iterative Solution Algorithm

For DOT-III, the inner iterative algorithm is required to determine phase space cell fluxes from a knowledge of the cell boundary conditions. The essence therefore of a good iterative algorithm is that the finite difference equation relating the cell centred flux and the boundary conditions represent a good approximation to the true variation of the flux in the cell, whilst being soluble quickly and efficiently on the computer. Since an exponential variation of the flux across the cell is too complicated, in general the expansion is truncated after only one or two terms giving a constant (known as the 'step function method') or linear interpolation (known as the 'diamond-difference scheme') respectively.

Table 6.8(A)

Comparison of Group Fluxes

Upper Energy Boundary	Σ^T	Penetration Depth			
		50 cm		60 cm	
keV	cm^{-1}	ϕ_{broad}	$\Sigma\phi_{fine}$	ϕ_{broad}	$\Sigma\phi_{fine}$
111.10	3.13 -1	1.27 -1	1.27 -1	1.80 -2	1.80 -2
86.50	2.11 -1	3.24 +0	6.78 +0	8.25 -1	2.84 +0
67.40	3.18 -1	3.23 +0	5.41 +0	8.42 -1	2.03 +0
52.48	3.88 -1	3.35 +0	5.16 +0	8.88 -1	1.84 +0
40.87	5.88 -1	2.40 +0	3.73 +0	6.39 -1	1.30 +0
31.83	1.61 +0	7.05 -1	1.11 +0	1.88 -1	3.84 -1
26.05	7.98 -2	8.89 +0	1.12 +1	3.59 +0	5.26 +0
24.79	3.19 -2	3.91 +1	4.01 +1	2.33 +1	2.45 +1
23.57	6.13 -2	3.15 +1	3.21 +1	1.84 +1	1.92 +1
21.87	1.30 -1	2.50 +1	2.51 +1	1.41 +1	1.45 +1
19.30	2.18 -1	3.00 +1	3.00 +1	1.64 +1	1.67 +1
15.03	3.19 -1	2.03 +1	2.02 +1	1.09 +1	1.10 +1
11.71	4.72 -1	1.35 +1	1.34 +1	7.20 +0	7.21 +0

Table 6.8(B)

Comparison of Integral Parameters

Penetration	50 cm		60 cm	
Response	Mn	Au	Mn	Au
Broad Group	1.11 +2	2.48 +3	6.24 +1	1.38 +3
Fine Group	1.15 +2	2.54 +3	6.56 +1	1.43 +3
% Difference	3.9	2.7	4.9	3.8

Table 6.9

Order of Quadrature Comparison

Position	Quadrature	S(n,p)	Rh(n,n')	In(n,n')	Au(n,γ)	Flux(25)*
50 cm	S_4	7.13 -1	4.47 +2	1.86 +1	9.99 +4	2.68 +0
	S_8	7.01 -1	4.45 +2	1.84 +1	9.98 +4	2.65 +0
70 cm	S_4	1.11 -2	8.43 +1	1.58 +0	5.45 +4	5.76 -2
	S_8	1.10 -2	8.40 +1	1.57 +0	5.43 +4	5.69 -2
100 cm	S_4	2.24 -5	7.43 +0	6.35 -2	1.75 +4	1.56 -4
	S_8	2.25 -5	7.40 +0	6.31 -2	1.75 +4	1.56 -4
120 cm	S_4	3.60 -7	1.32 +0	7.89 -3	6.45 +3	2.75 -6
	S_8	3.68 -7	1.31 +0	7.84 -3	6.46 +3	2.79 -6

* Flux in EURLIB group number 25

$$\phi(z) = \phi(z')e^{-\Sigma^T(|z-z'|)} \simeq \phi(z') - \phi(z')\Sigma^T(|z'-z|) + O(\Sigma^T \Delta z)^2 \qquad 6.4.1$$

More explicitly the cell centred flux ϕ_R can be represented in terms of the boundary fluxes ϕ_r and ϕ_{r+1} by:

$$\phi_R = a\phi_r + (1-a)\phi_{r+1} \qquad 6.4.2$$

where if:

(i) $a = 0$ or 1 'step function method'.

(ii) $a = \frac{1}{2}$ 'diamond difference method'.

(iii) $a \neq 0, \frac{1}{2}, 1$ 'weighted difference method'.

Although the linear interpolation method is the more accurate representation, it can become unstable. If, for example, the flux is decreasing so rapidly that the cell centred flux ϕ_R is less than one half the magnitude of the previous boundary flux ϕ_r, the extrapolated end point flux ϕ_{r+1}, will be negative and this instability is called "diamond difference breakdown"[122]. Such a condition usually occurs in positions where the phase space mesh is too large and an over-enthusiastic extrapolation has been attempted. It has been recognised in penetration problems that a negative end point flux, however insignificant, can cause subsequent fluxes to diverge in positive-negative oscillations, until the entire problem collapses into a sea of meaningless fluxes[114].

The DOT-III code has a flag which in the event of diamond difference breakdown switches the calculation to the step function method for the calculation of all variables in the offending phase space cell[114]. This circumvents the instability and returns to the linear interpolation algorithm for the contiguous cell. However, if this fix-up procedure is used for more than a few phase space cells, the accuracy of the calculation can suffer.

The weighted difference algorithm[123] mitigates the errors introduced when diamond difference breakdown occurs by adjusting the weight 'a' to make $\phi_{r+1} \geq 0$. If $\phi_{r+1} = 0$, the finite difference equations enter a class of methods known as 'set-to-zero and recompute'[115]. Generally such methods are more accurate in unstable situations than the 'standard fix-up and continue' algorithms[124,115]. For this reason the weighted difference mode of calculation was selected for use in the DOT-III calculation. Table 6.10 presents a summary of a survey of the methods of iteration in DOT-III conducted by Salvatores[124] in a comparison calculation for the ASPIS iron benchmark experiment using 26 group P_1 multi-

Table 6.10

Comparison of Models of Convergence using DOT-III with Different Mesh Interval Sizes (after Salvatores[124])

Detector	Position cm	Mixed			Weighted			Step	
		5.08	2.54	1.27	5.08	2.54	1.27	5.08	1.27
S(n,p)	10.16	3.44 -1	4.04 -1	4.49 -1	4.22 -1	4.00 -1	3.86 -1	5.12 -1	4.19 -1
	20.32	4.77 -2	5.52 -2	6.68 -2	7.15 -2	6.41 -2	6.10 -2	1.31 -1	7.87 -2
	35.56	2.85 -3	3.08 -3	3.34 -3	4.25 -3	3.82 -3	3.65 -3	1.74 -2	6.13 -3
	50.80	2.09 -4	1.73 -4	1.41 -4	2.79 -4	2.59 -4	2.49 -4	2.48 -3	5.38 -4
	76.20	2.33 -6	1.68 -6	1.36 -6	3.04 -6	3.00 -6	2.98 -6	1.01 -6	9.79 -6
	101.60	2.82 -8	3.40 -8	3.96 -8	2.96 -8	3.08 -8	3.24 -8	3.75 -6	1.59 -7
In(n,n')	10.16	4.69 -1	5.08 -1	5.31 -1	5.23 -1	5.02 -1	4.92 -1	5.92 -1	5.18 -1
	20.32	1.17 -1	1.29 -1	1.37 -1	1.43 -1	1.33 -1	1.29 -1	2.11 -1	1.49 -1
	35.56	1.66 -2	1.81 -2	1.99 -2	2.08 -2	1.92 -2	1.86 -2	4.44 -2	2.41 -2
	50.80	3.10 -3	3.40 -3	3.62 -3	3.80 -3	3.58 -3	3.42 -3	1.09 -2	4.79 -3
	76.20	2.29 -4	2.43 -4	2.67 -4	2.89 -4	2.64 -4	2.62 -4	1.22 -3	4.08 -4
	101.60	2.00 -5	2.28 -5	2.42 -5	2.52 -5	2.34 -5	2.30 -5	1.49 -4	3.95 -5

All values are for S_8 and are normalised at 5.08 cm to unit saturated d.p.s. per $\frac{\text{barn}}{\text{atom}}$.

group cross-sections derived from ENDF/B-IV.

6.4.5 Choice of Convergence Test

In discrete ordinates programs generally there are three convergence tests available:

(i) Scattering Integral Test.

(ii) Volume Integral Test.

(iii) Point Flux Test applicable to either the whole problem or to a zone of interest.

The scattering integral test may be written as:

$$\left| \frac{\int_r \sum_k^s (\underline{r}) \left(\phi_k^{(i)}(\underline{r}) - \phi_k^{(i-1)}(\underline{r}) \right) d\underline{r}}{\int_r \sum_k^s (\underline{r}) \, \phi_k^{(i)}(\underline{r}) \, d\underline{r}} \right| \leqslant \varepsilon \qquad 6.4.3$$

where the integration is usually over the volume of the system and $\phi^{(i)}(\underline{r})$ is the scalar flux at $\underline{r}$ as calculated by the i^{th} iteration. Although this criterion is satisfactory for reactor core calculations where the magnitude of the flux is relatively constant through the problem, it is unsuitable for deep penetration calculations because the integral is dominated by the flux near the source, which has the greatest magnitude and converges the most rapidly. The volume integral test is often formulated as:

$$\left| \frac{1}{V} \int_r \frac{\left(\phi_k^{(i)}(\underline{r}) - \phi_k^{(i-1)}(\underline{r}) \right)}{\phi_k^{(i)}(\underline{r})} \, d\underline{r} \right| \leqslant \varepsilon \qquad 6.4.4$$

where the integration is over the entire volume of the system. By the very nature of the inverse volume weighting, very large relative flux deviations can go undetected near the boundaries of the system. In other words, the majority of the system can be converged to a high degree of accuracy, whilst points may exist within the system (usually near the boundaries) where gross flux deviations still exist. The point flux test:

$$\text{Max} \left| \frac{\phi_k^{(i)}(\underline{r}) - \phi_k^{(i-1)}(\underline{r})}{\phi_k^{(i)}(\underline{r})} \right| \leqslant \varepsilon \quad \text{for all } \underline{r} \text{ and } k \qquad 6.4.5$$

represents the only satisfactory convergence criterion that can be applied to shielding calculations, although it can be grossly over-

sensitive when applied in 2-D geometries. For example there may be some unimportant point in an obscure corner of the problem, near a boundary, which refuses to converge and whose importance to accurate prediction of the response is negligible. The application of the point flux criterion in multi-dimensional geometries, is therefore often limited to a 'zone of interest'.

The extent of the zone of interest for the reference calculation was limited to a sub-region of the iron shield, away from the concrete-iron shield radial boundary where convergence could be difficult and the effect of the boundary fluxes on the axial measurements would be negligible. The maximum fractional flux deviation, ε, allowed was 0.1%. It is important to note that ε does not represent the error in the flux, which may be much greater than 0.1%; it only represents an end point to iteration at which the gain in accuracy per iteration is insufficient to warrant further computational expenditure. However given the dominant eigenvalue of the transport matrix, an estimate of 1% can be obtained for the real error in the fluxes for the ASPIS experiment reference calculation.

6.4.6 Acceleration Techniques

The number of iterations required to converge a discrete ordinates calculation is almost independent of the spatial mesh increment and the number of directions used. Nevertheless there has been a constant effort to accelerate the iterative process by use of a variety of scaling techniques. An analysis of the rate of convergence of a finite difference representation of the transport equation solved by power iteration has been given by Mynatt[114] who has shown that after many iterations, the rate of convergence $\mathcal{R}$ is dependent on the largest eigenvalue of the transport operator. If the error vector for the i^{th} iterate flux is $\underline{\varepsilon}^{(i)}$ then:

$$\underline{\varepsilon}^{(i)} = (\underline{\phi} - \underline{\phi}^{(i)}) \simeq \lambda_1^i \underline{\varepsilon}^{\circ} = \lambda_1 \underline{\varepsilon}^{(i-1)} \quad \text{for } i \gg 1 \qquad 6.4.6$$

whence:

$$\mathcal{R} = \ln \left\{ \frac{\underline{\varepsilon}^{(i-1)}}{\underline{\varepsilon}^{(i)}} \right\} = - \ln \lambda_1 \qquad 6.4.7$$

Moreover the dominance ratio λ_1 can be estimated[114] as:

$$\lambda_1 = \frac{\Sigma^{gg}}{\Sigma^{T}} < 1 \qquad 6.4.8$$

which since the self-scattering cross-section Σ^{gg} is less than the total cross-section Σ^{T} demonstrates that a convergent solution is always possible. The common aim of the various acceleration techniques, brought to bear on the inner iterative scheme of the discrete ordinates code DOT, is to reduce the dominance ratio. In the DOT-III code, four algorithms for the acceleration of the solution method are available. Two of these, space independent renormalisation and space dependent scaling are considered in some detail in Appendix D. The other techniques available are the Chebyshev polynomial method[125] and successive over-relaxation; Disney[121] asserts that the successive over-relaxation method cannot be used in deep penetration problems where large flux gradients exist and the experience of the author is that it leads to program abend. Chebyshev polynomial acceleration has been used with sucess in diffusion theory programs[126] and although it can be very beneficial in groups with high dominance ratio (~ 1), it often takes longer than no acceleration for other groups with low dominance ratio[114].

For the reference calculation both space dependent scaling and space independent renormalisation were used and an examination of the methods (Appendix D) will elucidate why it was necessary on several occasions, during the progress of the calculation, to switch from one to the other.

6.4.7 Initial Flux Guess

The expense of a 100 group DOT-III calculation can be formidable unless some reasonable initial flux guess is provided. The following methods were identified as producing useful starting flux guesses:

(i) The scalar fluxes from seperate radial and axial ANISN calculations can be used to synthesise a 2-D starting flux distribution for the problem and this can be used as an input to a S_2 DOT calculation. The S_2 flux dump can be used to start the full S_4 calculation.

(ii) The output scalar flux tape from a DOT-III calculation for a similar problem geometry can be utilised, within the bounds allowed by linear adjustment in the problem description parameters.

Nicks et al[127] have performed a DOT-III calculation for a simplified model of the ASPIS iron benchmark experiment[128] using the EURLIB-100 energy group scheme. A parametric comparison of the EURATOM calculations with the present reference calculation is given in Table 6.11. The EURATOM scalar flux tape was re-structured using the linear interpolation program EDIT to produce a flux starting guess compatible with the re-modelled

Table 6.11

Comparison of EURATOM Calculation with the ASPIS Iron DATAM Experiment Reference Calculation

Parameter	EURATOM	Reference Calculation
Point Flux Convergence Criterion	0.01	0.001
Number of Energy Groups	First 67 of EURLIB-100	EURLIB-100
Microscopic Nuclear Data Library	EURLIB-III	UKNDL DFN 908A
No. of Axial Mesh Intervals	80	135
No. of Radial Mesh Intervals	33	33
Order of P_1 Scattering Expansion	3	3
Order of S_n Angular Quadrature	4	4
Solution Algorithm	mixed - linear/step	weighted linear difference

benchmark geometry used in the present study. Method (i) above, involving ANISN, was used to furnish a flux guess in the lower 33 groups. It was impossible to assess the benefit gained from the use of the approximate answer, but the calculation set up as specified above required 5 MB of core storage under the MVS system on the Harwell IBM 370/168 and took approximately 10 hours of CPU time.

6.5 Comparison of the Reference Calculation Predictions with Measurement

The reference calculation has been used to predict values for all the observables measured during the iron benchmark experimental programme. The prediction of observables (count-rate vectors etc) rather than derived quantities (flux) obviates the problem of statistical and mathematical noise injected by the unfolding process. Although refolding lacks the one-to-one correspondence useful for diagnostic purposes, it preserves the quality and independence of the benchmark measurements.

The detectors used at a variety of distances through the iron shield were four hydrogen proportional chambers at 10, 3, 1 and ½ at. pressure, an argon-hydrogen proportional counter, an NE 213 organic scintillator and four activation foils. The gas counter response matrices were computed using the program PRC[7] and the response matrix for the organic scintillator was predicted from the light curve for the counter using the computer

code PRCM[102]. The detector cross-sections used for the integral detectors were those specified for use in the collaborative programme by Farinelli[129]. The sulphur (n,p) and rhodium (n,n') cross-sections were taken from the UKNDL - DFN's 97 and 94 respectively; the EURLIB data was used for In(n,n') and the cadium covered gold (n,γ) data were interpolated from tables of resonance detector cross-sections produced at Ispra. A discussion on the quality of these data is given in the next chapter.

A comparison of the integral detector results derived by the DOT-III reference calculation with the values inferred from measurement is given in Tables 6.12 to 6.15. Also given are the results obtained using an earlier EURLIB-15 group reference calculation by Grimstone et al[5] and the predictions of Salvatores et al[124] using their 26 group ENDF/B calculation. The early calculation of Grimstone appears to be discrepant in the calculation of all the threshold detector reaction-rates; this may be the result of the lack of energy resolution for the calculation of the fluxes for these detectors plus the fact that the mixed mode algorithm with integral convergence test were specified. The present results agree closely with the Salvatores results although the discrepancies increase with distance; likely causes could be the specification of a less rigorous convergence criterion or a genuine difference in the nuclear data sets. The vast discrepancies between the results of Salvatores calculation and the measurements for the Cd{Au(n,γ)} reaction-rates arise from the absence of any self-shielding correction to the cross-section data used by Salvatores. A comparison of the flux spectrum, derived by simultaneous unfolding of all the measurements at all positions using the RADAK[7] code, with the calculated flux distribution at four penetration depths are given as Figures 6.6. to 6.9. Figure 6.10 compares the calculated and measured attenuation of the activation detector response-rates with distance.

The details of the calculation and the results discussed above have defined the reference calculation for the ASPIS iron DATAM experiment, and have formed the basis for the consensus adjustment of the UKNDL iron data set. The chi-squared for the reference calculation was 1.9686 +4 which for 502 degrees of freedom gives χ^2/n to be 39.2.

6.6 Transformation to 1-D

6.6.1 Methods of Transformation

The 1-D code ANISN allows for simulation of 2-D leakage effects through the provision of a single geometric buckling which has utility in core calculations for the criticality or reactivity of a static

Table 6.12

S(n,p) Reaction-Rate - Axial Profile

Position (cm)	DOT-100	Measured[4]	DOT-15[5]	Salvatores[124]
5.08	1.06 +2	1.10 +2	7.79 +1	-
10.16	3.39 +1	3.75 +1	2.74 +1	4.25 +1
15.24	1.61 +1	1.35 +1	1.05 +1	-
20.32	6.70 +0	5.26 +0	4.07 +0	6.70 +0
25.40	2.80 +0	2.02 +0	1.59 +0	-
30.48	1.17 +0	7.75 -1	6.21 -1	-
35.56	4.88 -1	2.88 -1	2.44 -1	4.02 -1
40.64	2.04 -1	1.17 -1	9.64 -2	-
45.72	8.53 -2	4.51 -2	3.82 -2	-
50.80	3.50 -2	1.94 -2	1.52 -2	2.74 -2
55.88	1.48 -2	7.00 -3	6.05 -3	-
60.96	6.29 -3	3.19 -3	2.45 -3	-
66.04	2.61 -3	-	9.76 -4	-
76.20	4.57 -4	2.5 -4	1.61 -4	3.28 -4
81.28	1.92 -4	-	6.59 -5	-
91.44	3.38 -5	-	1.13 -5	-
101.60	5.97 -6	-	2.02 -6	3.56 -6

Table 6.13

Rh(n,n') Reaction-Rate - Axial Profile

Position (cm)	DOT-100	Measured[4]	DOT-15[5]
5.08	4.11 +3	3.86 +3	2.92 +3
10.16	2.38 +3	2.21 +3	1.60 +3
15.24	1.44 +3	1.32 +3	9.40 +2
20.32	9.05 +2	8.46 +2	5.80 +2
25.40	5.79 +2	5.27 +2	3.72 +2
30.48	3.77 +2	3.41 +2	2.47 +2
35.56	2.49 +2	-	1.69 +2
40.64	1.67 +2	1.56 +2	1.18 +2
45.72	1.13 +2	1.12 +2	8.32 +1
50.80	7.59 +1	7.90 +1	5.96 +1
55.88	5.23 +1	5.84 +1	4.30 +1
60.96	3.62 +1	4.02 +1	3.13 +1
66.04	2.49 +1	2.97 +1	2.28 +1
76.20	1.19 +1	1.66 +1	1.22 +1
81.28	8.30 +0	1.21 +1	8.99 +0
91.44	3.65 +0	7.62 +0	4.84 +0
101.60	1.94 +0	4.25 +0	2.59 +0

Reaction-rates are given as saturated disintegrations $s^{-1}atoms^{-1}$
barn^{-1} NESTOR watt^{-1}

Table 6.14

Au(n,γ) Reaction-Rate - Axial Profile

Position (cm)	DOT-100	Measured[4]	DOT-15[5]	Salvatores[124]
5.08	1.75 +5	1.13 +5	1.96 +5	-
10.16	1.23 +5	1.05 +5	1.23 +5	-
15.24	9.03 +4	8.47 +4	8.62 +4	-
20.32	6.89 +4	6.68 +4	6.42 +4	9.14 +4
25.40	5.43 +4	5.48 +4	5.01 +4	-
30.48	4.44 +4	4.57 +4	4.02 +4	-
35.56	3.71 +4	3.73 +4	3.27 +4	5.20 +4
40.64	3.15 +4	3.15 +4	2.68 +4	-
45.72	2.68 +4	-	2.19 +4	-
50.80	2.29 +4	2.24 +4	1.79 +4	2.94 +4
55.88	1.96 +4	-	1.45 +4	-
60.96	1.67 +4	1.56 +4	1.17 +4	-
66.04	1.42 +4	-	9.44 +3	-
76.20	1.01 +4	9.26 +3	6.04 +3	1.04 +4
81.28	8.41 +3	7.55 +3	4.44 +3	-
91.44	5.79 +3	5.18 +3	3.00 +3	-
101.60	3.93 +3	3.44 +3	1.84 +3	3.28 +3

Table 6.15

In(n,n') Reaction-Rate - Axial Profile

Position (cm)	DOT-100	Measured[4]	DOT-15[5]	DOT-15[5]	Salvatores[124]
5.08	6.19 +2	5.80 +2	3.92 +2	4.04 +2	-
10.16	2.92 +2	2.65 +2	1.72 +2	1.76 +2	2.80 +2
15.24	1.46 +2	1.32 +2	8.08 +1	8.27 +1	-
20.32	7.54 +1	6.44 +1	3.93 +1	4.03 +1	7.50 +1
25.40	3.97 +1	3.27 +1	1.99 +1	2.04 +1	-
30.48	2.12 +1	1.69 +1	1.05 +1	1.08 +1	-
35.56	1.17 +1	-	5.78 +0	5.95 +0	1.08 +1
40.64	6.51 +0	5.77 +0	3.36 +0	3.47 +0	-
45.72	3.71 +0	3.50 +0	2.04 +0	2.12 +0	-
50.80	2.12 +0	2.02 +0	1.30 +0	1.36 +0	1.98 +0
55.88	1.27 +0	1.27 +0	8.62 -1	8.99 -1	-
60.96	7.70 -1	-	5.88 -1	6.14 -1	-
66.04	4.65 -1	-	4.10 -1	4.29 -1	-
76.20	1.78 -1	-	2.09 -1	2.19 -1	1.52 -1
81.28	1.11 -1	-	1.36 -1	1.59 -1	-
91.44	4.40 -2	-	8.02 -2	8.42 -2	-
101.60	1.77 -2	-	4.26 -2	4.48 -2	1.33 -2
	EURLIB		UKNDL DFN 239	EURLIB	

Reaction-rates are given as saturated disintegrations s^{-1} $atoms^{-1}$ $barn^{-1}$ NESTOR $watt^{-1}$

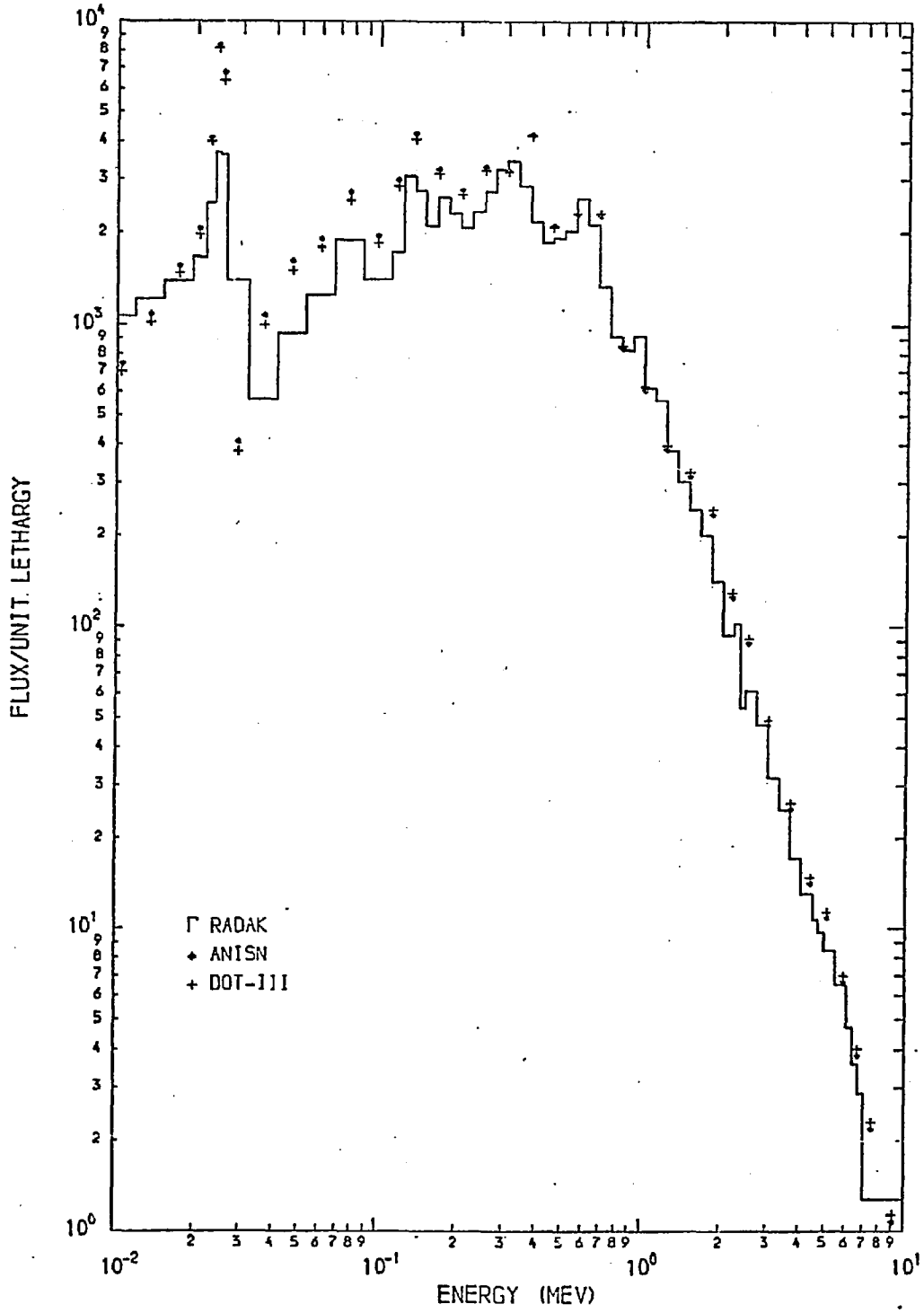


FIG. 6.6 COMPARISON OF CALCULATED FLUX PROFILES WITH RADAK UNFOLDED SPECTRUM MEASUREMENT AT 20.3CM POSITION.

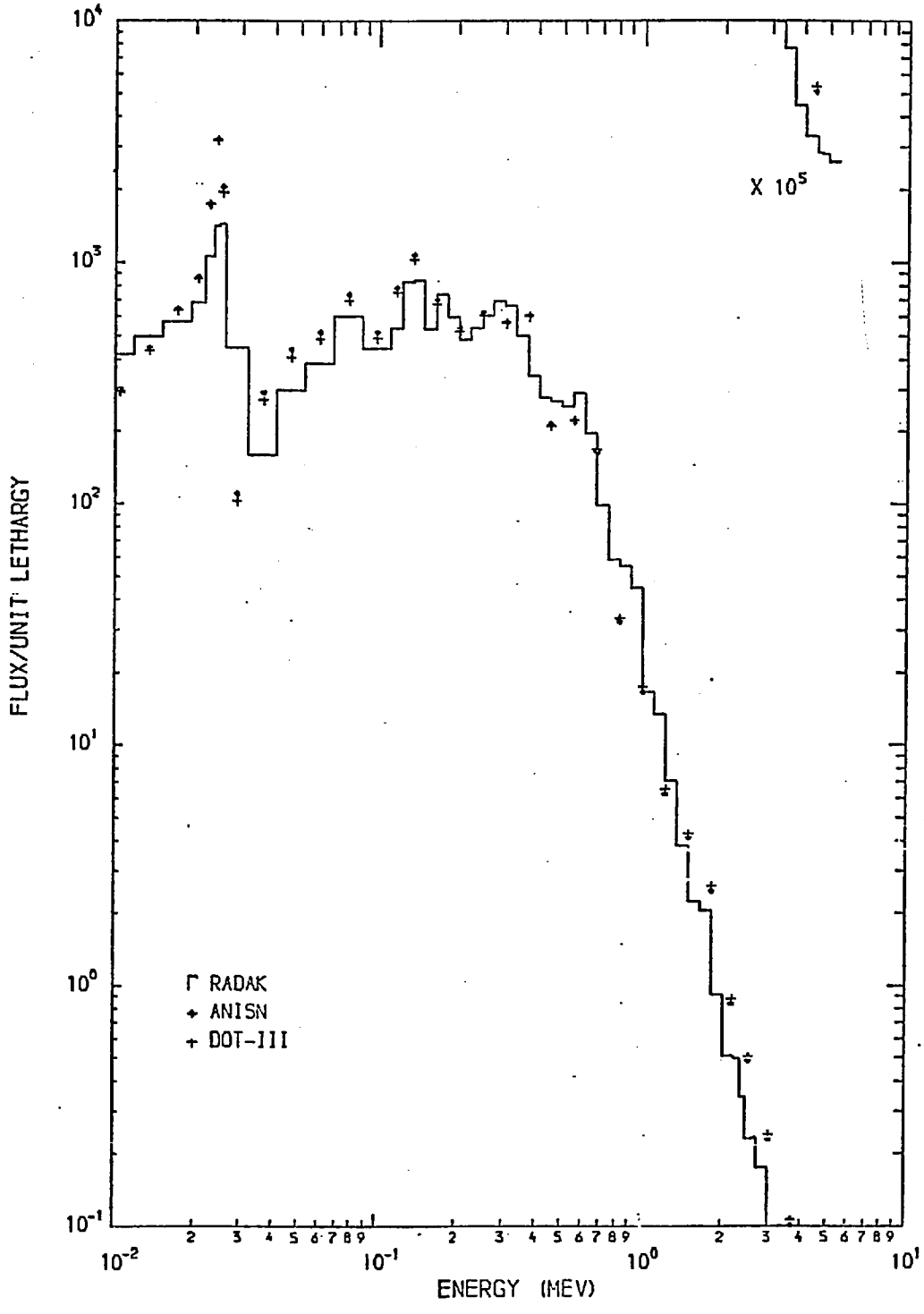


FIG. 6.7 COMPARISON OF CALCULATED FLUX PROFILES WITH RADAK UNFOLDED SPECTRUM MEASUREMENT AT 50.8CM POSITION.

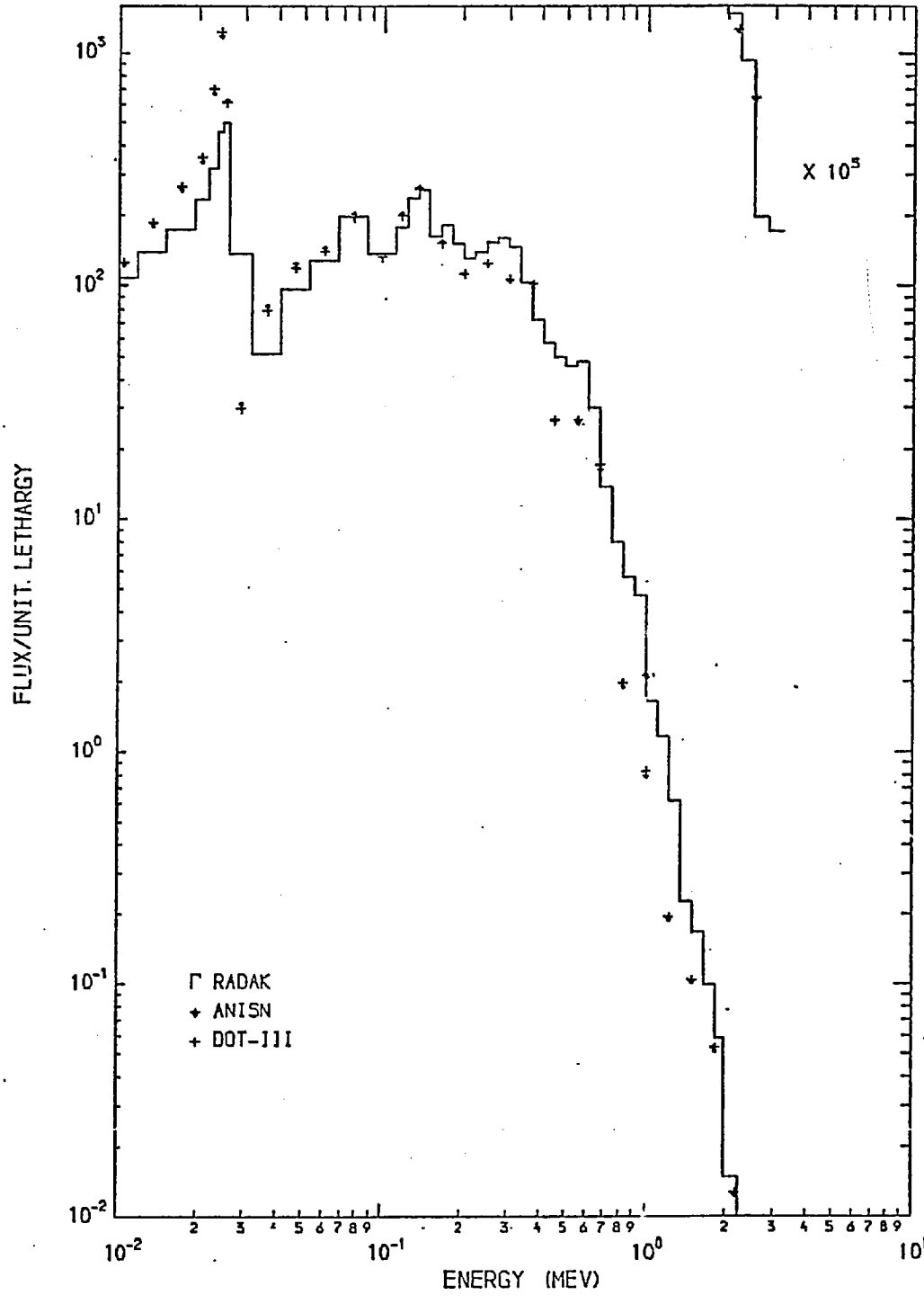


FIG. 6.8 COMPARISON OF CALCULATED FLUX PROFILES WITH RADAK UNFOLDED SPECTRUM MEASUREMENT AT 76.2CM POSITION.

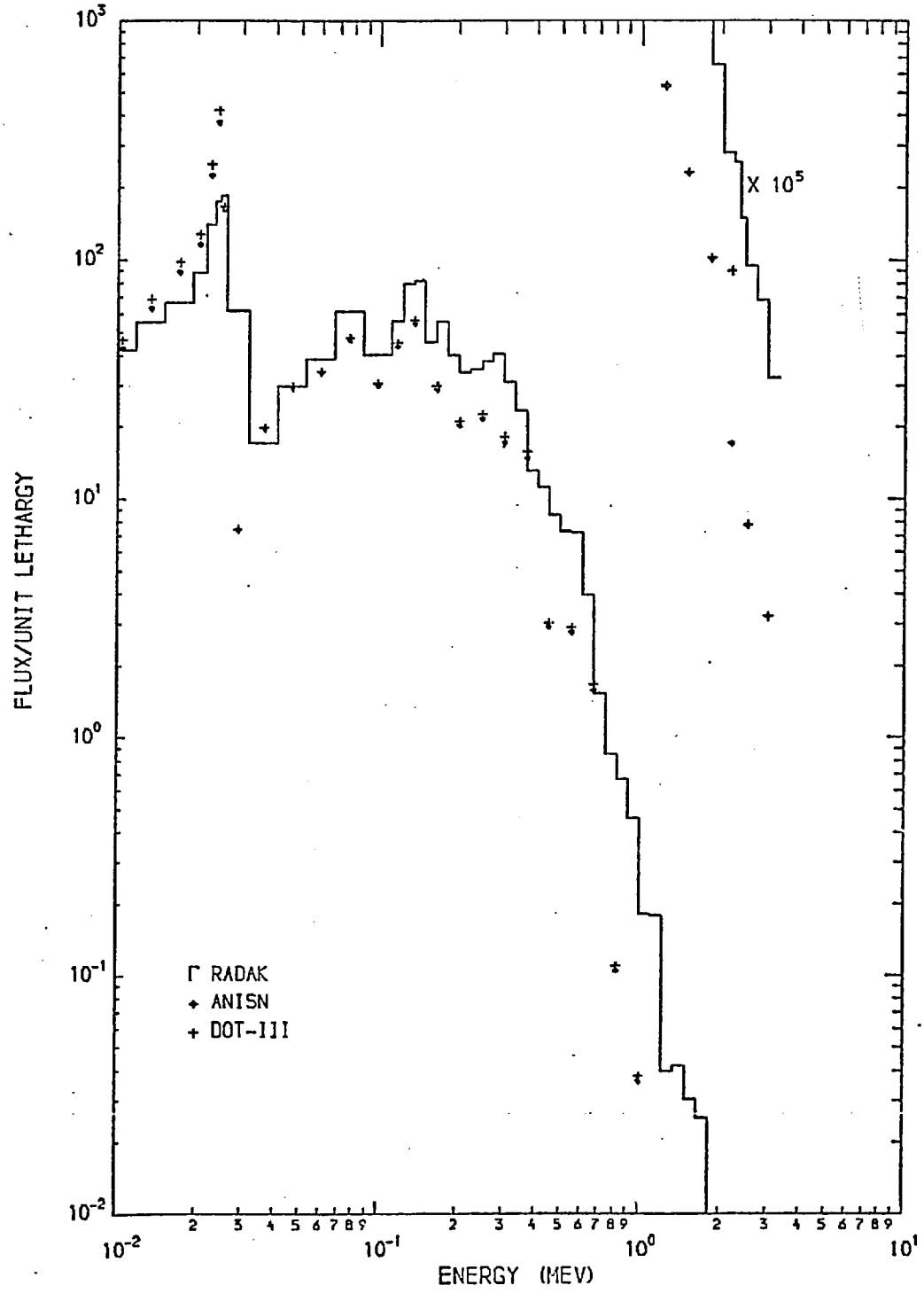


FIG. 6.9 COMPARISON OF CALCULATED FLUX PROFILES WITH RADAK UNFOLDED SPECTRUM MEASUREMENT AT 101.6CM POSITION.

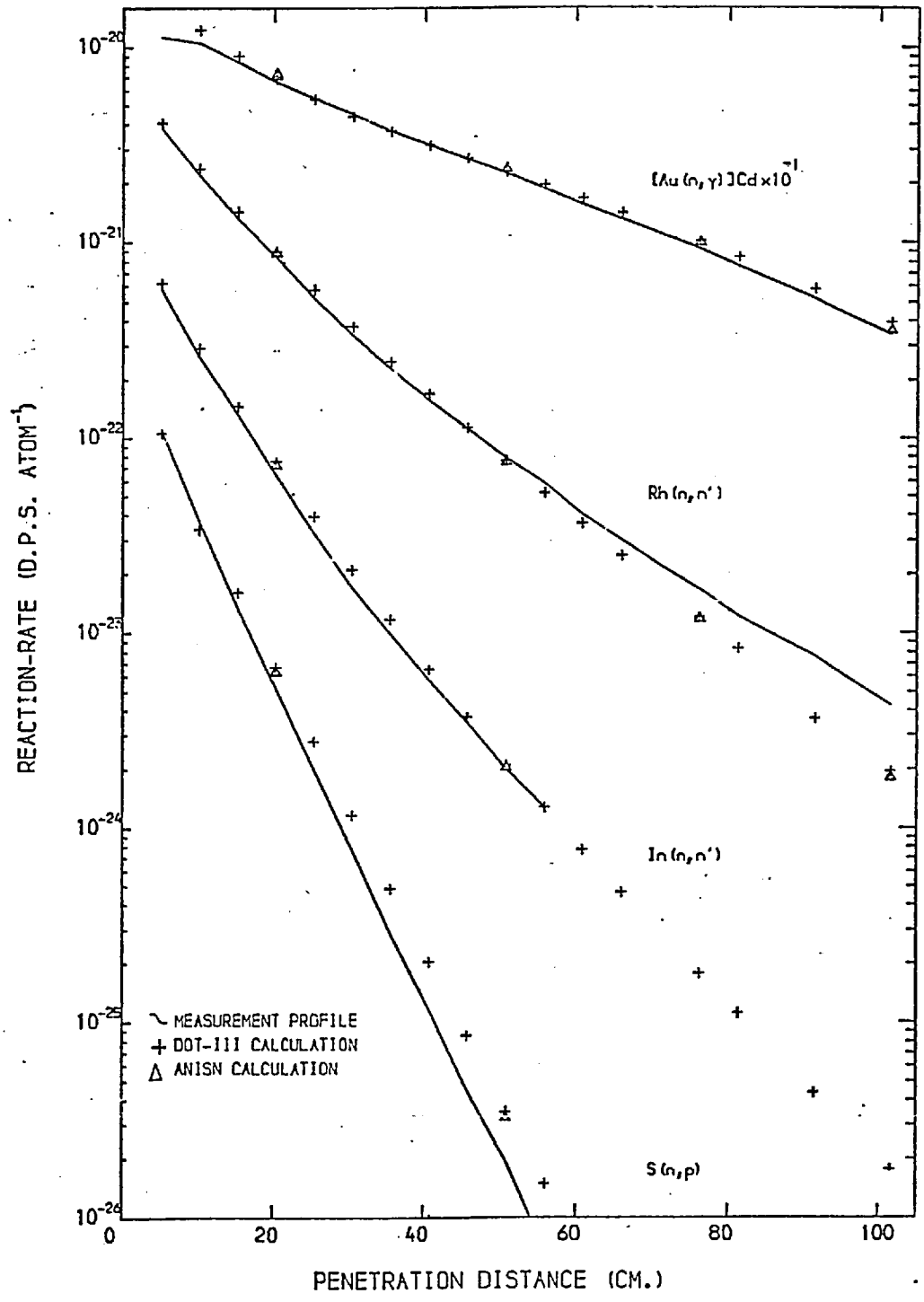


FIG. 6.10 COMPARISON OF MEASURED AND CALCULATED INTEGRAL DETECTOR REACTION-RATE PENETRATION PROFILES.

system. However in systems where the neutron population is not in quasi-equilibrium, as in propagation experiments, the total entropy of the neutron population will be increasing with neutron age, resulting in a broadening of the transverse profile of the neutron density with increasing penetration. The detailed energy-dependent behaviour of the profile perpendicular to the average current vector requires a knowledge of the scattering kernel, $\Sigma^{gg'}$, but it seems reasonable on heuristic grounds to believe that profiles for energies below the mean energy (flux weighted) of a non-equilibrated weakly absorbing system will broaden with decreasing energy as the in-scatter source assumes greater importance. The crux of this argument is that it is inappropriate to consider the use of a simple geometric buckling for simulation of 2-D leakage effects in 1-D calculations of deep penetration experiments.

In spite of this reservation about the adequacy of the ANISN buckling facility, it has been used by some authors[31,130] in benchmark calculations with limited sucess. The conclusion of this work is that the use of the fundamental mode plane wave approximation, or some corresponding zone and energy independent buckling, is insufficiently accurate for benchmark calculations. A measure of the agreement between the reference calculation and the 1-D ANISN simulation with buckling is given by a comparison of the respective chi-squared values.

Analysis of the radial profiles of the DOT-III reference calculation using a zeroth order Bessel function dependence of the form:

$$\phi(r) = A_o J_o(B(E,z).r) \qquad 6.6.1$$

gave a variety of geometric bucklings B(E,z) as indicated in Table 6.16. A subjective estimate of an average buckling, $\bar{B}$, on the basis of a flux weighted mean, and assuming a cosine distribution with equivalent leakage for the perpendicular profile in the 1-D slab geometry:

$$\phi(x,y) = A_o \cos\left\{\frac{\bar{B}x}{\sqrt{2}}\right\} . \cos\left\{\frac{\bar{B}y}{\sqrt{2}}\right\} \qquad 6.6.2$$

a 'transverse dimension' of approximately 100 cm was determined for use in ANISN. This value was in agreement with that chosen by Salvatores et al. A comparison of the chi-squared values for the 2-D reference calculation and the 1-D buckled calculation produced a fractional disagreement of 0.96 per degree of freedom. A comparison of the predicted reaction-

rates for a few of the integral detectors are given in Table 6.17.

An alternative method requires the utilisation of the results of the DOT-III reference calculation to define the elements of a dimensional transformation matrix Δ which allows reduction of the 2-D DOT-III calculation to a 1-D ANISN calculation with consequent conservation of axial leakage and detector response. Following an earlier treatment of the iron benchmark[5] the 2-D Boltzmann transport equation in cylindrical geometry solved by DOT-III may be written as:

$$\frac{dJ_z}{dz} + \frac{1}{r}\frac{d}{dr}(rJ_r) + \Sigma^T\phi = S \qquad 6.6.3$$

and the corresponding 1-D equation in slab geometry solved by ANISN is:

$$\frac{dJ_z'}{dz} + \Sigma^T\phi' = S \qquad 6.6.4$$

Then a transformation matrix can be defined such that:

$$\frac{dJ_z}{dz} + \Delta\phi + \Sigma^T\phi = S \qquad 6.6.5$$

where the energy and spatially dependent elements of Δ can be identified as:

$$\Delta(E,z) = \lim_{r\to 0} \frac{1}{r\,\phi(r,z,E)} \frac{d}{dr}[rJ_r(r,z,E)] \qquad 6.6.6$$

Substituting the discrete form of ϕ and J_r calculated by DOT-III and assuming the diamond difference algorithm for the spatial mesh cell:

$$\Delta_z^k = \frac{4 \times J_{r\,0,z}^k}{r_0 \times \phi_{0,z}^k} \qquad 6.6.7$$

The scalar flux and the moments of the flux are stored by DOT-III on tape[118]. The radial currents can be reconstructed from the moments of the scalar flux, which are an orthogonal Legendre decomposition of the flux, or by integration of the angular flux. The spatial dependence of the transformation coefficients was reduced by zone averaging and after symmetry considerations ten non-identical sets of coefficients remained for which the factors were ultimately adjusted by hand to give the best

Table 6.16

Bucklings derived from Bessel Function Approximation of DOT-III Radial Profiles

Group	Position (cm)							
	25.4		50.8		76.2		101.6	
	B	r_o	B	r_o	B	r_o	B	r_o
1	3.378-2	71.2	3.408-2	70.6	3.220-2	74.7	2.958-2	81.3
20	3.325-2	72.3	3.304-2	72.8	3.197-2	75.2	3.000-2	80.2
40	3.153-2	76.3	2.958-2	81.3	2.803-2	85.8	2.620-2	91.8
60	2.854-2	84.3	2.624-2	91.7	2.427-2	99.1	2.339-2	102.8
80	2.661-2	90.4	2.436-2	98.7	2.269-2	106.0	2.186-2	110.0
99	2.647-2	90.9	2.385-2	100.8	2.258-2	106.5	2.169-2	110.9

Precision ~ ± 5%

Table 6.17

Comparison of Buckled ANISN Prediction of Integral Parameters with DOT-III Calculation

Reaction Type	Calculational Method	Position (cm)			
		25.4	50.8	76.2	101.6
S(n,p)	DOT-III	2.80 +0	3.50 -2	4.57 -4	5.97 -6
	ANISN-B	2.60 +0	3.66 -2	5.29 -4	6.33 -6
Rh(n,n')	DOT-III	5.79 +2	7.59 +1	1.19 +1	1.94 +0
	ANISN-B	5.36 +2	6.80 +1	9.92 +0	1.35 +0
In(n,n')	DOT-III	3.97 +1	2.12 +0	1.78 -1	1.77 -2
	ANISN-B	3.72 +1	2.07 +0	1.68 -1	1.44 -2
Au(n,γ)	DOT-III	5.43 +4	2.29 +4	1.01 +4	3.93 +3
	ANISN-B	3.60 +4	1.21 +4	4.53 +3	1.46 +3

Table 6.18

Comparison of DOT and ANISN Reference Calculation Reaction-Rate Predictions at Various Penetrations

Position (cm)	Calculation	S(n,p)	Rh(n,n')	In(n,n')	Au(n,Y)
~ 5	DOT	1.152 +2	4.295 +3	6.584 +2	1.803 +5
	ANISN	1.112 +2	4.188 +3	6.374 +2	1.843 +5
	Δ %	-3.47	-2.49	-3.19	2.22
~ 50	DOT	3.498 -2	7.590 +1	2.133 +0	2.288 +4
	ANISN	3.337 -2	7.632 +1	2.088 +0	2.405 +4
	Δ %	-4.60	0.55	-2.11	5.11
~ 76	DOT	4.813 -4	1.223 +1	1.825 -1	1.017 +4
	ANISN	4.689 -4	1.213 +1	1.779 -1	1.019 +4
	Δ %	-2.58	-0.82	-2.52	0.20
~ 101	DOT	5.473 -6	1.867 +0	1.693 -2	3.809 +3
	ANISN	5.458 -6	1.786 +0	1.608 -2	3.587 +3
	Δ %	-0.27	-4.34	-5.02	-5.83

Reaction-rates are given as saturated disintegrations s^{-1} atoms^{-1} barn^{-1}

fit between ANISN and DOT and the fractional discrepancies for some typical integral detectors at different penetration depths are given in Table 6.18. The chi-squared per degree of freedom for the transformed ANISN calculation agreed to within 2.8% with that for the DOT-III reference calculation; the average flux difference at each of the measurement positions was ~1.5% with a maximum group value of 5.5%. The difference between the DOT-III and ANISN calculations for the prediction of all observables is about 5% which is within the standard deviation on the foil measurements and is very much less than the discrepancies due to data (medium neutron transport constants and measurement device response surfaces), as indicated by the values of the measurement chi-squared per degree of freedom.

The dimensional transformation coefficients represent an additive adjustment to the total cross-section and since radial leakage is a lossy process, conservation of medium interaction density is maintained by a similar adjustment to the absorption cross-section. The numerical value of Δ_z^k is sufficiently small for Δ_z^k/Σ_k^T to be negligible in comparison with the standard error assigned group-wise to the total cross-section except in regions containing interference minima. Table 6.19 shows that Δ_z^k in the iron shield makes only a 1-3% contribution to the total cross-section except over the region of the 24 keV cross-section window where the contribution rises to 19.5% and at about 350 keV where a 6% change is indicated. However the adjustment to the absorption cross-section cannot be neglected; the contribution ranges from 12% up to a factor 24.4 near the 24 keV interference window. The ratio Δ_z^k/Σ_k^A is tabulated in Table 6.19 and illustrates that the modification of the absorption cross-section is outside the standard deviation of the fine group absorption cross-section. Thus any adjustment $\delta\Sigma_k^A/\Sigma_k^A$ predicted by the optimisation procedure for the absorption cross-section which is less than Δ_z^k/Σ_k^A cannot be considered to reflect a significant discrepancy in the multi-group absorption cross-section for iron.

6.6.2 The Iron-Concrete Interface

The lack of a 2-D sensitivity code and economic considerations have made it impossible to optimise the concrete cross-sections in the radial shield of the 2-D model. The effect of the concrete albedo is incorporated in the dimensional transformation coefficients and it is important to show that concrete has a negligible effect on the meter readings for the observables. An assessment study has been made using a 1-D radial ANISN calculation comprising an infinite cylinder of iron 104 cm in radius and

Table 6.19

Ratios of Dimensional Transformation Coefficients with Absorption and Total Cross-Sections for the ASPIS Iron DATAM Experimental Shield

Group	Δ/Σ^A	Δ/Σ^T	Group	Δ/Σ^A	Δ/Σ^T	Group	Δ/Σ^A	Δ/Σ^T
1	3.38-1	2.70-2	35	9.26 0	2.16-2	68	4.64-1	7.23-4
2	3.34-1	2.46-2	36	1.29+1	4.77-2	69	1.75+0	1.50-3
3	3.69-1	2.26-2	37	7.77 0	1.98-2	70	8.47-1	9.87-4
4	4.27-1	2.08-2	38	5.56 0	1.05-2	71	1.56 0	9.01-4
5	4.92-1	1.90-2	39	6.47 0	1.27-2	72	5.23-1	4.37-4
6	5.82-1	1.75-2	40	3.27 0	3.80-2	73	4.31-1	7.05-4
7	7.04-1	1.63-2	41	5.88 0	1.04-2	74	7.45-1	6.80-4
8	8.10-1	1.55-2	42	1.47+1	6.03-2	75	2.24-2	4.90-4
9	8.93-1	1.56-2	43	1.02+1	1.87-2	76	4.76-1	5.45-4
10	9.74-1	1.50-2	44	7.52 0	1.08-2	77	3.84-1	5.00-4
11	1.13 0	1.51-2	45	9.64 0	2.13-2	78	2.82-1	4.57-4
12	1.39 0	1.47-2	46	4.40 0	6.81-3	79	7.81-2	3.38-4
13	1.82 0	1.43-2	47	5.88 0	1.19-2	80	1.86-2	1.80-4
14	2.03 0	1.38-2	48	2.95 0	4.43-3	81	9.19-2	3.94-4
15	2.12 0	1.34-2	49	5.62 0	1.58-2	82	1.34-1	3.95-4
16	2.47 0	1.37-2	50	3.88 0	7.99-3	83	1.24-1	3.91-4
17	3.22 0	1.39-2	51	6.45 0	2.79-2	84	1.10-1	3.84-4
18	4.70 0	1.54-2	52	5.00 0	2.10-2	85	9.63-2	3.78-4
19	6.42 0	1.43-2	53	4.42 0	1.10-2	86	8.43-2	3.74-4
20	9.88 0	1.52-2	54	1.96 0	3.79-3	87	7.41-2	3.70-4
21	1.20+1	1.26-2	55	2.17 0	8.38-3	88	6.45-2	3.66-4
22	1.67+1	1.49-2	56	1.79 0	3.62-3	89	5.64-2	3.62-4
23	1.92+1	1.73-2	57	2.56 0	2.42-3	90	4.95-2	3.59-4
24	1.93+1	1.40-2	58	7.27-1	1.04-3	91	4.33-2	3.56-4
25	2.18+1	1.64-2	59	1.66-1	1.56-4	92	3.58-2	3.54-4
26	2.27+1	1.99-2	60	9.94 0	7.23-2	93	2.94-2	3.51-4
27	1.93+1	1.62-2	61	2.44+1	1.95-1	94	2.42-2	3.45-4
28	2.08+1	1.86-2	62	6.88 0	6.66-2	95	1.86-2	3.41-4
29	1.72+1	1.48-2	63	1.01+1	1.56-2	96	1.43-2	3.35-4
30	2.44+1	2.86-2	64	9.47 0	6.97-3	97	1.10-2	3.28-4
31	1.85+1	2.23-2	65	2.34 0	3.11-3	98	8.24-3	3.21-4
32	1.71+1	3.26-2	66	7.91-1	1.36-3	99	8.12-3	4.01-4
33	1.12+1	2.18-2	67	1.28-1	1.93-4	100	2.07-3	3.52-4
34	5.65 0	7.98-3						

surrounded by an annulus of 18 cm of concrete. A flat fission spectrum source extended over the central region out to a radius of 69.0 cm; this was considered an extreme test since the flux profile in 2-D can be approximately described by a cosine curve or a zeroth order Bessel function. The maximum fractional discrepancy in the group fluxes at the centre with and without the concrete annulus was less than 1% for all groups. The effect of the concrete cross-sections on the centre axis flux appears therefore to be negligible which is in agreement with the radial flux profiles of the DOT-III calculation. This important conclusion asserts that the optimisation of the iron data set is in no way absorbing discrepancies in the concrete data.

6.7 Summary

In this chapter the purpose of the reference calculation has been outlined as that of demonstrating that the discrepancies between calculation and measurement arise from sources other than errors in the calculational method and geometric modelling. It has also been shown to be of value in defining a matrix of coefficients which will allow a more precise transformation to lower dimensional order than that of assuming a plane wave fundamental mode seperability of the equations. The modelling of the source has been shown to agree well with measurement and the calculational method parameters have been optimised by a series of 1-D ANISN survey calculations. The χ^2 test has been used as a measure of consistency between the 2-D reference calculation and the 1-D working analogue and as an indication of the magnitude of the discrepancies between calculation and measurement. A comparison of the unfolded measurement spectrum with the calculated flux distribution has been used as a diagnostic aid to indicate the energy regions in which the discrepancies are most likely to exist.

CHAPTER VII

AN EXAMINATION OF THE ASPIS IRON BENCHMARK EXPERIMENTAL MEASUREMENTS

7.1 Introduction

The utility and accuracy of the adjustments to nuclear data predicted from the analysis of a benchmark experiment depend upon the accuracies assigned to the group constants used in the calculation and on the errors attributed to the integral measurements with which ultimately the calculated values for the observables will be forced to agree. This chapter explores the errors in the integral measurement data resulting from both the experimental procedures and the assumptions made by the codes processing the raw data into a form amenable for comparison with calculation. Some consideration is given to the energy scale calibration error that can arise in proton recoil counter measurements and the effects of uncertainties in counter line-shapes and threshold detector cross-sections are assessed.

7.2 The Information Content of the Detectors

The detectors used in the ASPIS iron DATAM experiment[4] can be classified in order of decreasing energy into three types - threshold detectors, proton recoil counters and resonance sandwich foils. The threshold detectors monitor the high energy neutron flux and, as will be shown, most of the reaction-rate occurs near the threshold. The proton recoil counters used were of two types; the high energy region above 0.8 MeV was covered by an NE 213 organic scintillator and the energy range below 1.35 MeV down to about 7 keV was spanned by an argon-hydrogen gas counter and a variety of hydrogen gas proportional counters at different pressures and electronic gains. The low energy neutron behaviour was estimated over narrow ranges with resonance sandwich foils.

Although proton recoil counters are conventionally used to provide differential information with which to determine the energy-dependent flux, each channel M_i of the pulse height data output from the chamber can be considered as an integral measurement from a threshold detector whose cross-section is represented by the row of the integral response matrix corresponding to the counting channel. Table 7.1 lists the detectors used in the experiment with their corresponding energy ranges. The lower energy boundary of the hydrogen gas proportional counters represents the energy E_γ at which Compton electrons, produced by γ-ray interaction in the chamber wall, start to make a significant contribution to the pulse height distribution obtained from the counter. The upper energy boundary E_{max} represents the energy limit above which the information produced by the counter is so dominated by "wall effect" that stable unfolding is not possible. E_γ represents an experimental limitation whereas E_{max} may

Table 7.1

Detectors Used in the ASPIS Iron Benchmark Experiment

Detector	Type	Working Energy Range
$Al^{27}(n,\alpha)Na^{24}$	threshold	E > 5.2 MeV
$S^{32}(n,p)P^{32}$	threshold	E > 1.6 MeV
$In^{115}(n,n')In^{115m}$	threshold	E > 0.4 MeV
$Rh^{103}(n,n')Rh^{103m}$	threshold	E > 40 keV
NE 213	proton recoil (organic scintillator)	E > 0.8 MeV
Argon/Hydrogen	proton recoil (gas proportional)	300 keV - 1.75 MeV
10 at. Hydrogen	proton recoil (gas proportional)	.160 keV - 930 keV
3 at. Hydrogen	proton recoil (gas proportional)	100 keV - 500 keV
1 at. Hydrogen	proton recoil (gas proportional)	40 keV - 235 keV
½ at. Hydrogen	proton recoil (gas proportional)	24.8 keV - 110 keV
1 at. Hydrogen with High Gain	proton recoil (gas proportional)	10 keV - 85 keV
½ at. Hydrogen with High Gain	proton recoil (gas proportional)	7 keV - 60 keV
Cd{Au(n,γ)}	activation foil	0.55 eV - 100 keV
$Cu^{63}(n,\gamma)$	resonance sandwich foil	580 eV
$W^{186}(n,\gamma)$	resonance sandwich foil	18.8 eV
$Au^{197}(n,\gamma)$	resonance sandwich foil	4.9 eV

be specified by either processing difficulties or by counting statistics.

7.3 Proton Recoil Counter Line-Shapes

7.3.1 Hydrogen Proportional Counter Line-Shapes

For an infinite counter the line-shape for a mono-energetic neutron source can be specified by the rectangular equi-probable distribution. The extension of this to provide the recoil proton energy distribution, $b(E)$, arising from a neutron flux spectrum, $\psi(E)$ is immediate and can be shown to be:

$$b(E) = \int_E^\infty \frac{\psi(E')\,\Sigma_H(E')\,dE'}{E'} \qquad 7.3.1$$

where $\Sigma_H(E)$ is the macroscopic energy-dependent hydrogen scattering cross-section for the counter. For finite counters, however, a correction to the infinite medium response is required because recoil protons created in the counter can leak out of the detection volume before depositing all their energy. This "wall effect" is most easily evaluated for spherical counters which have an isotropic response function. The fraction of recoil protons leaking from the counter can be determined either by Monte Carlo calculation[131] where the accuracy is limited by statistics, or by an analytic technique due to Snidow and Warren[132] in which if b_T is the total number of recoil protons in the counter, then the fraction of recoil protons detected with energy E can be expressed as:

$$\frac{b(E)}{b_T} = \frac{f(E)}{E_n} + \frac{1}{E_n}\int_E^{E_n} N(R(E') - R(E'-E))\,\frac{dR}{dE}(E'-E)\,dE' \qquad 7.3.2$$

where $R(E)$ is the range of a recoil proton with energy E, E_n is the source neutron energy and $f(E)$ is the fraction of protons with energy E which will deposit all their energy in the counter. Equation 7.3.2 can be shown to produce a trapezoidal line-shape[133] for neutron energies such that $R(E_n)/a < 0.7$ where 'a' is the counter radius, and the expression is used in the program PRC[7] which calculates proton recoil counter response matrices. Since the upper limit of the working range of the hydrogen chambers, as defined in Table 7.1, satisfies approximately the criterion that $R(E_n)/a = 0.5$, the line-shapes for the counters are approximately trapezoidal. In cases where a neutron flux above the upper limit, E_{max}, contributes to the proton density in the chamber, response functions for $R(E_n)/a > 0.7$ have to be computed; in this regime the program PRC integr-

ates equation 7.3.2 using Simpson's rule, dividing the energy interval until a 2% convergence criterion is met.

Kemshall[133] has compared measured response functions with the shapes predicted by the method of Snidow et al and has demonstrated that significant discrepancies exist. The measured spectra have a region, between the detection of γ-events and the start of the proton edge, which was approximately linear. Kemshall found using a least squares fitting technique that there was a disagreement between the calculated and measured gradients (Table 7.2). Moreover the discrepancies appeared to be independent of pressure for a given $R(E_n)/a$. Accordingly he defined a "slope correction factor" as the ratio of the response function value at mid-energy ($E_n/2$) to that at the proton edge. In the terms of Figure 7.1 the correction factor was x/y. These correction factors have been tabulated at intervals up to $R(E_n)/a = 1.6$ and have been included in the PRC program as modification factors for the Snidow et al response prediction. However for $R(E_n)/a > 0.7$ statistical scatter and the finite resolution broadening of the counter produce an increasingly large error in the determination of the response height at the proton edge.

Table 7.2

Percentage Difference in Gradient for Calculated and Measured Line-Shapes (after Kemshall (133))

$R(E_n)/a$	Difference w.r.t. Measurement %
0.15	55.80
0.30	34.30
0.45	22.20
0.60	14.50
0.75	11.00
0.90	10.20
1.10	8.24
1.25	6.30
1.40	5.50
1.60	3.40

The reason suggested for the slope error[133] is that a distortion is produced in the measured pulse height distribution because of the non-uniformity of the electric field near the ends of the anode wire. In this 'polar cap' region comprising up to 10% of the counter volume, the field falls from its mean value to zero. For low energy recoil protons contained in this region, lower gas amplification for ionization events occurs producing a lower than expected pulse height. As the energy of the protons

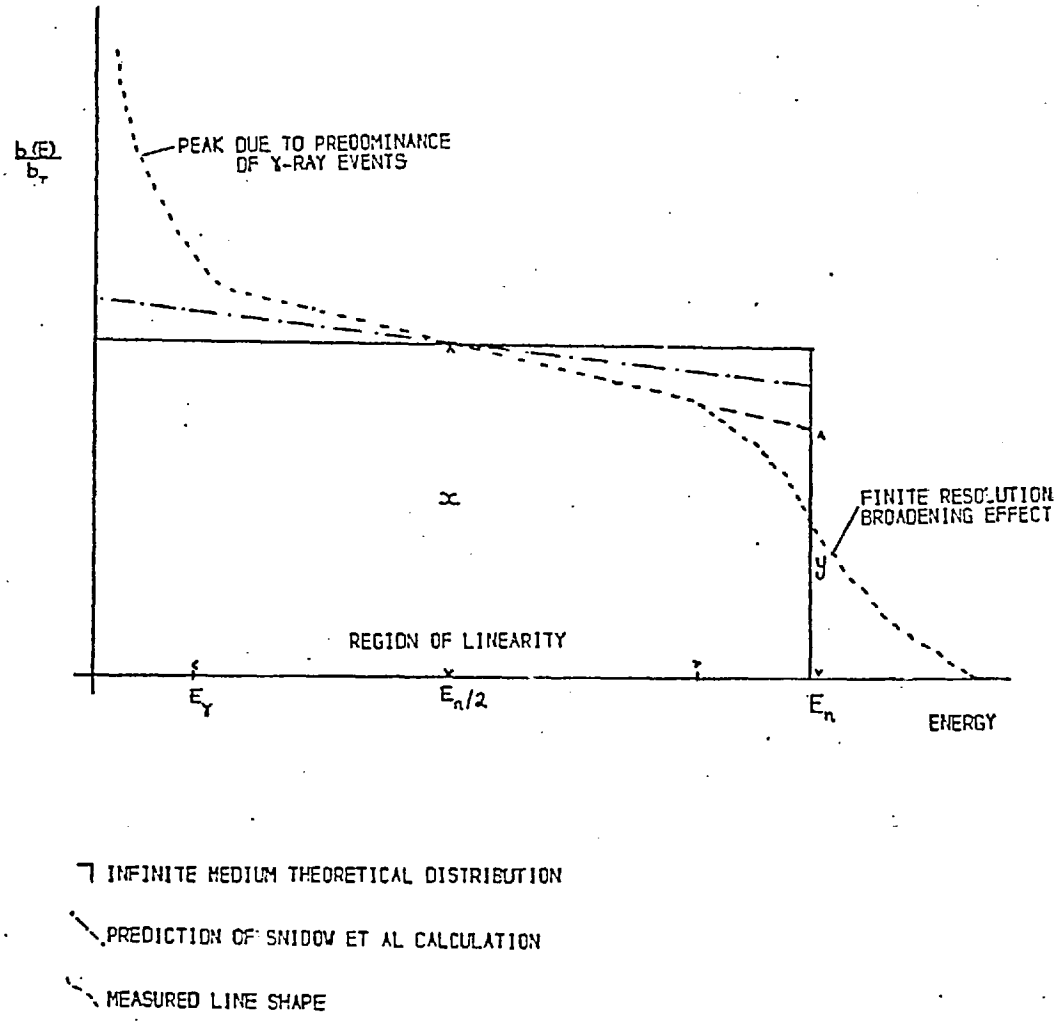


FIG. 7.1 SCHEMATIC DIAGRAM OF THEORETICAL AND MEASURED HYDROGEN CHAMBER LINE SHAPES.

increases, less of the ionization track is to be found in the effected region resulting in a less pronounced distortion. This explanation has been validated by Monte Carlo calculation.

For $R(E_n)/a > 1.5$ the response function can no longer be considered to be trapezoidal and the statistics at the proton edge produce large uncertainties in the correction factor. Although the field distortion effect should be small at these energies, discrepancies still exist between the measured and calculated line-shapes. Kemshall has found that better agreement can be produced if the proton ranges in hydrogen are extended by 1% per atmosphere pressure from the value predicted using the inverse pressure-range relationship:

$$R(E,P) = \frac{(1 + P/100)}{P} R_o(E) \qquad 7.3.3$$

The proposal for increased range really means that less energy must be deposited in the counter for a specific energy or if it really is deposited in the counter, then the losses due to capture and recombination of the electron-ion pairs must be greater at higher pressures. The latter may stem from the fact that at any one energy the track is more densely ionised at higher pressure.

From an examination of the response functions given by Kemshall[133] it is possible to determine the accuracy of the elements of the response matrix derived on the basis of the trapezoidal representation of the line-shape. The matrix element r_{ij}, defined in equation 7.3.4, is for a counting channel bounded by the proton energies E_i and E_{i+1} and for unit neutron flux at E_j:

$$r_{ij} = \int_{E_i}^{E_{i+1}} a(E_j) + b(E_j)\, E'\, dE' \qquad 7.3.4$$

The line-shape for a neutron energy E_j is therefore defined by the energy intercept $a(E_j)$ and the gradient $b(E_j)$. The accuracy with which these parameters can be measured and utilised in Kemshall's correction factors reflects the uncertainty in the gas counter response cross-sections.

$$\delta r_{ij} = \delta a_j (E_{i+1} - E_i) + \frac{\delta b_j}{2} (E_{i+1}^2 - E_i^2) \qquad 7.3.5$$

Squaring and taking expectation values:

$$\mathrm{Var}(r_{ij}) = (E_{i+1} - E_i)^2 \mathrm{Var}(a_j) + (E_{i+1}^2 - E_i^2)^2 \frac{\mathrm{Var}(b_j)}{4} + (E_{i+1} - E_i)(E_{i+1}^2 - E_i^2)\, \mathrm{Cov}(a_j, b_j) \qquad \ldots\ldots\ldots 7.3.6$$

The variances and covariances on the fitting parameters were determined by the code ROKELS using linear regression on Kemshall's measured data. The results of the analysis are presented in Table 7.3 for the five gas proportional counters used in the ASPIS measurement programme. For values of $R(E_n)/a > 0.7$ the line-shape is non-linear but since this occurs for energies above the assigned working range for the counters (Table 7.1) and the flux is generally flat or monotonically decreasing (Figure 6.8) the contribution to the grouped count-rate vector is sufficiently small that errors in the line-shape above the linear regime can be ignored. The data of Table 7.3 represent the relative error on the line-shape; errors due to the normalisation of the counter cross-section are discussed in a later section.

The data of Table 7.3 can be considered to typify a worst case error estimate since in an energy-dependent neutron flux the observable difference on spectrum parameters will to some extent be reduced because of the self-cancelling nature of the errors. Moreover since the line-shapes are generated in multi-group form for a neutron energy at the centre of the corresponding group, resolution broadening of the proton edge does not normally contribute a large error.

7.3.2 Organic Scintillation Counter Line-Shapes

The argon-hydrogen proportional counter is about the largest gas chamber that can be accommodated in a benchmark experiment without unacceptably perturbing the differential energy neutron flux spectrum being measured. For proton recoil measurements at higher energies (above ~ 1 MeV) it is necessary to reduce the range of the knock-on protons by using an hydrogeneous liquid. In the Nuclear Enterprises Counter Type 213 (NE 213) the knock-on protons, caused by neutron elastic scattering, lose energy by excitation of the molecular species in the xylene napthalene liquid detection medium. The excited molecular states decay by the emission of phosphorescent radiation; the total number of quanta emitted is related to the energy of the incident particles depositing energy in the detector. The charge collection time on the output of the photo-multiplier used to collect the emitted photons is related to the type of particle detected. Pulse decay time analysis can therefore be used to discriminate between Y-ray Compton electrons and neutron produced knock-on protons. The lower energy threshold of the counter ($E_\gamma \sim 0.82$ MeV) represents the energy at which Y-ray events dominate the counting producing a large counter dead-time with the resultant reduction in neutron counting statistics. This threshold however allows a sufficient overlap with the

gas counters to produce a continuous neutron spectrum. The upper limit of the working range of the counter is usually dictated by counting statistics. In the iron benchmark experiment, measurements could be made at energies up to 10 MeV after 20 cm of iron, but up to only ~ 2 MeV after 75 cm penetration. At 10 MeV the range of the knock-on protons in the 3.4 cm^3 right circular cylindrical counter is comparable with the radius of the counter and an underestimation of 11% at 10 MeV falling to 5% at 7 MeV is made if the effective proton leakage is ignored in constructing the counter response surface. The lower energy line-shape for a mono-energetic neutron flux is the theoretical rectangular function of Figure 7.1. However above 7 MeV, the proton energy distribution function departs from the equi-probable energy distribution taking a negative gradient. The integral and differential proton counting distribution response surfaces for neutrons were calculated by modification of the PRC program to include the range-energy data for the NE 213 counter detection medium[134]. For the purposes of these calculations the right circular cylindrical detector was approximated as a sphere of the same volume. The effect of this approximation has been investigated by unfolding measurements made on a Cf^{252} neutron fission spectrum. These measurements, reported in a later section, also served to validate the measured light function over a wide range of energies.

The molecular excitation process in the NE 213 counter detection medium is a non-linear phenomenon and for this reason the pulse height output from the detection system is not proportional to the energy deposition in the sensitive volume of the counter. The response kernel for the system therefore contains a 'light function', L(E), defined as the fraction of quanta emitted relative to the number emitted at the Cs^{137} edge (1.667 MeV neutron equivalent energy) as a function of the proton energy incident upon the detector (Figure 7.2). The light function has been derived by a least squares log-log fit to data derived from two independent sets of measurements made on the IBIS accelerator at AERE Harwell by Carter et al. The function has been expressed in the form:

$$\ln L(E)\,dE = [\alpha + \beta \ln E + \gamma (\ln E)^2]\,dE \qquad 7.3.7$$

where the parameters α, β and γ estimated from the fit had fractional standard deviations of 1.03%, 1.16% and 7.52% respectively. The extension to a cubic polynomial fit, by linear regression, did not increase the goodness-of-fit by χ^2 test so the simpler quadratic representation was

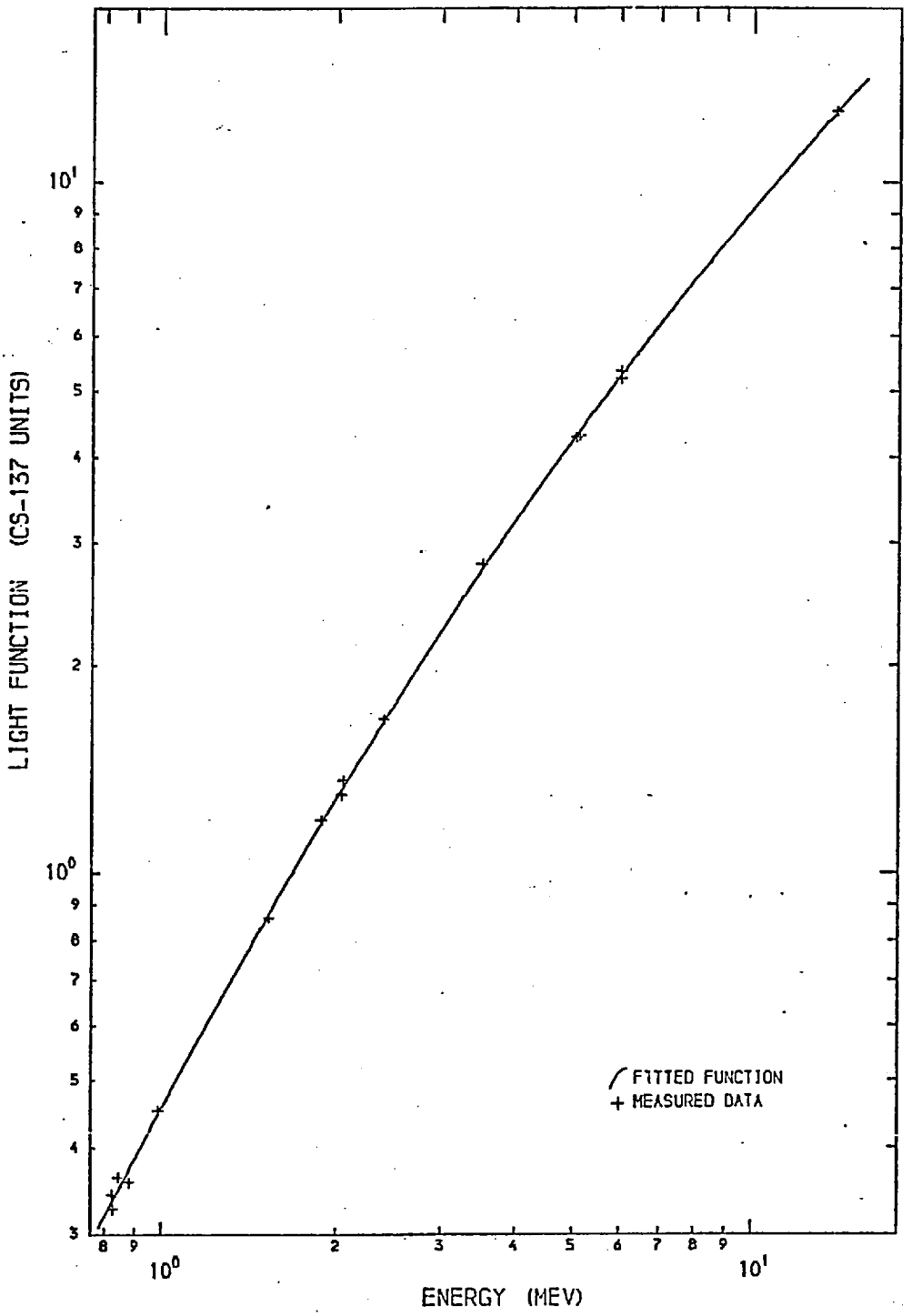


FIG. 7.2 FUNCTIONAL FIT OF LIGHT FUNCTION TO EXPERIMENTAL DATA.

chosen (Table 7.4). Utilising the variances and covariances on α, β and γ, the fractional error in estimating the light output in Cs^{137} units at proton energies of 1.0 and 10.0 MeV has been computed to be 1.03% and 2.1% respectively.

The light output distribution, c(l)dl, which corresponds to the recoil proton energy distribution b(E)dE can be shown to be related to the neutron flux spectrum $\Psi(E_n')$ in such a way that the integral group count-rate M_i may be expressed as:

$$M_i = \int_{l_i}^{l_{i+1}} c(l')\,dl' = \int_{E_{P_i}}^{\infty} \int_{E_{P_i}}^{E_{P_{i+1}}} R(E,E_n')\,\Psi(E_n')\,dE_n'\,dE \qquad 7.3.8$$

where the proton energy boundaries Ep_i and Ep_{i+1} are related to the light emission pulse height boundaries l_i and l_{i+1} through the light function 7.3.7. For the differential count-rate response equation (conventionally used for count-rate unfolding), use is made of the relationship:

$$b(E) = c(l).\frac{dl(E)}{dE} \qquad 7.3.9$$

The corresponding differentiated proton recoil energy distribution is then calculated using this equation in the NE 213 program[7] along with the theoretical differential matrix elements. No correction for knock-on proton leakage is made in this program and the corrected matrix elements have to be calculated using the program PRCM.

The behaviour of the NE 213 neutron spectrometer is in essence simple, but inaccuracies in the interpretation of the measured data can arise from four identifiable sources:

(i) the pulse decay time discrimination between neutron and gamma-ray induced events

(ii) the determination and functional fitting of the light curve

(iii) the approximation of the counter as a sphere for the purposes of calculating the leakage of knock-on protons and therefore the modifications to the line-shape at higher energies (E_p > 7 MeV)

(iv) the exact number density of hydrogen atoms in the sensitive volume of the counter.

Using a Cf^{252} fission source, Carter et al have made spectrum measurements with the NE 213 counter and an argon-hydrogen chamber over the range

Table 7.3

Fractional Error on Gas Proportional Counter Line-Shapes

Counter Type	$R(E_n)/a = 0.20$		$R(E_n)/a = 0.54$	
	Energy (MeV)	$\sigma(a_{ij})/a_{ij}$ %	Energy (MeV)	$\sigma(a_{ij})/a_{ij}$ %
Argon-Hydrogen	0.990	2.52	1.831	3.33
10 at. Counter	0.579	2.09	1.033	2.27
3 at. Counter	0.271	1.03	0.516	1.58
1 at. Counter	0.102	0.64	0.242	0.94
½ at. Counter	0.046	0.47	0.143	0.79

Table 7.4

Least Squares Fit to NE 213 Counter Light Function

Proton Energy MeV	Normalised Light Output Cs^{137} units	Fractional Deviation from Fit %	
		Quadratic	Cubic
0.824	0.343	2.5	2.6
0.826	0.326	-3.0	-2.9
0.845	0.363	4.1	4.2
0.880	0.357	-4.1	-4.1
0.990	0.453	0.8	0.8
1.532	0.864	-1.4	-1.6
1.884	1.194	0.9	0.8
2.040	1.300	-1.8	-2.0
2.056	1.363	1.8	1.7
2.400	1.674	0.9	0.8
3.522	2.795	1.4	1.5
5.070	4.283	-0.7	-0.6
5.132	4.301	-1.7	-1.6
6.012	5.209	-1.0	-0.9
6.027	5.349	1.3	1.5
13.900	12.690	0.4	0.1

$$\ln L(E) = \alpha + \beta \ln E + \gamma (\ln E)^2 + \delta (\ln E)^3$$

Quadratic Parameters

α = -0.784023

β = 1.57937

γ = -0.120634

Cubic Parameters

α = -0.783524

β = 1.58544

γ = -0.129063

δ = 0.002429

500 keV to 10 MeV and the unfolded spectrum has been compared with the Maxwellian fit of Grundl and Eisenhauer[135,136] which is the present NBS standard for the Cf^{252} fission spectrum. Agreement above 1 MeV was within 5% (1σ) for the flux grouped into 0.1 lethargy width bins (Figure 7.3). This would appear to validate the experimental and theoretical procedures adopted in interpreting the data obtained with the NE 213 counter.

7.4 An Assessment of the Integral Detector Response Data Uncertainties

7.4.1 Integral Detector Response Cross-Section Uncertainty Analysis

The hybrid two tier optimisation philosophy is centred on the comparison of the measured observable parameters, including count-rate distributions, with the response-rates predicted by calculation. Adjustment on the basis of unfolded flux comparison is considered by the author to be unwise because of the mathematical noise and the uncertain correlations injected into the flux data as a result of the unfolding process. Moreover a unique unfolded flux solution cannot be predicted and the solution spectrum is arbitrary in that it may depend on the starting flux guess and the mathematical termination criterion. Data unfolded by the RADAK code is therefore used only for a diagnostic comparison of fluxes. Although the refolding process introduces less noise into the comparators, an accuracy assessment of the detector cross-sections is necessary to estimate the uncertainties in the calculated response-rates.

The cross-section data for the integral foil threshold detectors have been taken from those recommended by Farinelli et al[129,137,138] for the NEA/OECD Collaborative Benchmark programme. The uncertainty estimates assumed to apply to these cross-sections have been taken from the SAND-II error file[139] given by McElroy et al[37] for all cross-sections except rhodium, where the author has evaluated an error file from the curves given by Vlasov et al[140]. The error estimates derived by the author from the Vlasov et al curve for indium were some 50% lower than the corresponding SAND-II values. The error estimates for rhodium were therefore scaled by a factor 2 to give greater consistency with the SAND-II estimates for the other detectors. Moreover since the Vlasov et al curves furnished no error information for rhodium near the threshold, a standard error of 30% was assumed, being symptomatic of the general uncertainty for cross-section measurement near the threshold of an inelastic level.

The response-rate of a detector i can be written as:

$$R_i = \sum_j a_{ij} \phi_j \qquad j = 1,G \qquad 7.4.1$$

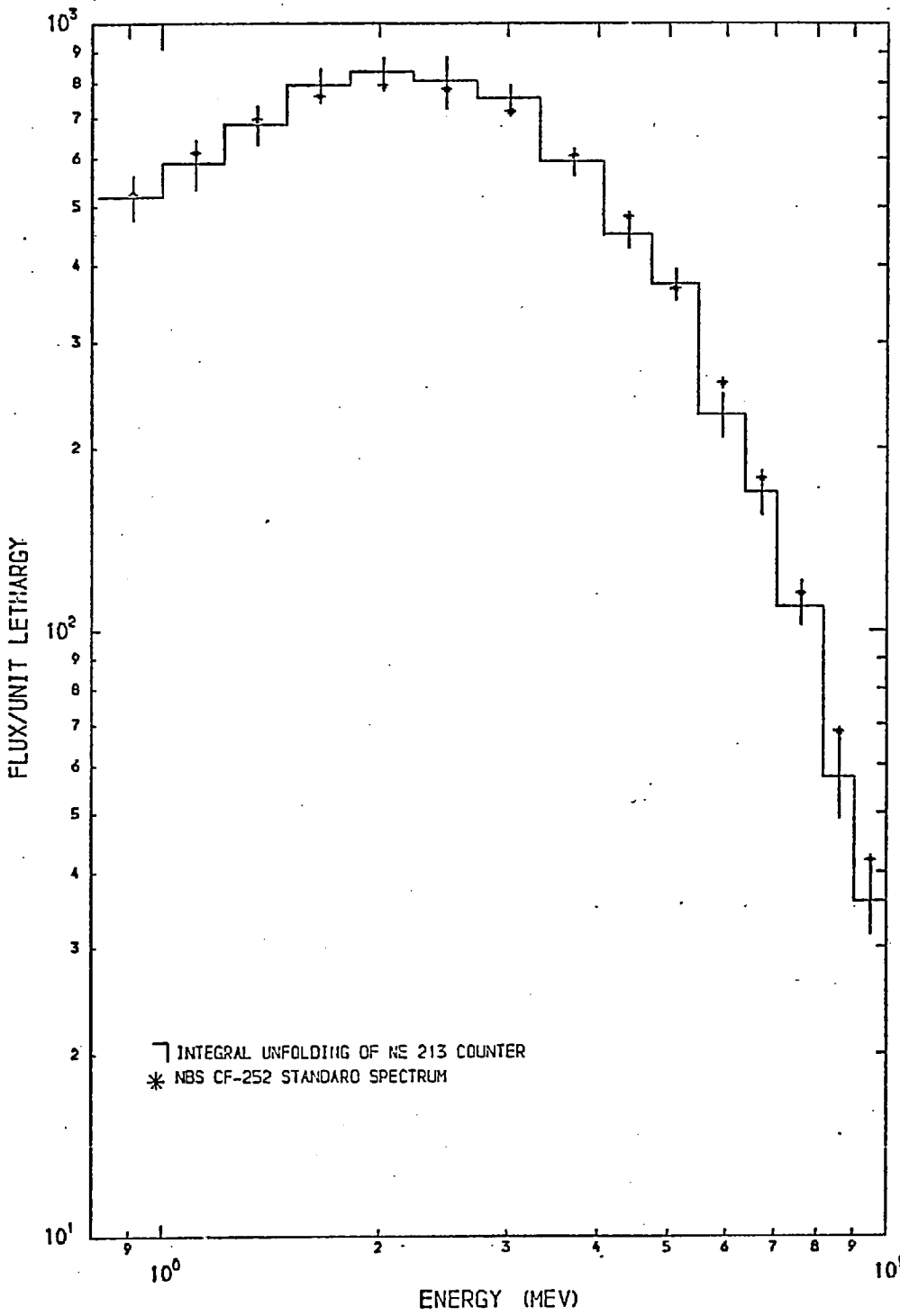


FIG. 7.3 COMPARISON OF UNFOLDED CF-252 FISSION SPECTRUM WITH NBS STANDARD.

and for the first order of small changes:

$$\delta R_i = \sum_j \delta a_{ij}\,\phi_j + a_{ij}\,\delta\phi_j \qquad 7.4.2$$

The term in $\underline{\delta\phi}$ depends on both the perturbation to the transmission cross-section data and on the perturbation to the response function data for thick detectors. If it is assumed that the detector is of a different material to that of the bulk transport medium and is thin compared with the shortest group mean free path in the detector material, the term in $\underline{\delta\phi}$ may be neglected, so that the variance on the response-rate may be approximated by:

$$\mathrm{Var}(R_i) \simeq \sum_j \sum_{j'} \phi_j\,\phi_{j'}\,\mathrm{cov}(a_{ij}, a_{ij'}) \qquad 7.4.3$$

In similarity with the uncertainty analysis of Chapter II, equation 7.4.3 can only be evaluated for the general case if the energy-dependent covariance matrix for the detector cross-section data is known; otherwise only lower and upper expected error bounds, corresponding to zero and full energy-dependent correlation respectively, can be assigned to the domain of R_i. The upper fully correlated limit corresponds to the situation where the cross-section has been normalised to a single absolute measurement and the value of the variance is therefore group scheme independent. In contradistinction, the lower uncertainty bound is critically dependent on the energy group scheme and in calculations for the ASPIS iron benchmark experiment, credance had to be taken of the fact that the fractional group cross-section uncertainties of Table 7.5 were those appropriate to a 15 group subset of the 620 group SAND-II library. The results of the uncertainty analysis for upper and lower bound energy-dependent correlation assumptions are given in Table 7.6 for the four primary integral activation detectors for four different penetration positions in the ASPIS iron shield.

7.4.2 Integral Detector Response-Rate Profiles

The behaviour displayed in Table 7.6 can be elucidated by reference to the reaction-rate (or detector sensitivity) profiles of Figures 7.4 to 7.7. For sulphur the reaction-rate per unit lethargy profiles at the 50.8 cm and 76.2 cm positions are broadly similar in shape falling rapidly on either side of the maximum sensitivity at 2.3 MeV. The increasing

Table 7.5

Fractional Uncertainty Estimates on Activation Detector Cross-Sections (after (37) and (140))

Lower Boundary (MeV)	S(n,p) %	In(n,n') %	Rh(n,n') %	Au(n,γ) %
1.0 -10	-	-	-	0.5
4.0 -7	-	-	-	4
1.0 -5	-	-	-	5
1.0 -2	-	-	30	6
1.0 -1	-	30	6	6
6.0 -1	-	20	6	7
1.4 0	100	10	6	7
2.2 0	20	10	9	7
3.0 0	8	10	9	7
4.0 0	8	8	5	7
5.0 0	8	8	5	7
6.0 0	8	8	5	7
8.0 0	8	8	6	7
1.1 +1	8	10	6	7
1.3 +1	8	10	10	7
1.6 +1				

Table 7.6

Upper and Lower Energy-Dependent Correlation Bounds for the Expected Fractional (%) Error on the Integral Response-Rate as a Function of Penetration

Position cm.	$S^{32}(n,p)$		$In^{115}(n,n')$		$Rh^{103}(n,n')$		$Au^{197}(n,\gamma)$	
	lower	upper	lower	upper	lower	upper	lower	upper
20.3	15.5	24.3	8.6	15.1	3.6	6.5	3.4	4.7
50.8	22.2	31.0	13.9	21.2	4.7	7.0	3.3	4.5
76.2	28.7	40.5	17.3	24.0	5.3	7.6	3.1	4.3
101.6	35.1	43.6	19.3	24.9	5.6	8.0	2.9	4.0

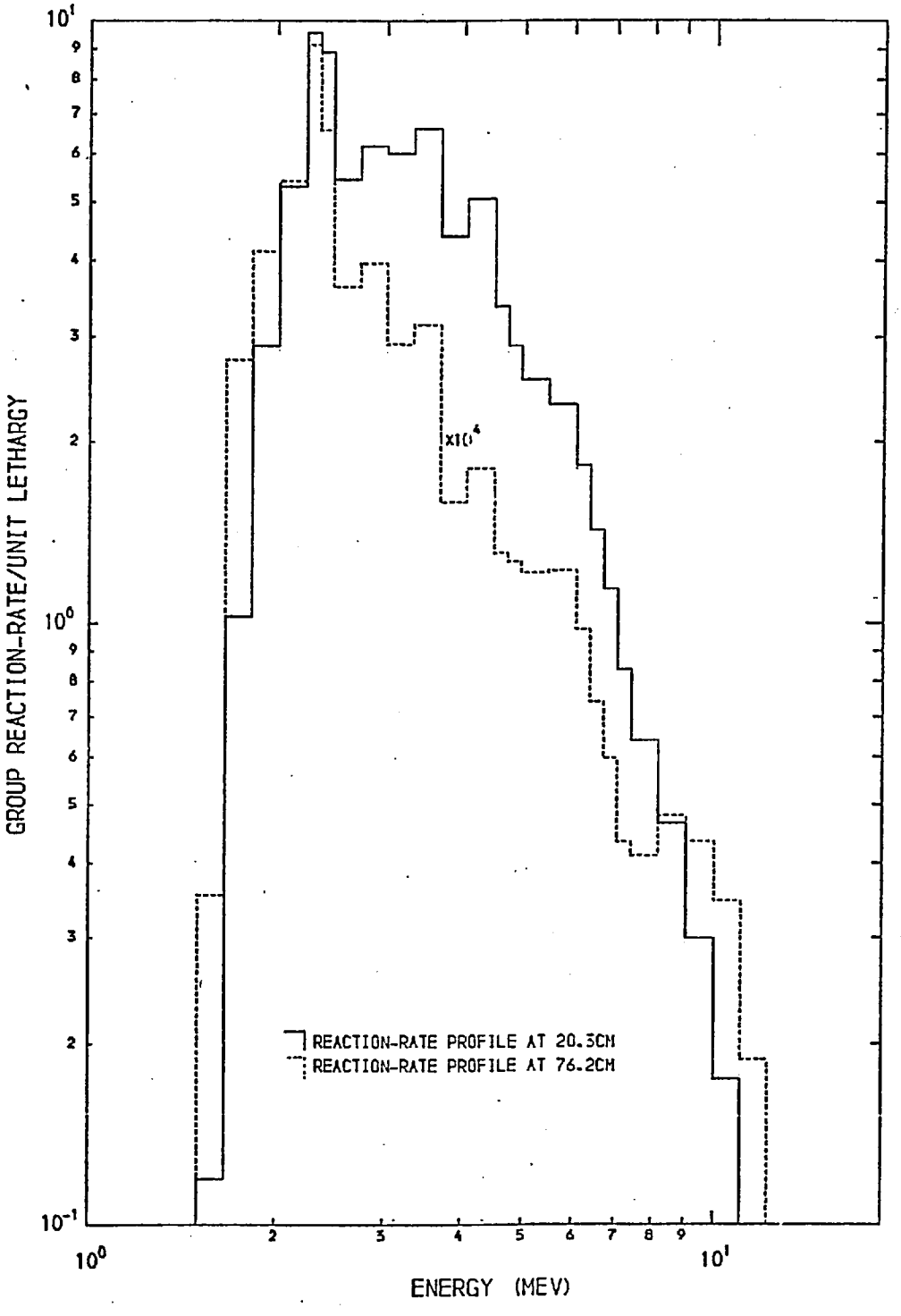


FIG. 7.4 VARIATION IN S(N,P) REACTION-RATE PROFILE AS A FUNCTION OF PENETRATION.

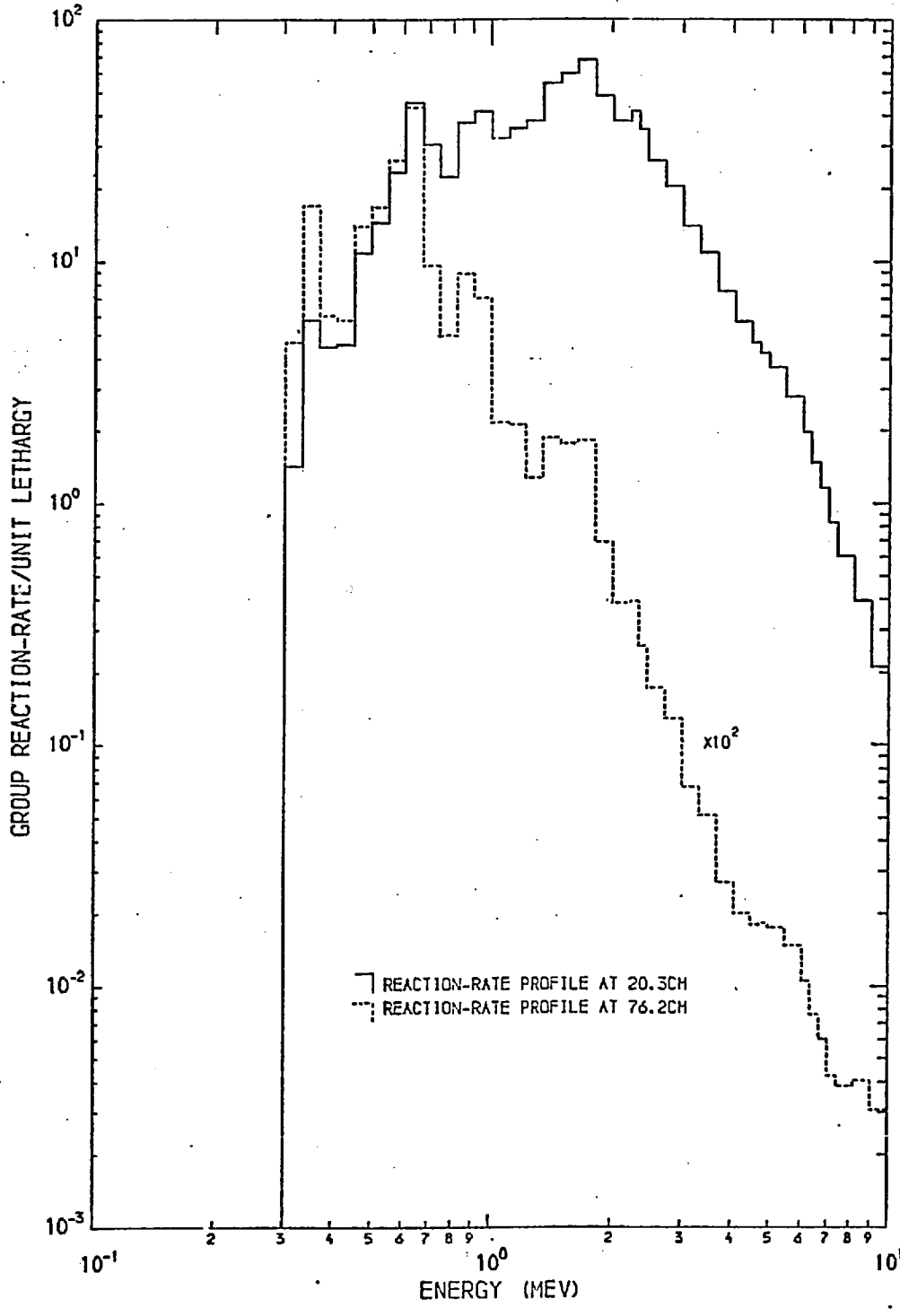


FIG. 7.5 VARIATION IN IN(N,N') REACTION-RATE PROFILE AS A FUNCTION OF PENETRATION.

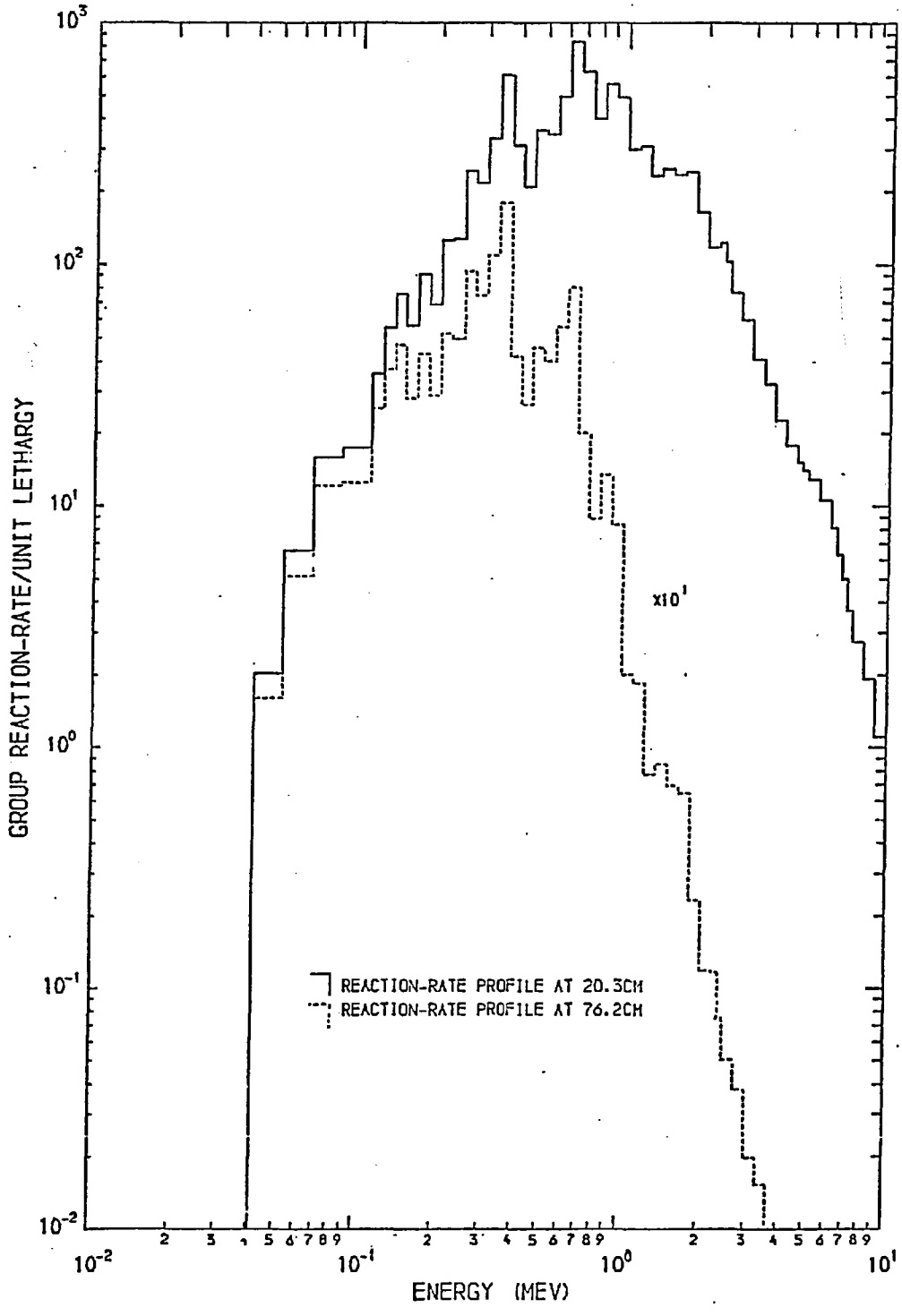


FIG. 7.6 VARIATION IN RH(N,N') REACTION-RATE PROFILE AS A FUNCTION OF PENETRATION.

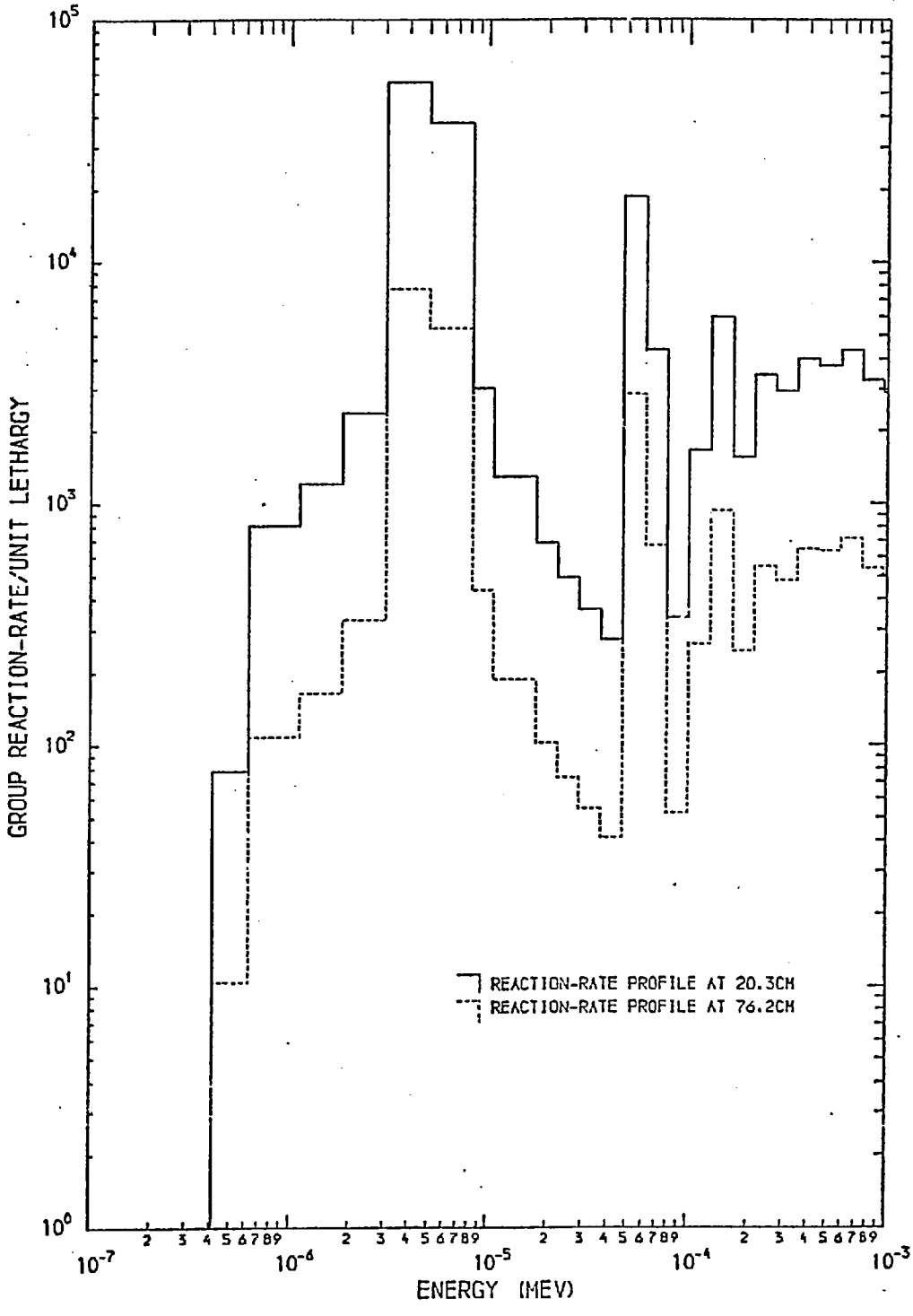


FIG. 7.7 VARIATION IN AU(N,γ) REACTION-RATE PROFILE AS A FUNCTION OF PENETRATION.

importance of the threshold region of the response function with penetration accounts for the degradation of the quality of the information with depth into the shield. The 20.3 cm measurement has a broader sensitivity profile with much of the reaction-rate being derived from the rather better known plateau region of the cross-section above 3.0 MeV.

The reaction-rate of the indium foil near the source appears to be dominated by the flux around 600 keV and the fission source distribution around 2 MeV. As would be expected the importance of the fission source falls off at deeper penetrations with the reaction-rate being influenced mainly by the flux at 600 keV and at very deep penetrations (76.2 cm) by the threshold itself. The importance of the threshold results primarily from the high energy gradient of the penetration flux. Similarly the high sensitivity at about 600 keV is not a feature of the response cross-section, but is a characteristic of the penetration flux in iron. At the 76.2 cm position, the DOT-III reference calculation shows a change in the flux per unit lethargy by a factor 10 from 600 keV to 700 keV. This build up of neutrons at 600 keV probably represents the result of inelastic scattering of source energy neutrons. Figure 7.8 shows that 600 keV lies well down the shoulder of the cross-section threshold which rises from ~ 300 keV at threshold up to 2 MeV, which, according to some evaluations, represents the start of a plateau. The 20% cross-section uncertainty assignment by McElroy et al for the SAND-II groups in this region dominates the upper bound correlated error calculation. The expected fractional error on the reaction-rate increases slightly with penetration reflecting the growing importance of the less well-known shoulder of the cross-section.

For rhodium the 20.3 cm reaction-rate profile shows that the detector samples a wide range of the flux and the weight on any part of the cross-section is small. At deep penetration though the contribution to the reaction-rate is more selective, and the threshold region gains importance causing the lower bound independent correlation estimates of the expected fractional error to increase with penetration.

The reaction-rate profile for the cadmium covered gold foils is entirely that which would be expected from examination of the suppressed cross-section. The majority of the reaction-rate derives from the wide (Γ_γ = 124 meV) 4.9 eV resonance with smaller contributions from the higher energy resonances notably at 58 eV and 150 eV. The shape of the profile does not change significantly with penetration and the uncorrelated lower bound expected error on the reaction-rate remains relatively constant at about 3% with penetration. It is difficult to establish the range of the

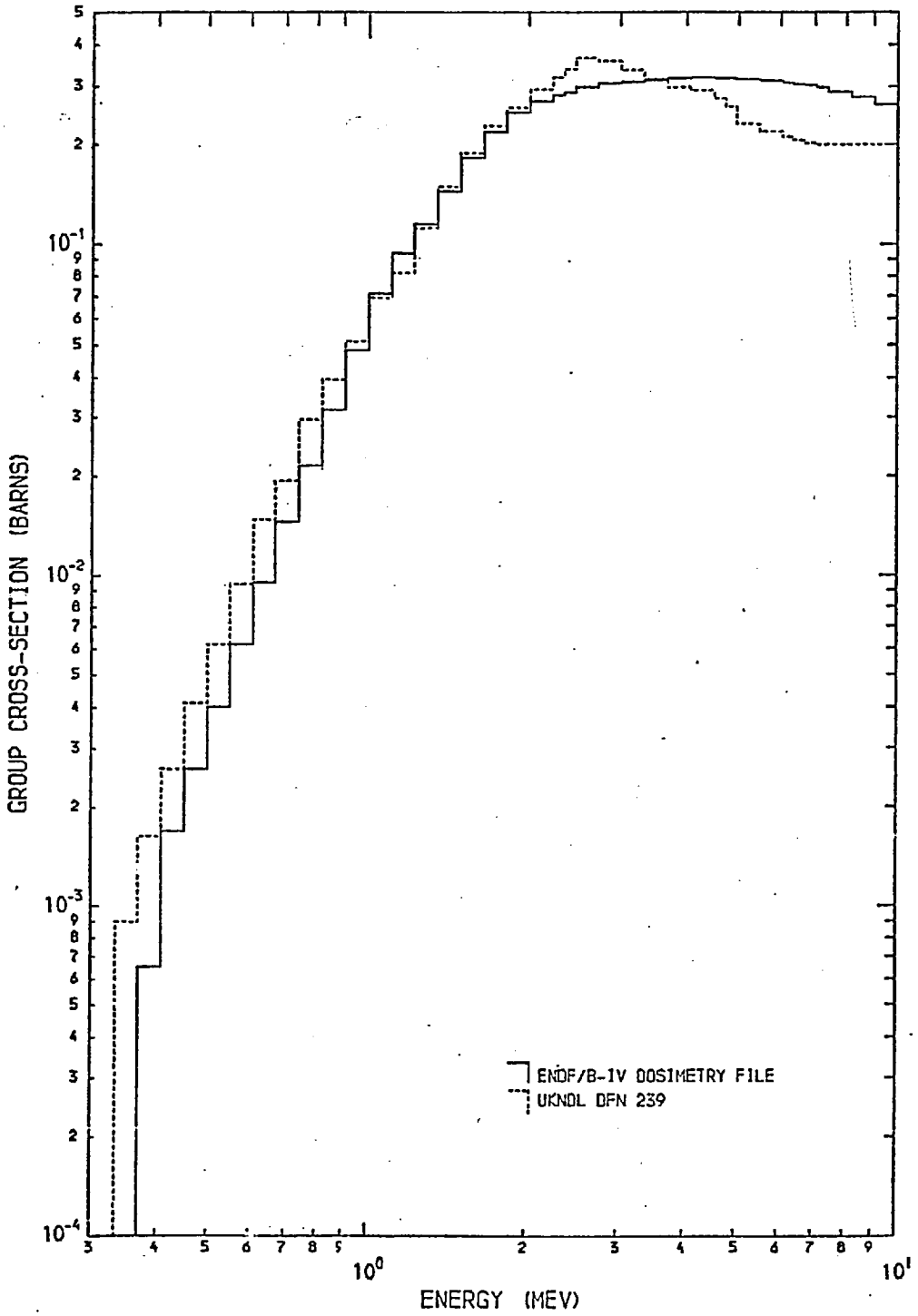


FIG. 7.8 COMPARISON OF IN-115(N,N') MULTI-GROUP CROSS-SECTION DATA FROM DIFFERENT SOURCES.

energy-dependent correlation for the gold cross-section, but one might expect, that owing to the plethora of measured data, the largest and longest range correlation would be that imposed by the evaluator in defining the mean of the measured data and the model parameters for the resonances.

The foregoing discussion on the detector sensitivity profiles has established those areas where the uncertainty on the detector cross-sections has most influence on the predicted reaction-rate. It is in these areas where not only the variance on the cross-section need be known, but also the fourth moment of the evaluated cross-section data. Together the reaction-rate profile and the cross-section uncertainty data can establish the usefulness of a detector in a benchmark experiment.

7.4.3 The Consistency of the SAND-II Error Data for the Response Cross-Sections

Since the results of Table 7.6 indicate that the uncertainties in the response data for the integral detectors could contribute significantly to the C/M ratios determined for the ASPIS iron benchmark experiment, it is necessary to assess the validity of the error values given in the SAND-II error file. No details of the derivation of the uncertainty assignments have been given by either McElroy et al[37] or Zijp, who has used the file in the error analysis routine of the unfolding code SAND-PET[141]. Two cross-checks of the assigned error data have however been possible. From the differential viewpoint, extensive use has been made of a compilation of threshold detector cross-sections by Liskien and Paulsen[142] and of the handbook for the ENDF/B-IV dosimetry file[143], which contain details of the measured data and associated errors. A survey of the quality of the cross-section data for the four response cross-sections of interest as compared with the SAND-II error file estimates can be found in Appendix E.

A second, integral, approach to assessing the errors arising from the detector response data is afforded by a comparison of the reaction-rates determined from different sets of data. Where possible a comparison of the response-rates calculated using the SAND-II library, the UKNDL and the ENDF/B-IV dosimetry file can furnish estimates of the expected errors on the detector activation-rates. Table 7.7 displays the values obtained from the different libraries compared with the detector responses derived using the data recommended by Farinelli.

The SAND-II sulphur file is believed to be a relatively old evaluation which does not include recent evaluations[144] of either the sulphur

Table 7.7

Ratio of Response-Rates Calculated Using Different Data Libraries Compared with the Response-Rates Determined Using the Recommended Response Data as a Function of Penetration in the ASPIS Iron Benchmark Experiment

Position (cm)	$S^{32}(n,p)$		$In^{115}(n,n')$			$Au^{197}(n,\gamma)$	
	SAND / UKNDL	ENDF/B / UKNDL	SAND / EURLIB	ENDF/B / EURLIB	UKNDL / EURLIB	UKNDL-222 / EURLIB	UKNDL-1208 / EURLIB
20.3	0.80	0.96	1.00	0.88	0.98	1.04	0.96
50.8	0.73	0.95	1.00	0.73	0.97	1.05	0.96
76.2	0.68	0.93	1.00	0.60	0.94	1.04	0.96
101.6	0.63	0.92	1.00	0.52	0.92	1.04	0.96

cross-section or the $U^{235}(n,f)$ cross-section against which much of the older sulphur measurements have been made. Moreover the cross-section may have been adjusted using the SAND-II program to obtain consistency with the results of integral benchmarks. The very good agreement between the SAND-II predictions for indium and the EURLIB calculations may indicate that since they are not primary libraries, they have a common source. A further caveat must be made concerning the data of Table 7.7; the number of independent measurements of these cross-sections is small so that the primary libraries, i.e. ENDF/B and UKNDL, represent two samples from a sparse population of measured data and the differences between these libraries may reflect more about the credibility of the evaluator than of the data per se. Nevertheless this "evaluation systematic" is an important part of the error on any piece of data and its quantification as a contribution to the fractional expected error is included in the data of Table 7.7.

An important feature of Table 7.7 is the measure of disagreement between the ENDF/B-IV dosimetry file prediction of the $In^{115}(n,n')$ reaction-rate and that of other libraries. The discrepancy arises because of the completely different cross-section evaluations which exist between the files (Figure 7.8). The reaction-rate profile for indium demonstrates that the important region of the indium cross-section, for this type of experiment, lies between 0.4 and 1 MeV.

The gold reaction-rates for the ASPIS iron benchmark experiment were calculated using a table of 1/E weighted suppressed cross-section data supplied by EURATOM. The comparison of the predictions of these data with an old UKNDL (DFN 222) evaluated gold file and with the more recently evaluated UKNDL (DFN 1208B) gold dosimetry file[145] is given

in Table 7.7. The multi-group suppressed cross-section data were derived from the raw nuclear data files using the SUPPRES code[146] which incorporates the use of a single scatter removal kernel for the fine group calculation prior to a Fermi spectrum (1/E) condensation to the required multi-group form. The acceptability of the fine group structure has been examined by a variation of parameters method. A plot of the old and new UKNDL gold files for the (n,Y) reaction, in suppressed multi-group form, is given as Figure 7.9. Substantial changes in the cross-sections by factors varying between 2 and 10 are observed for some groups. The resonance integrals, above the cadmium cut-off (0.55 eV), of the old and new evaluated files, for a 5.08×10^{-3} cm thick foil, were determined using the SUPPRES code to be 416.3 and 413.7 barns respectively, which compare very closely with the measured value of 414 barns obtained by Packwood and McCracken[147] on the GLEEP reactor at AERE Harwell. The 4% error of Table 7.7 reflects the change in the resonance parameters by the evaluator and would be seen to substantiate the choice of the $Au^{197}(n,Y)$ reaction as a category I detector[148].

7.5 Measurement Errors

In the previous sections of this chapter, the uncertainties in the detector response data have been considered; these errors can be included in the statistical model of the optimisation method. This section is concerned with the errors injected into the measured data during the processing of the observables into a form suitable for comparison with theoretical prediction. These 'measurement errors' cannot easily be modelled and their magnitude must be examined. Whilst the activation foils furnish a single meaningful reaction-rate, the pulse height data from a proton recoil counter requires processing into either an integral or differential group form.

7.5.1 The Differential Approach

For an infinite proton recoil counter, the differential response equation can be shown to be:

$$-\frac{dM_i}{dE} = \left(\frac{\overline{\Sigma_H(E)}}{E}\right)_j \phi_j \delta_{ij} \qquad 7.5.1$$

where M_i is the i^{th} signal channel count-rate defined by equation 7.3.8, and the relation 7.3.9 has been used to transform the infinite medium Fredholm equation (7.3.1) into terms of observed pulse-height. The term

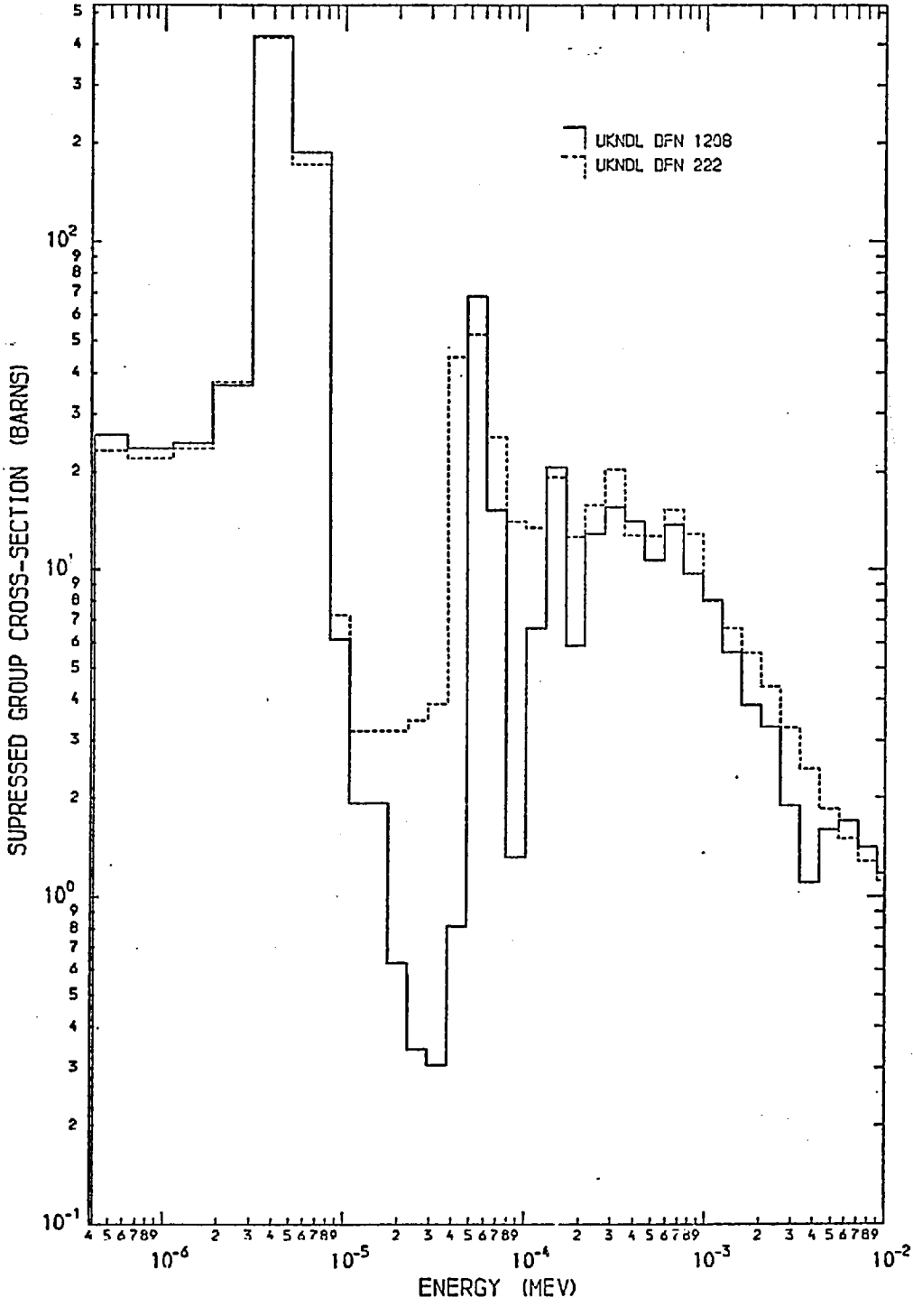


FIG. 7.9 COMPARISON OF SELF-SHIELDED AU(N,γ) MULTI-GROUP CROSS-SECTION DATA FROM DIFFERENT SOURCES.

in brackets represents the average of $\Sigma_H(E)/E$ over the neutron group j. For a finite counter the implied leakage corrections are obtained by substituting equation 7.3.2 for 7.3.1. The energy differential of the counting distribution can be determined by the count-processing code NE 213[7] and the differential matrix elements are computed for finite spherical counters by the program PRCM[102]. Owing to the finite size of the counter, the differential matrix is not diagonal but upper triangular. In the working range of the counter, the pivotal elements dominate the response and it is for this reason, of one-to-one correspondence between differentiated signal channel count-rate and group flux, that the differential matrix is to be preferred for unfolding of the count-rate distribution for prediction of the neutron spectrum. Moreover, owing to this diagonal dominance, the differential matrix is amenable to rapid and accurate inversion so that a less ill-conditioned solution is obtained. It is this simple dependence of the proton recoil spectra on the ratio $\Sigma_H(E)/E$ which allows the information obtained from the counters to be utilised easily. Also the hydrogen scattering cross-section is very well defined over most of the energy range normally covered by such counters, and since departures from theory for the differential matrix are small, the information provided by such counters can be unfolded with a high degree of precision.

The proton recoil distribution output from a neutron spectrometer is collected and stored as a histogram representation of pulse heights. These channel counts, c_l, are usually integrated into a signal channel count-rate, M_i, which is normalised to counts s^{-1} NESTOR Watt^{-1} with an associated statistical variance of counts/(time^2 x power^2). No γ-background subtraction from the counts is necessary as the lower energy boundary of the counter working range, E_γ, is taken to be the energy at which γ-events in the chamber start to contribute significantly to the counting statistics. Using equations 7.3.8 and 7.3.9 it can be shown that:

$$\frac{dM_i}{dE} = b(E_{P_{i+1}}) - b(E_{P_i}) \qquad 7.5.2$$

The proton distribution at the centre of the channel i can be determined by using equation 7.3 9 so that for a pulse height channel width Δl and allowing for non-linearity of the detection system:

$$b(E_{P_{i+1/2}}) = \frac{c_l}{\text{Time} \times \text{Power}} \cdot \frac{dl}{dE} \cdot \frac{1}{\Delta l} \qquad 7.5.3$$

with an associated variance of:

$$\mathrm{Var}\left[b(E_{p_{i+\frac{1}{2}}})\right] = \frac{c_l}{\mathrm{Time}^2 \times \mathrm{Power}^2} \cdot \left\{\frac{dl}{dE}\right\}^2 \cdot \frac{1}{(\Delta l)^2} \qquad 7.5.4$$

The function b(E) is evaluated at the boundaries of the signal channel Ep_i either by linear interpolation from one pulse height channel on either side or by fitting a polynomial function to all the pulse height channels (with a maximum of ten either side for the NE 213 program) within an energy resolution ΔR of the signal channel boundary. This latter approach is effectively resolution smoothing of the proton recoil spectrum within the energy range $Ep_i \pm \Delta R/2$. The resolution width for smoothing, if chosen as the resolution of the counter, can reflect the fact that variations in the proton energy distribution within the resolution width of the counter can only be due to statistical uncertainties in the method rather than genuine information about the distribution being sampled. Accordingly the effect of resolution smoothing on the predicted differentiated group count-rate has been assessed with the aim of evaluating the accuracy with which the differential can be determined. The data of Table 7.8 indicates that the precision with which the fitting/interpolation procedure can be performed is no better than 2%; the inference is therefore that the typical error on the differentiated group count-rate arising from count processing is about 3%

7.5.2 The Integral Approach

The integral response equation for an infinite proton recoil counter can be shown to be:

$$M_i = \sum_{j=1}^{G} \overline{\left(\frac{\Sigma_H(E)}{E}\right)_j} \left(E_{p_{i+1}} - E_{p_i}\right) \phi_j \qquad 7.5.5$$

and the modifications for the finite counter can be derived from equation 7.3.2. The rather flat form of the elements of the integral response matrix make it unsuitable for unfolding count-rate distributions by matrix inversion processes; response function uncertainties have increased importance and because of the generally connected behaviour of the response surface, the propagation and possible amplification of errors from the higher to the lower energies can occur. For this reason the integral approach is normally only used in the refolding situation where

Table 7.8

Effect of Resolution Smoothing on Proton Recoil Counter Differential Data

Counter Type	Energy	Count Vector Element for a Given Resolution				Statistical Count Variance
		0%	2½%	5%	10%	
Ar/H	E_γ	1.757 0	1.836 0	1.763 0	1.729 0	1.00 -4
	mid-range	4.873 -2	4.947 -2	4.692 -2	4.557 -2	2.60 -6
	E_{max}	5.316 -4	4.104 -4	4.444 -4	4.189 -4	1.66 -8
10 at.	E_γ	2.070 +1	2.049 +1	2.049 +1	2.071 +1	7.86 -3
	mid-range	8.571 -1	8.649 -1	8.525 -1	8.563 -1	1.44 -4
	E_{max}	4.534 -2	4.534 -2	4.377 -2	4.423 -2	3.61 -6
3 at.	E_γ	1.214 +1	1.218 +1	1.206 +1	1.204 +1	1.05 -2
	mid-range	3.404 0	3.435 0	3.383 0	3.350 0	2.29 -3
	E_{max}	3.253 -1	3.140 -1	3.169 -1	3.108 -1	1.29 -4
1 at.	E_γ	6.758 0	6.721 0	6.838 0	6.661 0	1.38 -2
	mid-range	3.507 0	3.524 0	3.540 0	3.525 0	1.44 -3
	E_{max}	9.708 -1	1.005 0	1.011 0	1.009 0	1.38 -3
½ at.	E_γ	1.897 +1	1.850 +1	1.839 +1	1.908 +1	2.64 -2
	mid-range	3.982 0	4.041 0	4.198 0	4.042 0	1.76 -2
	E_{max}	2.267 0	2.126 0	2.220 0	2.236 0	4.80 -3
1 at. with high gain	E_γ	4.143 +1	-	4.137 +1	-	2.71 -1
	mid-range	7.444 0	-	7.381 0	-	6.93 -2
	E_{max}	5.857 0	-	5.735 0	-	1.05 -2
½ at. with high gain	E_γ	2.306 +1	-	2.346 +1	-	5.29 -1
	mid-range	1.867 +1	-	1.870 +1	-	2.01 -1
	E_{max}	3.246 0	-	3.205 0	-	6.49 -2

the calculated fluxes are used to predict the independent elements of the signal channel count-rate vector.

The integration to obtain the signal channel count-rate is performed by adding the pulse height channel counts and proportioning the channel if the boundary lies within it. The data of Table 7.9 compare the integral signal channel data collected on two independent runs of the NE 213 counter whilst monitoring a Cf^{252} fission neutron source. The reproducibility of the data is usually within the assigned errors showing that the variance assigned to the signal channel count-rate, assumed normal, is consistent with the sampling variance.

Table 7.9

Comparison of Repeated Runs with Statistical Variance Prediction

Channel No.	Fractional Difference Between Runs	Average Statistical Standard Deviation
1	-3.63 -3	9.42 -4
2	9.90 -4	1.02 -3
3	-3.70 -4	1.21 -3
4	-2.92 -3	1.42 -3
5	-5.45 -3	1.73 -3
6	4.91 -3	1.02 -3
7	-5.02 -5	2.40 -3
8	1.72 -3	2.90 -3
9	2.55 -3	3.55 -3
10	-4.80 -3	4.28 -3
11	-4.83 -3	6.81 -3
12	9.97 -4	7.55 -3
13	7.11 -3	1.31 -2
14	-3.01 -2	2.75 -2
15	-2.36 -2	4.73 -2
16	-9.07 -2	7.62 -2
17	-9.29 -2	9.01 -2

7.5.3 Measurement Uncertainties

Prior to processing of the observed data, certain corrections, which are not included in the statistical model, are made to the measurements. The uncertainties in the observed data include:

(i) Source reactor neutron background. Owing to the low power[4] of the converter plate (7 Watts), the contribution to the penetration flux in the shield from neutrons leaking out of the NESTOR driver reactor (30 KW maximum) is not negligible. Packwood and Carter[110] measured the reactor neutron background using a dummy converter plate and concluded that a correction factor of 0.9 should be applied to the measurements.

(ii) A special shield plate with a slot cut at the centre was required to allow measurements to be made using the proton recoil counters (SP2 counter radius 2 cm). Comparison of the results of integral detectors at the positions with and without the slot indicated that the flux in the slot was 10% low at all energies. A correction factor 1.1 was applied to the measurements in the slot.

(iii) In shields where the spatial flux gradient is large, errors in the positioning of the detectors can produce quite large uncertainties in the measured reaction-rates. The error in the positioning of the integral foils has been assumed to be $\pm$ 1 mm. The error in the foil measurements is however negligible since the average of several repeated measurements was taken. For the proton recoil counters, a smoothing of the effective positioning error (assumed to be $\pm$ 3 mm) occurs because the counters perform the integral of the neutron flux over the counter volume, and thereby only predict the average flux in that position.

In this section on measurement errors the routes for processing proton recoil data have been considered and shown to be adequate. Moreover the assignment of statistical errors to the signal channel data by the processing programs has been shown to be consistent with repeated sampling. Finally other extraneous uncertainties in the measured data, which have not been included in the statistical model have been considered and either removed or shown to be negligible.

7.6 Energy Scale Calibration Errors

7.6.1 Introduction

An error in the calibration of the energy scale of a proton recoil counter manifests itself by predicting well documented resonance features to be 5 - 10% different in energy than that attributed to them in cross-section evaluations. Carter[149] has consistently found that features arising from the asymmetric resonance-anti-resonance pair in iron in the 24 - 27 keV region are 5 - 10% higher in energy than would be expected after folding in a Gaussian resolution filter for the counter. In regions of fairly flat flux the magnitude and shape of the unfolded flux profile appear to be about correct, but have been translated through a fractional energy shift. In regions of high energy gradient the magnitude of the flux is also wrong.

Energy scale calibration errors have significance in the ASPIS iron

benchmark experiment. Figure 6.8 illustrates the multiply unfolded flux spectrum given by RADAK. After allowance for the counter resolution, a factor ignored by RADAK, the energy appropriate to the iron 27 keV resonance flux is overpredicted by some 10%. Features in the range 70 to 200 keV, spanned by the 3 at. counter, appear to agree well with calculation. The overprediction of the flux in the high energy region 0.8 - 2 MeV may be due in part to energy scale calibration and for data adjustment purposes it is important to decouple the effects of this type of error from the removal cross-section uncertainties.

7.6.2 Calibration of the Gas Counters

All the spherical gas-filled proportional (SP2) counters have a small Pu^{239} α-particle source at the centre on the anode wire. The 3 at. counter was compared with a reference counter containing 0.1% of He^3. The Q value of the $He^3(n,p)T$ reaction obtained in a thermal neutron flux is 764 keV. With a knowledge of the channel and the energy of the proton-triton sum peak, the calibration line of incident proton energy against channel can be drawn on the basis of the assumption that the line passes through the origin. Such a procedure amounts to the assumption that the specific ionization, w_p, of a proton is independent of energy. For the reference counter the energy of the Pu^{239} 5.15 MeV α-source ionization peak is read off to an accuracy of about 2%. The proportional counters used in the ASPIS iron benchmark experiment did not contain He^3 because the spectrum arising from He^3 can be troublesome in an experimental facility displaying a high thermal flux. Moreover the stopping power of hydrogen below 3 at. is insufficient to allow He^3 calibration.

The five gas proportional counters were therefore calibrated on the basis of the energy assigned to the Pu^{239} α-source peak and the origin. The calibration of each of the ASPIS counters was therefore independent. A check on the accuracy and consistency of this approach is afforded by measurement of a structured spectrum, say in iron, and examining the region of overlap of each counter. Owing to the variation of counter resolution, such a method can serve only as a diagnostic check on the actual α-source calibration and could not be used in its own right to intercalibrate the counters.

7.6.3 Calibration Errors (Proportional Counters)

The assumptions and procedures used to calibrate a counter are now examined and possible explanations leading to energy scale errors are proposed.

(i) The finite resolution of the reference counter although usually

small (3%) can lead to uncertainty in the assignment of a channel number to structure in the counting distribution.

(ii) The use of the triton + proton sum peak as a calibration marker may be invalid. The assumption inherent in this method is that the specific ionization of the triton is the same as the proton and is non-nuclear in origin. Theory predicts that the ratio of the proton edge energy to the triton edge energy should be 3:1 and that the proton energy to the sum peak energy should be in the ratio 3:4. Recent measurements by Carter[149] have shown that by reading off the calibration curve the energy assigned to the proton peak, and scaling by the theoretical factor 4/3, the energy assignment for the proton + triton sum peak would be 780 keV. Two explanations of this experimental observation are possible. Firstly it may be that the specific ionization of the triton is not the same as that of the proton, in which case all future counter calibrations should be normalised to the proton edge. Such a conclusion worsens the existing observed energy scale error. Alternatively, it should be remembered that the proton and triton edges arise because the events creating them have occurred so close to the counter wall that the direction and range of the associated particle have been sufficient for it to escape from the counter. Near the counter wall, peculiar ionization effects may occur including the ejection of electrons from the negatively charged counter wall. In this case the proton edge would appear at the wrong energy and could not be used as a calibration marker.

(iii) The use of the origin as the second reference point depends on the assumption that w_p is independent of energy. Experiments to determine the specific ionization of protons, w_p, have shown non-linear behaviour at low energies[150,151] which may be due to an actual energy dependence of w_p at low energies or may be an effect attributable to the excitation of impurity ions in the gas filling of the counter[152] (e.g. water or palladium). Recent work at Birmingham[153] has shown that the non-linearity in w_p is counter dependent, a result which may support the impurity theory. Although the effective w_p for a counter may be non-linear, it also seems physically reasonable that the calibration curve should have a finite energy intercept. Mono-energetic protons have a well-defined range beyond which

no ionization occurs and the ionization which they do produce has a maximum called the Bragg peak near the end of the range. In this region of high ionization density the probability of electron loss due to recombination or electron leakage is high. Such an energy loss would be reflected in the proton energy-pulse height curve by a non-zero intercept.

(iv) The assignment of the energy to the Pu^{239} α-source peak can be uncertain due to the finite resolution of the counter and the peak may be asymmetric due to the attenuation of the α-particles in the source. Moreover calculations by Kemshall[133] have shown that a shift in the source position by 3 mm from the centre of the SP2 counter can reduce the average energy by 5% for pressures corresponding to $R(E_\alpha)/a < 2$.

Table 7.10

The Pressure Variation of the α-source Calibration Energy for SP2 Counters (after 133)

Pressure (at.H_2)	Equivalent Proton Energy E'_α Deposited by Internal α-Source	Resolution %	$\frac{E'_\alpha}{E_{max}}$
1	0.35 - 0.37	10 ± 2	1.53
3	1.15 - 1.19	10 ± 2	2.34
10	4.30 - 4.80	20 ± 5	4.89

The poor resolution of the peak can be interpreted in terms of electron loss in the densely ionised track, whilst the difference in peak energy of 4.8 MeV for total α-energy deposition in the counter and the α-source energy of 5.15 MeV can be attributed to the difference in the specific ionization of α-particles and protons.

Although the above uncertainties apply to the calibration established for the reference counter, the last two points (iii) and (iv) can also be applied to the calibration of the spectrometers against the reference counter.

7.6.4 Calibration Errors (Electronics)

There are three types of error in the pulse analysing electronics which could manifest themselves as energy scale errors. They are in order of discussion the effect of gain change errors in the main amplifier, non-linearity of the main amplifier or the pulse height analyser (P.H.A.) and back bias errors in the multi-channel analyser.

(i) Table 7.10 shows the relationship between the α-source calibration

energy E'_x and the upper boundary of the working range of the counter E_{max}. If E_{max} is positioned just below full scale on the P.H.A., an increase in gain by 1.5 for the 1 at. counter and by 5.0 for the 10 at. counter is necessary after calibration has been completed and before spectrum measurements are made. The change is usually achieved by a change in the main amplifier gain. Kemshall[133] has investigated the effect of a 5% main amplifier gain change error on a typical fast reactor spectrum. The conclusion reached was that the effect of the error in the resulting spectrum was of order half the gain change error for the 3 and 10 at. counters, but was magnified threefold for the 1 at. counter. The effect on the 3 at. and 10 at. counters, where the ratio of the number of events in the counter due to neutrons below E_{max} to the number resulting from neutrons above E_{max} is large, arises mainly from the energy translation of $\Sigma_H(E)/E$. The large factor for the low pressure counter, however, may result from the very large contribution to the recoil proton density from neutrons above E_{max} and the low stopping power of the counter, producing a relatively small 'difference spectrum'. An error in the assignment of E_{max} would then result in a large change in the difference spectrum. Moreover, the change in proton density due to energy scale error is greatest where the gradient of the trapezoidal line-shape is largest, i.e. near E_{max}. The evidence would therefore indicate that errors in gain change and gain drift must be kept below 1% if 3% accuracy is required in the spectrum at low energies. The nominal gain change can be established normally to within 0.1% using an accurately calibrated pulse generator.

(ii) Differential non-linearity resulting from a variation of the channel width in a P.H.A. can have a two-fold effect; both the energy assigned to a particular channel and the number of counts recorded in a channel will be in error. The magnitude of the error will be greater for the differentiated signal channel count-rate distribution because quite small integral errors are magnified by differentiation. The size of the non-linearity can be determined by a sweeping pulse generator and for a typical P.H.A. the error should be no greater than 0.5%. As assessed from the gradient of a line-shape for $R(E_n)/a = 1.02$, the effect of a 0.5% deviation from linearity near E_{max} should

be no more than 2%.

(iii) Back bias errors can occur in the assignment of the channel number corresponding to zero pulse height. For a 100 channel P.H.A. the zero channel can be determined by line fitting to within ± 0.2 channels; the lower energy measurements in the ASPIS iron benchmark were made with a 400 channel P.H.A. giving a still further reduction in the back bias uncertainty. The error resulting from back bias uncertainty will be largest at low energies, near E_γ, and will manifest itself in the overlap region of the spectrum as determined by SPEC-4[154] from the different counters provided it is larger than the change in resolution width between the counters. The result of the effect on the spectrum has been assessed[133,154] to be no greater than 2%.

7.6.5 Calibration Errors (NE 213 Counter)

The calibration of the NE 213 counter requires the assignment of a linear energy scale to the pulse height distribution and the normalisation of the light function of the counter to the channel number of the Cs^{137} Compton edge. The position of the Cs^{137} edge, corresponding to the channel number at half-height, is determined from the pulse height distribution collected from a low intensity Cs^{137} γ-ray source. In this way the edge can be located to within ± 0.2 channels, corresponding to a 0.5% error for a normal run, and since there is no amplifier gain change between calibration and running, the uncertainty in the assignment of the Cs^{137} edge represents the energy scale calibration error for the NE 213 counter.

The NE 213 data of Carter[149] shown in Table 7.11 affords an opportunity to assess the magnitude of the day-to-day drift of the counter and electronics over a two week period. The dispersion error on the data is 0.75% which includes the energy scale calibration uncertainty of 0.5%; drift in the pulse processing electronics can therefore be neglected.

Table 7.11

Calibration Data for the NE 213 Counter as a Function of Time

Day No.	1	2	3	5	8	10	12
Cs^{137} Edge Channel No.	42.9	43.1	43.3 ± 0.2	43.4	44.0	43.5	43.8

The importance of including energy scale calibration errors in the prescription for data adjustment cannot be overemphasised. The effect of this type of error, especially in a flux region with a high energy gradient, could easily be attributed to inadequacies in the removal cross-section data. A decoupling of the effects is necessary before the maximum likelihood data can be obtained. It is important to note that the combination of the effects may cancel out the severe calculation-to-measurement discrepancies that really exist if the sense of the respective errors is opposite. In other words, if the energy scale is too low and the removal cross-section in specific energy groups is too high, then the χ^2 value may be lower than that obtained if the true energy scale could be estimated. The magnitude of the fractional uncertainty in the energy calibration for each of the counters used in the experiment is given in Table 7.12. A typical composition of the estimated calibration uncertainty for the 3 at. hydrogen chamber is given in Table 7.13; the values derived in this way for each counter have been adjusted in the light of experience gained through the use of the counters.

7.7 Detector Partition Coefficients

The detector partition coefficients are variables which account for fractional systematic uncertainties in the normalisation of the response surface for a counter. The factors are used in the optimisation schemes of the RADAK spectrum unfolding code and the PLATO nuclear data adjustment suite. The partition coefficients and their uncertainties have been given by Carter and Packwood and are summarised in Table 7.14.

The mutual consistency of these values assigned to the partition coefficients and their standard deviations has been assessed by a multi-position unfolding of the measured signal data using the RADAK code. The changes to the coefficients were within the assigned errors and no significant adjustments were observed.

7.8 Unfolded Measurement Spectra

The measurement distributions at four positions in the ASPIS iron benchmark experiment have been simultaneously unfolded using the RADAK code[104], which seeks a maximum likelihood solution for the flux spectrum whilst allowing adjustments to be made to the partition coefficients and the energy dependence of the response functions. Moreover the code uses a Monte Carlo sampling technique to provide an estimated variance-covariance matrix on the flux solution. The results of the unfolding have been compared with the calculated prediction in Chapter VI, and the energy displacement of features corresponding to the 27 keV resonance has been

Table 7.12

Estimated Fractional Energy Scale Error for Proton Recoil Counters

Counter	% Error
½ at.	3
1 at.	3
3 at.	3
10 at.	4
Ar/H	5-6
NE 213	0.5

Table 7.13

Composition of a Typical Energy Scale Error Estimate

Source of Energy Scale Error	'Worst' Case Estimate		Typical Integral Estimate for 3 at. Counter
	Diffl.	Integral	
Data Processing Errors	3%	-	-
Counter Resolution for E_α Error	1½%	1½%	1½%
Uncertainty in Q for $He^3(n,p)T$	2%	2%	2%
Use of Origin for Calibration	?	?	?
Position of α-Source on Anode	2%	2%	-
Main Amplifier Gain Uncertainty	0.3%	0.3%	0.3%
Differential Linearity of P.H.A.	2%	2%	2%
P.H.A. Back Bias Error	2%	2%	2%
Total (Random) Estimate	5.2%	4.3%	3.5%

Table 7.14

Partition Coefficients and Standard Errors Used in the ASPIS Iron Benchmark Experiment (after 4)

Detector	Partition Coefft.	% Standard Error	Comments
S(n,p)	1.00	8	Error represents burning-off efficiency + $4\pi\beta$ counter efficiency for P^{32} β^-
In(n,n')	1.00	5	Calibration efficiency of NaI(Tl) counter for 330 keV γ-ray uncertain to 5 %
Rh(n,n')	1.00	10	Uncertainty in internal conversion ratio
Au(n,γ) W(n,γ) Cu(n,γ)	1.00	5	Uncertainty in NaI(Tl) photopeak calibration
Ar/H	0.83	5	Number density of H atoms in the counter considered to be lower than specified
All other gas counters	1.00	5	5% uncertainty in efficiency of chamber
NE 213	1.00	10	This counter has never been absolutely calibrated. Only consistency checks with multiple RADAK unfolding have been performed

discussed in an earlier section of this chapter. It is noteworthy that if the calculated (C_i) and measured (M_i) responses are compared, no discrepancy is apparent.

In section 7.5 it was noted that conventional unfolding codes invert the differential response matrices of the proton recoil counters in order to obtain a better conditioned solution. Differentiated response matrices have also been used to obtain the multiply unfolded solution spectra of Figures 6.6 to 6.9. However since RADAK seeks the maximum likelihood solution by an iterative perturbation technique, searching for a global minimum in χ^2 with a positive flux constraint, the conditioning of the response matrix is of lesser importance and it is meaningful to seek a solution to the integral unfolding problem. This corresponds to treating each signal channel of a proton recoil spectrometer as a threshold detector rather than having the conventional δ-function response. A comparison of the integrally and differentially unfolded measurement distribution at the 50 cm position with the calculated flux prediction is given in Figure 7.10. It can be seen that the integral approach is unable to obtain the same magnitude for the flux dip in the resonance as the calculation (which may not necessarily be correct), but on the other hand no spurious structure such as that injected by the differential unfolding approach is given. Moreover it can be seen that at higher energies the integral unfolding gives considerably better agreement with the calculation than does the differential solution; it is this arbitrariness in the solution of the unfolding equation that makes the optimisation of nuclear data on the basis of a flux comparison unwise.

The effect of artificially produced energy scale calibration errors on the integrally unfolded spectrum at 76.2 cm position of the ASPIS iron benchmark experiment has been investigated. The DOT-III reference calculation was used in a refolding mode to generate a measurement spectrum which was subsequently unfolded again to test the consistency of the integral method. No measureable difference was observed. The signal channel boundaries were then perturbed in the positive and negative senses by the amounts given in Table 7.12 prior to integral unfolding. The results are compared with the unperturbed solution in Figures 7.11 and 7.12.

The inference is that whilst the integral unfolding approach afforded by the iterative solution of the response equation implemented in the RADAK code may not lead to a completely satisfactory solution of the energy scale shift observed in conventionally unfolded spectra, it does indicate that the error may arise at least in part from a methods' problem. Moreover

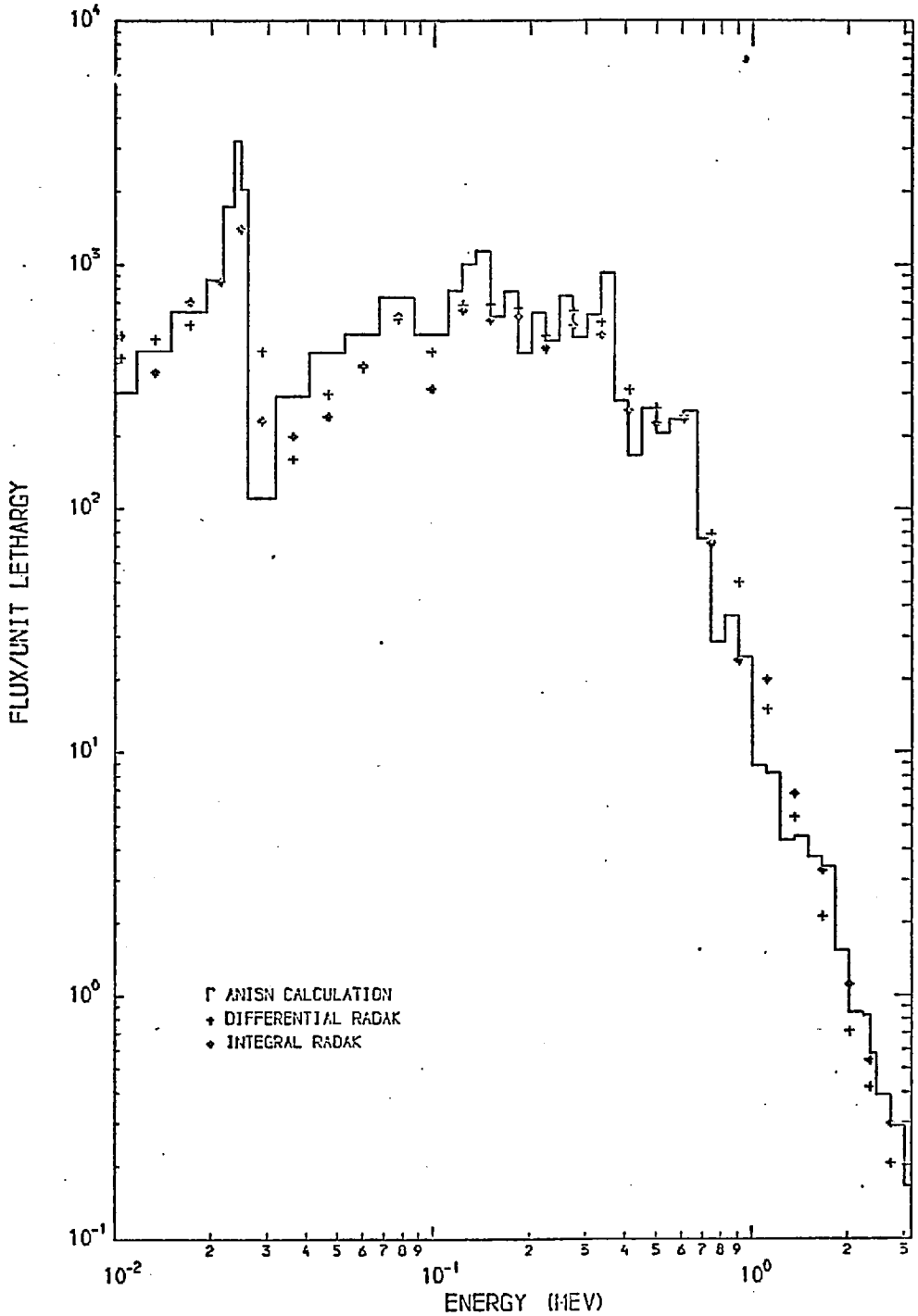


FIG. 7.10 COMPARISON OF CALCULATED FLUX PROFILES WITH RADAK UNFOLDED SPECTRUM MEASUREMENTS AT 50.8CM POSITION.

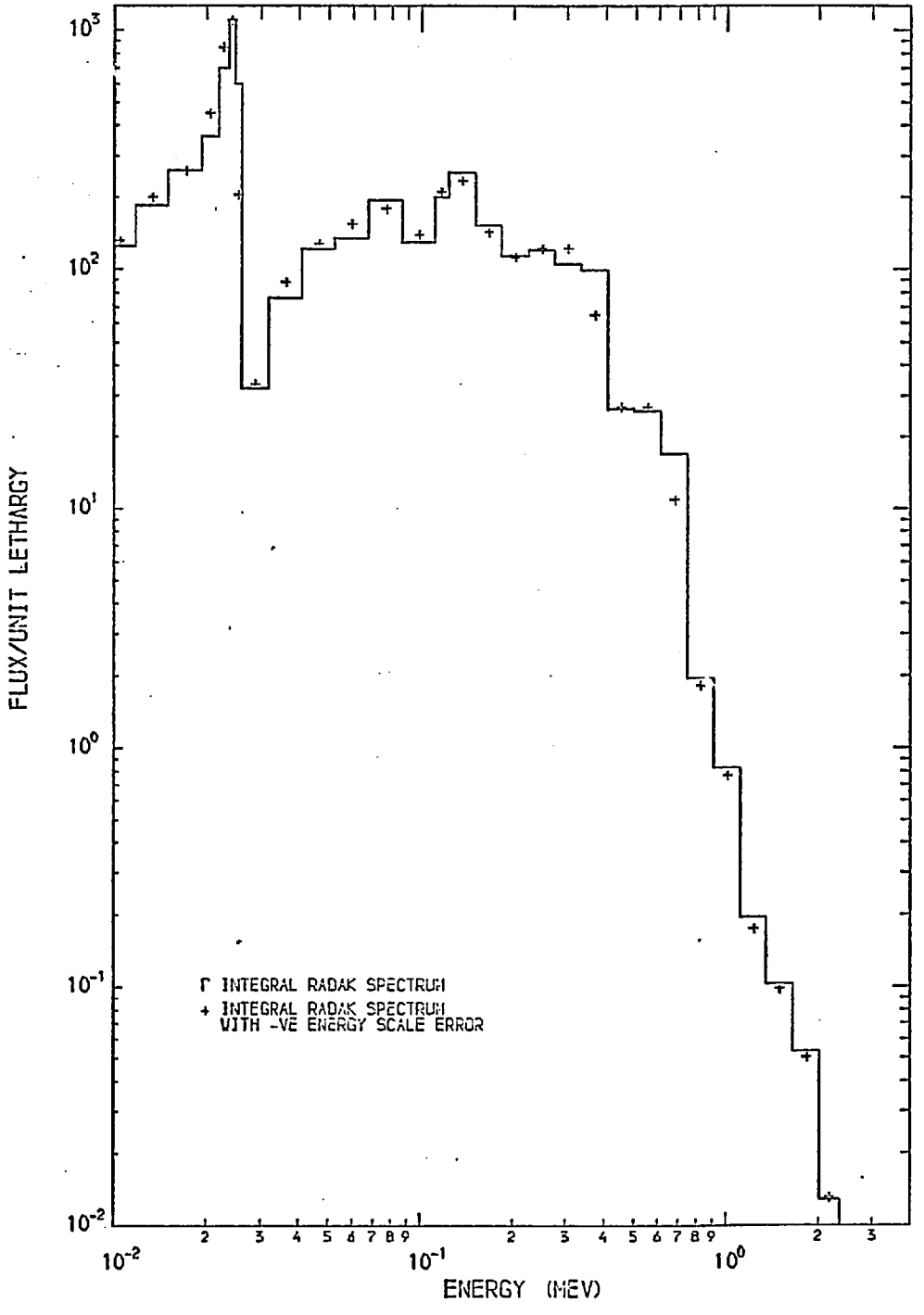


FIG. 7.11 COMPARISON OF RADAK UNFOLDED FLUX SPECTRA WITH AND WITHOUT ENERGY SCALE CALIBRATION ERRORS.

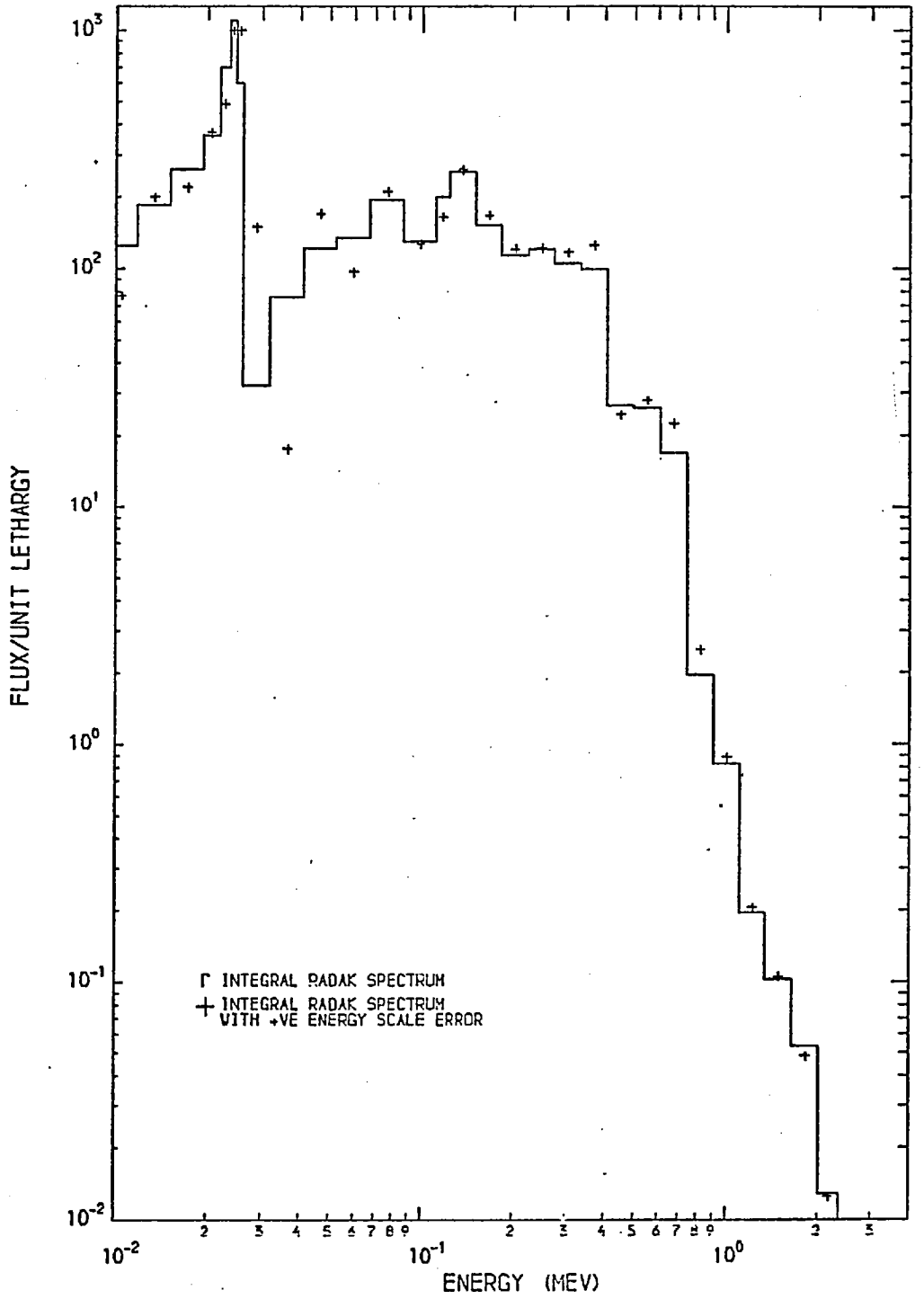


FIG. 7.12 COMPARISON OF RADAK UNFOLDED FLUX SPECTRA WITH AND WITHOUT ENERGY SCALE CALIBRATION ERRORS.

the integral method has shown the wide admissability of appropriate flux solutions which can arise even when a rigorous statistical principle, such as the requirement of a maximum likelihood solution, is used to choose the best.

7.9 Summary

In this chapter a survey has been conducted of the uncertainties and errors in the response data and the processing of the measurements into a form suitable for comparison with calculation. The status of the response functions for both integral activation detectors and neutron spectrometers have been examined and the lack of adequate data for the $In^{115}(n,n')$ reaction noted. A discussion of the energy scale calibration error and possible experimental sources have been given and an indication of a possible methods' contribution has been highlighted by the use of the RADAK code in an integral unfolding mode.

CHAPTER VIII

THE PLATO COMPUTER CODE SUITE

8.1 Introduction

The algebraic analysis of Chapters IV and V has been coded in FORTRAN-IV for use in optimising multi-group nuclear data libraries on the basis of experimental integral benchmark data. The suite of programs, called PLATO, use Perturbed Linear Adjustments To Optimise the nuclear data set; the suite can either be run under automatic control for a complete adjustment cycle (outer iteration) or be used interactively, component by component, in inner iteration mode. A flow diagram of the suite with the data requirements is displayed as Figure 8.1. In the automatic outer iteration mode, in which the structure of the suite is transparent to the user, an adjustment cycle for a problem comprising 100 energy groups and 500 experimental reaction-rates distributed over 5 measurement positions in 1 m of iron requires about one hour of CPU time and some 5.5 MB of core storage running under the MVS system on the Harwell IBM 370/198. In general this represents the minimum cost for the suite since user interaction and therefore input/output is kept to a minimum. However sufficient output is retained at the end of each component program for an automatic restart to be initiated in the event of a system break. It is estimated, however, that the time per cycle could be reduced by as much as 30% upon implementation of the following amendments:

(i) The updating of the DS_n transport code ANISN to treat mixed positive and negative sources for the adjoint calculations performed in determining the expansion coefficients for the $\delta\phi$ terms.

(ii) Programming of time-consuming subroutines in assembly or machine language.

(iii) Utilising the angular flux dump and restart facilities of the PRINCETON[155] version of the ANISN DS_n code.

In the remaining sections of this chapter attention will be concentrated on the physics and computational aspects of the suite and will follow the path of a complete adjustment cycle. General guidance will be given on the input and output requirements of the suite; detailed input for the suite and component codes with documented error exit pathways form the subject matter of the User's Manual[156]. A flow diagram of the OPTOR code, the main data management and optimisation code, is given as Figure 8.2.

8.2 Calculation of Adjoint Sources

Upon initiation of the outer iteration the routine CONTRL of the OPTOR code controls the storage of the data and the passage of control.

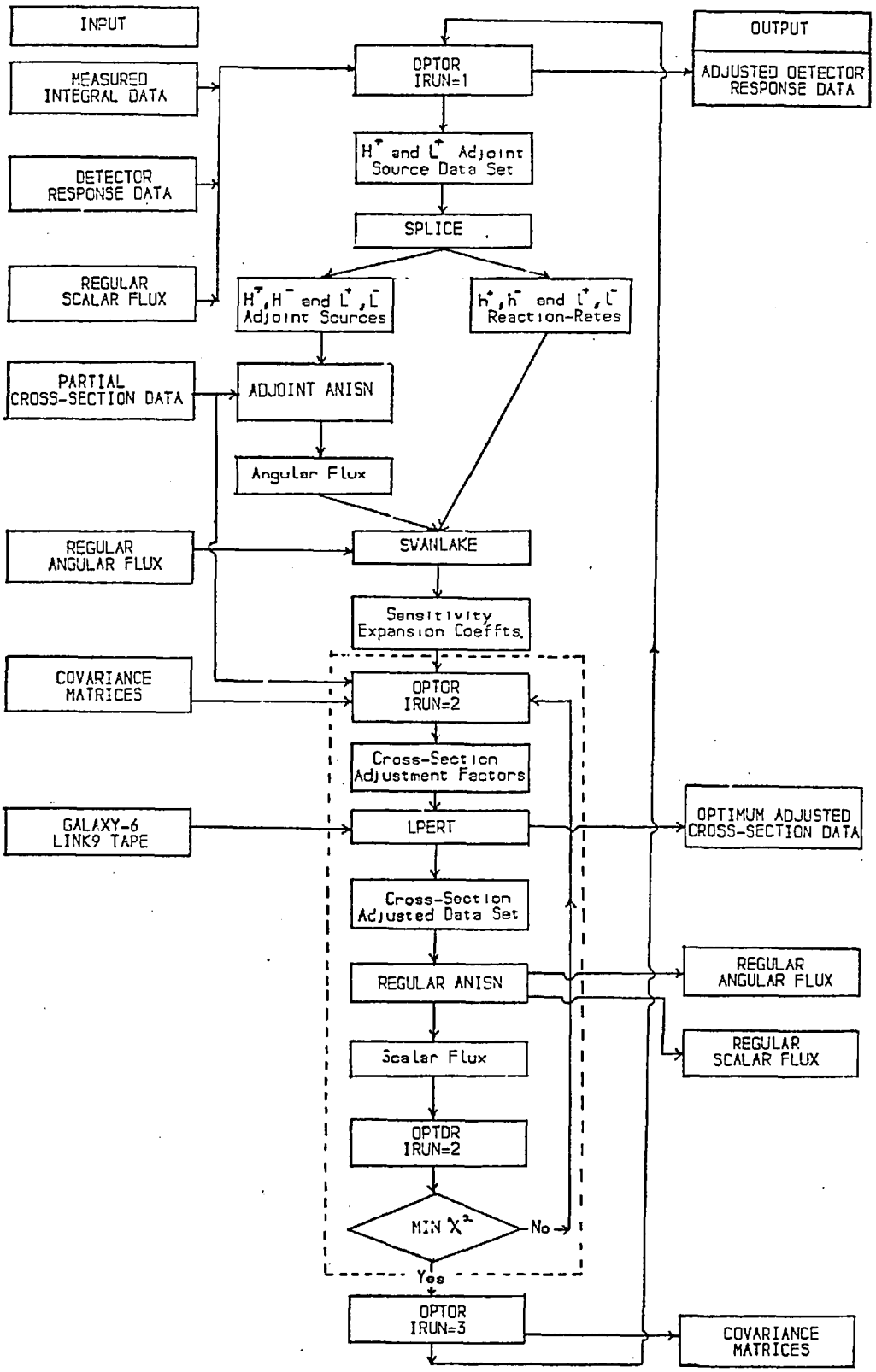


FIG. 8.1 CONTROL FLOW CHART FOR THE PLATO CODE SUITE.

OUTPUT

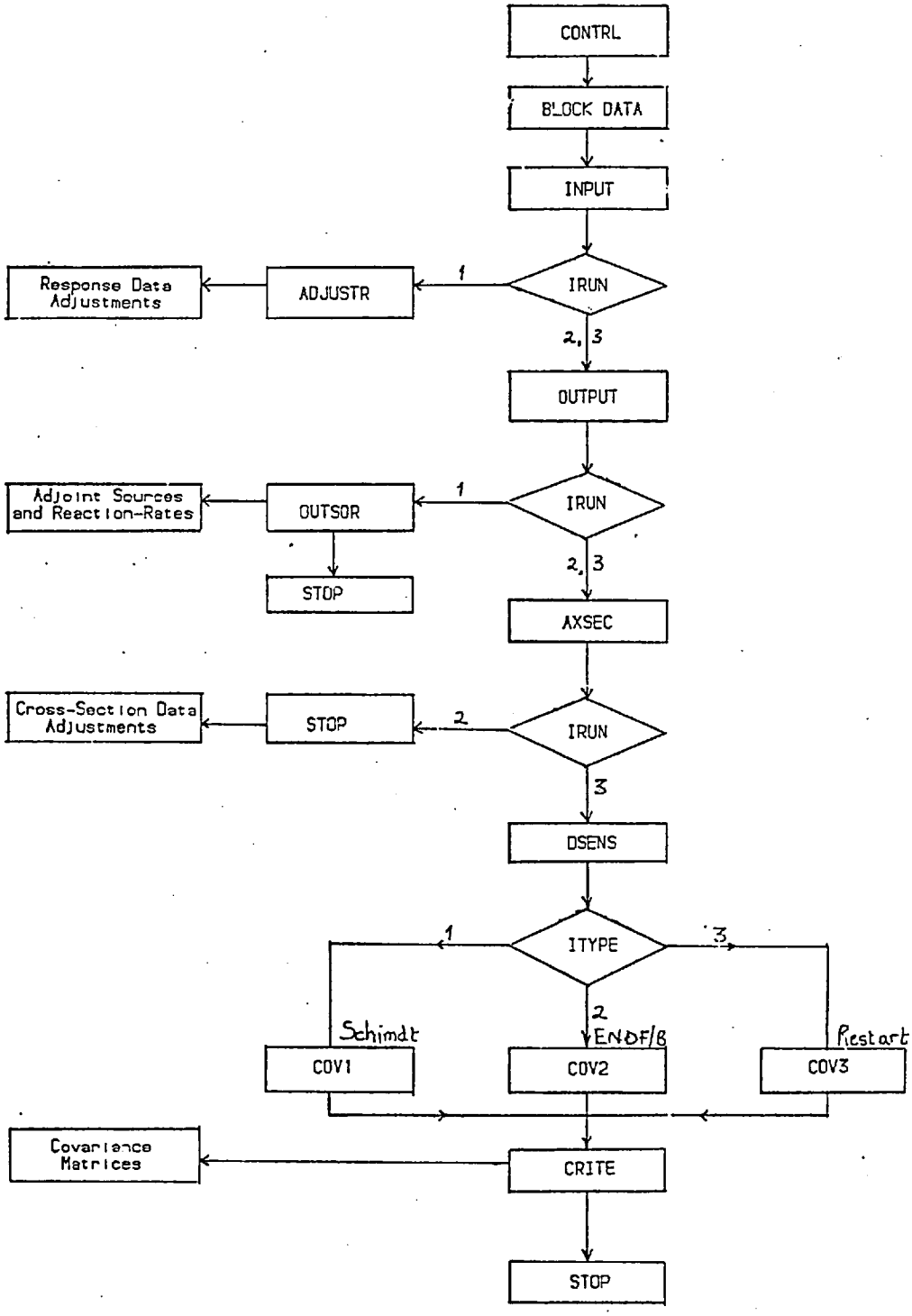


FIG. 8.2 FLOW DIAGRAM FOR THE OPTOR CODE.

All the input data is read free format into the program, each measurement position at a time, by the INPUT subroutine. The response matrix data for each position is ordered and addressed and the adjoint sources for the adjustment $\{H_j^+\}$ and variance-covariance $\{L_j^+\}$ cross-section expansion coefficients are calculated in the INCAL subprogram. The sources with their corresponding reaction-rates are formatted in FIDO format[10] using OUTSOR and passed to subsequent adjoint ANISN and SWANLAKE calculations. At present ANISN as implemented for the Winfrith Radiation Physics and Shielding Group cannot accept negative sources. For this reason four adjoint ANISN/SWANLAKE calculations have to be performed utilising the positive and absolute value of the negative components for the multi-position adjoint sources $\{H_{j,r}^+\}$ and $\{L_{j,r}^+\}$; the seperation and transfer to ANISN is achieved by the SPLICE code. The four sets of angular adjoint fluxes, output by ANISN, are stored on a scratch tape and subsequently used in SWANLAKE with the forward angular flux (given as input) to calculate the sensitivity expansion coefficients $\{U_k^{p,h}\}$. The sensitivity coefficients corresponding to the absorption, elastic and total cross-sections for each of the four adjoint sources overwrite the adjoint sources on scratch tape and control is passed back to the main program CONTRL.

8.3 Calculation of Response Data Adjustments

Prior to the calculation of the cross-section adjustment and the variance-covariance adjoint sources, the adjustments to the response data are calculated by the simultaneous solution of the matrix equations derived in Chapter IV. The adjustments are obtained directly and do not require any scaling calculations to be performed. It has been found by trial and error that the response data adjustments have always been properly conditioned in the sense of reducing χ^2 and are those values that give minimum χ^2 for that state of the optimisation cycle. In other words there is no evidence to suggest that re-cycling for the adjustments to the response data produces any change in the evaluates. For this reason a direct solution without a subsequent check on χ^2 has been implemented in the OPTOR code. The routine ADJUST, which calculates the response data adjustments, as implemented only determines adjustments to the partition factors for the detectors and the energy scale calibration error indicators. The equations for activation foil response cross-section adjustments and the source normalisation error parameter were not implemented in the routine at the time of running the calculations cited in Chapter IX. The ADJUSTR routine is coded to pass the new updated values of the response data to INCAL for use in the calculation of the adjoint sources and to

terminate the run (by setting a condition code) should values of the energy scale calibration error parameter exceed 20% of the standard deviation assumed for the proton distribution energy scale of the response matrices.

8.4 Cross-Section Adjustment

The cross-section sensitivities appropriate to the positive U_k^{p,h^+} and negative U_k^{p,h^-} components of the multi-position detector distribution are passed from the INPUT routine to AXSEC where they are combined to furnish the partial cross-section sensitivities appropriate to the $\{H_{j,r}^+\}$ adjoint source distribution:

$$U_k^{p,h} = \frac{h^+ U_k^{p,h^+} - |h^-| U_k^{p,h^-}}{h^+ - |h^-|} \qquad 8.4.1$$

where h^+ and h^- are the positive and negative components of the multi-channel detector reaction-rates respectively. These combined sensitivities are then transformed to independent cross-section sensitivities, $\Gamma_k^{p,h}$, and are used in conjunction with the independent cross-section variance-covariance data to calculate the partial cross-section adjustments. The adjustments are scaled arbitrarily by some pre-determined factor such that the parameter λ is set equal to unity for the first cycle and may be less than 1 for subsequent cycles:

$$\max(\delta x_k^r) = \lambda\sigma(x_k^p) \text{ for some p and k} \qquad 8.4.2$$

A linear search is then performed to determine the maximum value of λ for which the cycle χ^2 is a minimum. The set of routines which perform this search are those contained in the hatched box on the flow diagram for the PLATO suite. The partial cross-section adjustment factors scaled to a maximum value of one standard deviation on any group cross-section are used by the program LPERT to generate a new adjusted cross-section data set in FIDO format. To achieve this LPERT requires the GALAXY LINK9[101] output tape for the original data set in order to apply adjustment factors seperately to the inelastic and elastic cross-sections prior to the generation of the total scattering matrix used by ANISN.

A new forward transport calculation is performed using the adjusted cross-section set and χ^2 for the optimisation system is calculated. If χ^2 is reduced, a new adjusted set is determined such that:

$$\max(\delta x_k^p) = (1+R)\sigma(x_k^p) \text{ for some p and k} \qquad 8.4.3$$

for some user input resolution parameter R. For the first cycle R is set to 1 and the maximum value of λ will thus correspond to an integral number of standard deviations for some partial cross-section. In subsequent cycles R may be specified to be less than 1. The linear search is continued by increasing λ in steps of R until χ^2 starts to increase. The value of λ then that gives a minimum χ^2 can thus be determined to within $\pm$ R/2, by fitting the values of λ and χ^2. At present the Winfrith Radiation Physics and Shielding Group version of ANISN is not capable of being restarted using an angular flux guess, and although it will accept a scalar flux guess, the plethora of angular fluxes that can be derived from a single scalar flux means that little gain in computing velocity is achieved. In contradistinction the PRINCETON version of ANISN can be restarted from an angular flux dump and considering the small values of the cross-section perturbations between cycles (typically 4 - 5% maximum), much gain in efficiency can be expected, especially near the converged state where perturbations become small. The angular and scalar flux output of the optimum data set transport calculation are stored permanently on tape for the next outer iteration. The cross-section adjustments are both stored permanently and transferred back to the OPTOR code for further use.

It is worth pointing out that in the AXSEC routine for the expansion of the $\sum_j H_j^+ \delta\phi_j$ term in a set of independent cross-section perturbations, the non-elastic cross-section is assumed to exist only if the inelastic cross-section exists. Below the inelastic threshold only the absorption and total cross-sections are considered. Thus for $x^{n'} > 0$:

$$\sum_j H_j^+ \delta\phi_j = h \sum_k \Gamma_k^{A,h} \frac{\delta x_k^A}{x_k^A} + \Gamma_k^{x,h} \frac{\delta x_k^x}{x_k^x} + \Gamma_k^{T,h} \frac{\delta x_k^T}{x_k^T} \qquad 8.4.4$$

where $\{\Gamma_k^{p,h}\}$ are defined in Chapter II. However for $x^{n'} = 0$:

$$\sum_j H_j^+ \delta\phi_j = h \sum_k \Gamma_k^{A,h} \frac{\delta x_k^A}{x_k^A} + \Gamma_k^{T,h} \frac{\delta x_k^T}{x_k^T} \qquad 8.4.5$$

where $\frac{\Gamma_k^{A,h}}{x_k^A} = \frac{U_k^{A,h}}{x_k^A} - \frac{U_k^{N,h}}{x_k^N}$ and $\frac{\Gamma_k^{T,h}}{x_k^T}$ is as defined before.

8.5 The Variance-Covariance Calculation

In the final stage of the outer iteration of an adjustment cycle, the differential of the independent cross-section sensitivities and of

the adjustment multi-channel detector reaction-rate are calculated in the DSENS subroutine before control is passed to one of the three covariance routines. The subprograms, COV1, COV2 and COV3, for calculating the covariance matrices for the adjusted data set after a Schmidt-type, ENDF/B-type and cycle restart-type start respectively, have been coded seperately in order to reduce the overheads and using an overlay scheme a space saving is also obtained because only the appropriate root segment is contained in computer core at any one time. The most general routine, corresponding to the situation at the end of the second cycle when all the cross-section parameters are correlated, has a series of four nested 'DO' loops and in the present calculation the inner most loop performs 10^8 (G^4) iterations. Since decision-making processes are expensive in computer cycle time, an external decision making tree multiplexed with a series of purpose built option routines has been implemented to achieve economy[157]. The updated covariance matrices, calculated by one of the COV routines, are output to a permanent data set using CRITE which compresses the matrices and stores the data in the most compact form possible.

CHAPTER IX

THE APPLICATION OF THE PLATO ADJUSTMENT SUITE TO THE ASPIS IRON BENCHMARK

9.1 Introduction

The two tier hybrid optimisation method outlined in Chapters IV and V and implemented in the PLATO suite as the code OPTOR described in Chapter VIII has been used to adjust a multi-group iron data set derived from UKNDL DFN 908A, on the basis of the discrepancies observed between the transformed 1-D reference calculation and the measured channel reaction-rates at various penetration depths in the ASPIS iron benchmark experiment. In this chapter consideration is given to the data testing qualities of the experiment and how these compare with the sensitivity profiles derived from the multi-channel detector distribution used in the optimisation formalism. The source of cross-section error data is reviewed and the dependence of the evaluated adjustments and the corresponding covariance matrix on the initial error data is discussed. The convergence of the cross-section adjustments is examined and the final cycle adjustments are shown to be attributable to particular cross-section features. Flux profiles at four different penetration depths are constructed at different stages of the optimisation and the results of the final cycle multi-position optimisation are compared with the predictions obtained using the ENDF/B-IV library and the adjusted FD5 fast reactor data set. The differences between a single position and a multi-position treatment are assessed with a view to determining the minimum amount of measurement coverage required and to illustrating the special nature of some of the higher energy adjustments. Finally a discussion of the variance-covariance matrix appropriate to the adjusted data set is given and the implications of the error correlation matrix for uncertainty analysis are considered.

9.2 Sensitivity Profiles

The total sensitivity profiles for the sulphur, indium and rhodium activation foil reaction-rates as a function of penetration distance into the iron shield are given as Figures 9.1 to 9.3; the sensitivity profile of the multi-position multi-channel detector distribution is shown in Figure 9.4 to the total, absorption and inelastic cross-section data for iron. The regions of high sensitivity correspond to the inelastic cross-section threshold and various interference minima in the elastic cross-section. The initial multi-position, multi-channel detector distribution is plotted as Figure 9.5. From Figure 9.4 it can be seen that the data inspection range of the ASPIS experiment spans the three decades from 10 MeV down to 10 keV.

The total sensitivity of the multi-channel detector distribution H_j^+ comprising the measurement data at the 76.2 cm position to the elemental

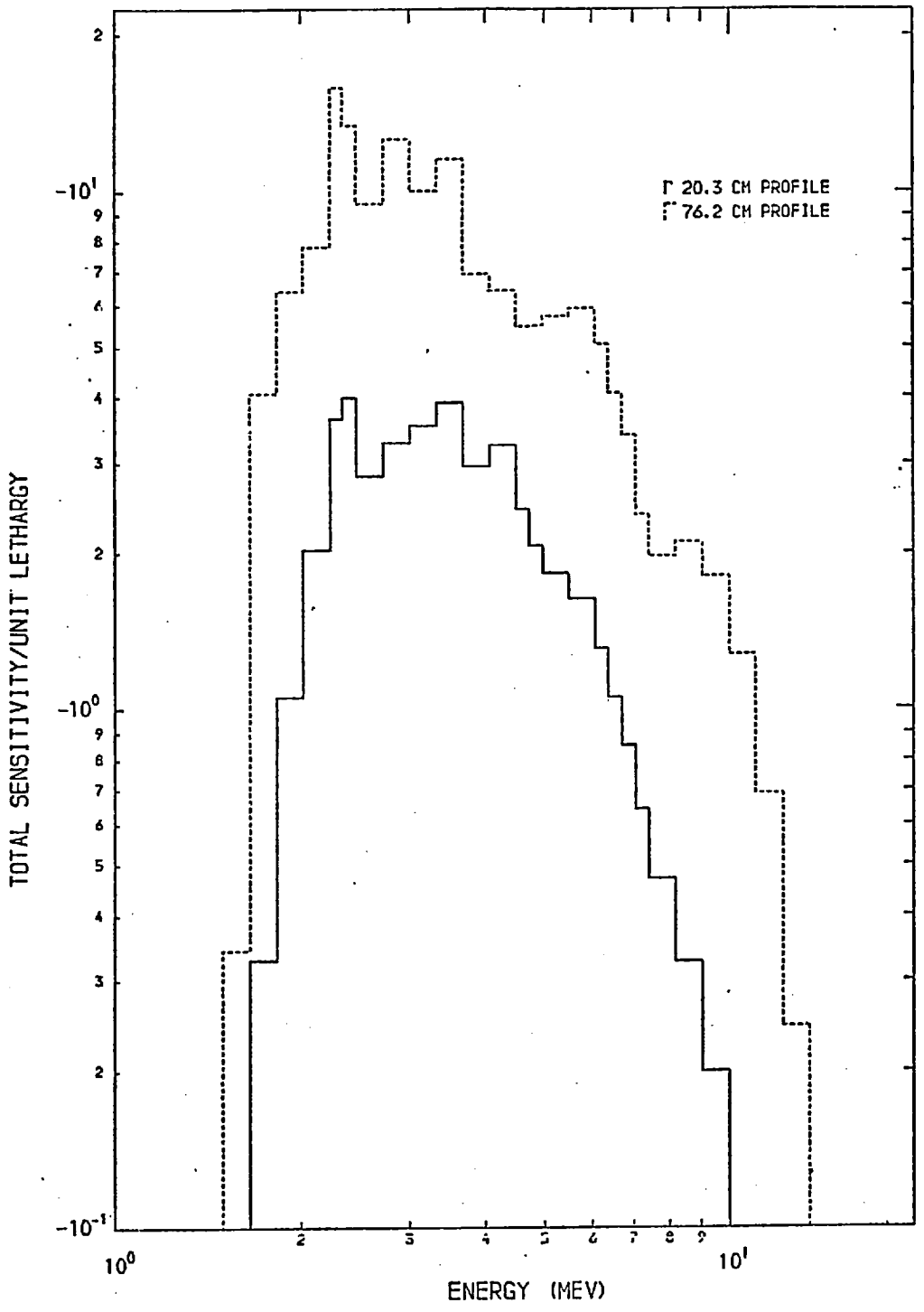


FIG. 9.1 SPATIAL DEPENDENCE OF SULPHUR (N,P) REACTION-RATE TOTAL SENSITIVITY PROFILE TO IRON CROSS-SECTION DATA.

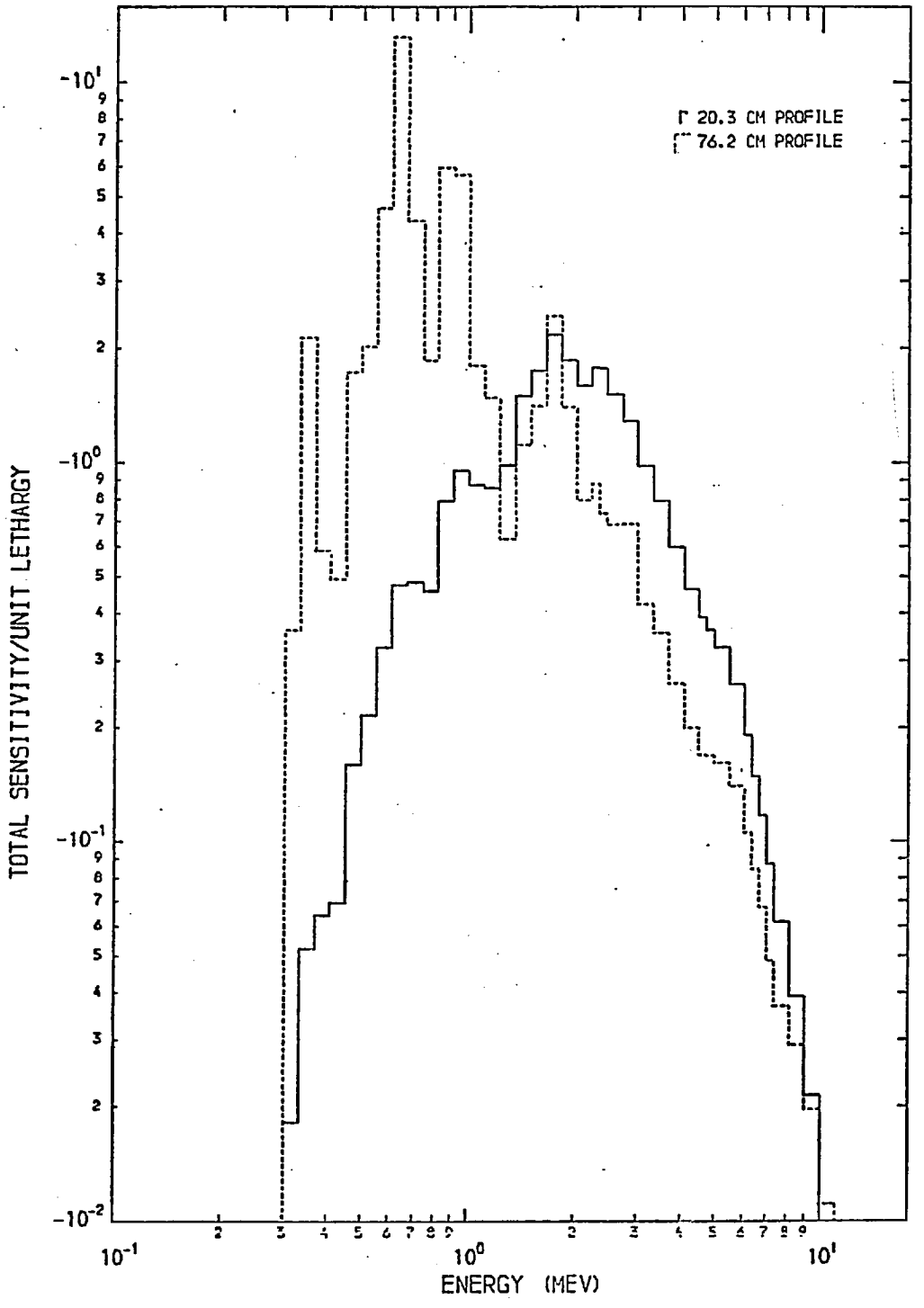


FIG. 9.2 SPATIAL DEPENDENCE OF INDIUM (N,N') REACTION-RATE TOTAL SENSITIVITY PROFILE TO IRON CROSS-SECTION DATA.

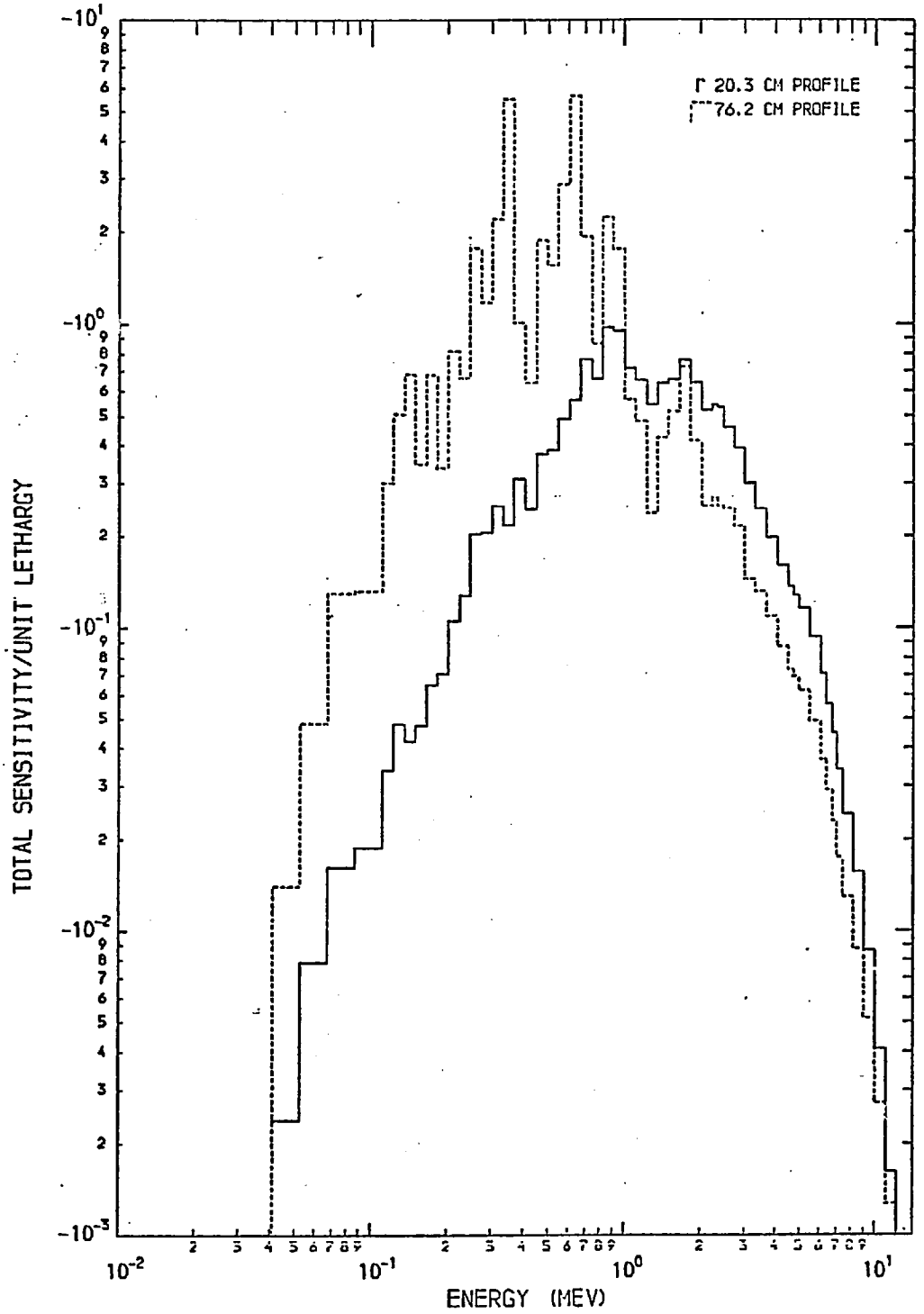


FIG. 9.3 SPATIAL DEPENDENCE OF RHODIUM (N,N') REACTION-RATE TOTAL SENSITIVITY PROFILE TO IRON CROSS-SECTION DATA.

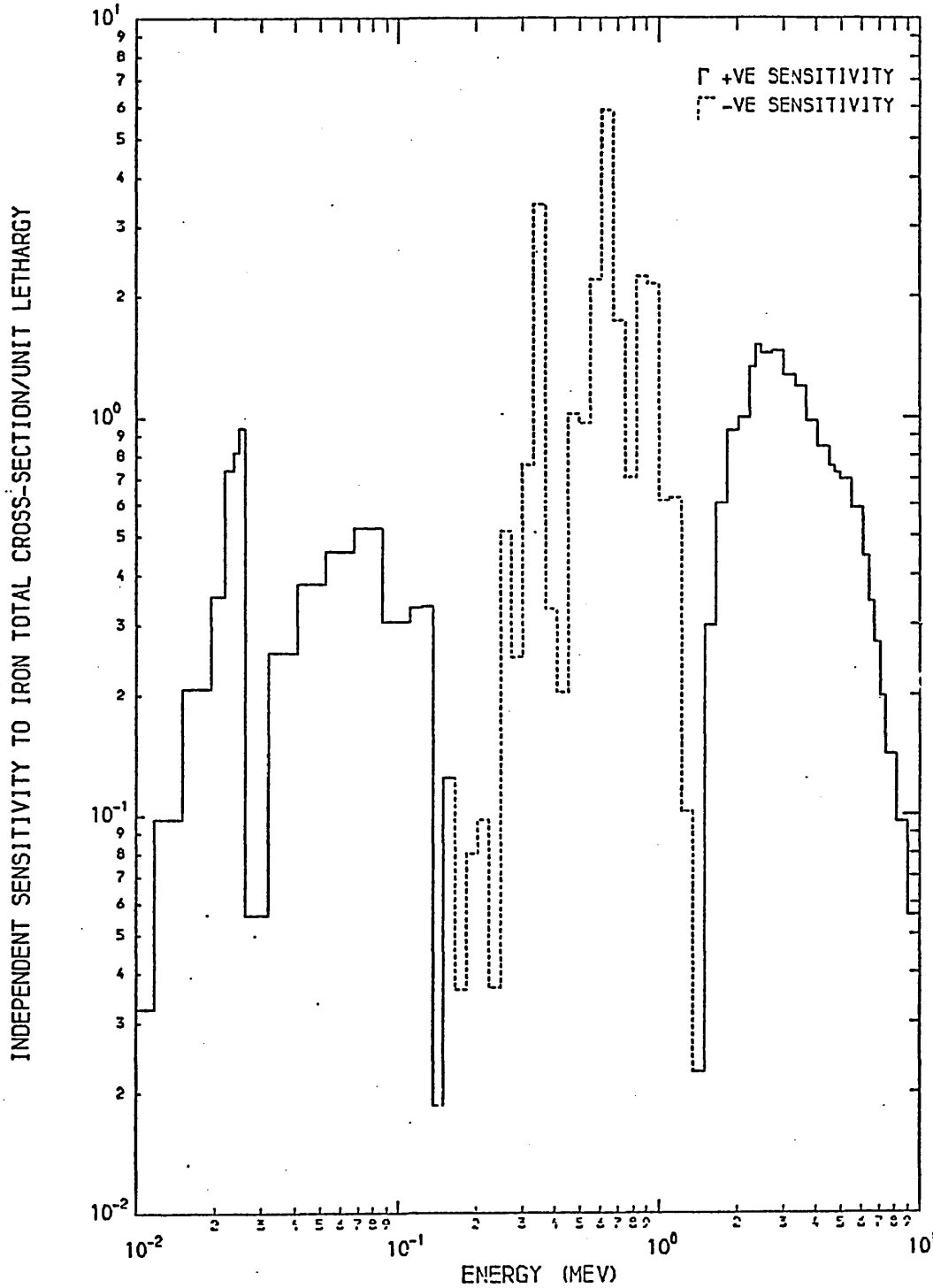


FIG. 9.4(A) SENSITIVITY PROFILE FOR MULTI-POSITION MULTI-CHANNEL DETECTOR REACTION-RATE TO IRON CROSS-SECTION DATA.

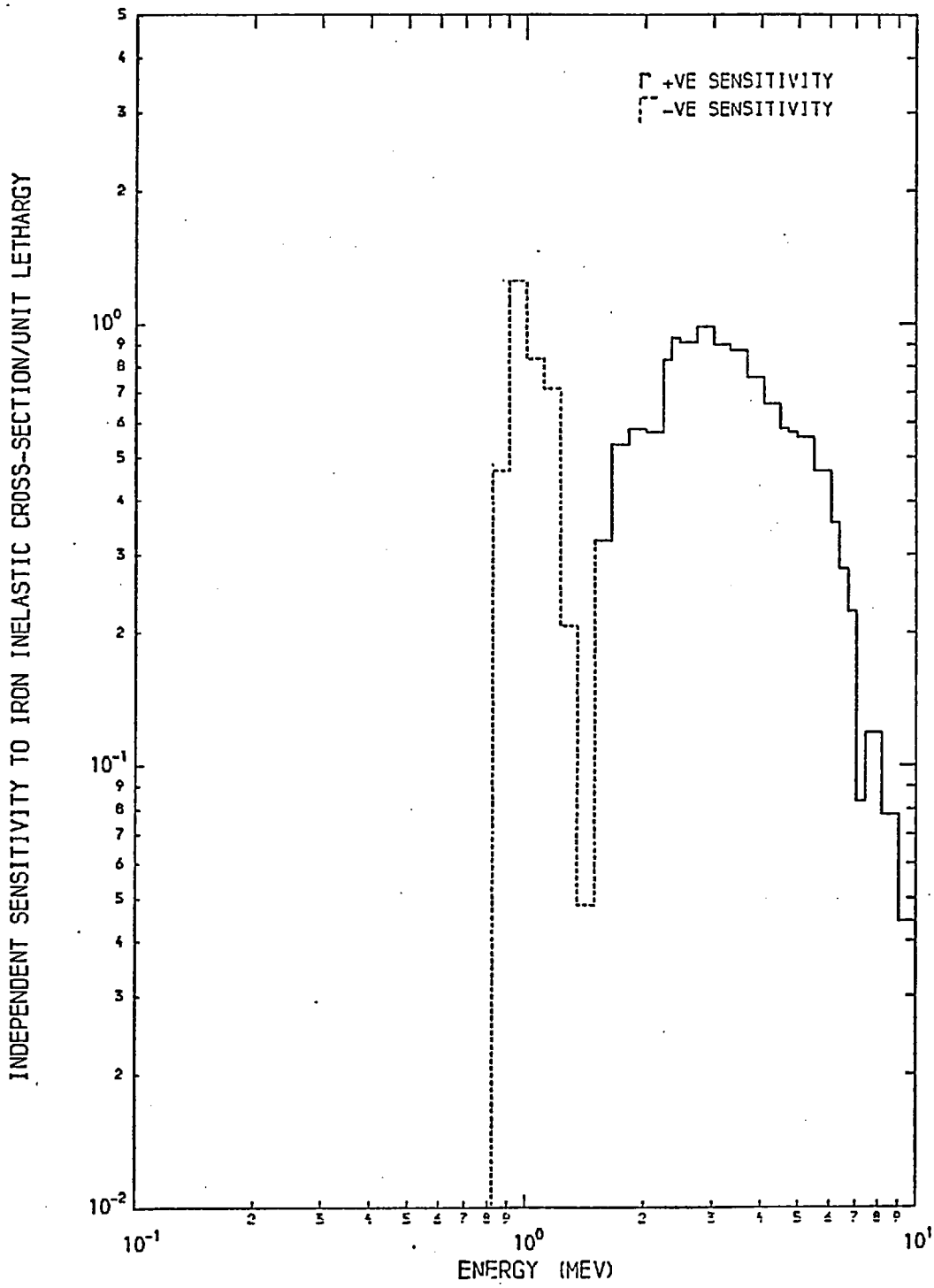


FIG. 9.4(B) SENSITIVITY PROFILE FOR MULTI-POSITION MULTI-CHANNEL DETECTOR REACTION-RATE TO IRON CROSS-SECTION DATA.

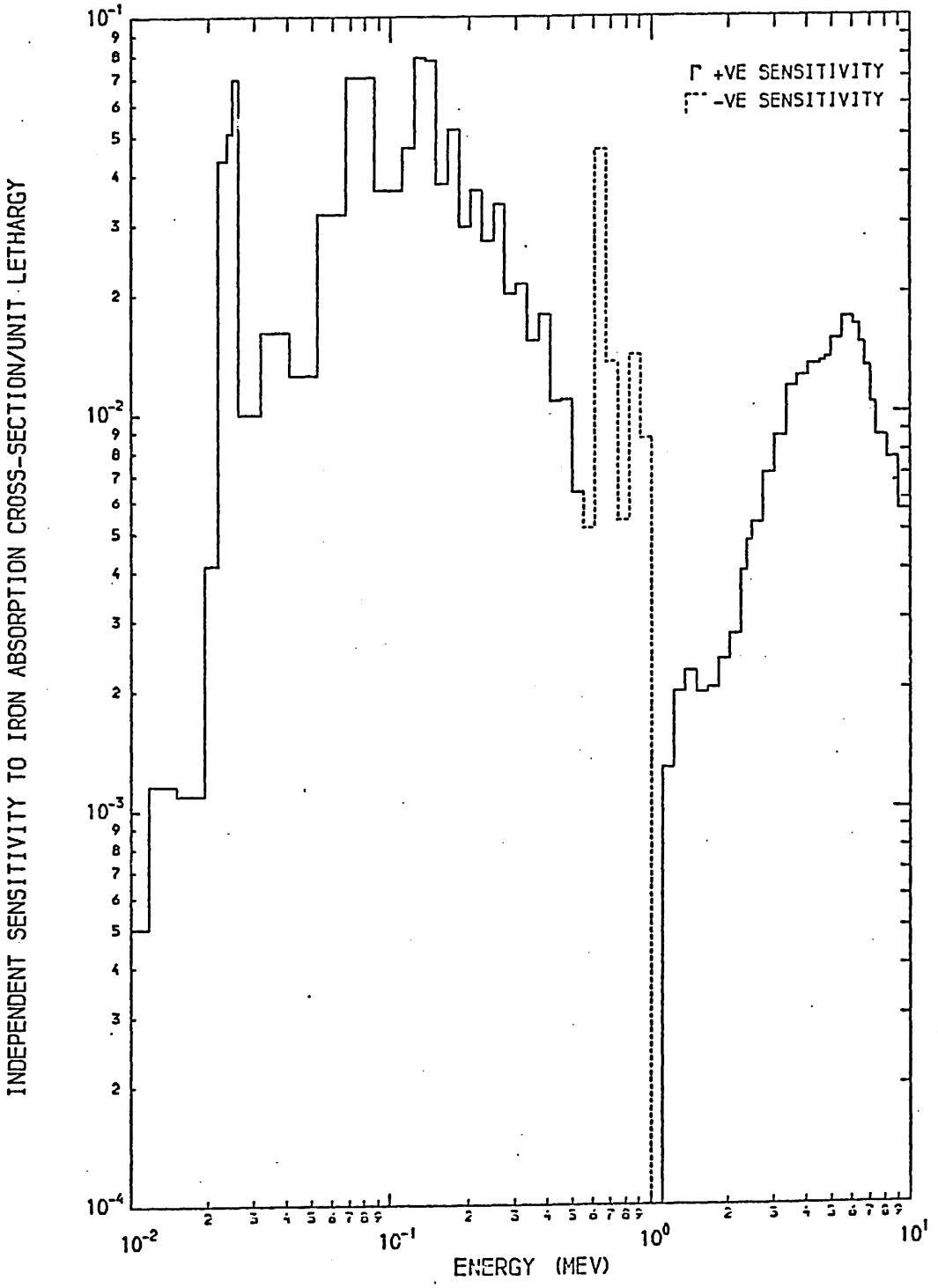


FIG. 9.4(C) SENSITIVITY PROFILE FOR MULTI-POSITION MULTI-CHANNEL DETECTOR REACTION-RATE TO IRON CROSS-SECTION DATA.

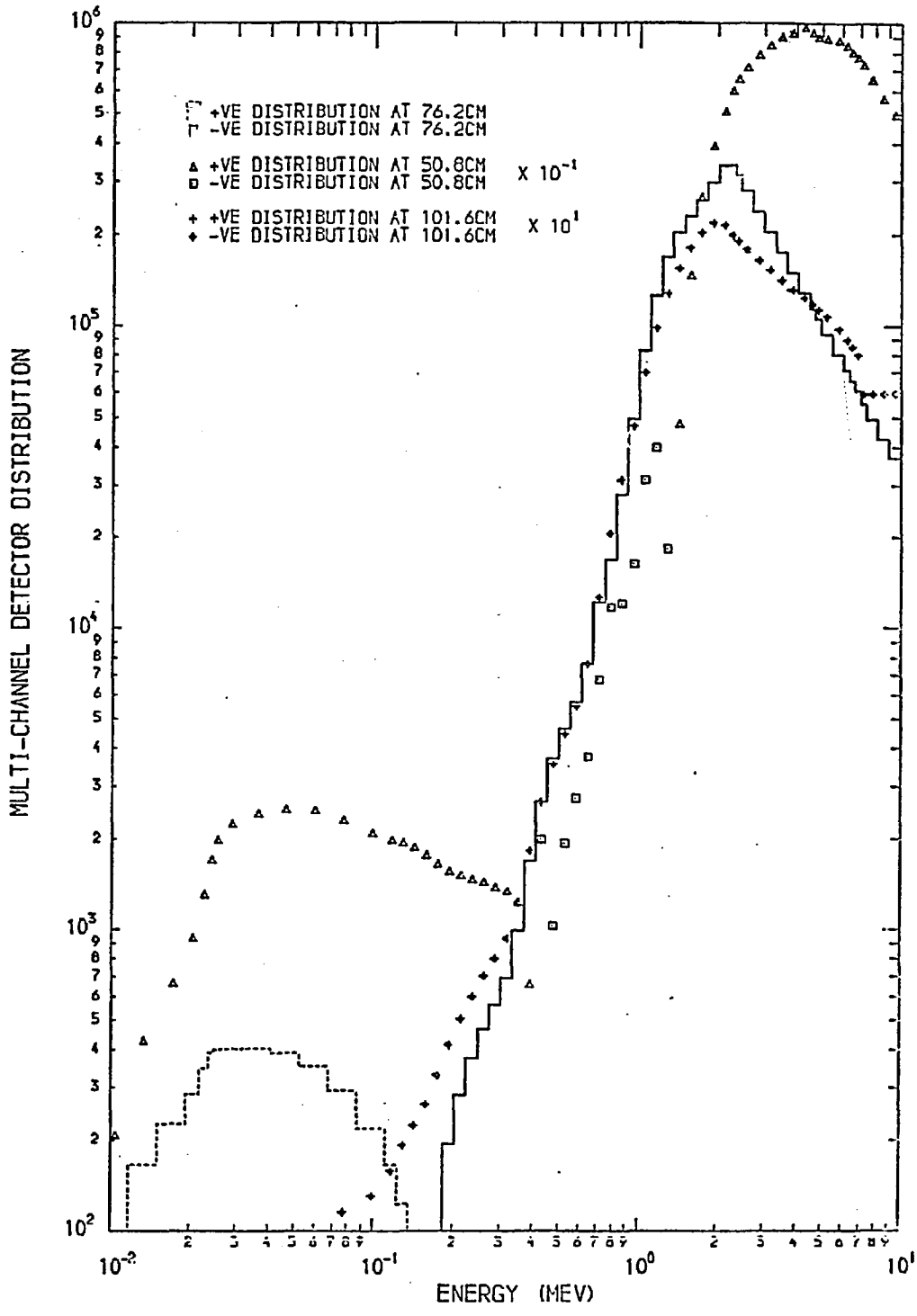


FIG. 9.5 SPATIAL DEPENDENCE OF THE INITIAL MULTI-CHANNEL DETECTOR DISTRIBUTION.

constituents of the iron shield is displayed in Table 9.1. It is seen that although iron is the dominant element, the dimensional transformation coefficients can also contribute significantly to the total sensitivity of the experiment. It is implicitly assumed in the analysis that the dimensional transformation coefficients are constant and cannot be adjusted; in reality such an assumption can only be true if the leakage distribution does not change significantly as a result of data optimisation. As the iterative optimisation scheme proceeds the observational discrepancies are reduced resulting in a change in the multi-position multi-channel detector distribution, $H^{+}_{j,r}$. The change in the multi-position multi-channel detector distribution sensitivity profile for the end of the fourth optimisation cycle as compared with the initial profile is given as Figure 9.6.

Table 9.1

Sensitivity of the Elemental Constituents of the Iron Shield to the Multi-Channel Detector Distribution at the 76.2 cm Position

Element	Total Sensitivity
Hydrogen	5.73 -2
Carbon	1.29 -1
Iron	1.85 +0
Manganese	1.20 -1
Dimensional Transformation Coeffts.	3.10 -1

The sensitivity profile of the experiment has a dual rôle. Firstly it identifies those energy regions where the cross-section data are deemed to be inadequate and are to be adjusted. Regions with low sensitivity may arise either from the fact that none of the observations are dependent upon the cross-section data in that region, or that there are no discrepancies in that region so that to within the accuracy of the extensive observations, the nuclear data is considered satisfactory. Thus energy domains with low sensitivity to the prediction of the multi-position multi-channel detector distribution reaction-rate either pass no useful comment upon the nuclear transmission parameters in that energy range or pass very useful comment upon the data, in that, since there are no observed discrepancies between calculation and high quality measurement, the data in that energy range is, as far as the experiment can detect, perfectly adequate.

The second use of the sensitivity profile for the experiment is in characterising those situations where the optimised data set would be expected to produce better predictions (in the sense of being more likely)

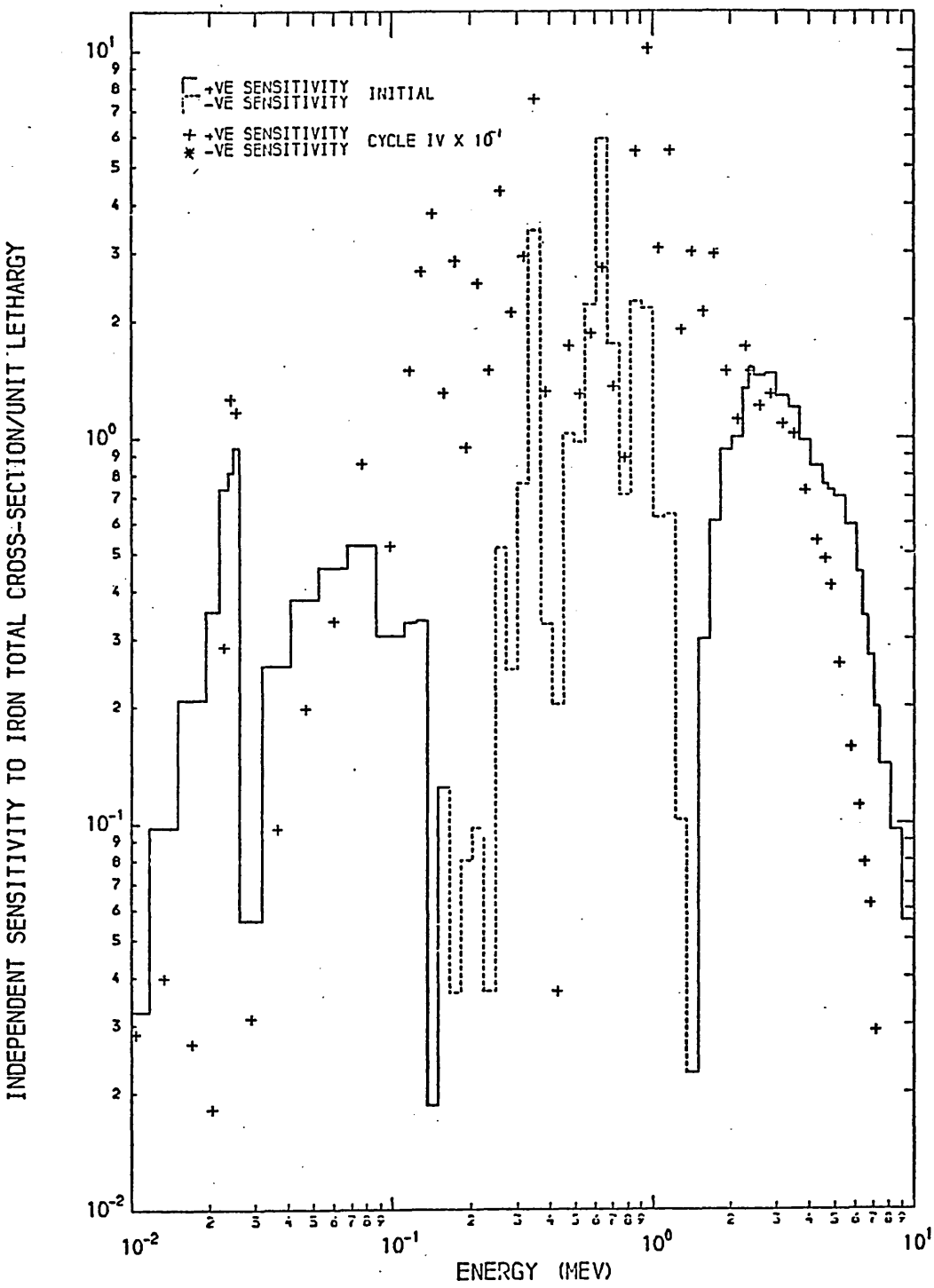


FIG. 9.6 COMPARISON OF INITIAL AND CYCLE 4 MULTI-POSITION MULTI-CHANNEL DETECTOR DISTRIBUTION SENSITIVITY PROFILES.

than the prior data. For example, if in a design study the sensitivity profile is entirely different from the benchmark profile, being largest in regions where no cross-section adjustment has been made, then the optimised data set is unlikely to produce a prediction that is much different from that of the prior data set. Such a situation would be typified by the prediction of the damage-rate in the pressure vessel of a PWR such as that specified by Hehn and Koban[49] where the important data requirements are around 7 MeV (Chapter II). In contradistinction, if, as in the case of the FBR benchmark problem, the sensitivity profile for the parameter to be predicted (e.g. damage-rate) is most sensitive in an energy region where the adjustment profile is large, then the optimised data set can be expected to provide a more likely prediction of the design parameter and its associated uncertainty. Thus the sensitivity profile for the multi-channel detector distribution is important both to the nuclear data evaluator, in that it furnishes information about where the experiment has tested the data and found it unsatisfactory and also to the designer, who may wish to test if a particular reactor shielding problem is derived from the same population of data-dependent problems as the benchmark itself.

9.3 The Data for the Optimisation Code

The adjustment of the iron data matrix has been conducted on the basis of measurements taken at five different penetration depths in the ASPIS iron benchmark. The four primary measurement positions 20.3, 50.8, 76.2 and 101.6 cm have been discussed in reference 4 and signal information was obtained for all the detectors included in Table 7.1 except that the high energy flux after about 60 cm was insufficient to provide measurable activities in the S(n,p) pellets and the In(n,n') foils and the count-rate of the NE 213 counter at the 101.6 cm position was so low that statistically significant measurements were unobtainable. The fifth measurement position at 22.8 cm represented a set of special high energy measurements made by Carter et al[171] in 1978 in an attempt to extend the informative range of the experiment to the higher energy data on which PWR pressure vessel damage-rate calculations appear to be dependent. The measurements made included the NE 213 pulse height distribution and the S(n,p), In(n,n'), Rh(n,n') and Al(n,α) reaction-rates; a higher fission source power corresponding to an enriched uranium converter plate was used to increase the high energy neutron flux and a source normalisation factor has been established to within 2.5% by Arcipiani and Chestnutt[172] for use in scaling these new measurements to a level compatible with the original

experiment. The reaction-rates from the Al(n,α) foils were inconsistent with the NE 213 pulse height distribution and with the calculation-to-measurement ratio expected from other detectors and have therefore been omitted from the optimisation. The NE 213 observations extended the flux spectrum characterisation up to 7 MeV.

The measurement standard deviations for the activation foils have been given in reference 4 and in Chapter VII. The standard errors appropriate to the elements of the grouped proton recoil data have been assessed as a combination of the statistical counting error, discussed in Chapter VII and a reproducibility factor, varying between 2 - 5%, assessed from repeated runs. The standard errors on the response parameters of the statistical model, viz. the source normalisation, the partition coefficients and the energy scale calibration for the proton recoil counters have all been assessed in Chapter VII. At this stage of testing of the hybrid optimisation philosophy, the response function data for the activation detectors have not been adjusted as the appropriate routine had not been fully implemented in the OPTOR program. This was seen as a further development and the error incurred in the evaluated transmission cross-section adjustments is considered to be negligible due to the good coverage of the proton recoil data in the sensitive regions. The effect of response function adjustment is expected to display the changes in the response data necessary for consistency with the proton recoil data (in a similar way to that performed by the RADAK unfolding code) and a reduction in the ensemble χ^2; the weight, or information content, of the activation detector reaction-rates is small compared with the spectrometer data so that no change in the predicted transmission cross-section adjustments is expected.

Table 9.2

Fractional Uncertainties on Multi-Group Iron Cross-Section Data[36]

Upper Energy Boundary (MeV)	Lower Energy Boundary (MeV)	$\frac{\sigma(x^A)}{x^A}$	$\frac{\sigma(x^x)}{x^x}$	$\frac{\sigma(x^\tau)}{x^\tau}$
1.4918 +1	2.2313 +0	0.15	0.10	0.05
2.2313 +0	9.0718 -1	0.15	0.10	0.04
9.0718 -1	8.2085 -1	0.15	0.15	0.04
8.2085 -1	4.5049 -1	0.15	-	0.04
4.5049 -1	1.5846 -3	0.15	-	0.05
1.5846 -3	1.0677 -5	0.15	-	0.03
1.0677 -5	1.0000 -10	0.04	-	0.03

Arising from the lack of any better data, the error assignments for

the transmission cross-sections have been taken from Schmidt (Table 9.2). The range error estimates have been interpreted fairly loosely as being appropriate to all the data within a neutron group (i.e. full energy-dependent correlation across the group) with each group being independent. Some idea of the possible range of the cross-section correlations at high energies is given in the covariance matrices constructed by Orphan and published in the work of Gerstl et al[38]; the Orphan matrices given for the absorption, inelastic and total cross-sections (Tables 9.3, 9.4 and 9.5) cover the energy range from 14.9 MeV to approximately 2 MeV in groups of 0.1 lethargy width. The EURLIB-100 group scheme is similarly defined by groups of 0.1 lethargy width in this region with a few exceptionally high energy resolution groups. The correlation data of Table 9.5 for the total cross-section shows that the correlation at high energies falls quite rapidly with increasing group displacement, achieving a uniform value of ~ 0.15 after about $\overset{10}{\wedge}$ groups. At lower energies the correlation is of longer range, a trait also displayed by the inelastic and absorption cross-sections. On the other hand the recent coarse 15 group ENDF/B correlation matrices, published by Drischler and Weisbin[47], indicate that in most cases the energy-dependent correlation does not extend over more than 10 to 15 EURLIB groups and may indeed have a much shorter range; a notable exception to this is the absorption cross-section where the ENDF/B evaluation displays full energy-dependent correlation over most of the range from 14.9 MeV to 1.35 MeV. As to the magnitude of the group cross-section variances, the values for the total cross-section appear to be in rough agreement if the simple assumptions of smooth cross-section energy-dependence and lethargy weighting are used to collapse to the broad group scheme; however the assignments of both workers for the inelastic cross-section are generally greater than the Schmidt values and for the absorption cross-section the estimates are substantially different over most of the energy range.

The effect of poor error data, in particular ignoring the energy-dependent correlations, has not as yet been examined but in benchmark experiments with many signal channels of high quality information the prior error data will furnish only weak constraints on the adjustments. Moreover in a cyclic optimisation scheme in which the adjustment step length is restricted for each iteration, the prior constraints will only have an effect if no large discrepancies between calculation and measurement are observed and the benchmark is being used to fine tune the data close to maximum likelihood. In the present study the maximum adjustment

	1	2	3	4	5	6	7	8	9	10	11	12	13	14	15	16	17	18	19	20	F. STD. DEV.
1	1.000	.6611	.6989	.3611	.2844	.2293	.1888	.1582	.1332	.1142	.0987	.0000	.0000	.0000	.0000	.0000	.0000	.0000	.0000	.0000	0.300E 00
2	.6611	1.000	.6133	.5544	.4400	.3593	.2990	.2536	.2166	.1873	.1640	.0000	.0000	.0000	.0000	.0000	.0000	.0000	.0000	.0000	0.300E 00
3	.6989	.6133	1.000	.7678	.6122	.5019	.4210	.3586	.3087	.2669	.2360	.0000	.0000	.0000	.0000	.0000	.0000	.0000	.0000	.0000	0.300E 00
4	.3611	.5544	.7678	1.000	.7989	.6570	.5523	.4721	.4083	.3541	.3147	.0000	.0000	.0000	.0000	.0000	.0000	.0000	.0000	.0000	0.300E 00
5	.2844	.4400	.6122	.7989	1.000	.8235	.6930	.5929	.5141	.4503	.4000	.0000	.0000	.0000	.0000	.0000	.0000	.0000	.0000	.0000	0.300E 00
6	.2293	.3593	.5019	.6570	.8235	1.000	.8427	.7351	.6275	.5492	.4887	.0000	.0000	.0000	.0000	.0000	.0000	.0000	.0000	.0000	0.292E 00
7	.1888	.2990	.4210	.5523	.6930	.8427	1.000	.8577	.7462	.6540	.5826	.0000	.0000	.0000	.0000	.0000	.0000	.0000	.0000	.0000	0.284E 00
8	.1582	.2536	.3586	.4721	.5929	.7227	.8577	1.000	.8699	.7641	.6811	.0000	.0000	.0000	.0000	.0000	.0000	.0000	.0000	.0000	0.276E 00
9	.1332	.2166	.3087	.4083	.5141	.6275	.7462	.8699	1.000	.8783	.7828	.0000	.0000	.0000	.0000	.0000	.0000	.0000	.0000	.0000	0.268E 00
10	.1142	.1873	.2669	.3541	.4503	.5492	.6540	.7641	.8783	1.000	.8868	.0000	.0000	.0000	.0000	.0000	.0000	.0000	.0000	.0000	0.260E 00
11	.0987	.1640	.2360	.3147	.4000	.4887	.5826	.6811	.7828	.8868	1.000	.0000	.0000	.0000	.0000	.0000	.0000	.0000	.0000	.0000	0.250E 00
12	.0000	.0000	.0000	.0000	.0000	.0000	.0000	.0000	.0000	.0000	.0000	1.000	.9038	.8222	.7522	.6916	.6385	.5914	.5500	.4990	0.289E 00
13	.0000	.0000	.0000	.0000	.0000	.0000	.0000	.0000	.0000	.0000	.0000	.9038	1.000	.9095	.8324	.7648	.7068	.6550	.6089	.5535	0.323E 00
14	.0000	.0000	.0000	.0000	.0000	.0000	.0000	.0000	.0000	.0000	.0000	.8222	.9095	1.000	.9148	.8410	.7773	.7207	.6706	.6088	0.354E 00
15	.0000	.0000	.0000	.0000	.0000	.0000	.0000	.0000	.0000	.0000	.0000	.7522	.8324	.9148	1.000	.9198	.8498	.7879	.7336	.6662	0.382E 00
16	.0000	.0000	.0000	.0000	.0000	.0000	.0000	.0000	.0000	.0000	.0000	.6916	.7648	.8410	.9198	1.000	.9237	.8570	.7976	.7246	0.408E 00
17	.0000	.0000	.0000	.0000	.0000	.0000	.0000	.0000	.0000	.0000	.0000	.6385	.7068	.7773	.8498	.9237	1.000	.9275	.8635	.7848	0.433E 00
18	.0000	.0000	.0000	.0000	.0000	.0000	.0000	.0000	.0000	.0000	.0000	.5914	.6550	.7207	.7879	.8570	.9275	1.000	.9389	.8460	0.456E 00
19	.0000	.0000	.0000	.0000	.0000	.0000	.0000	.0000	.0000	.0000	.0000	.5500	.6089	.6706	.7336	.7976	.8635	.9309	1.000	.9090	0.479E 00
20	.0000	.0000	.0000	.0000	.0000	.0000	.0000	.0000	.0000	.0000	.0000	.4990	.5535	.6088	.6662	.7246	.7848	.8205	.9090	1.000	0.514E 00

TABLE 9.3 CORRELATION MATRIX FOR IRON ABSORPTION CROSS-SECTION (AFTER GERSTL ET AL).

	1	2	3	4	5	6	7	8	9	10	11	12	13	14	15	16	17	18	19	20	F. STD. DEV.
1	1.000	.7536	.5669	.4273	.3229	.2421	.0000	.0000	.0000	.0000	.0000	.0000	.0000	.0000	.0000	.0000	.0000	.0000	.0000	.0000	0.250E 00
2	.7536	1.000	.7534	.5675	.4281	.3219	.0000	.0000	.0000	.0000	.0000	.0000	.0000	.0000	.0000	.0000	.0000	.0000	.0000	.0000	0.304E 00
3	.5669	.7534	1.000	.7536	.5675	.4271	.0000	.0000	.0000	.0000	.0000	.0000	.0000	.0000	.0000	.0000	.0000	.0000	.0000	.0000	0.350E 00
4	.4273	.5675	.7536	1.000	.7531	.5676	.0000	.0000	.0000	.0000	.0000	.0000	.0000	.0000	.0000	.0000	.0000	.0000	.0000	.0000	0.319E 00
5	.3229	.4281	.5675	.7531	1.000	.7541	.0000	.0000	.0000	.0000	.0000	.0000	.0000	.0000	.0000	.0000	.0000	.0000	.0000	.0000	0.285E 00
6	.2421	.3219	.4271	.5676	.7541	1.000	.0000	.0000	.0000	.0000	.0000	.0000	.0000	.0000	.0000	.0000	.0000	.0000	.0000	.0000	0.246E 00
7	.0000	.0000	.0000	.0000	.0000	.0000	1.000	.7544	.5660	.4259	.3200	.2400	.1850	.1400	.1050	.0800	.0600	.0450	.0350	.0250	0.200E 00
8	.0000	.0000	.0000	.0000	.0000	.0000	.7544	1.000	.7543	.5686	.4271	.3217	.2441	.1831	.1387	.1054	.0777	.0610	.0444	.0333	0.180E 00
9	.0000	.0000	.0000	.0000	.0000	.0000	.5660	.7543	1.000	.7532	.5692	.4301	.3226	.2403	.1834	.1391	.1012	.0759	.0569	.0443	0.158E 00
10	.0000	.0000	.0000	.0000	.0000	.0000	.4259	.5645	.7532	1.000	.7538	.5653	.4221	.3241	.2412	.1809	.1357	.1055	.0754	.0603	0.133E 00
11	.0000	.0000	.0000	.0000	.0000	.0000	.3200	.4271	.5692	.7538	1.000	.7500	.5700	.4300	.3200	.2400	.1800	.1400	.1000	.0800	0.100E 00
12	.0000	.0000	.0000	.0000	.0000	.0000	.2400	.3217	.4301	.5653	.7500	1.000	.7500	.5700	.4300	.3200	.2400	.1800	.1400	.1000	0.100E 00
13	.0000	.0000	.0000	.0000	.0000	.0000	.1850	.2441	.3226	.4221	.5700	.7500	1.000	.7500	.5700	.4300	.3200	.2400	.1800	.1400	0.100E 00
14	.0000	.0000	.0000	.0000	.0000	.0000	.1400	.1831	.2403	.3090	.4300	.5700	.7500	1.000	.7500	.5700	.4300	.3200	.2400	.1800	0.100E 00
15	.0000	.0000	.0000	.0000	.0000	.0000	.1050	.1387	.1834	.2412	.3200	.4300	.5700	.7500	1.000	.7500	.5700	.4300	.3200	.2400	0.100E 00
16	0000	.0000	.0000	.0000	.0000	.0000	.0800	.1054	.1391	.1809	.2400	.3200	.4300	.5700	.7500	1.000	.7500	.5700	.4300	.3200	0.100E 00
17	.0000	.0000	.0000	.0000	.0000	.0000	.0600	.0777	.1012	.1357	.1800	.2400	.3200	.4300	.5700	.7500	1.000	.7500	.5700	.4300	0.100E 00
18	.0000	.0000	.0000	.0000	.0000	.0000	.0450	.0610	.0759	.1055	.1400	.1800	.2400	.3200	.4300	.5700	.7500	1.000	.7500	.5700	0.100E 00
19	.0000	.0000	.0000	.0000	.0000	.0000	.0350	.0444	.0569	.0754	.1000	.1400	.1800	.2400	.3200	.4300	.5700	.7500	1.000	.7500	0.100E 00
20	.0000	.0000	.0000	.0000	.0000	.0000	.0250	.0333	.0443	.0603	.0800	.1000	.1400	.1800	.2400	.3200	.4300	.5700	.7500	1.000	0.100E 00

TABLE 9.4 CORRELATION MATRIX FOR IRON INELASTIC CROSS-SECTION (AFTER GERSTL ET AL).

	1	2	3	4	5	6	7	8	9	10	11	12	13	14	15	16	17	18	19	20	F. STD. DEV.
1	1.000	.7500	.6250	.5000	.4375	.3750	.3125	.2425	.2357	.1721	.1677	.1677	.1637	.1599	.1564	.1531	.1500	.1500	.1500	.1500	0.400E-01
2	.7500	1.000	.8125	.6250	.5625	.4375	.3750	.3032	.2946	.2294	.2236	.2236	.2182	.2132	.2085	.2041	.2000	.2000	.1500	.1500	0.400E-01
3	.6250	.8125	1.000	.8125	.6875	.5625	.5000	.4244	.3536	.2868	.2795	.2795	.2728	.2665	.2606	.2552	.2500	.2500	.2000	.2000	0.400E-01
4	.5000	.6250	.8125	1.000	.8125	.6875	.6250	.5457	.4714	.4015	.3913	.3913	.3273	.3198	.3128	.3062	.3000	.2500	.2500	.2500	0.400E-01
5	.4375	.5625	.6875	.8125	1.000	.8125	.7500	.6063	.5303	.4588	.4472	.4472	.3819	.3731	.3649	.3572	.3500	.3000	.3000	.3000	0.400E-01
6	.3750	.4375	.5625	.6875	.8125	1.000	.8750	.7276	.6482	.5735	.5031	.5031	.4910	.4264	.4170	.4082	.4000	.3500	.3500	.3500	0.400E-01
7	.3125	.3750	.5000	.6250	.7500	.8750	1.000	.8489	.7660	.6882	.6149	.5590	.5455	.4797	.4692	.4593	.4000	.4000	.4000	.3500	0.400E-01
8	.2425	.3032	.4244	.5457	.6063	.7276	.8489	1.000	.8575	.7790	.7050	.6508	.5822	.5688	.5563	.4951	.4851	.4366	.4366	.3881	0.412E-01
9	.2357	.2946	.3536	.4714	.5303	.6482	.7660	.8575	1.000	.8652	.7906	.7379	.6686	.6533	.5898	.5292	.5185	.5185	.4714	.4714	0.424E-01
10	.1721	.2294	.2868	.4015	.4588	.5735	.6882	.7790	.8652	1.000	.8721	.8208	.7509	.6848	.6697	.6088	.5965	.5506	.5047	.5047	0.436E-01
11	.1677	.2236	.2795	.3913	.4472	.5031	.6149	.7050	.7906	.8721	1.000	.9000	.8295	.7628	.7460	.6847	.6261	.6261	.5814	.5814	0.447E-01
12	.1677	.2236	.2795	.3913	.4472	.5031	.5590	.6508	.7379	.8208	.9000	1.000	.9271	.8581	.8393	.7759	.7155	.7155	.6708	.6261	0.447E-01
13	.1637	.2182	.2728	.3273	.3819	.4910	.5455	.5822	.6686	.7509	.8295	.9271	1.000	.9305	.9100	.8463	.7856	.7419	.6983	.6983	0.458E-01
14	.1599	.2132	.2665	.3198	.3731	.4264	.4797	.5688	.6533	.6848	.7628	.8581	.9305	1.000	.9336	.8704	.8528	.8102	.7675	.7249	0.469E-01
15	.1564	.2085	.2606	.3128	.3649	.4170	.4692	.5563	.5898	.6697	.7460	.8393	.9100	.9336	1.000	.9364	.9175	.8758	.8341	.7924	0.480E-01
16	.1531	.2041	.2552	.3062	.3572	.4082	.4593	.4951	.5292	.6088	.6847	.7759	.8463	.8704	.9364	1.000	.9390	.8981	.8573	.8165	0.490E-01
17	.1500	.2000	.2500	.3000	.3500	.4000	.4000	.4851	.5185	.5965	.6261	.7155	.7856	.8528	.9175	.9390	1.000	.9600	.9200	.8800	0.500E-01
18	.1500	.2000	.2500	.2500	.3000	.3500	.4000	.4366	.5185	.5506	.6261	.7155	.7419	.8102	.8758	.8981	.9600	1.000	.9600	.9200	0.500E-01
19	.1500	.1500	.2000	.2500	.3000	.3500	.4000	.4366	.4714	.5047	.5814	.6708	.6983	.7675	.8341	.8573	.9200	.9600	1.000	.9600	0.500E-01
20	.1500	.1500	.2000	.2500	.3000	.3500	.3500	.3881	.4714	.5047	.5814	.6261	.6983	.7249	.7924	.8165	.8800	.9200	.9600	1.000	0.500E-01

TABLE 9.5 CORRELATION MATRIX FOR IRON TOTAL CROSS-SECTION (AFTER GERSTL ET AL).

to any cross-section has been 4 standard deviations from the à priori value, which represents a χ^2 penalty of 16 for the independent cross-section model. The only noticeable effect expected from the inclusion of transmission cross-section error correlation data is that the range of data adjustment might be extended to areas both above and below the sensitive energy range of the experiment; such adjustments would not really be tested by the experiment and would be wholly reliant upon the adequacy of the à priori correlation data.

In the cyclic optimisation scheme, after the first cycle, the updated variance-covariance matrices have mathematical correlations injected from the adjustment procedure. If the à priori evaluated energy-dependent correlations were small, then for large cross-section adjustments the injected group correlation may dominate the original correlation so that after the first cycle or so the predicted adjustments become progressively less dependent upon the assumed correlation data and more dependent upon the injected consistent errors. Such a situation is apparent around the inelastic threshold where a large positive energy-dependent correlation is injected after the first adjustment cycle.

9.4 The Transmission Cross-Section Adjustments

In the present work only four outer iterations of the multi-position adjustment procedure have been performed. The adjustments to the DFN 908A multi-group data set obtained at the end of the fourth cycle for the total, absorption, inelastic and elastic (derived) cross-sections are shown in Figure 9.7. The results show that a 25% reduction in the inelastic scattering cross-section is required around the threshold; at higher energies the predicted inelastic adjustments are less negative and above 1.5 MeV an increase of between 10 and 15% is sought for most groups up to 6 MeV, falling to 5% at this energy and decaying to zero at about 11 MeV. For the elastic cross-section, a reciprocal behaviour is observed in that above 1.5 MeV a small (up to 5%) reduction in elastic scattering cross-section is indicated. Between 1.0 and 1.5 MeV a small compensatory increase in elastic cross-section is predicted and below 1 MeV a small reduction is required. No significant adjustments are made to the high energy absorption cross-section and the changes predicted for the total cross-section result largely from a sympathetic behaviour to the inelastic cross-section, but are less than one standard deviation except for the region covering the inelastic threshold.

Below the inelastic threshold, the total cross-section is dominated by elastic processes. Large adjustments to the total cross-section are

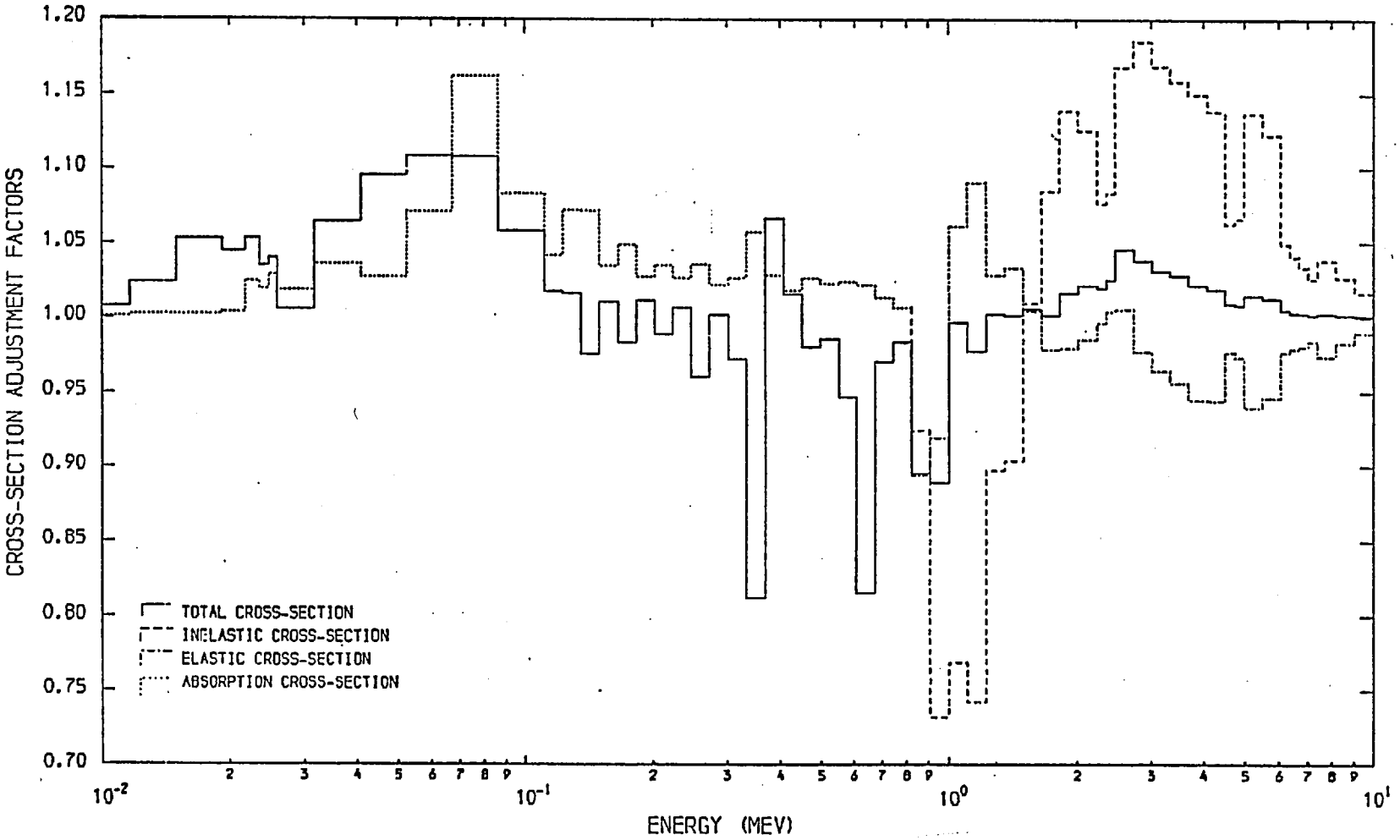


FIG. 9.7 PARTIAL CROSS-SECTION ADJUSTMENT FACTORS AT END OF CYCLE IV.

predicted for the interference minima above 600 keV and around 340 keV, with reductions of over 4 standard deviations being required. A 10% increase in cross-section in the region from 40 to 86 keV is also predicted although the large 27 keV resonance appears to be adequately described. For the absorption cross-section below the inelastic cross-section a small increase ($2\frac{1}{2}$ - 5%) is required except in the neighbourhood of the 80 keV resonance where a 15% (1σ) increase is predicted. No adjustments are made above 11 MeV or below 9 keV. The adjustment profiles after cycle 4 for the inelastic and total group interaction constants are compared with the structure of the multi-group $1/E\,\Sigma^{T}(E)$ averaged cross-sections for the respective processes in Figure 9.8.

In Figure 9.9 the build up of the adjustments as a function of iterative cycle for the inelastic and total cross-sections is explored. The adjustment process can be seen to be converging with iteration. In the case of the inelastic cross-section, over half the predicted adjustments are obtained after the first cycle. This is consistent with the cycle step length or scaling parameter λ predicted from the linear search routine in PLATO, which is given as a function of cycle number in Table 9.6. In contradistinction, the adjustments to the total cross-section in the proximity of the 340 keV and 600 keV minima are almost fully predicted after the first cycle, whereas the adjustments to the total cross-section in the 40 to 80 keV region require 3 cycles before achieving convergence. Table 9.6 also shows the fractional reduction from the initial χ^2 per measurement degree of freedom, which includes the effect of adjustments to the source power normalisation and the detector partition coefficients.

Table 9.6

Linear Search Scaling Parameter λ and the Fractional Reduction in χ^2 as a Function of Outer Iteration for the Multi-Position Optimisation

Cycle No.	λ	% Reduction in χ^2	
1	16% ($4\sigma(x_T^T)$)	35.2	
2	8% ($2\sigma(x_T^T)$)	64.5	$(46.1)^+$
3	4% ($1\sigma(x_T^T)$)	70.3	$(68.5)^+$
4	4% ($1\sigma(x^T)$)	77.7	$(72.7)^+$

+ Effect arising from transmission cross-section adjustment only.

In Figure 9.10 the adjustments to the total and inelastic cross-section derived after two cycles of a single position (76.2 cm) multi-channel detector distribution are shown. Trends similar to those of the

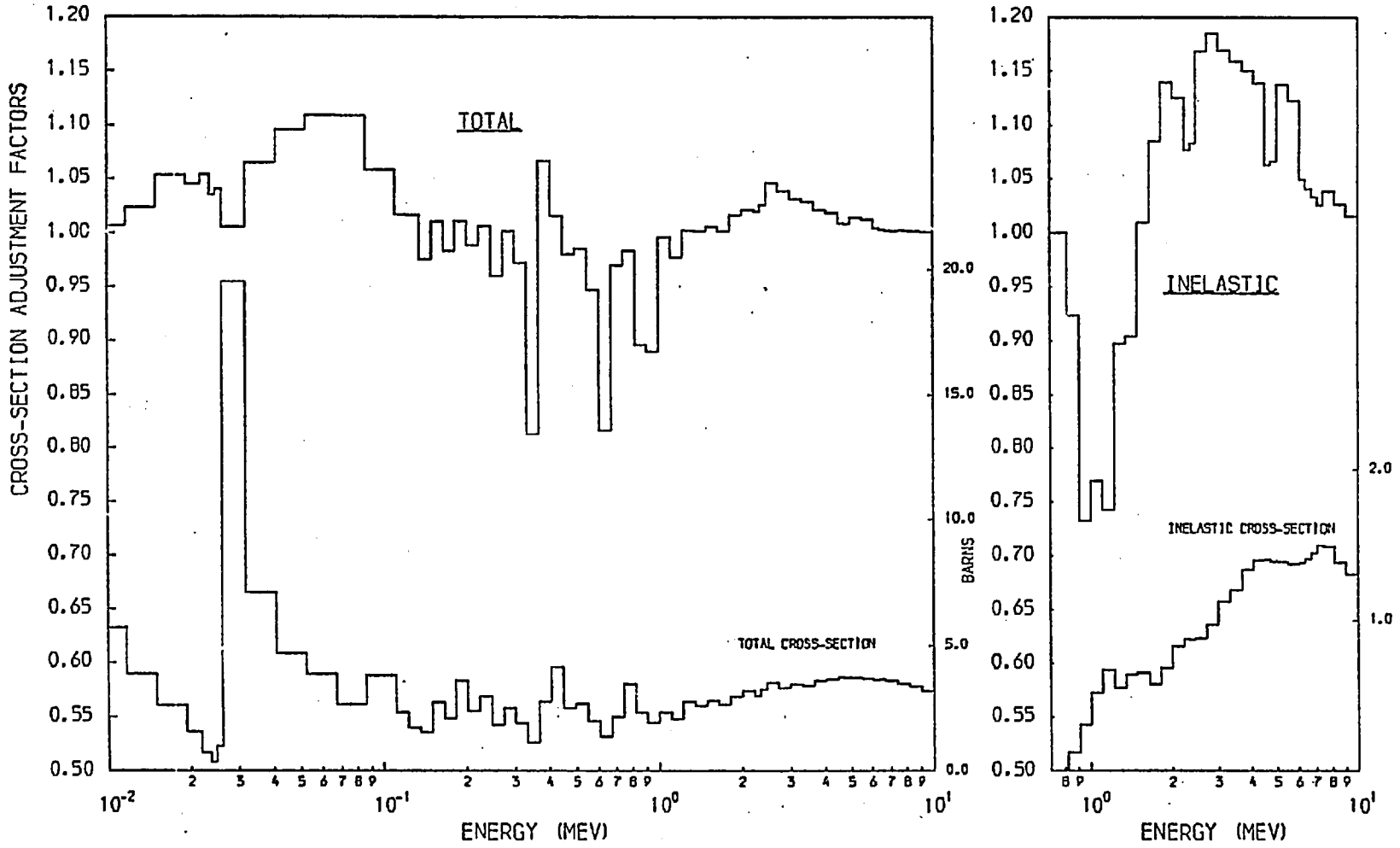


FIG. 9.8 COMPARISION OF CROSS-SECTION ADJUSTMENTS WITH MULTI-GROUP CROSS-SECTION PROFILE.

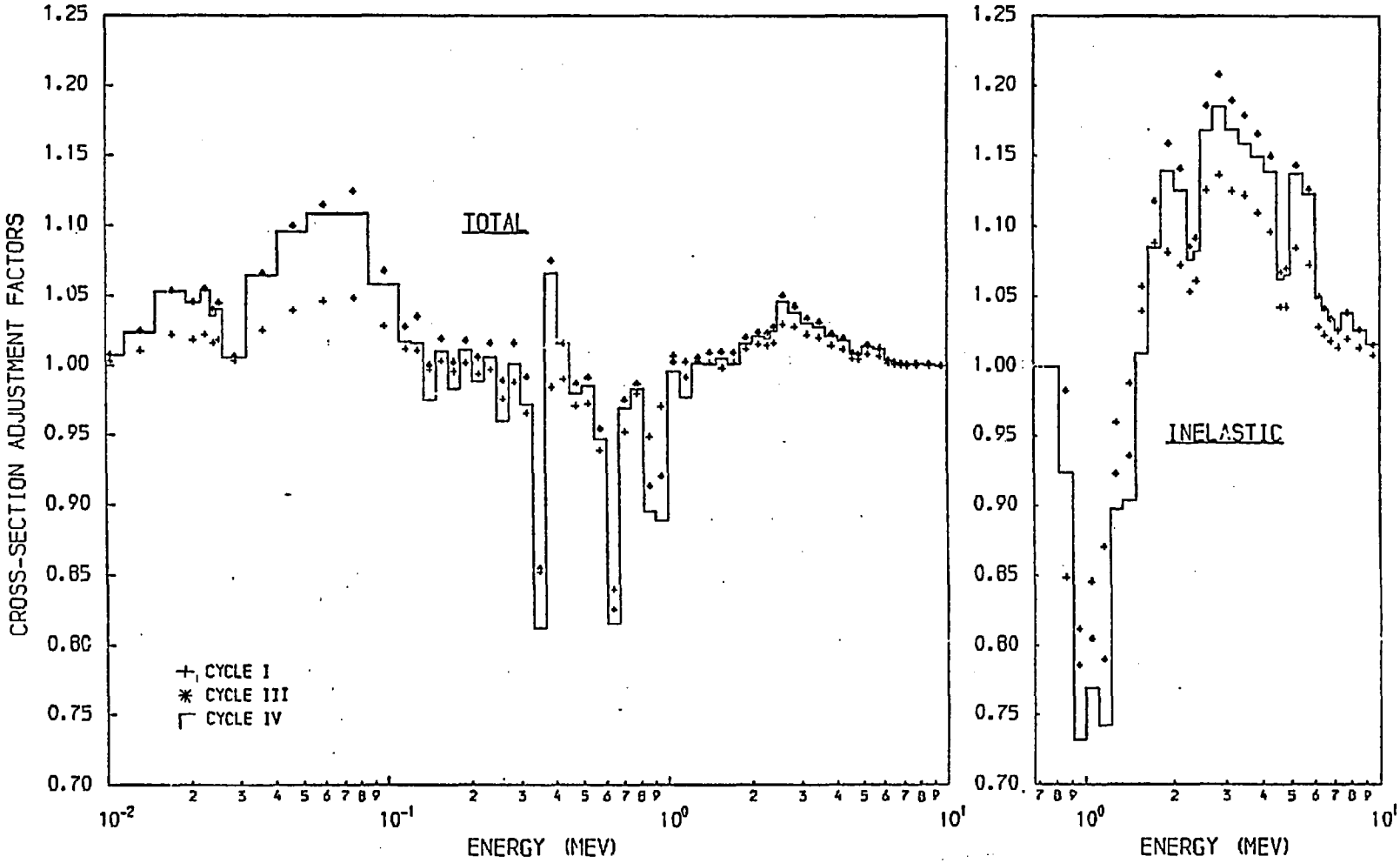


FIG. 9.9 CONVERGENCE OF CROSS-SECTION ADJUSTMENTS AS A FUNCTION OF CYCLIC ITERATION.

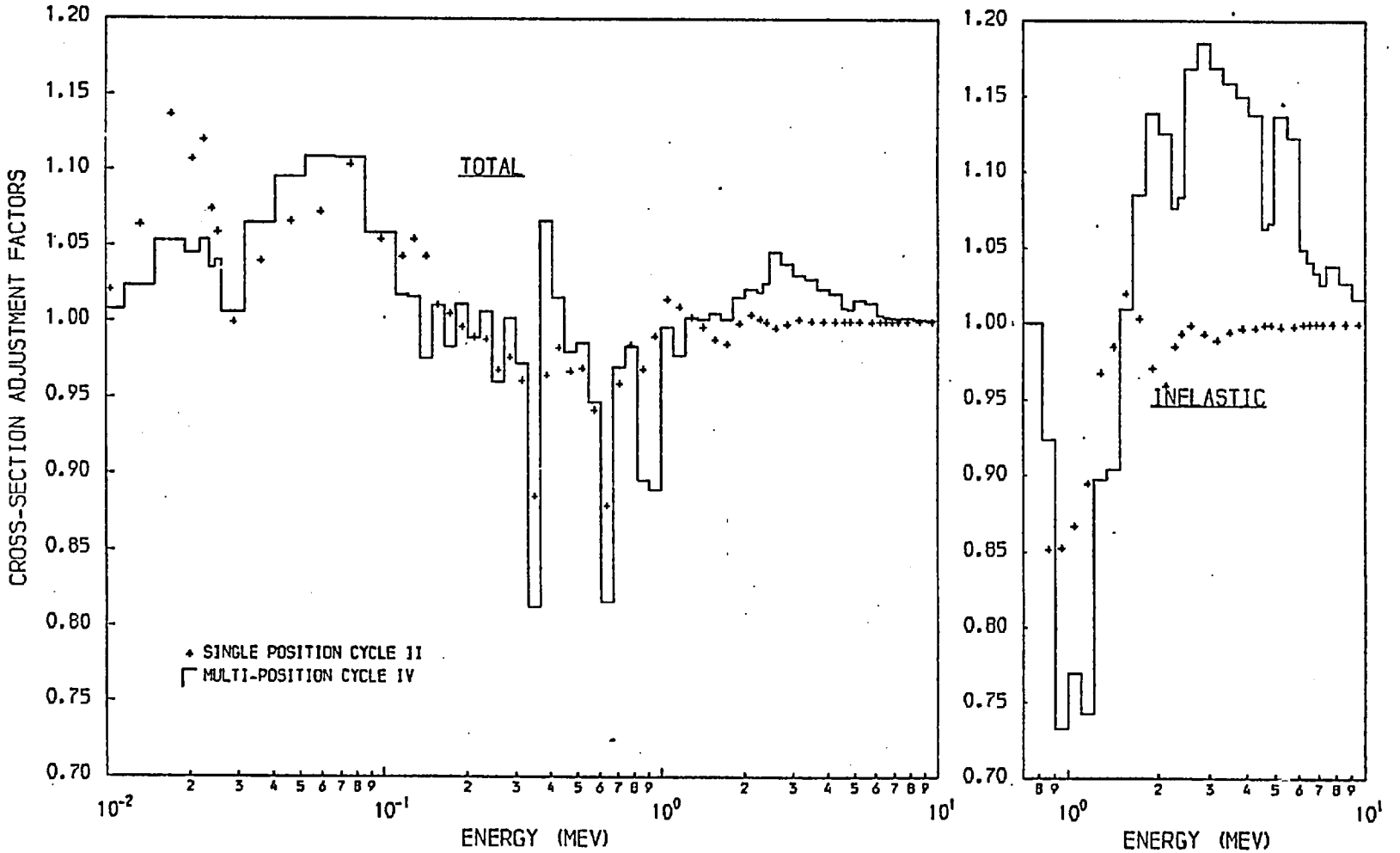


FIG. 9.10 COMPARISON OF SINGLE POSITION AND MULTI-POSITION CROSS-SECTION ADJUSTMENT PROFILES.

multi-position multi-channel detector distribution are found, though there are insufficient high energy observations (mostly obtained from the 22.8 cm measurements) to predict adjustments above ~ 2 MeV. The difference in magnitude for the adjustments around the inelastic threshold may derive from the rather large uncertainties on the high energy observations at 76.2 cm. The rather large change between 10 and 20 keV in the total cross-section is of unknown origin. The fractional reduction in χ^2 per iteration for the single position optimisation is given in Table 9.7.

Table 9.7

Fractional Reduction in χ^2 as a Function of Outer Iteration for the Single Position (76.2 cm) Optimisation

Cycle No.	% Reduction in χ^2
1	86.9 (59.8)
2	91.8
3	94.7

9.5 Adjustments to the Detector Response Data

The adjustment of the partition coefficients for the detectors on the basis of the multi-position data can be thought of as a renormalisation of the body of the observed data. The optimised partition coefficient data at the end of the fourth cycle are given in Table 9.8 and are compared with the multi-position predictions of the RADAK code used in both integral and differential mode. Although RADAK cannot check the absolute normalisation of the detector response surfaces, it can inspect, at least in the middle energy range, the mutual consistency of the partition coefficients, arising from the overlap of the counter sensitivity domains. The evidence of Table 9.8 implies that the partition coefficients for all the counters except the gain change counters are consistent with the ascribed standard deviations. The hydrogen gas chambers at high gain are physically the same as the normal 1 and $\frac{1}{2}$ at. counters; thus the difference in the partition coefficients would appear to arise from the gain change of the main amplifier.

The multi-position optimisation process, however, can not only test the mutual consistency of the partition coefficient values, it can also choose the most likely magnitude of the response surface normalisation which is consistent with the statistical model. The poor data of Table 9.8 arises from the fact that in attempting to remove the observed calculation-to-measurement discrepancies, the calculation in many areas is being

Table 9.8

The Adjustments to the Detector Response Parameters

Counter Type	Partition Coefficient α_q					Energy Scale Calibration Parameter g_q after cycle 1
	Initial	Multi-Position Cycle 4	RADAK		Single Position Cycle 3	
			Diff.	Int.		
Ar/H	0.83	0.83	0.84	0.84	0.82	-7.8 -5
10 at.	1.00	0.86	0.99	1.04	1.02	8.4 -3
3 at.	1.00	0.86	1.04	1.04	1.01	-2.8 -3
1 at.	1.00	0.84	0.96	0.93	0.98	-1.6 -4
½ at.	1.00	0.92	0.98	0.98	1.02	-1.0 -3
1 at. (h.g.)	1.00	0.77	1.02	0.89	0.89	-1.8 -3
½ at. (h.g.)	1.00	0.74	0.93	0.80	0.79	6.8 -4
NE 213	1.00	0.90	0.84	0.83	1.13	-5.3 -4

The values for the integral activation detectors are not quoted because the requisite routine in ADJUSTR had not been coded and tested at the time when this study started.

increased due to reductions in the transmission cross-section data, and the measurements are being reduced by modification of the partition coefficients. At this stage in the testing of the two tier hybrid optimisation philosophy, the source normalisation adjustment evaluator was not free to be adjusted ($\sigma(S) = 0$) and it seems probable that some of the partition coefficient adjustments would be absorbed by a reduction of the source normalisation by some 15%. However both of these adjustments are attempts by the optimisation scheme to ascribe the discrepancies arising from poor transmission cross-section data to the uncertainties in the detector response data. This shift in emphasis of the scheme arises from the use of linear perturbation theory and the consequent requirement of an iterative adjustment scheme. It is recommended therefore in future that the cross-section data should be adjusted iteratively over a number of cycles with fixed detector data until a genuine minimum of χ^2 is found; only then should the fine tuning of the hypothesised parameter set with interplay between the transmission and detector data be allowed. If this scheme is followed the adjustments predicted for the cross-section data will be somewhat larger than those obtained at the end of the fourth cycle. Also contained in Table 9.8 are the end of cycle 3 single position (76.2 cm) optimisation adjusted partition coefficients; this set appears to be in much closer agreement with the integral RADAK values for all counters except the NE 213. The increase in the NE 213 counter partition coefficient on the basis of the 76.2 cm data alone is, however, in accord with the requirements of the prior C/M ratio for the data as will be illustrated in a later section.

Table 9.8 also shows the likelihood evaluates at the end of the first adjustment cycle for the energy scale calibration error parameter. There is no evidence to suggest the existence of an energy scale error and all the counter values satisfy the requirements of the model specified in Chapter IV.

9.6 Comparison of Calculated Flux Profile with Unfolded Measurement Spectrum

The discrepancies between the measured unfolded flux derived from the counting distributions using RADAK and the original reference calculation transformed to 1-D are shown in Figures 9.11 to 9.14 for the measurement positions representing penetrations of 20.3, 50.8, 76.2 and 101.6 cm respectively. Also shown are the flux profiles predicted by the cycle 4 multi-position adjusted data set. At the 50.8 cm position, the flux above 1.5 MeV is slightly over-predicted by the DFN 908A data set,

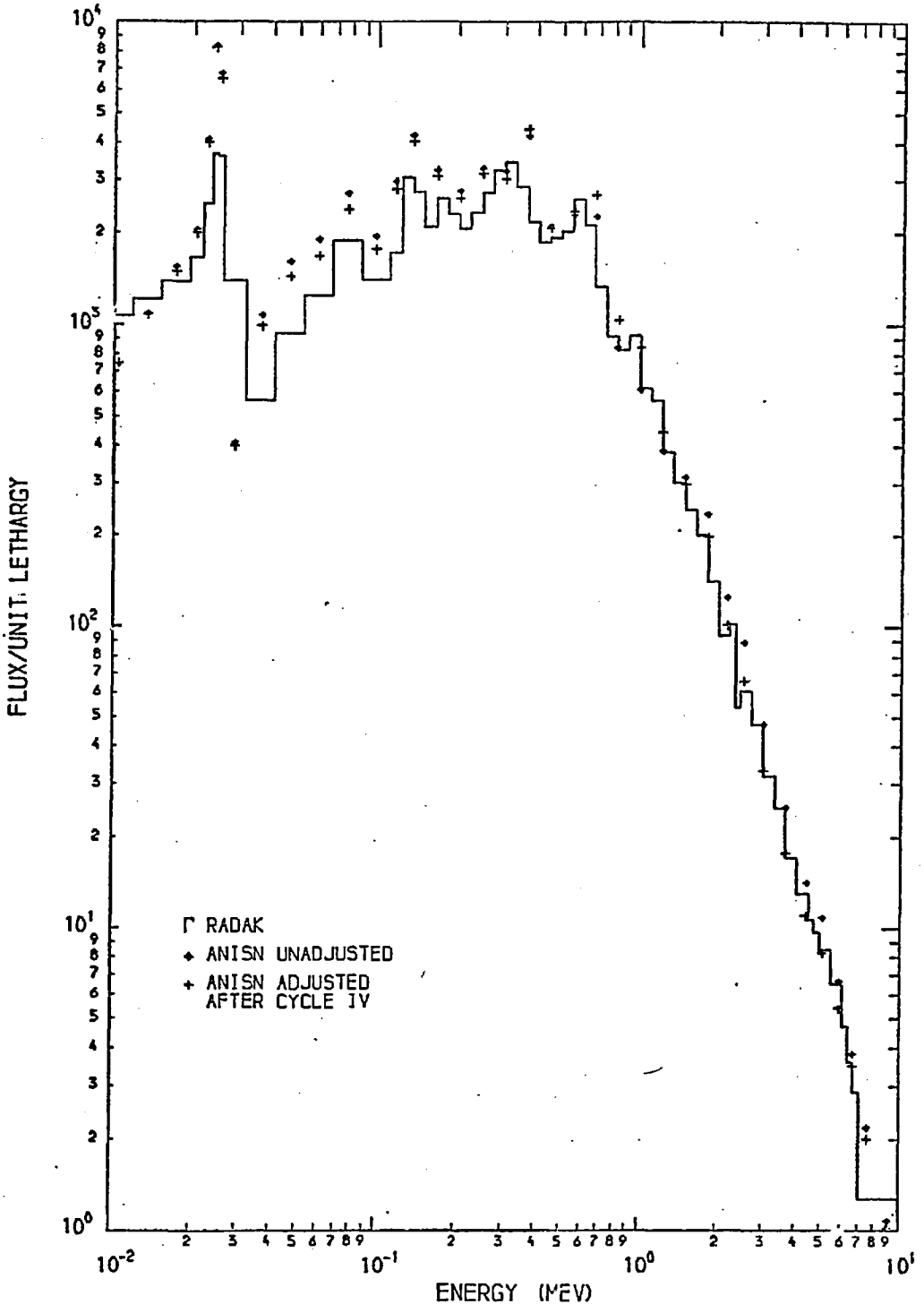


FIG. 9.11 COMPARISON OF CALCULATED FLUX PROFILES WITH RADAK UNFOLDED SPECTRUM MEASUREMENT AT 20.3CM POSITION.

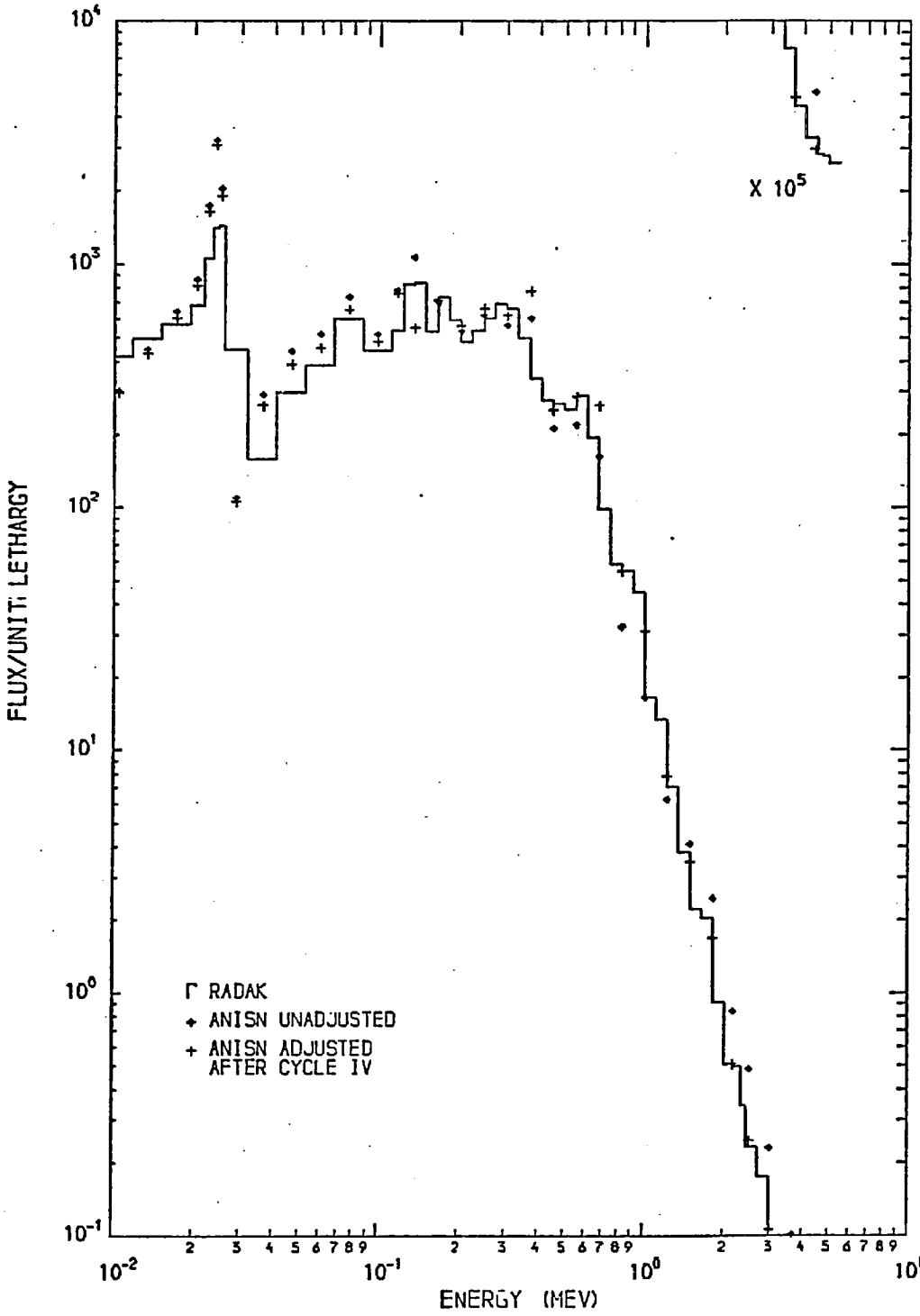


FIG. 9.12 COMPARISON OF CALCULATED FLUX PROFILES WITH RADAK UNFOLDED SPECTRUM MEASUREMENT AT 50.8CM POSITION.

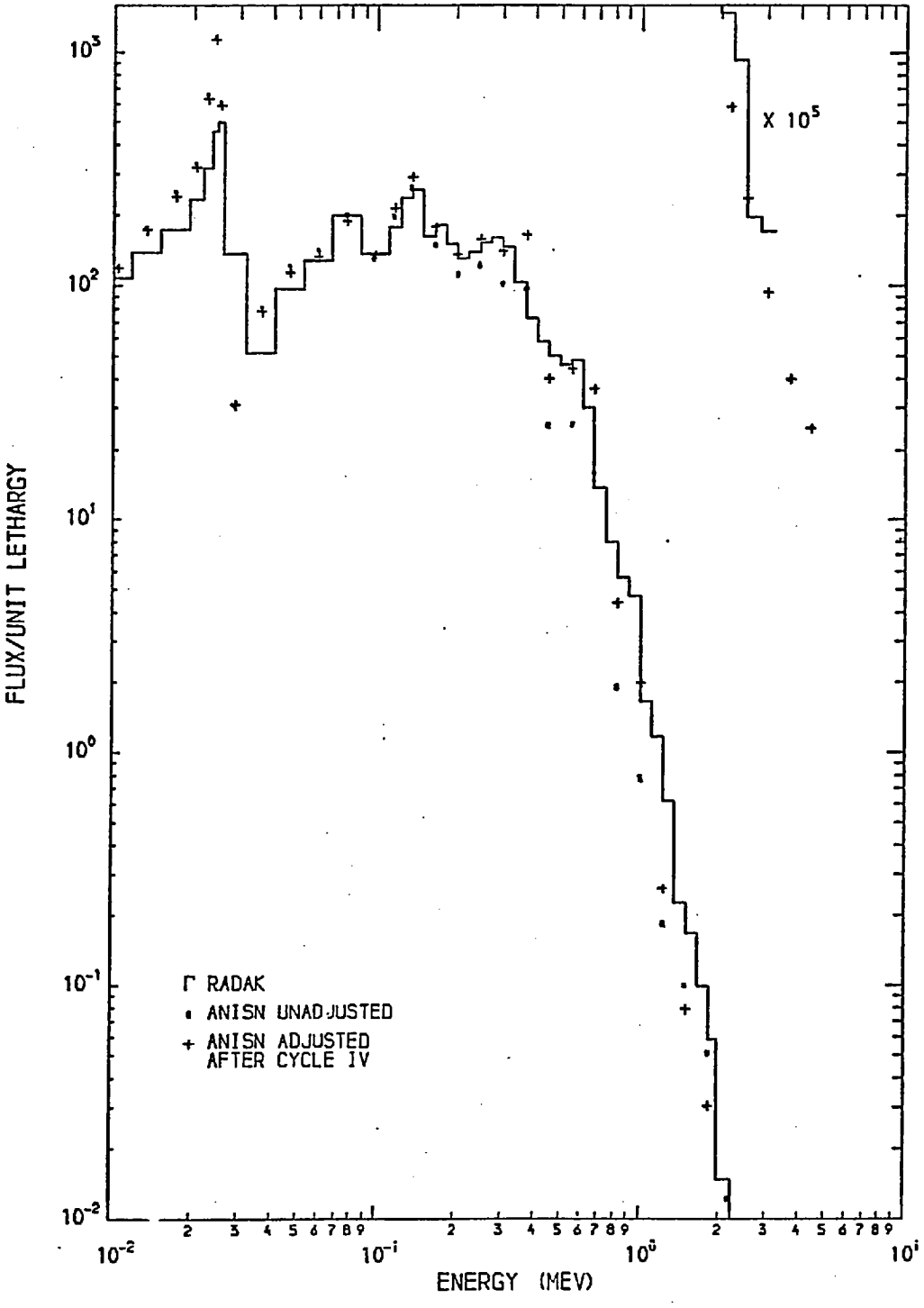


FIG. 9.13 COMPARISON OF CALCULATED FLUX PROFILES WITH RADAK UNFOLDED SPECTRUM MEASUREMENT AT 76.2CM POSITION.

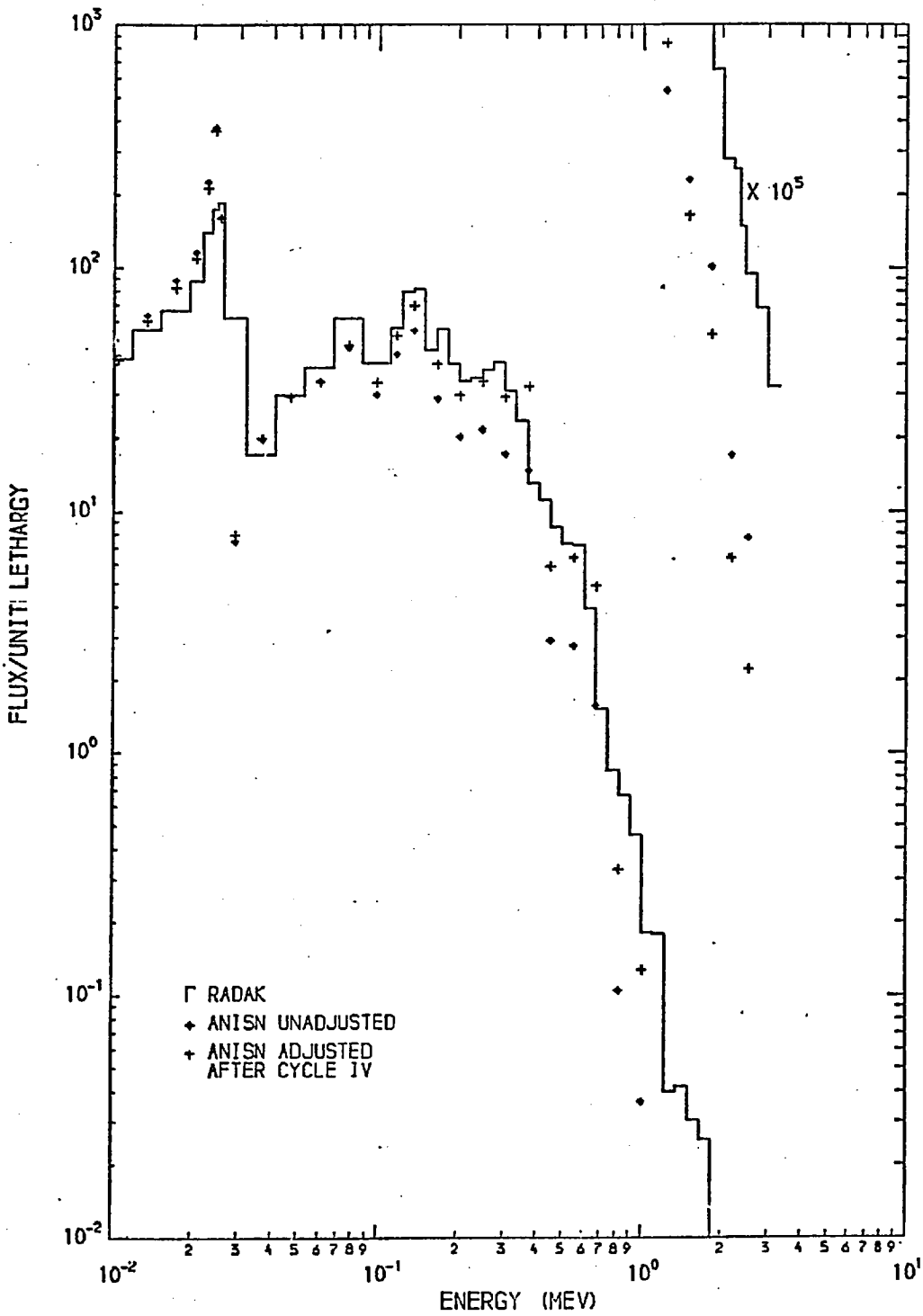


FIG. 9.14 COMPARISON OF CALCULATED FLUX PROFILES WITH RADAK UNFOLDED SPECTRUM MEASUREMENT AT 101.6CM POSITION.

and in the multi-position optimisation an attempt is made to reduce the flux to give greater consistency with the RADAK results. Below 1.5 MeV and especially in the regions containing the inelastic threshold, above 860 keV, and the 600 - 670 keV window in the elastic cross-section, a considerable improvement in flux prediction is obtained. The agreement over the whole energy range is good but could probably be improved by further optimisation cycles. In the region below 50 keV the RADAK unfolding code operating on the differential count-rate information is unable to accurately represent the rapid flux-energy gradients found in the 27 keV resonance and the 24 keV interference minimum. The discrepancies between calculation and measurement cannot therefore in this region be judged using the unfolded flux profile and recourse has to be made to a comparison of the integral count-rates.

A more rigorous test of the neutron transmission data is afforded by the flux comparison for the 76.2 cm position; at this large penetration the errors in the transmission data should dominate all other uncertainties (source normalisation, response data etc.) which contribute to the observed discrepancies. Figure 9.13 shows that the unadjusted flux is under-predicted below 2.5 MeV. The statistics on the flux at higher energies are insufficient to allow meaningful comparisons to be made. The effect of data adjustment on the profile below 1 MeV is very clearly illustrated in Figure 9.13, especially in the regions around 300 and 600 keV where large reductions in the elastic cross-sections have been made and in the area containing the inelastic threshold where better agreement with measurement has been obtained. Above 1.5 MeV a change-over occurs and the unadjusted flux appears to give a better prediction than the adjusted data set although the uncertainties on the unfolded measurement spectrum are large ($\sim 20\%$), being characterised by only the NE 213 spectrometer. The adjustments above 1.5 MeV appear to be dictated by the measurement data closer to the source which is of higher quality and thus dominates the multi-position multi-channel detector distribution. The minimisation of the χ^2 for the model at higher energies appears to require that agreement be sought in the shallow penetration regions, where the measurement uncertainties are small, at the expense of the agreement at deeper penetrations where the measurement errors on the count-rate data are larger. A possible source of the change-over from over-prediction near the source to under-prediction at deep penetration, which is also witnessed by the integral threshold detector measurements, may be derived from the inadequacy of the $1/E\,\Sigma^T(E)$ weighting function at the higher

energies where anisotropic scattering begins to have an effect.

The flux comparison in the region of the inelastic threshold after a penetration of 1 m indicates that discrepancies still exist after four optimisation cycles. An improvement by a factor 3 has been achieved although a further change by a factor 2 is required for statistical agreement. There appears to be no reason to believe that such a change would not accrue from further iteration. Significant improvements in the region below the inelastic threshold have been obtained.

In Figure 9.15 the flux profile calculated using the adjustments predicted after cycle 2 of the single position detector distribution is shown. The flux fit is everywhere better than the unadjusted profile though only small changes have been made above ~ 1 MeV; this is consistent with the lack of measurement information for energies above 1 MeV, which is reflected in the single position cross-section adjustment profiles.

In Figure 9.16 and Table 9.9 the effect of the multi-position data adjustment procedure on the activation detector reaction-rate penetration profiles is considered. At the 20.3 cm position the sulphur reaction-rate which depends on the high energy flux has been improved from a 23% over-prediction to a 7% under-prediction. On the other hand the agreement of the Rh(n,n') reaction-rate has become worse, rising from a 6% to a 13% over-prediction. The indium reaction-rate appears to be insensitive to the data adjustments at this depth. The picture after a penetration of 50.8 cm is somewhat confused. The sulphur response-rate has been significantly improved from a 72% over-prediction to a 4% under-prediction and is a result of the flux changes above 1.5 MeV. However, although the initial calculated flux and the unfolded measurement spectrum disagreed below 1.5 MeV, the Rh(n,n') and In(n,n') reaction-rates were in excellant agreement (within one standard deviation); as a result of obtaining a better flux agreement by data adjustment on the basis primarily of the proton recoil counter data, the Rh(n,n') and In(n,n') reaction-rates have been increased to furnish an over-prediction of some 20% and 40% respectively. This may be an indication either of poor quality integral measurements for these two counters or that adjustments to the detector response functions are required. Only rhodium and gold have been measured at the 76.2 cm position and the adjustment process has produced considerable improvement in the rhodium reaction-rate prediction. Similarly at the 101.6 cm position the discrepancy for rhodium has been more than halved, although the 24%, 2.4σ, under-prediction is still unacceptable. Further iteration may however improve agreement.

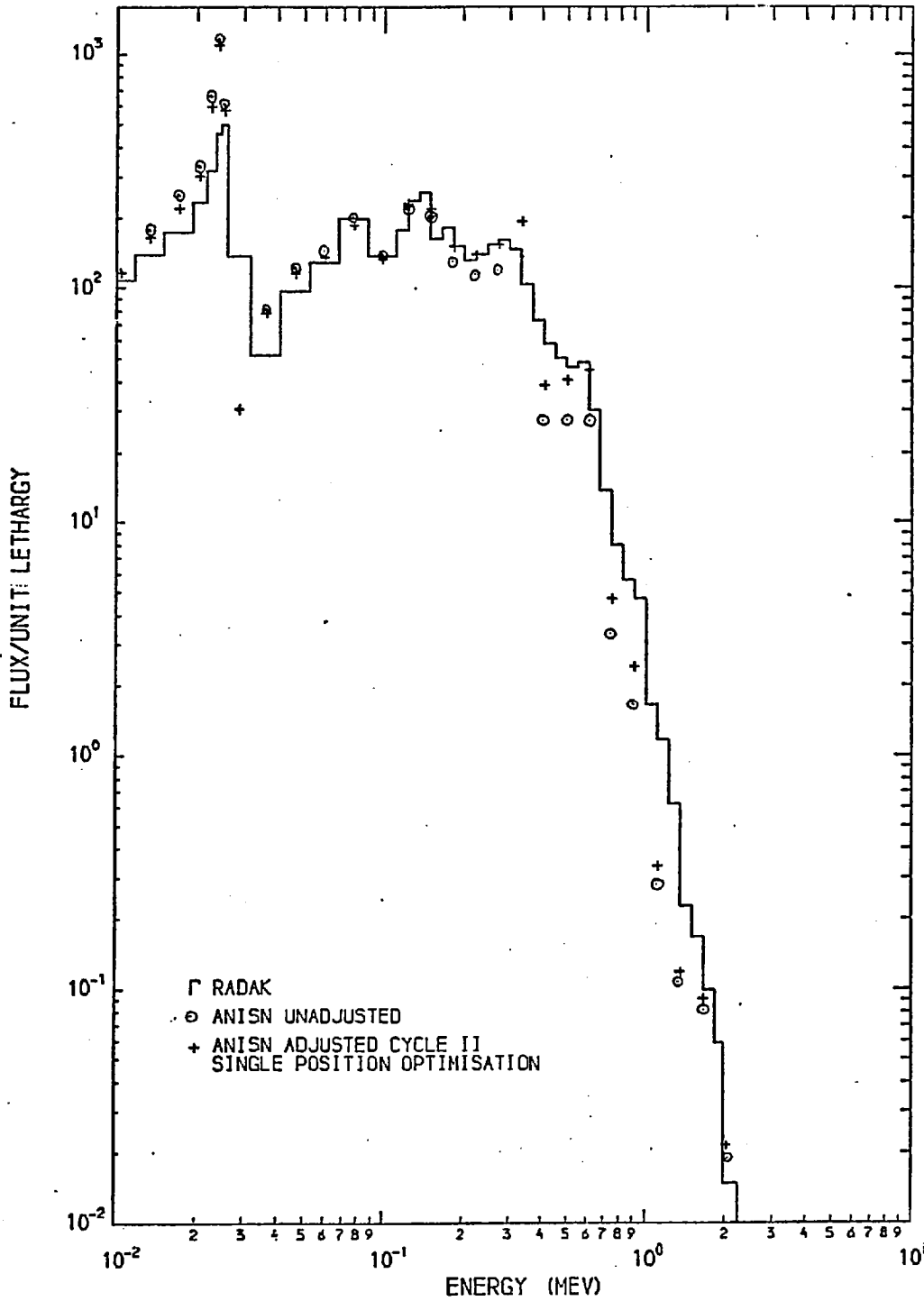


FIG. 9.15 COMPARISON OF CALCULATED FLUX PROFILES WITH RADAK UNFOLDED SPECTRUM MEASUREMENT AT 76.2CM POSITION.

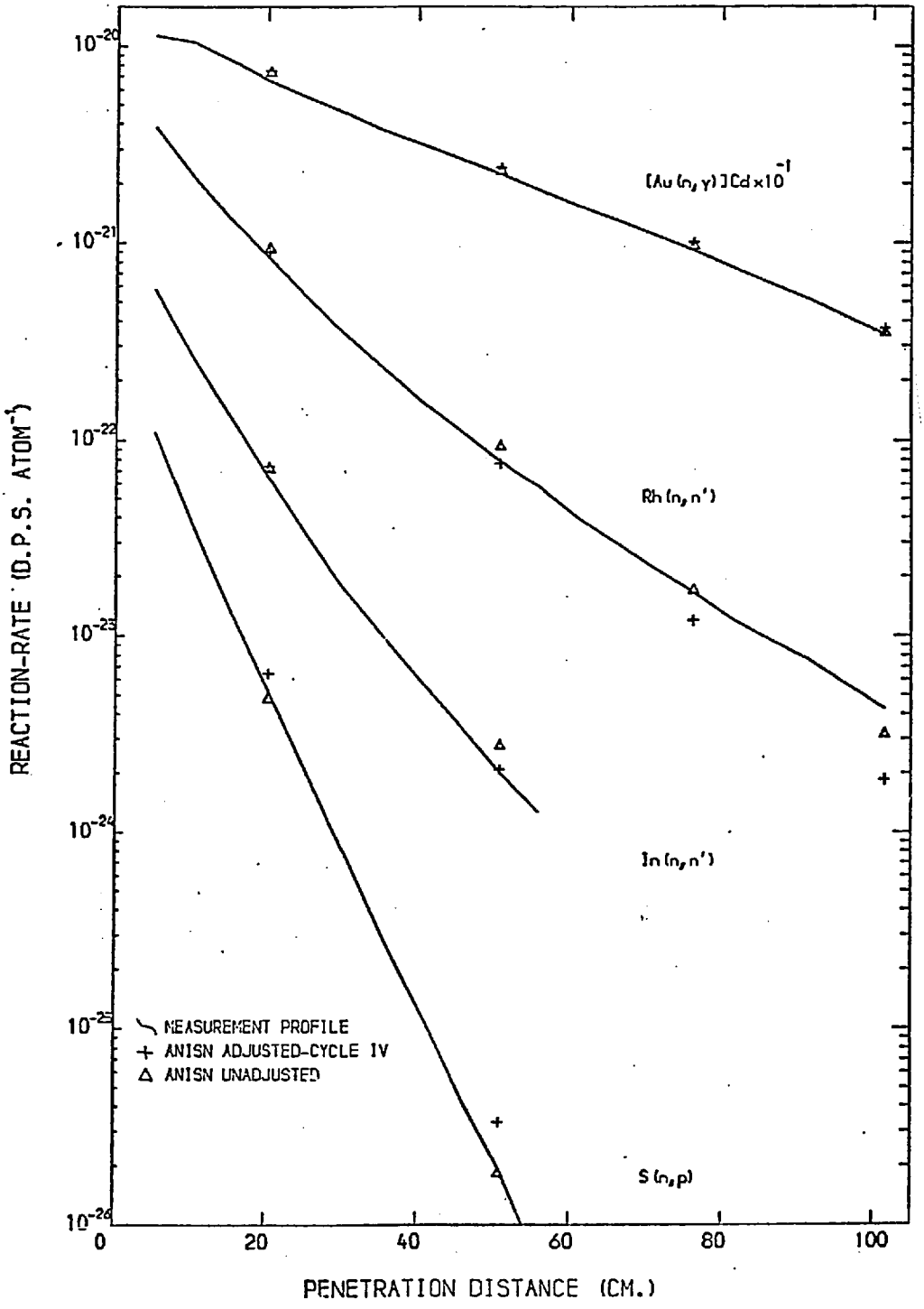


FIG. 9.16 COMPARISON OF MEASURED AND CALCULATED INTEGRAL DETECTOR REACTION-RATE PENETRATION PROFILES.

Table 9.9

Comparison of Activation Detector Reaction-Rates Derived from Different Libraries

Position	Library - Data Set	S(n,p)	In(n,n')	Rh(n,n')	Au(n,γ)
20.3 cm	Unadjusted	6.45 0	7.36 +1	8.98 +2	7.48 +4
	PLATO(4)	4.88 0	7.34 +1	9.59 +2	7.49 +4
	Measurements	5.26 0	6.44 +1	8.46 +2	6.68 +4
	ENDF/B-IV	5.67 0	7.82 +1	9.84 +2	7.23 +4
	FD5	6.14 0	7.69 +1	9.81 +2	7.23 +4
22.8 cm	Unadjusted	4.36 0	5.51 +1	7.36 +2	-
	PLATO(4)	3.22 0	5.57 +1	7.94 +2	-
	Measurements	3.33 0	5.41 +1	7.15 +2	-
	ENDF/B-IV	3.79 0	5.96 +1	8.12 +2	-
	FD5	4.13 0	5.83 +1	8.15 +2	-
50.8 cm	Unadjusted	3.34 -2	2.09 0	7.63 +1	2.41 +4
	PLATO(4)	1.87 -2	2.82 0	9.52 +1	2.39 +4
	Measurements	1.94 -2	2.02 0	7.90 +1	2.24 +4
	ENDF/B-IV	2.56 -2	3.00 0	8.70 +1	2.42 +4
	FD5	2.95 -2	2.74 0	1.02 +2	2.34 +4
76.2 cm	Unadjusted	-	-	1.19 +1	1.01 +4
	PLATO(4)	-	-	1.72 +1	9.85 +3
	Measurements	-	-	1.66 +1	9.26 +3
	ENDF/B-IV	-	-	1.30 +1	1.04 +4
	FD5	-	-	1.89 +1	1.03 +4
101.6 cm	Unadjusted	-	-	1.85 0	3.66 +3
	PLATO(4)	-	-	3.21 0	3.56 +3
	Measurements	-	-	4.25 0	3.44 +3
	ENDF/B-IV	-	-	1.91 0	3.77 +3
	FD5	-	-	3.56 0	3.95 +3

All reaction-rates are expressed as saturated disintegrations s^{-1} $atom^{-1}$ $barn^{-1}$ at 1 watt of NESTOR reactor power.

In Figure 9.17 the efficacy of each iteration of the optimisation scheme in converging towards the unfolded flux profile is displayed. The largest changes in the flux prediction occur for the first cycle since the scaling parameter λ, determined to give a local minimum in χ^2, took the value $4\sigma(x^T)$ corresponding to a 16% reduction in the total cross-section in the group spanning the energy range 0.6 to 0.67 MeV. In the later cycles, the largest changes occur in the higher energy flux, indicating that as convergence occurs in the intermediate energy groups (0.1 - 1.0 MeV) the higher energy discrepant data gain importance resulting in a broadening of the sensitivity profile to include these data in the optimisation process. The evidence of Figure 9.17 implies that further iteration, whilst only producing relatively small changes in χ^2 will lead to greater agreement between the higher energy unfolded and predicted flux spectra.

Thus in the limit of many iterations the agreement between the unfolded and calculated flux profiles at all positions should be within the unfolding statistics. Since the ASPIS iron benchmark experimental measurements cover the range from 4.9 eV to 10 MeV or more specifically test the continuous energy-dependent transmission cross-section data between 7 keV and 10 MeV, it should be possible to maximise the support for a hypothesised nuclear data set over this entire range. In practice, however, economic and physics requirements dictate an end-point to the iteration procedure. For example the cycle 4 data set would probably be quite good enough to calculate the damage and activation requirements specified by Barré[52] for the NEA FBR benchmark exercise. In contradistinction, the data set would be expected to provide only marginally better predictions for the damage-rate in the pressure vessel of the PWR theoretical benchmark exercise specified by Hehn et al[49], since in this case, as shown in Chapter II, it is the nuclear data around 7 MeV that is important. It seems obvious therefore that the end point for the optimisation process must be chosen with a view to the physics of the situation in which the data set will be applied. Indeed the exercise could be considerably reduced by inclusion of only those observations in the optimisation process which test the transmission data in the energy region of interest.

9.7 Comparison of Predicted and Observed Response-Rates

Figures 9.11 to 9.14 have displayed a comparison of the calculated and unfolded measurement spectra and have been used in the analysis only in a diagnostic manner. This comparison is invalid in the region of the

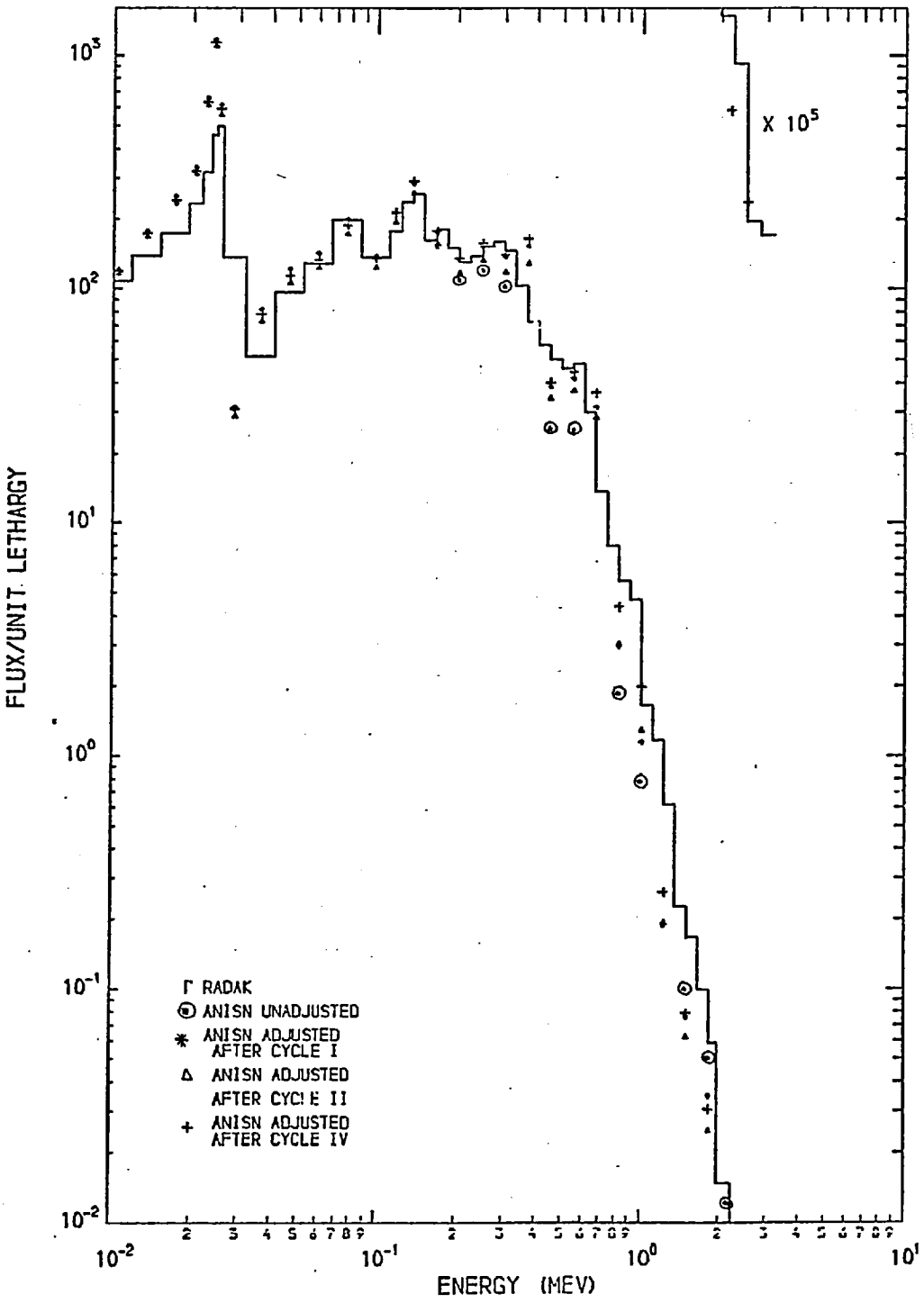


FIG. 9.17 CONVERGENCE OF FLUX PROFILES AT 76.2CM POSITION AS A FUNCTION OF MULTI-POSITION ITERATION

24 - 27 keV resonance-anti-resonance pair where the unfolding program is unable to adequately predict the flux spectrum and a breakdown may occur to a lesser extent in other energy regions. The quality of the data set can only be faithfully tested by comparison of the predicted and measured values of the observables. Figures 9.18 to 9.22 examine the relative observed discrepancies for the original data set and for the cycle 4 adjusted data set at all the five major measurement positions.

Figure 9.18 illustrates that the gross discrepancies found for the argon-hydrogen, NE 213, 1 at. and $\frac{1}{2}$ at. counters at high gain at the 20.3 cm position have all been removed by the adjustment process and that nearly all the C/M ratios lie within the measurement statistics. Similarly the high energy NE 213 measurements made at the 22.8 cm position have been unresisted in forcing the calculation to agree with observation and after four cycles the C/M ratios for the NE 213 data all lie within statistics. Only the In(n,n') reaction-rate has moved out of agreement.

At the 50.8 cm position most of the calculated response-rates have been brought into closer agreement with measurement. A notable exception, however, is the argon-hydrogen counter data which at the high energy end of the counting distribution appears to have become more discrepant. A similar behaviour can be seen at the 76.2 cm position. The statistical errors on the NE 213 measurements are large but there still appears to be a large residual discrepancy. The rhodium detector response-rate however has moved into agreement. It would appear that good quality high energy measurements are required in order to force calculational agreement.

The pictorial representation of Figure 9.22 shows that after a penetration of 1 m the adjusted data set is tending to give a better prediction of the observables than the prior data set, though in some cases, large residual discrepancies still exist. It would seem that the situation will improve with further iteration, since, as the discrepancies at the shorter penetration distances disappear the multi-position multi-channel detector distribution will assign greater importance to the 1 m data. The region of the argon-hydrogen counter where no C/M ratios are shown arises because the values are too small to be on scale ($\sim 8.8\ -3$).

The C/M profiles give a much clearer view of the kind of agreement that has been achieved using the cycle 4 adjusted data set and also give an indication of the accuracy likely to be obtained for the prediction of an integral parameter as a function of penetration and energy.

9.8 Variance-Covariance Data

There are two philosophies which can be adopted over the use of

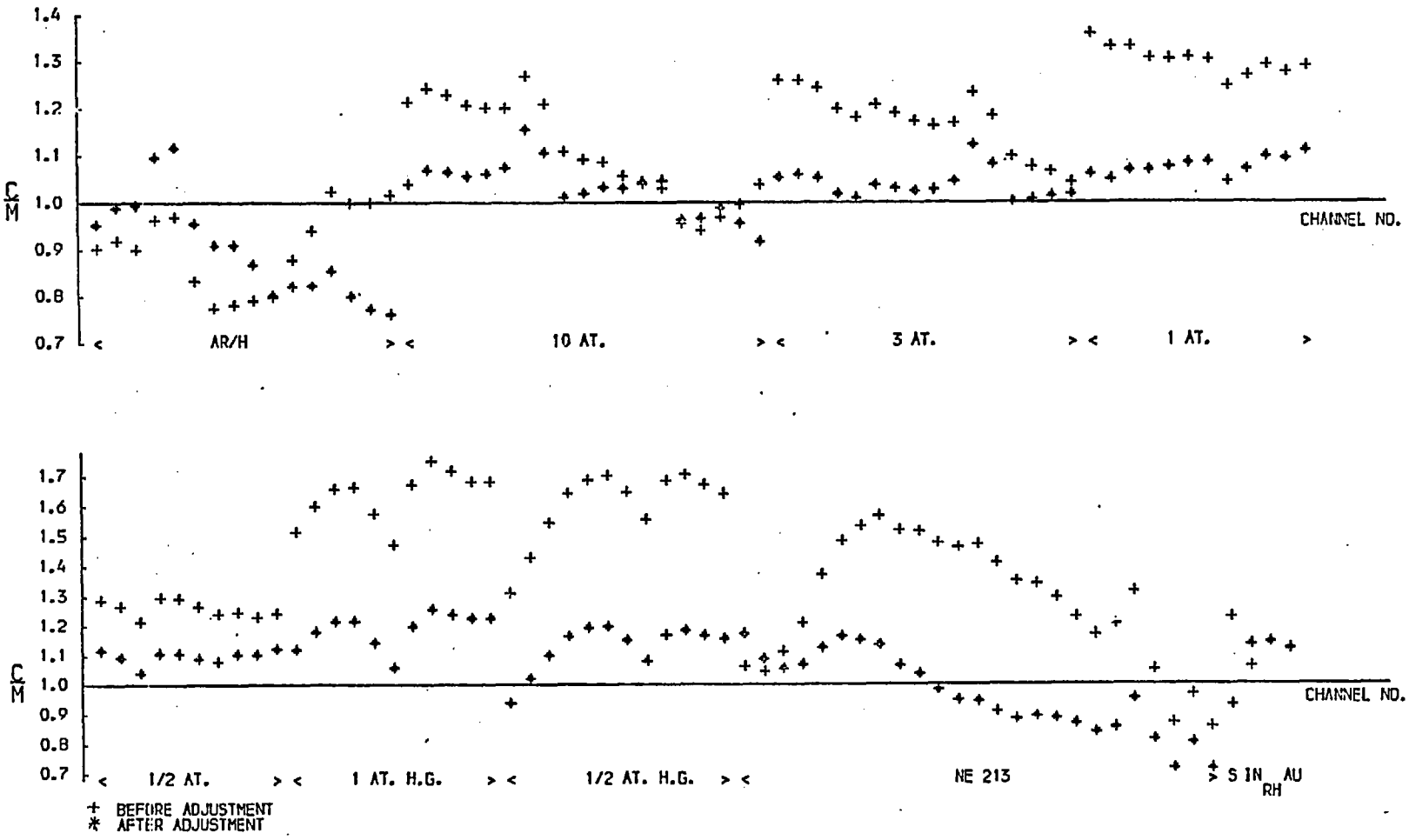


FIG. 9.18 COMPARISON OF CALCULATED RESPONSE-RATES AT 20.3CM WITH MEASUREMENT.

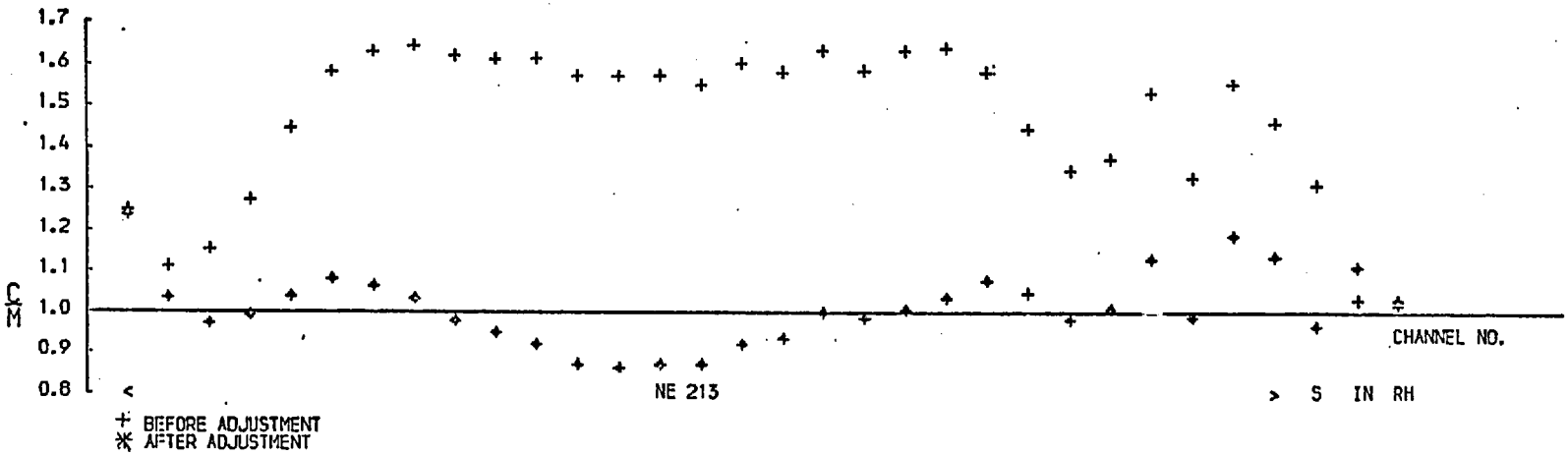


FIG. 9.19 COMPARISON OF CALCULATED RESPONSE-RATES AT 22.8CM WITH MEASUREMENT.

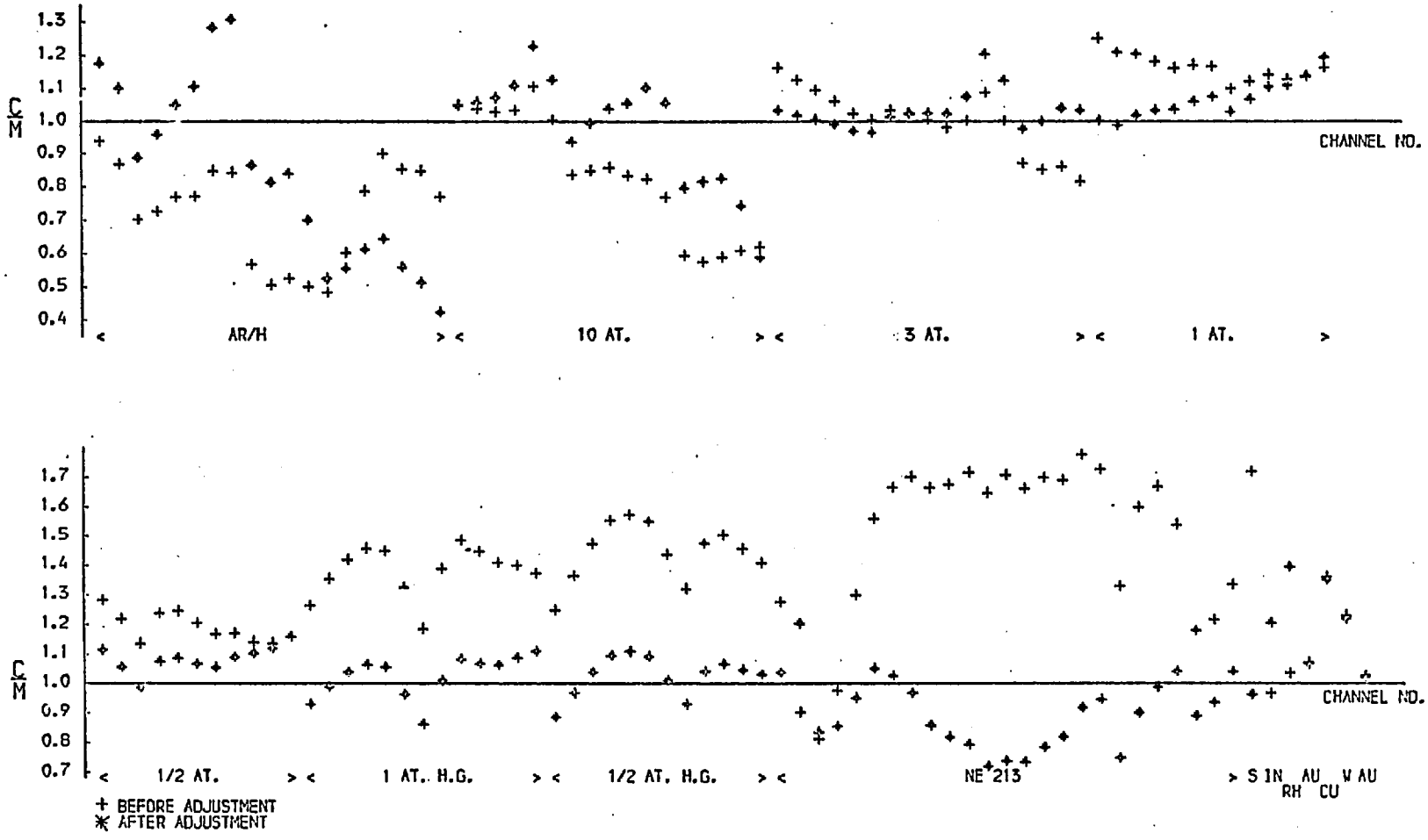


FIG. 9.20 COMPARISON OF CALCULATED RESPONSE-RATES AT 50.8CM WITH MEASUREMENT.

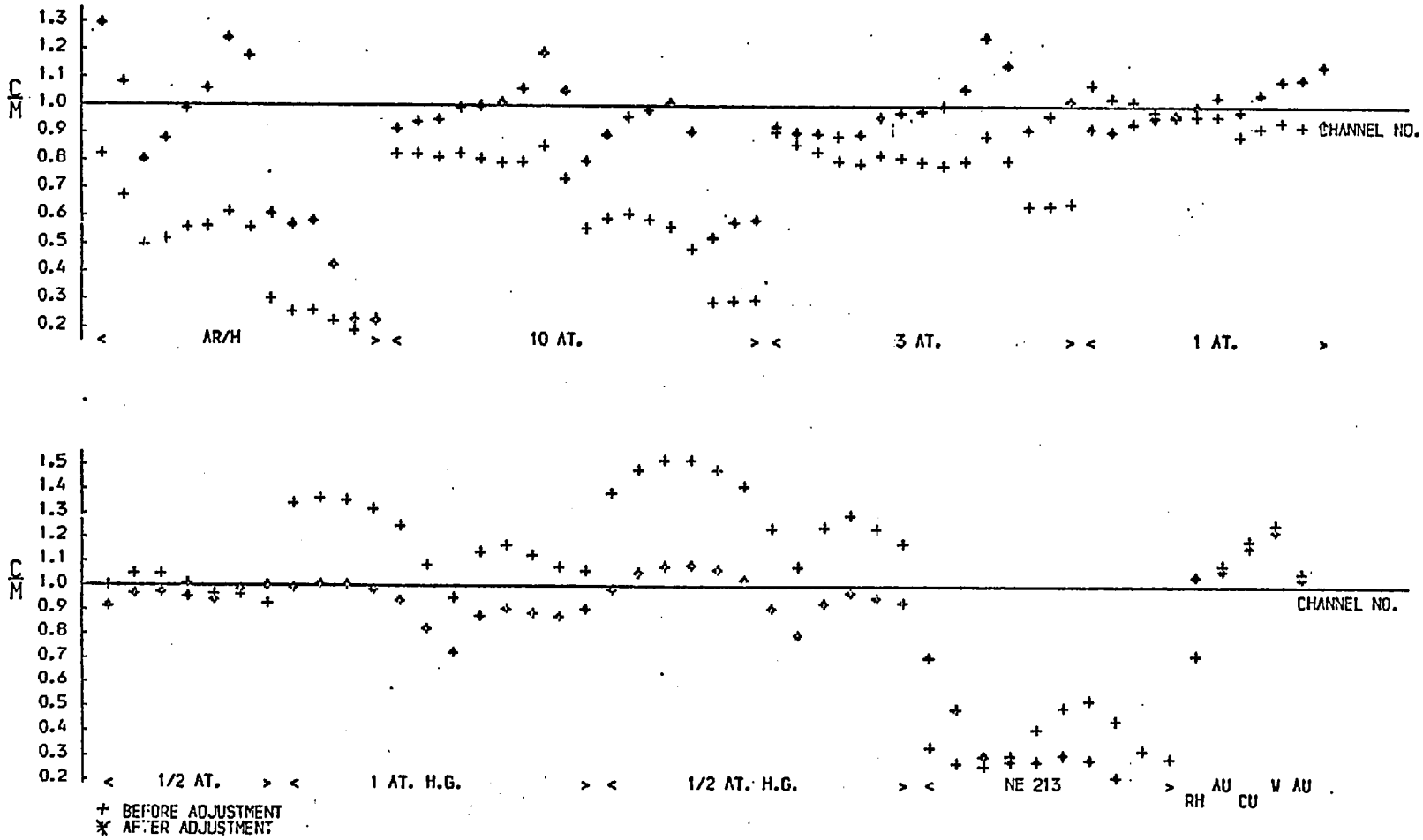


FIG. 9.21 COMPARISON OF CALCULATED RESPONSE-RATES AT 76.2CM WITH MEASUREMENT.

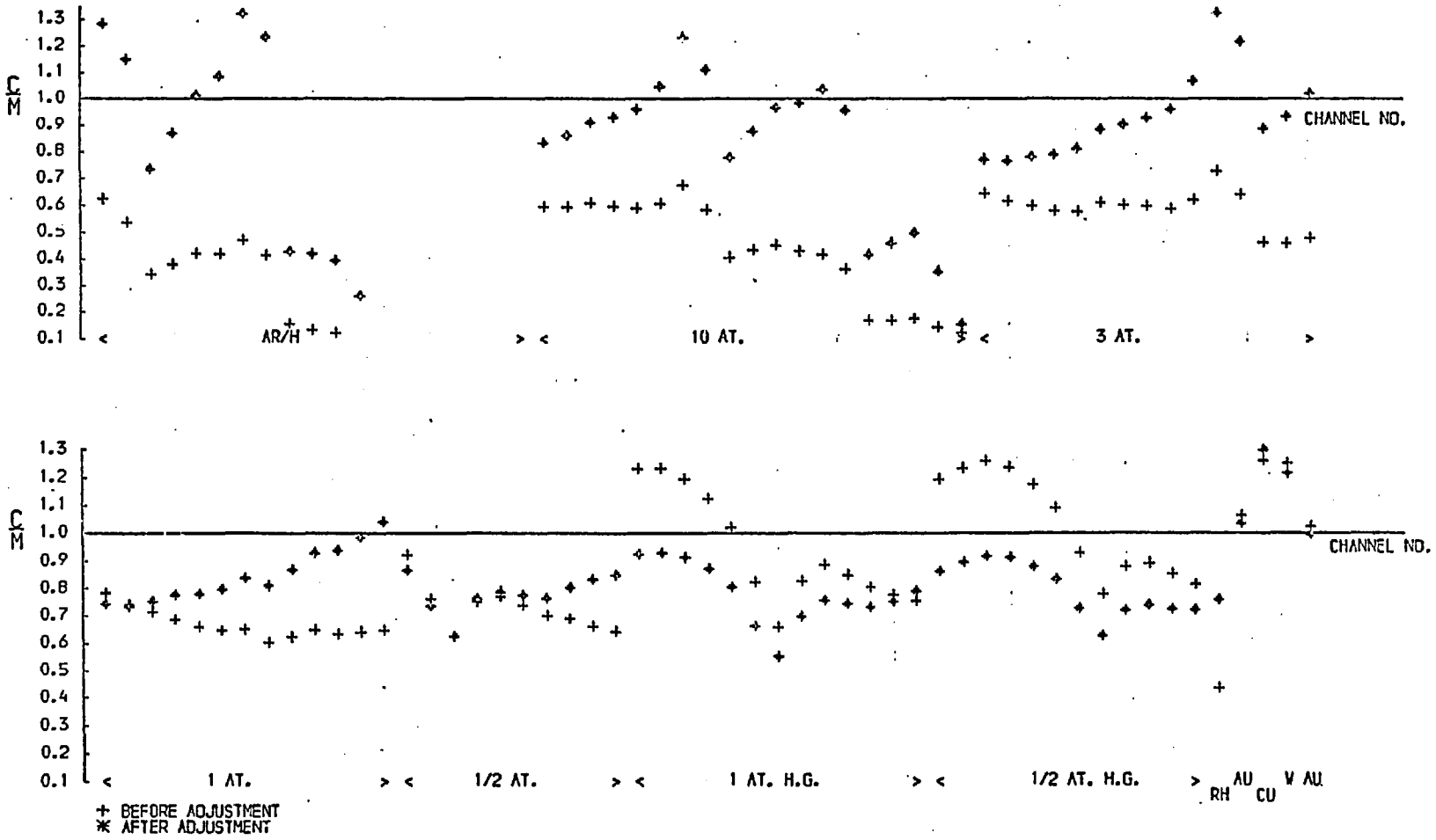


FIG. 9.22 COMPARISON OF CALCULATED RESPONSE-RATES AT 101.6CM WITH MEASUREMENT.

variance-covariance data for the start of a new optimisation cycle. The first and simplest is to consider that the adjusted data set is simply a new library and that the Schmidt error data are still as appropriate to this new library as they were to the prior library. This simply amounts to a re-posing of the optimisation problem, since the choice of starting library is arbitrary and the prior uncertainty data for the transmission cross-sections are largely uncertain. Whilst providing a more likely set of evaluates, the span of the multi-dimensional likelihood surface about the evaluates will not be reduced. Thus the optimised data set can be used to predict a more likely value of a target quantity of interest, but if the adjustments are small so that the requirements of linear perturbation theory are satisfied then the uncertainty bounds on the new prediction of the target quantity will be the same as those for the old prediction; it is obvious therefore that information contained in the extensive observations has been wasted.

The second approach is to use the formalism developed in Chapter V to update the prior variance-covariance matrices and to evaluate correlation matrices for all the cross-section parameters predicted at the end of an adjustment cycle. Examples of such correlation matrices for the non-elastic and total cross-sections are given as Tables 9.10 to 9.12. As required by the intuitive arguments of Chapter V, the correlations are strongest in the proximity of groups for which large cross-section adjustments have been made - around the threshold of the inelastic cross-section and in the vicinity of the 600 and 300 keV interference minima.

It will be observed that for energy groups requiring large reductions in the prior cross-section data, the updated expected fractional standard deviation on the adjusted cross-section can be larger than the prior data. This local loss of information on a cross-section parameter can arise due to inconsistency between the prior data and the extensive observations in that they do not come from the same population of possible measurements of the cross-section parameter. The possibility of the à posteriori standard deviation being larger than the prior value can be seen immediately from a consideration of the algebra:

$$\langle \delta\hat{x}^2 \rangle = \langle \delta x^2 \rangle + \langle \delta \epsilon^{x^2} \rangle + 2 \langle \delta x \delta \epsilon^x \rangle \qquad 9.8.1$$

$$\mathrm{Var}(\hat{x}) = \mathrm{Var}(x) + \mathrm{Var}(\epsilon^x) + 2\,\mathrm{cov}(x, \epsilon^x) \qquad 9.8.2$$

Whether or not the updated variance is larger is dependent upon the sign and magnitude of the correlation between the prior cross-section data and

ENERGY (MEV)		1	2	3	4	5	6	7	8	9	10	11	12	13	14	15	16	17	18	19	20	F. STD. DEV.
0.497E 01	1	1.000	.0359	.0757	.0844	.0918	.0930	.0995	.0946	.0508	.0432	.0545	.0608	.0687	.0468	-.0167	-.0408	-.1086	-.1224	-.1374	-.0965	0.977E-01
0.472E 01	2	.0359	1.000	.0753	.0840	.0914	.0926	.0990	.0941	.0506	.0430	.0543	.0605	.0683	.0466	-.0166	-.0406	-.1081	-.1218	-.1367	-.0960	0.977E-01
0.449E 01	3	.0757	.0753	1.000	.1771	.1926	.1951	.2087	.1984	.1066	.0907	.1144	.1276	.1440	.0982	-.0350	-.0856	-.2278	-.2568	-.2883	-.2024	0.995E-01
0.407E 01	4	.0844	.0840	.1771	1.000	.2148	.2175	.2327	.2212	.1188	.1011	.1275	.1422	.1606	.1095	-.0391	-.0954	-.2541	-.2864	-.3215	-.2258	0.101E 00
0.368E 01	5	.0918	.0914	.1926	.2148	1.000	.2367	.2531	.2406	.1292	.1100	.1387	.1547	.1747	.1191	-.0425	-.1038	-.2765	-.3116	-.3498	-.2457	0.102E 00
0.333E 01	6	.0930	.0926	.1951	.2175	.2367	1.000	.2564	.2437	.1309	.1113	.1403	.1565	.1769	.1206	-.0432	-.1053	-.2804	-.3161	-.3549	-.2494	0.102E 00
0.301E 01	7	.0995	.0990	.2087	.2327	.2531	.2564	1.000	.2607	.1400	.1191	.1502	.1675	.1892	.1290	-.0462	-.1126	-.2998	-.3379	-.3794	-.2666	0.103E 00
0.273E 01	8	.0946	.0941	.1984	.2212	.2406	.2437	.2607	1.000	.1331	.1133	.1429	.1594	.1799	.1227	-.0437	-.1069	-.2846	-.3207	-.3600	-.2528	0.102E 00
0.247E 01	9	.0508	.0506	.1066	.1188	.1292	.1309	.1400	.1331	1.000	.0608	.0766	.0855	.0966	.0659	-.0236	-.0575	-.1532	-.1727	-.1939	-.1363	0.977E-01
0.235E 01	10	.0432	.0430	.0907	.1011	.1100	.1113	.1191	.1133	.0608	1.000	.0650	.0725	.0821	.0560	-.0203	-.0492	-.1310	-.1477	-.1659	-.1169	0.974E-01
0.223E 01	11	.0545	.0543	.1144	.1275	.1387	.1403	.1502	.1429	.0766	.0650	1.000	.0908	.1032	.0705	-.0262	-.0627	-.1667	-.1881	-.2115	-.1495	0.972E-01
0.202E 01	12	.0608	.0605	.1276	.1422	.1547	.1565	.1675	.1594	.0855	.0725	.0908	1.000	.1151	.0787	-.0293	-.0700	-.1859	-.2098	-.2359	-.1668	0.974E-01
0.183E 01	13	.0687	.0683	.1440	.1606	.1747	.1769	.1892	.1799	.0966	.0821	.1032	.1151	1.000	.0890	-.0323	-.0782	-.2080	-.2346	-.2635	-.1856	0.985E-01
0.165E 01	14	.0468	.0466	.0982	.1095	.1191	.1206	.1290	.1227	.0659	.0560	.0705	.0787	.0890	1.000	-.0219	-.0531	-.1414	-.1594	-.1791	-.1259	0.976E-01
0.150E 01	15	-.0167	-.0166	-.0350	-.0391	-.0425	-.0432	-.0462	-.0437	-.0236	-.0203	-.0262	-.0293	-.0323	-.0219	1.000	.0177	.0475	.0533	.0595	.0407	0.102E 00
0.135E 01	16	-.0408	-.0406	-.0856	-.0954	-.1038	-.1053	-.1126	-.1069	-.0575	-.0492	-.0627	-.0700	-.0782	-.0531	.0177	1.000	.1198	.1348	.1509	.1048	0.107E 00
0.122E 01	17	-.1086	-.1081	-.2278	-.2541	-.2765	-.2804	-.2998	-.2846	-.1532	-.1310	-.1667	-.1859	-.2080	-.1414	.0475	.1198	1.000	.3599	.4030	.2803	0.139E 00
0.111E 01	18	-.1224	-.1218	-.2568	-.2864	-.3116	-.3161	-.3379	-.3207	-.1727	-.1477	-.1881	-.2098	-.2346	-.1594	.0533	.1348	.3599	1.000	.4535	.3152	0.153E 00
0.100E 01	19	-.1374	-.1367	-.2883	-.3215	-.3498	-.3549	-.3794	-.3600	-.1939	-.1659	-.2115	-.2359	-.2635	-.1791	.0595	.1509	.4030	.4535	1.000	.3525	0.175E 00
0.907E 00	20	-.0965	-.0960	-.2024	-.2258	-.2457	-.2494	-.2666	-.2528	-.1363	-.1169	-.1495	-.1668	-.1856	-.1259	.0407	.1048	.2803	.3152	.3525	1.000	0.202E 00
0.821E 00																						

TABLE 9.10 SAMPLE SUBMATRIX OF END OF CYCLE 1 ENERGY DEPENDENT CORRELATION MATRIX FOR NON-ELASTIC CROSS-SECTION.

ENERGY (MEV)		1	2	3	4	5	6	7	8	9	10	11	12	13	14	15	16	17	18	19	20	F. STD. DEV.
0.135E 01	1	1.000	.0005	.0023	-.0099	-.0155	-.0073	-.0151	-.0255	-.0182	-.0102	-.0110	-.0036	-.0054	-.0244	-.0112	-.0049	-.0091	-.0021	-.0034	-.0003	0.399E-01
0.122E 01	2	.0005	1.000	.0023	-.0099	-.0155	-.0072	-.0151	-.0253	-.0180	-.0101	-.0108	-.0035	-.0053	-.0243	-.0111	-.0048	-.0089	-.0021	-.0033	-.0003	0.399E-01
0.111E 01	3	.0023	.0023	1.000	-.0314	-.0491	-.0225	-.0474	-.0802	-.0564	-.0313	-.0333	-.0103	-.0159	-.0757	-.0334	-.0140	-.0263	-.0054	-.0090	-.0000	0.399E-01
0.100E 01	4	-.0099	-.0099	-.0314	1.000	.1955	.0892	.1882	.3193	.2236	.1236	.1315	.0403	.0625	.3000	.1311	.0544	.1025	.0204	.0343	-.0006	0.441E-01
0.907E 00	5	-.0155	-.0155	-.0491	.1955	1.000	.1394	.2940	.4988	.3492	.1931	.2054	.0630	.0976	.4686	.2048	.0849	.1601	.0318	.0536	-.0010	0.506E-01
0.821E 00	6	-.0073	-.0072	-.0225	.0892	.1394	1.000	.1341	.2276	.1591	.0879	.0934	.0286	.0443	.2135	.0930	.0384	.0725	.0142	.0241	-.0007	0.421E-01
0.743E 00	7	-.0151	-.0151	-.0474	.1882	.2940	.1341	1.000	.4802	.3360	.1857	.1974	.0605	.0937	.4508	.1967	.0814	.1535	.0303	.0512	-.0012	0.496E-01
0.672E 00	8	-.0255	-.0253	-.0802	.3193	.4988	.2276	.4802	1.000	.5702	.3152	.3353	.1028	.1593	.7652	.3342	.1384	.2611	.0518	.0872	-.0017	0.111E 00
0.608E 00	9	-.0182	-.0180	-.0564	.2236	.3492	.1591	.3360	.5702	1.000	.2202	.2342	.0716	.1110	.5350	.2331	.0963	.1818	.0357	.0604	-.0016	0.549E-01
0.550E 00	10	-.0102	-.0101	-.0313	.1236	.1931	.0879	.1857	.3152	.2202	1.000	.1292	.0394	.0611	.2955	.1284	.0529	.0999	.0194	.0330	-.0011	0.439E-01
0.498E 00	11	-.0110	-.0108	-.0333	.1315	.2054	.0934	.1974	.3353	.2342	.1292	1.000	.0418	.0649	.3141	.1364	.0561	.1061	.0206	.0349	-.0012	0.443E-01
0.450E 00	12	-.0036	-.0035	-.0103	.0403	.0630	.0286	.0605	.1028	.0716	.0394	.0418	1.000	.0197	.0960	.0414	.0168	.0320	.0060	.0103	-.0006	0.508E-01
0.408E 00	13	-.0054	-.0053	-.0159	.0625	.0976	.0443	.0937	.1593	.1110	.0611	.0649	.0197	1.000	.1489	.0643	.0263	.0498	.0095	.0162	-.0008	0.516E-01
0.369E 00	14	-.0244	-.0243	-.0757	.3000	.4686	.2135	.4508	.7652	.5350	.2955	.3141	.0960	.1489	1.000	.3127	.1291	.2437	.0478	.0809	-.0022	0.111E 00
0.334E 00	15	-.0112	-.0111	-.0334	.1311	.2048	.0930	.1967	.3342	.2331	.1284	.1364	.0414	.0643	.3127	1.000	.0553	.1048	.0200	.0342	-.0016	0.556E-01
0.302E 00	16	-.0049	-.0048	-.0140	.0544	.0849	.0384	.0814	.1384	.0963	.0529	.0561	.0168	.0263	.1291	.0553	1.000	.0426	.0078	.0136	-.0010	0.512E-01
0.273E 00	17	-.0091	-.0089	-.0263	.1025	.1601	.0725	.1535	.2611	.1818	.0999	.1061	.0320	.0498	.2437	.1048	.0426	1.000	.0151	.0260	-.0016	0.534E-01
0.247E 00	18	-.0021	-.0021	-.0054	.0204	.0318	.0142	.0303	.0518	.0357	.0194	.0206	.0060	.0095	.0478	.0200	.0078	.0151	1.000	.0045	-.0007	0.502E-01
0.224E 00	19	-.0034	-.0033	-.0090	.0343	.0536	.0241	.0512	.0872	.0604	.0330	.0349	.0103	.0162	.0809	.0342	.0136	.0260	.0045	1.000	-.0009	0.505E-01
0.202E 00	20	-.0003	-.0003	-.0000	-.0006	-.0010	-.0007	-.0012	-.0017	-.0016	-.0011	-.0012	-.0006	-.0008	-.0022	-.0016	-.0010	-.0016	-.0007	-.0009	1.000	0.499E-01
0.183E 00																						

TABLE 9.11 SAMPLE SUBMATRIX OF END OF CYCLE 1 ENERGY DEPENDENT CORRELATION MATRIX FOR TOTAL CROSS-SECTION.

TOTAL →

ENERGY (MEV)		1	2	3	4	5	6	7	8	9	10	11	12	13	14	15	16	17	18	19	20
0.497E 01	1	.0107	.0106	.0223	.0249	.0271	.0274	.0293	.0279	.0150	.0127	.0160	.0179	.0202	.0138	-.0049	-.0120	-.0321	-.0361	-.0406	-.0285
0.472E 01	2	.0120	.0121	.0252	.0281	.0306	.0310	.0332	.0315	.0169	.0144	.0181	.0202	.0229	.0156	-.0056	-.0136	-.0363	-.0409	-.0459	-.0323
0.449E 01	3	.0259	.0258	.0547	.0607	.0660	.0668	.0715	.0680	.0365	.0310	.0391	.0436	.0493	.0336	-.0121	-.0294	-.0783	-.0882	-.0990	-.0696
0.407E 01	4	.0281	.0279	.0589	.0659	.0714	.0723	.0774	.0735	.0395	.0336	.0423	.0472	.0534	.0364	-.0131	-.0318	-.0847	-.0955	-.1072	-.0754
0.368E 01	5	.0340	.0338	.0713	.0795	.0868	.0876	.0937	.0891	.0478	.0407	.0512	.0572	.0646	.0441	-.0158	-.0385	-.1026	-.1156	-.1298	-.0913
0.333E 01	6	.0458	.0455	.0960	.1070	.1164	.1182	.1261	.1199	.0644	.0548	.0691	.0770	.0870	.0594	-.0213	-.0518	-.1380	-.1555	-.1746	-.1227
0.301E 01	7	.0469	.0466	.0983	.1098	.1192	.1207	.1294	.1228	.0659	.0560	.0705	.0787	.0890	.0607	-.0219	-.0532	-.1417	-.1597	-.1794	-.1262
0.273E 01	8	.0217	.0216	.0455	.0507	.0552	.0559	.0598	.0570	.0305	.0259	.0326	.0363	.0412	.0281	-.0102	-.0248	-.0658	-.0742	-.0834	-.0588
0.247E 01	9	.0250	.0249	.0525	.0586	.0637	.0645	.0690	.0656	.0354	.0299	.0377	.0420	.0476	.0324	-.0118	-.0285	-.0759	-.0855	-.0961	-.0677
0.235E 01	10	.0281	.0280	.0590	.0657	.0715	.0724	.0775	.0737	.0395	.0338	.0423	.0472	.0534	.0364	-.0132	-.0320	-.0851	-.0960	-.1078	-.0759
0.223E 01	11	.0296	.0295	.0621	.0693	.0754	.0763	.0816	.0776	.0417	.0354	.0448	.0498	.0563	.0384	-.0138	-.0336	-.0895	-.1009	-.1133	-.0797
0.202E 01	12	.0168	.0187	.0394	.0439	.0478	.0484	.0518	.0493	.0264	.0224	.0280	.0314	.0356	.0243	-.0091	-.0216	-.0575	-.0649	-.0729	-.0516
0.183E 01	13	-.0025	-.0025	-.0052	-.0059	-.0064	-.0066	-.0070	-.0065	-.0036	-.0034	-.0048	-.0054	-.0053	-.0035	.0000	.0016	.0046	.0050	.0052	.0025
0.165E 01	14	-.0034	-.0034	-.0071	-.0080	-.0087	-.0088	-.0094	-.0089	-.0048	-.0042	-.0056	-.0062	-.0067	-.0045	.0011	.0033	.0091	.0101	.0112	.0074
0.150E 01	15	-.0000	-.0000	-.0001	-.0001	-.0001	-.0002	-.0002	-.0001	-.0001	-.0003	-.0007	-.0008	-.0004	-.0002	-.0006	-.0007	-.0016	-.0019	-.0024	-.0024
0.135E 01	16	.0038	.0038	.0081	.0090	.0098	.0098	.0105	.0101	.0054	.0045	.0055	.0061	.0071	.0049	-.0021	-.0047	-.0125	-.0142	-.0161	-.0116
0.122E 01	17	.0037	.0037	.0078	.0087	.0094	.0095	.0102	.0097	.0052	.0044	.0053	.0059	.0069	.0048	-.0020	-.0045	-.0119	-.0135	-.0153	-.0110
0.111E 01	18	.0133	.0132	.0279	.0311	.0339	.0343	.0367	.0349	.0187	.0160	.0201	.0225	.0253	.0173	-.0061	-.0150	-.0400	-.0450	-.0505	-.0355
0.100E 01	19	-.0591	-.0588	-.1240	-.1383	-.1505	-.1526	-.1631	-.1549	-.0833	-.0712	-.0905	-.1010	-.1131	-.0769	.0261	.0654	.1746	.1965	.2200	.1533
0.907E 00	20	-.1073	-.1068	-.2252	-.2511	-.2732	-.2771	-.2962	-.2813	-.1514	-.1293	-.1644	-.1834	-.2054	-.1397	.0473	.1188	.3169	.3568	.3997	.2782
0.821E 00																					

← NON-ELASTIC

TABLE 9.12 SAMPLE SUBMATRIX OF END OF CYCLE 1 ENERGY DEPENDENT CROSS-CORRELATION BETWEEN TOTAL AND NON-ELASTIC CROSS-SECTIONS.

the adjustment evaluator. On a simple heuristic model it can be seen that for positive adjustments, any increase in the prior data will lead to a decrease in the adjustment evaluate, so that they are negatively correlated. In contradistinction for negative adjustments any increase in the initial cross-section data will require the evaluation of a larger cross-section adjustment in order to obtain consistency with the extensive observations. Thus there is a positive correlation between the prior cross-section data and the evaluated adjustment for groups requiring a reduction in the group cross-section. This positive correlation is indeed found for all groups for which the adjustments reduce the prior cross-section data and is observed to become smaller as the cross-section adjustments converge towards maximum likelihood.

Table 9.12 displays the correlations between the adjusted non-elastic and total cross-sections. These correlations are again largest in energy domains where large adjustments have been made, but it must be emphasised that they are non-observational. They are correlations injected by the nature of the statistical model chosen to weigh the various hypothesised parameter sets and they represent a general 'stiffening' of the error surface appropriate to the evaluated parameter set as a result of the 'connected' nature of the information contained in the extensive observations. It is the correlations such as those contained in Table 9.12 which can help to reduce the uncertainty bounds predicted for a target quantity calculated with the optimised data set.

9.9 Comparison of the Adjusted Data Set with Other Libraries

The questions now arise as to how good is the adjusted data set and what evidence exists for the discrepancies of the magnitude found by the optimisation scheme? The iron data file used in the analysis of the iron benchmark, UKNDL DFN 908A, is a MISSIONARY[173] conversion of the ENDF/B-III file above 330 keV; below this energy the resonance parameters have been evaluated by Pope and Story[174]. A comparison with the more recent ENDF/B-IV data has therefore been performed. The ENDF/B-IV data used was the EURLIB-III iron file prepared by Hehn in the EURLIB-100 group structure using $1/E\sigma_x^T(E)$ weighting. This modification of the weighting function (from $1/E\,\Sigma^T(E)$) is everywhere negligible except in the region of the 24 keV interference minimum, where the omission of the background contribution from manganese[175] would be most likely to lead to a higher flux in the window and the adjacent lower energy groups. To quantify this effect a similar calculation has been performed using the EURLIB-I library for which ENDF/B-III was the source. The results are displayed in

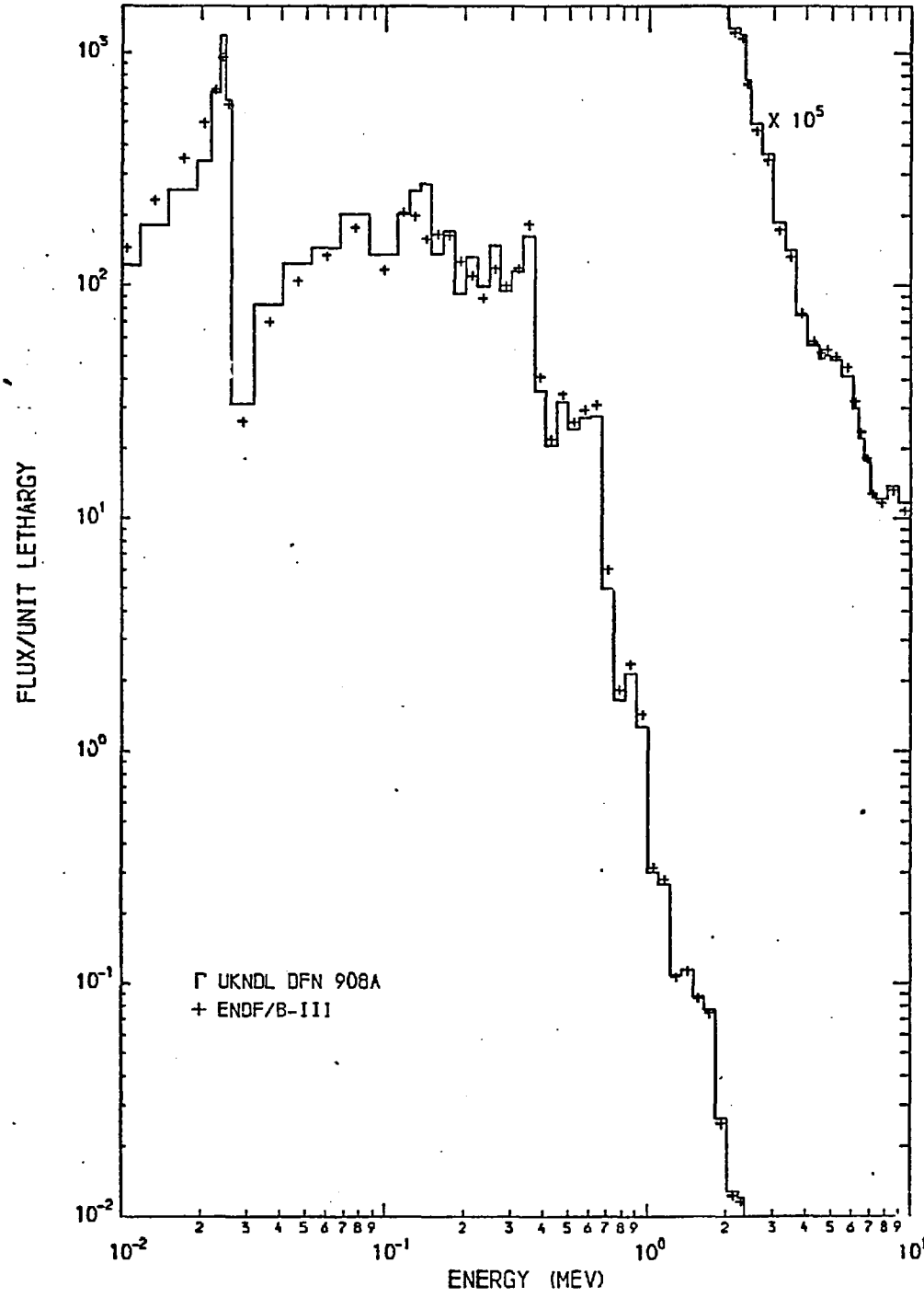


FIG. 9.23 COMPARISON OF ENDF/B-III FLUX PROFILE WITH UKNDL DFN 908A FLUX PROFILE AT 76.2CM POSITION.

Figure 9.23; the discrepancies between the ENDF/B-III and UKNDL DFN 908A multi-group data set predictions below 100 keV probably arise from both the omission of the background cross-section correction and the different resonance parameters assigned by Pope and Story.

Figures 9.24 to 9.26 show a comparison of the unadjusted DFN 908A, the cycle 4 optimised data set and the ENDF/B-IV flux predictions with the unfolded measurement spectrum profiles at the 50.8, 76.2 and 101.6 cm penetration depths. Above 0.4 MeV the sense and magnitude of the flux adjustments derived by the optimisation process are consistent with those shown by ENDF/B-IV. Below 0.4 MeV, and in particular in the region spanning 0.08 to 0.4 MeV the adjusted flux is in serious disagreement with the ENDF/B-IV prediction and indeed the flux discrepancies in this region are greater for ENDF/B-IV than those obtained using the DFN 908A resonance evaluation of Pope and Story. This is an important point since it highlights the fact that the changes from UKNDL DFN 908A to ENDF/B-IV, in this energy region, are in the wrong sense. It is in this region however that the highest density of good quality benchmark measurements exists and so it would be expected that the maximum likelihood evaluators of the cross-section adjustments would be very well defined at these energies. The comparison with ENDF/B-IV does serve to validate the sense and magnitude of the cross-section adjustments made in the region of the inelastic cross-section threshold (Figure 9.27), but there is no evidence to support the reduction in the cross-section at 600 keV; the change between ENDF/B-III and ENDF/B-IV at around 300 keV appears to be in the wrong sense.

The iron benchmark experiment comprises a single calculational situation in which other sets of either differential or integro-differential (optimised using integral measurements of benchmark quality) data can be compared and assessed. In a previous section it was noted that adjusted data sets are tailored to meet the requirements of the calculational framework in which they are to be used. It is particularly interesting therefore to take a data set such as the FD5 iron multi-group data set, which has been optimised (using the LSQ[35] program on ZEBRA-8 integral measurements) to meet the requirements of fast reactor core calculations and apply it, in a many group form, to the ASPIS iron benchmark experiment. In deriving the FD5 iron data, Rowlands et al[176] adjusted the total scattering and capture cross-sections of the UKNDL file DFN 906B, collapsed to a ten broad group scheme with a typical fast reactor core weighting spectrum. The fast reactor core benchmark experiments in the ZEBRA reactor at Winfrith were not tuned particularly to test the iron data since the

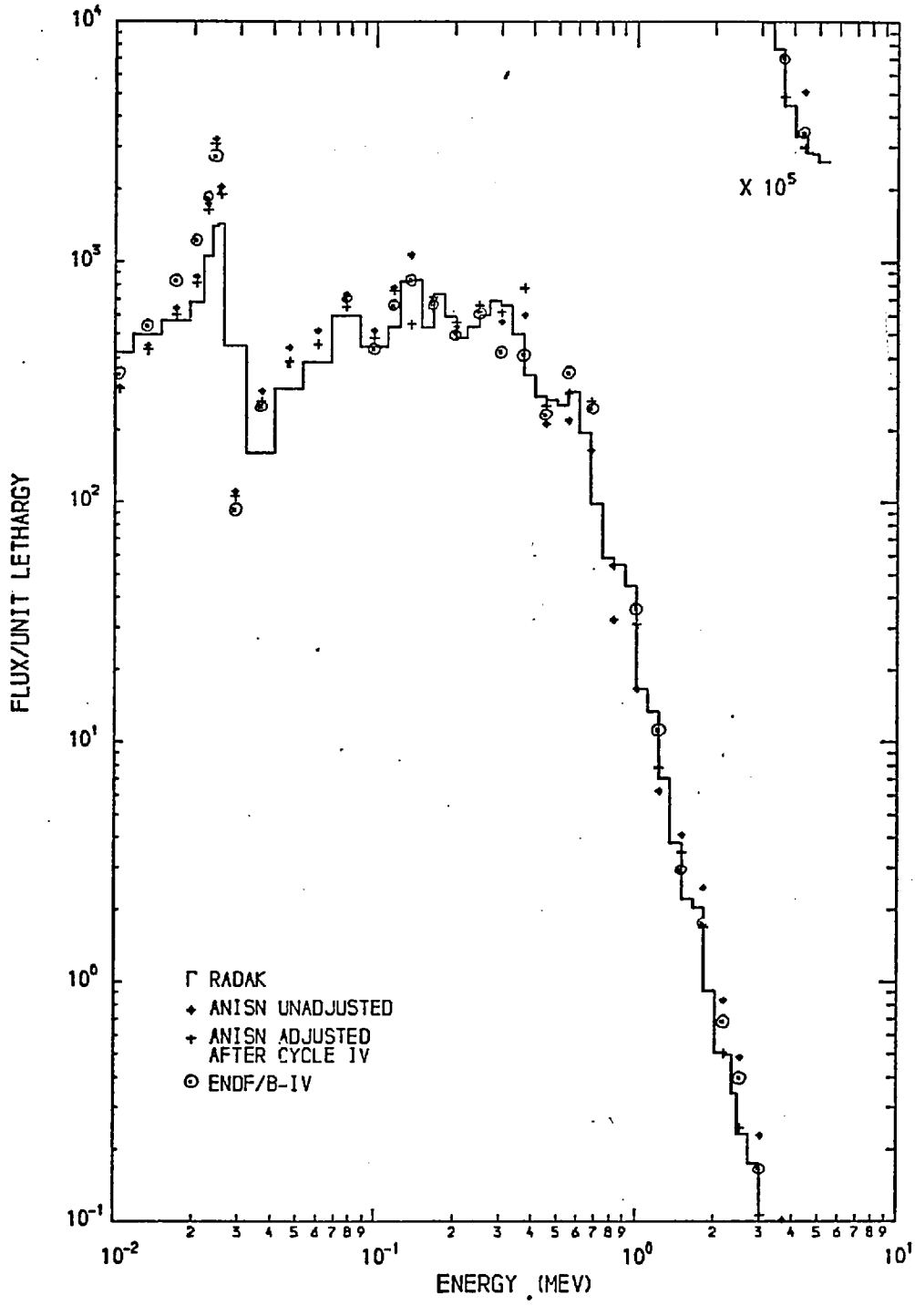


FIG. 9.24 COMPARISON OF ADJUSTED FLUX PROFILE WITH ENDF/B-IV LIBRARY PREDICTION AT 50.8CM POSITION.

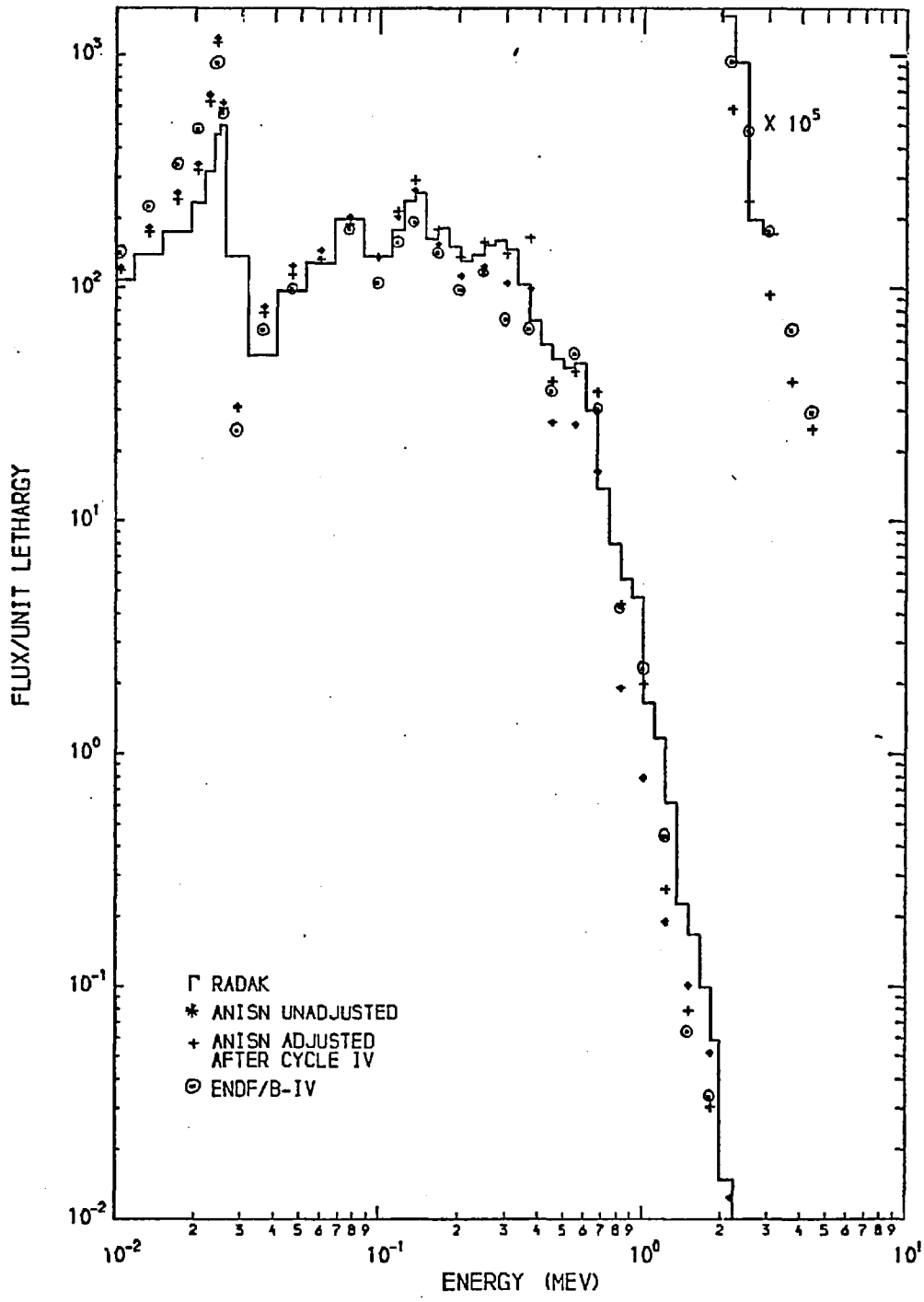


FIG. 9.25 COMPARISON OF ADJUSTED FLUX PROFILE WITH ENDF/B-IV LIBRARY PREDICTION AT 76.2CM POSITION.

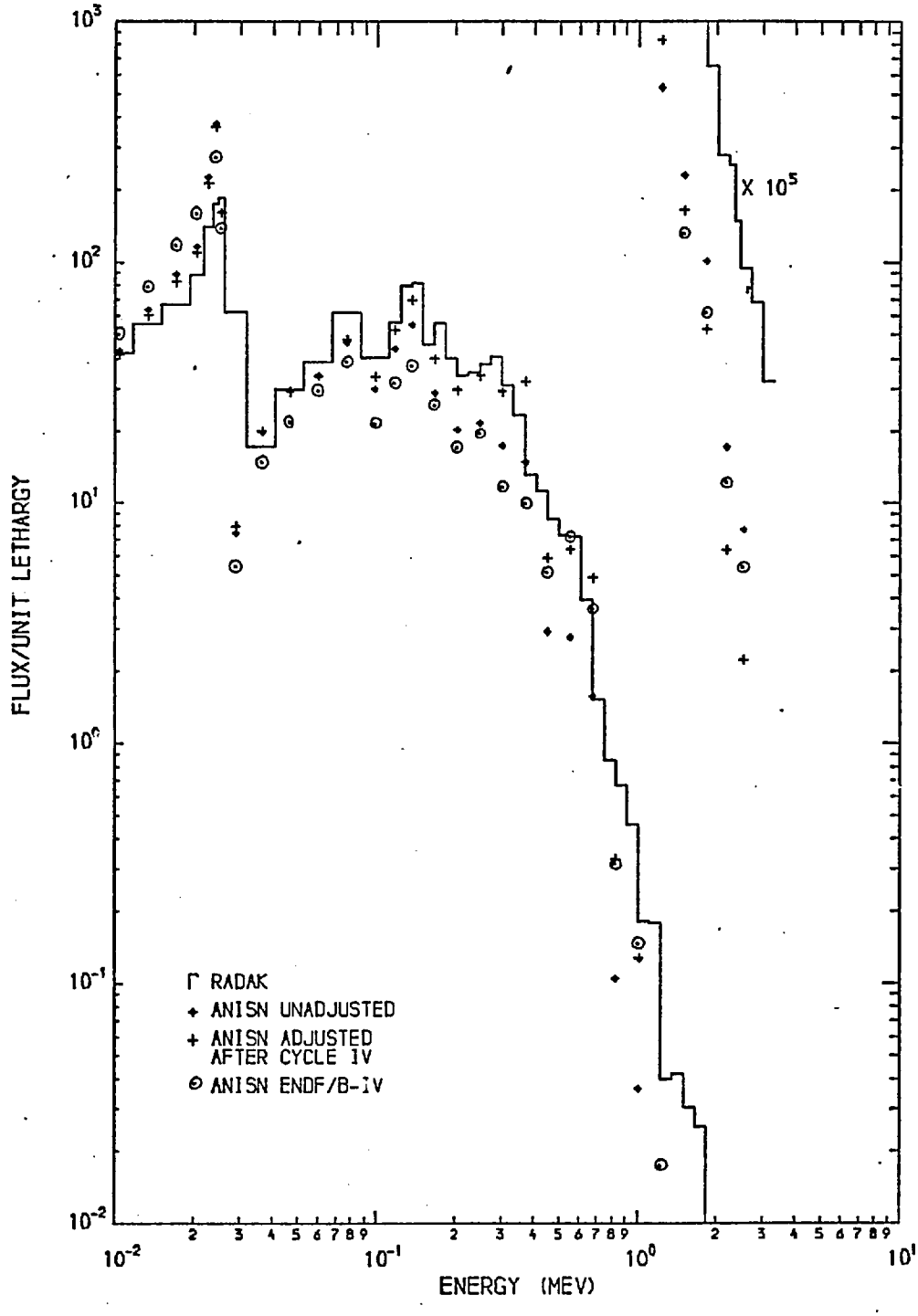


FIG. 9.26 COMPARISON OF ADJUSTED FLUX PROFILE WITH ENDF/B-IV LIBRARY PREDICTION AT 101.6CM POSITION.

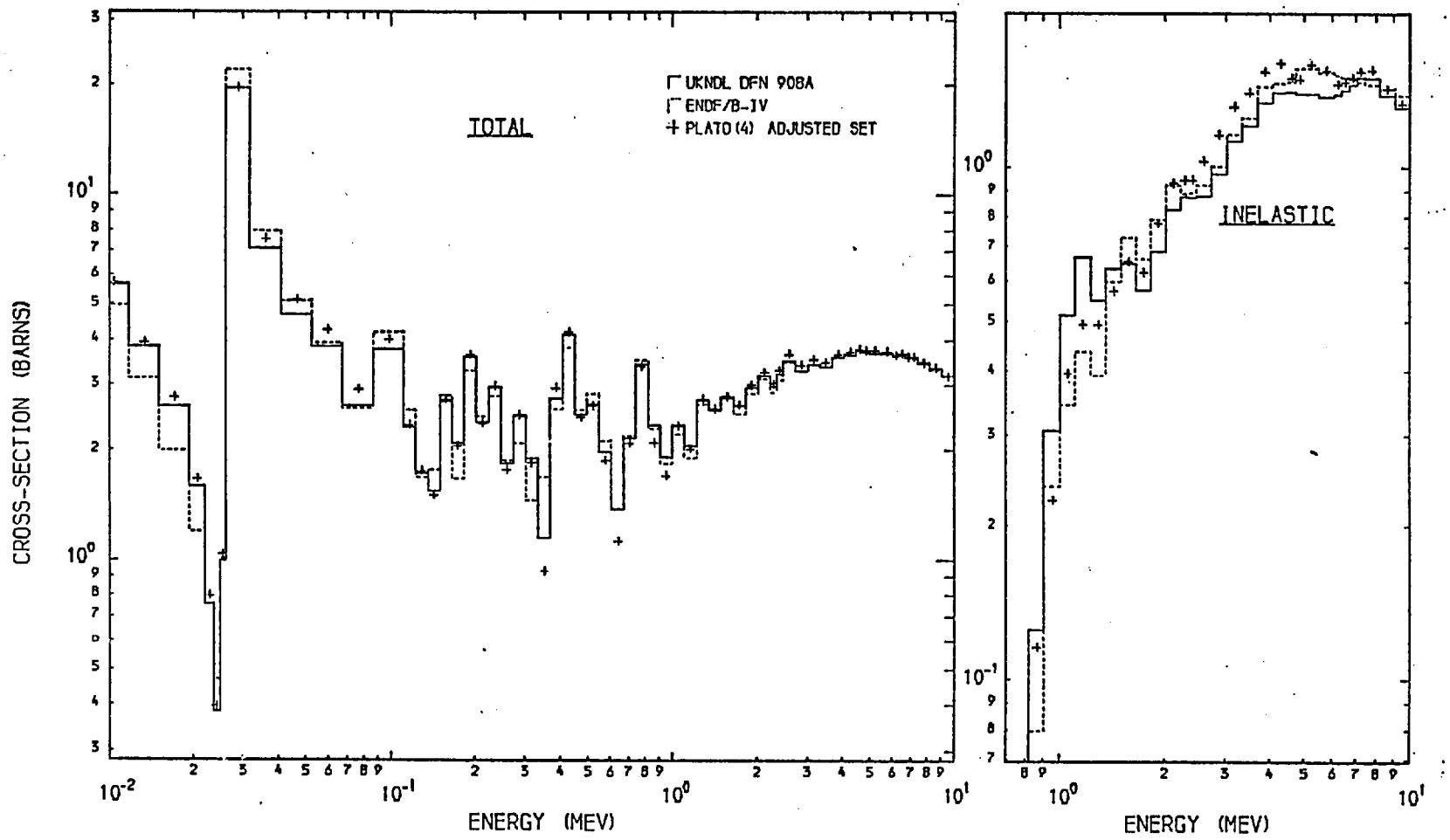


FIG. 9.27 COMPARISON OF MULTI-GROUP CROSS-SECTION PROFILES FROM UKNDL, ENDF/B-IV AND PLATO(4).

simultaneous optimisation of data for uranium, plutonium, chromium, nickel, sodium etc. was also performed. A comparison of the situations in which the two adjusted data sets FD5 and PLATO(4) (data set for cycle 4) were derived is given in Table 9.13. Despite the quite different requirements of the two data sets, the comparison of the flux profiles obtained at 50.8 and 101.6 cm (Figures 9.28 and 9.29) using the FD5 data set and the ASPIS iron benchmark adjustments yields some interesting features. The FD5 profiles of the ASPIS experiment were obtained by collapsing the nuclear data for the background components of the mild steel shield with the iron data file UKNDL DFN 906B to the EURLIB-100 group structure using the GALAXY code[101]. The broad group boundaries of the 10 group LSQ adjustment scheme were co-incident with the EURLIB-100 boundaries so that the adjustments were made to the absorption and scattering (elastic + inelastic) cross-sections using the 10 group factors in LPERT. The approximations inherent in this method are that:-

(i) The effect of the weighting function on the group data is negligible.

(ii) The adjustments do not account for deficiencies in the use of diffusion theory in a heterogeneous fast reactor core.

(iii) The dimensional transformation coefficients for the shielding calculation are only weakly dependent upon the data set used in the calculation.

The flux profiles derived from the FD5 adjustments show a considerable improvement in the agreement with the unfolded flux spectrum in the region above 0.3 MeV after 50.8 cm penetration; good agreement is obtained in the proximity of the inelastic threshold and the 0.6 MeV elastic cross-section minimum. Below 0.3 MeV the FD5 profile is worse than the unadjusted DFN 908A profile. At the 101.6 cm position the agreement is much better than the unadjusted profile above 0.07 MeV, but is not as good as the PLATO(4) profile in either the 0.6 MeV window or in the inelastic threshold region. Below 0.07 MeV agreement with both the unadjusted calculation and the integral measurements is poor; a possible reason for this may be the attribution of adjustments to the iron data arising from uncertainties in the other nuclides present in the experiments - notably chromium and nickel. Arising from this poor agreement the χ^2 for the system predicted using the FD5 adjustments is larger than that for the unadjusted DFN 908A data set!

Figure 9.30 shows the results of the FD5 adjusted data set predictions for the activation detector reaction-rates. The results for rhodium are

Table 9.13

Characteristics Pertaining to the Derivation of the FD5 and PLATO(4) Adjusted Data Sets

Characteristic	FD5	PLATO(4)
Number of Groups	10	100
Source Data File	UKNDL DFN 906B	UKNDL DFN 908A
Variable Parameters	$x^{s}; x^{A}$	$x^{T}, x^{X}, x^{A}, S, g, \alpha$
Collapsing Spectrum	Typical F.R. Core Spectrum	$1/E\Sigma^{T}(E)$
Calculational Method	Diffusion Approximation	Transport Theory
Experimental Situation	Multi-Material, Heterogeneous Core	Deep Penetration, Single Material
Integral Parameters	k_{eff}, critical sizes, fission-rates, spectra.	Activation reaction-rates, spectra (proton reccil).

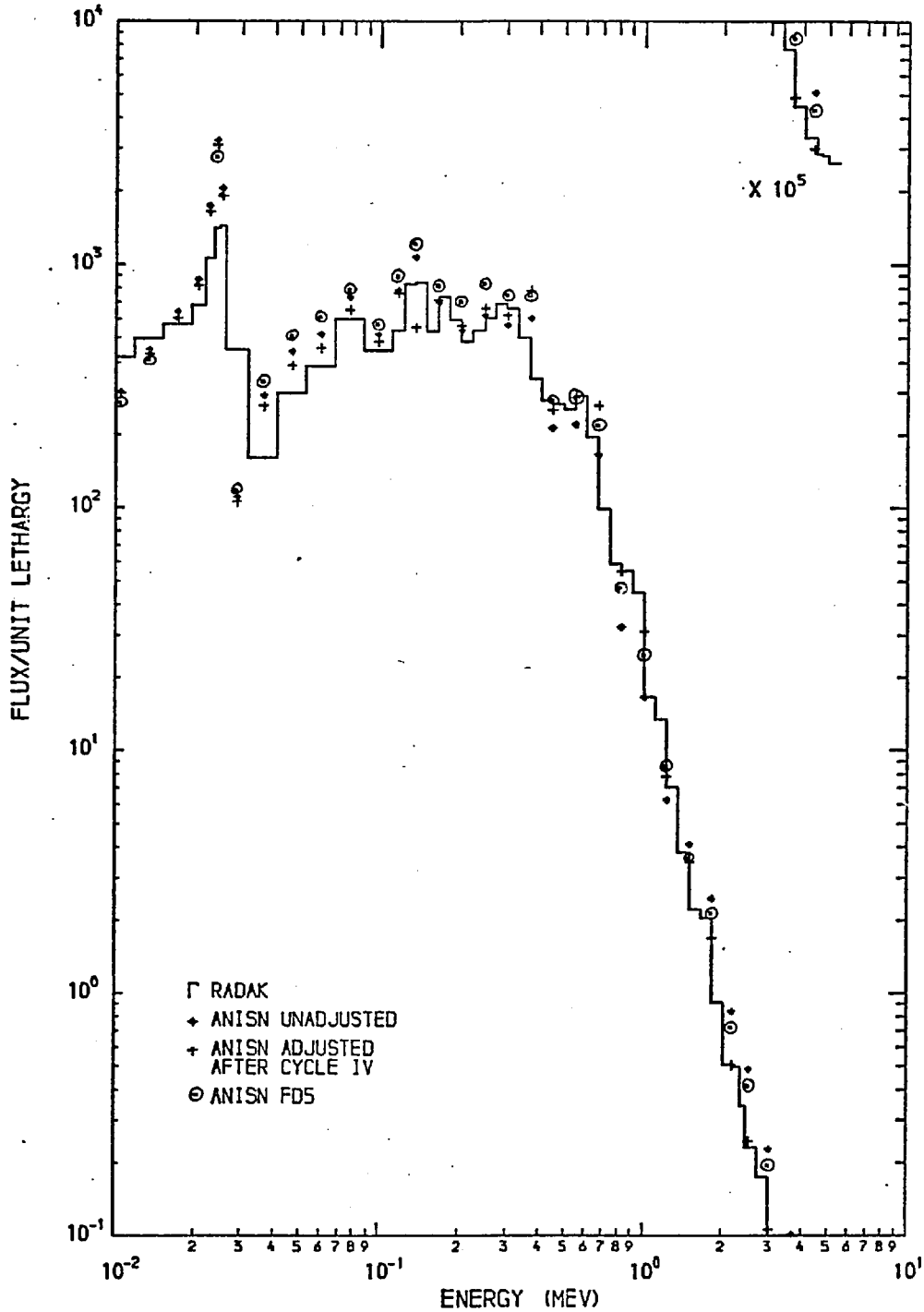


FIG. 9.28 COMPARISON OF ADJUSTED FLUX PROFILE WITH FD5 ADJUSTED DATA SET PREDICTION AT 50.8CM POSITION

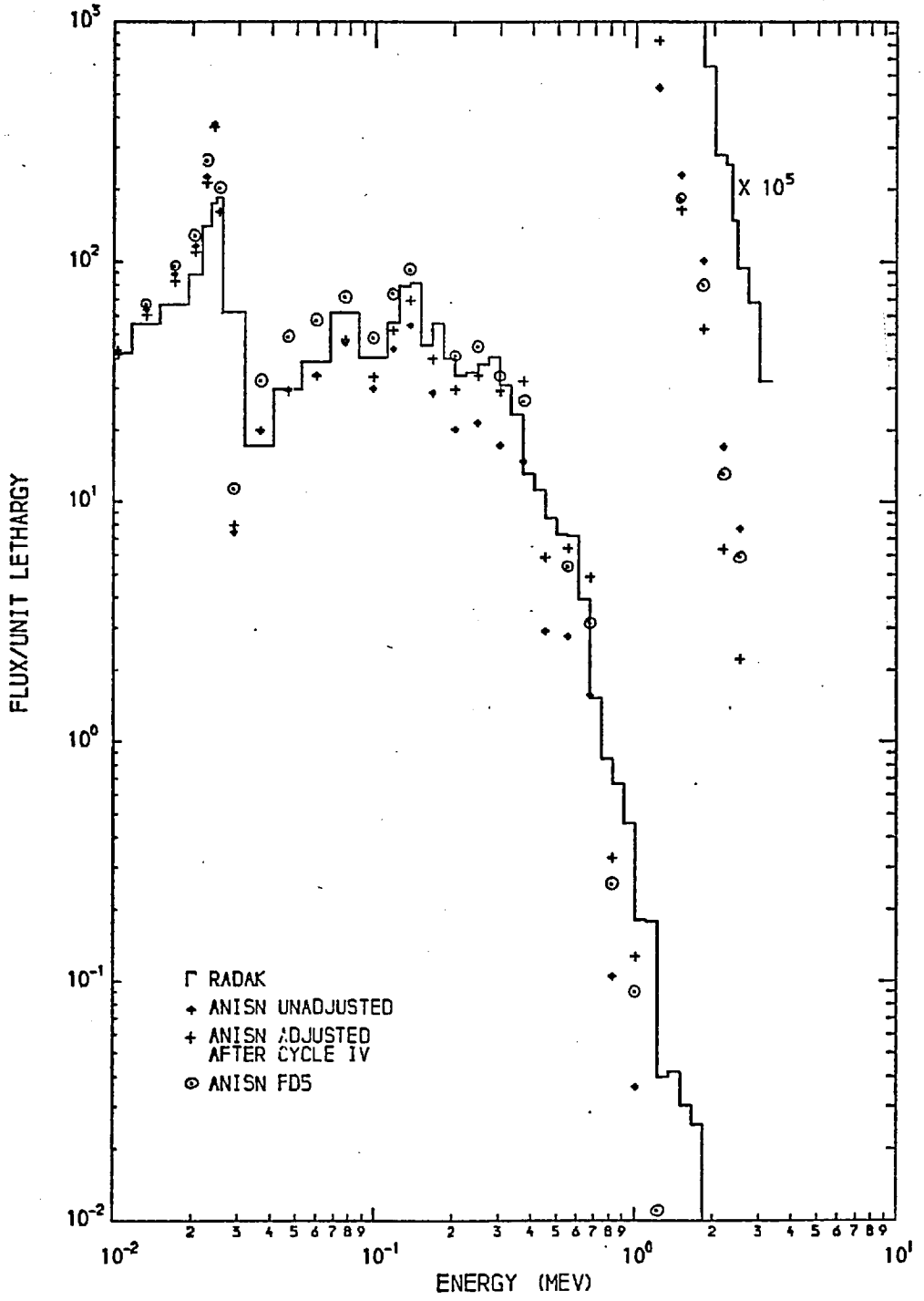


FIG. 9.29 COMPARISON OF ADJUSTED FLUX PROFILE WITH FD5 ADJUSTED DATA SET PREDICTION AT 101.6CM POSITION

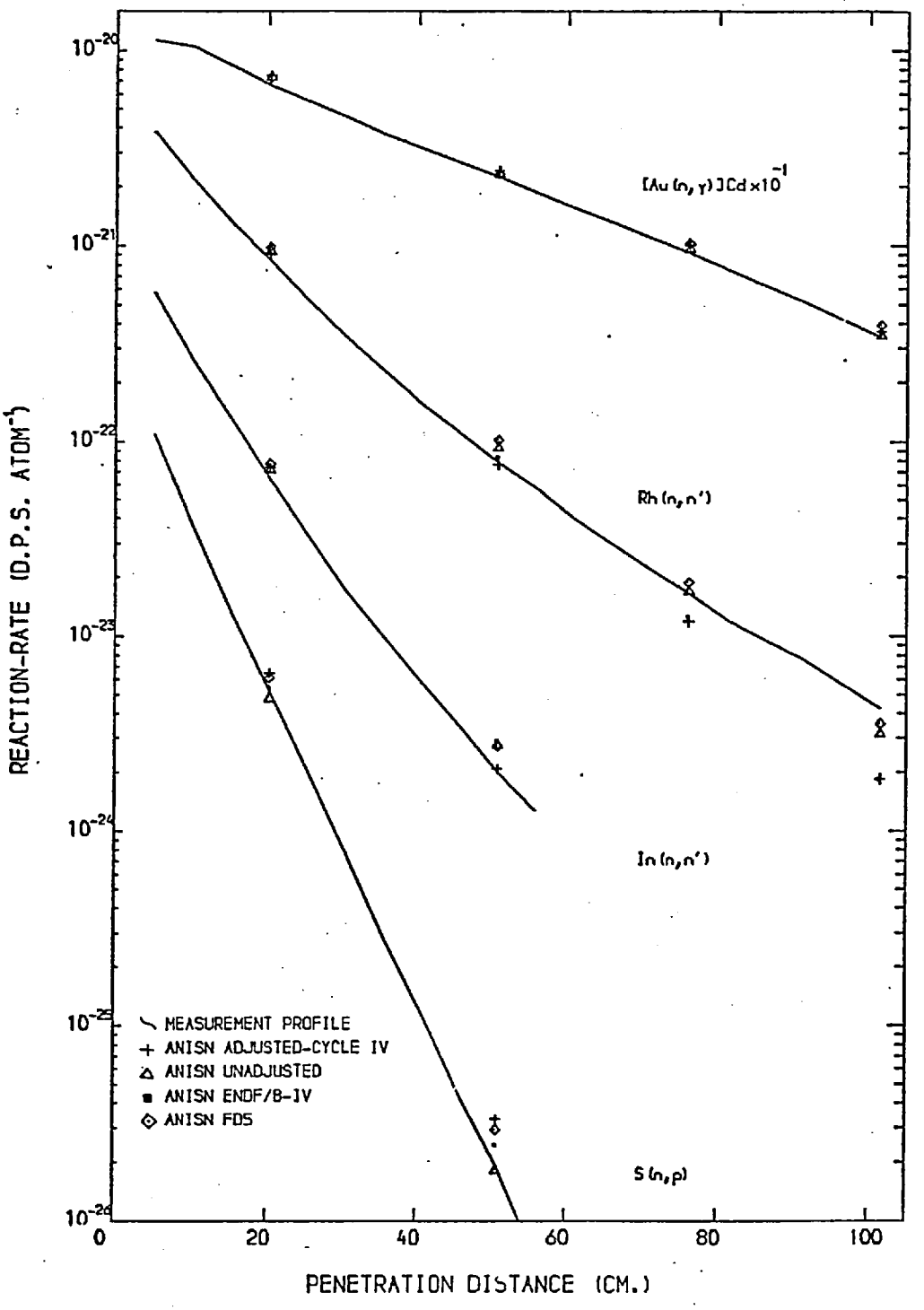


FIG. 9.30 COMPARISON OF MEASURED AND CALCULATED INTEGRAL DETECTOR REACTION-RATES FOR DIFFERENT LIBRARIES.

slightly worse at the 50.8 and 76.2 cm positions but are much better at the 101.6 cm position. For gold the results are comparable with the unadjusted predictions as would be expected since no adjustments were made to the low energy data. Similarly only small adjustments were made to the high energy data (above 1.35 MeV), so that whilst the FD5 adjusted sulphur reaction-rates are slightly better than the unadjusted values, large discrepancies nevertheless exist. The FD5 adjusted data set is compared with the unadjusted DFN 908A data set and the PLATO(4) set in Figure 9.31.

Table 9.14

Initial χ^2 Values per Degree of Freedom for Various Data Sets

Data Set	χ^2/n
UKNDL DFN 908A	39.2
EURLIB-I (ENDF/B-III)	38.4
EURLIB-III (ENDF/B-IV)	34.3
FD5	51.8
PLATO(4)	8.7

9.10 Interpretation of the Observed Adjustments

The optimisation of the iron data set using extensive measurements from the ASPIS experiment has identified three energy domains where the multi-group cross-section data is deemed to be unsatisfactory. Around 330 keV and 600 keV the total cross-section, which at these energies comprises almost entirely elastic processes, has been reduced by nearly five standard deviations; in the region of the inelastic cross-section threshold the non-elastic data has been reduced by over 2.5 standard deviations. The magnitude of these adjustments is so large that the source of these discrepancies should be sought.

One possible source is that the method of resonance averaging and the use of a global weighting function such as $1/E\Sigma^T(E)$ in the GALAXY data file processing code are entirely inappropriate in these energy domains. Hehn et al[61] have demonstrated that large changes occur in the total cross-section at ~ 300 keV and ~ 600 keV as result of changing the weighting function from the constant lethargy Fermi spectrum to the narrow resonance approximation. It is possible that the Bondarenko formalism, whilst giving a more suitable collapsing function, is still a gross simplification of the real fine structure flux. The method of resonance averaging contained in the codes has also come under criticism. In a recent

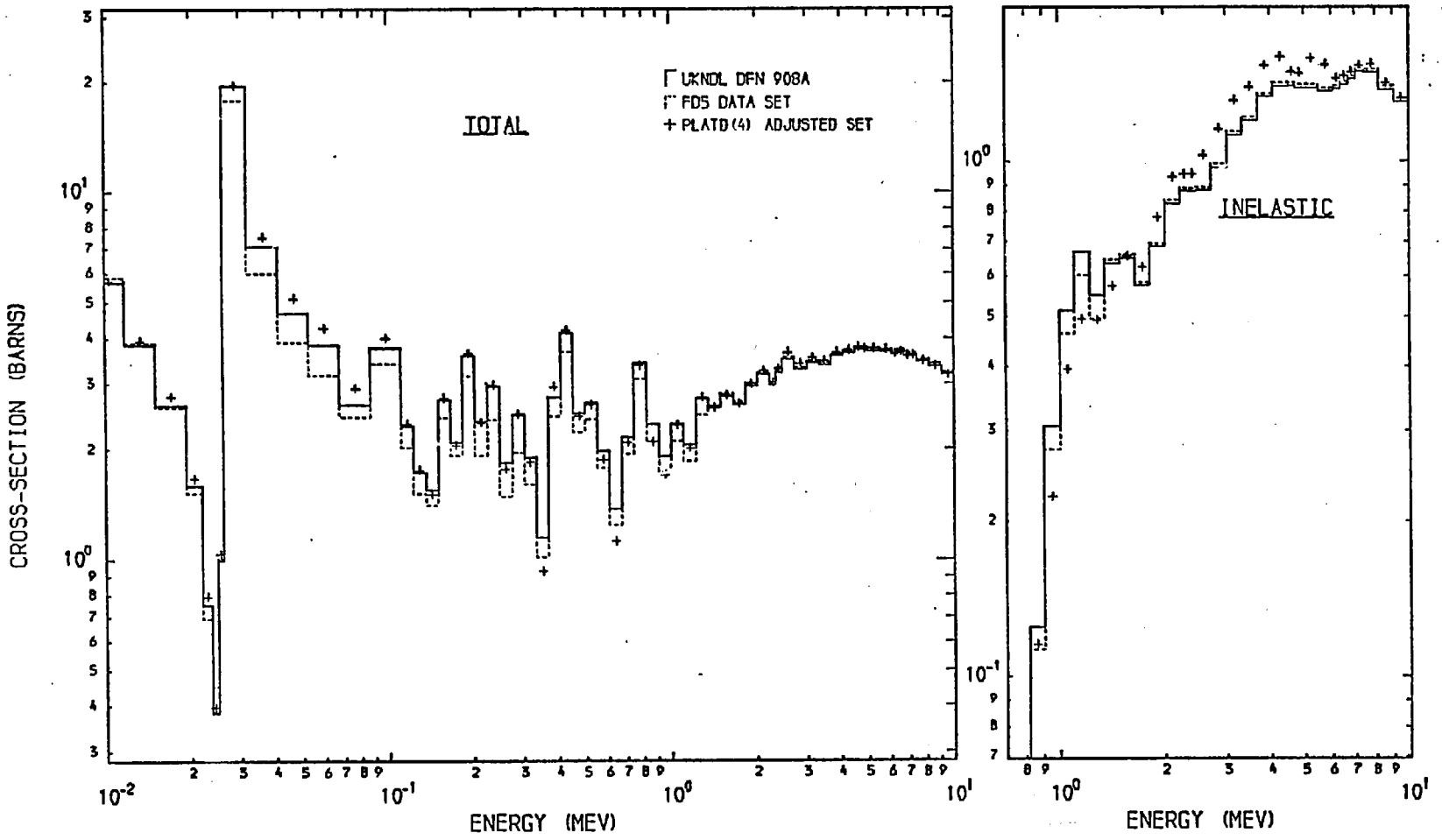


FIG. 9.31 COMPARISON OF MULTI-GROUP CROSS-SECTION PROFILES FROM UKNDL, FD5 AND PLATO(4)

fast reactor theoretical benchmark study[91], calculations submitted by three different laboratories, using ENDF/B-IV as a source library, but using different cross-section processing routes, were in gross disagreement with each other. Figure 9.32 similarly shows the multi-group iron data sets derived at two different laboratories using the AMPX[178] code system; quite large differences are observed in the regions of interest. A MISSIONARY[173] conversion of ENDF/B-IV has not been undertaken so that a GALAXY comparison with these other processed data sets has not been possible. However a comparison of the GALAXY processed UKNDL DFN 908A file which is a MISSIONARY conversion of ENDF/B-III above 330 keV with the EURLIB-I library which has been derived from ENDF/B-III using SUPERTOG[177] shows only very small differences and these may arise from the translation of the interpolation procedures to those appropriate to UKNDL format[179] rather than any difference arising from the data processing codes per se. It is recognised that the resonance averaging method in AMPX is superior to that of SUPERTOG.

A second possible explanation of the observed adjustments may be that the scalar cross-sections are absorbing errors in underlying parameters which have not been explicitly included in the statistical model. It has been inherently assumed from the outset (in the proposed statistical model) that any discrepancies observed in the transport calculation must be derived from inadequate scalar cross-section data - these are the only parameters which the model is allowed to penalise. Thus if the observed discrepancies arise from poor secondary angular distribution data or inadequate specification of the secondary energy distribution, the cause and effect are not coupled through the statistical model. Instead the effect attempts to remove the cause by modification of the scalar cross-section even though it may be perfectly adequate. In other words if the transfer probability from group j to group j', as derived from the elastic and inelastic secondary energy and angular distributions, is grossly in error (too large say), the statistical model will attempt to reach optimal consistency by a reduction in the total and non-elastic cross-sections for group j - i.e. it simply reduces the total number of events occurring in group j. A more detailed statistical model might on the other hand consider the collision density for group j to be adequately known and identify the output channel transistion probabilities to be poorly assigned; $x_{jj'}$ would therefore be reduced and the extra resulting neutrons would be distributed amongst the x_{jk} for all the other k admissable output channels.

This criticism that the model prejudges the result is entirely valid.

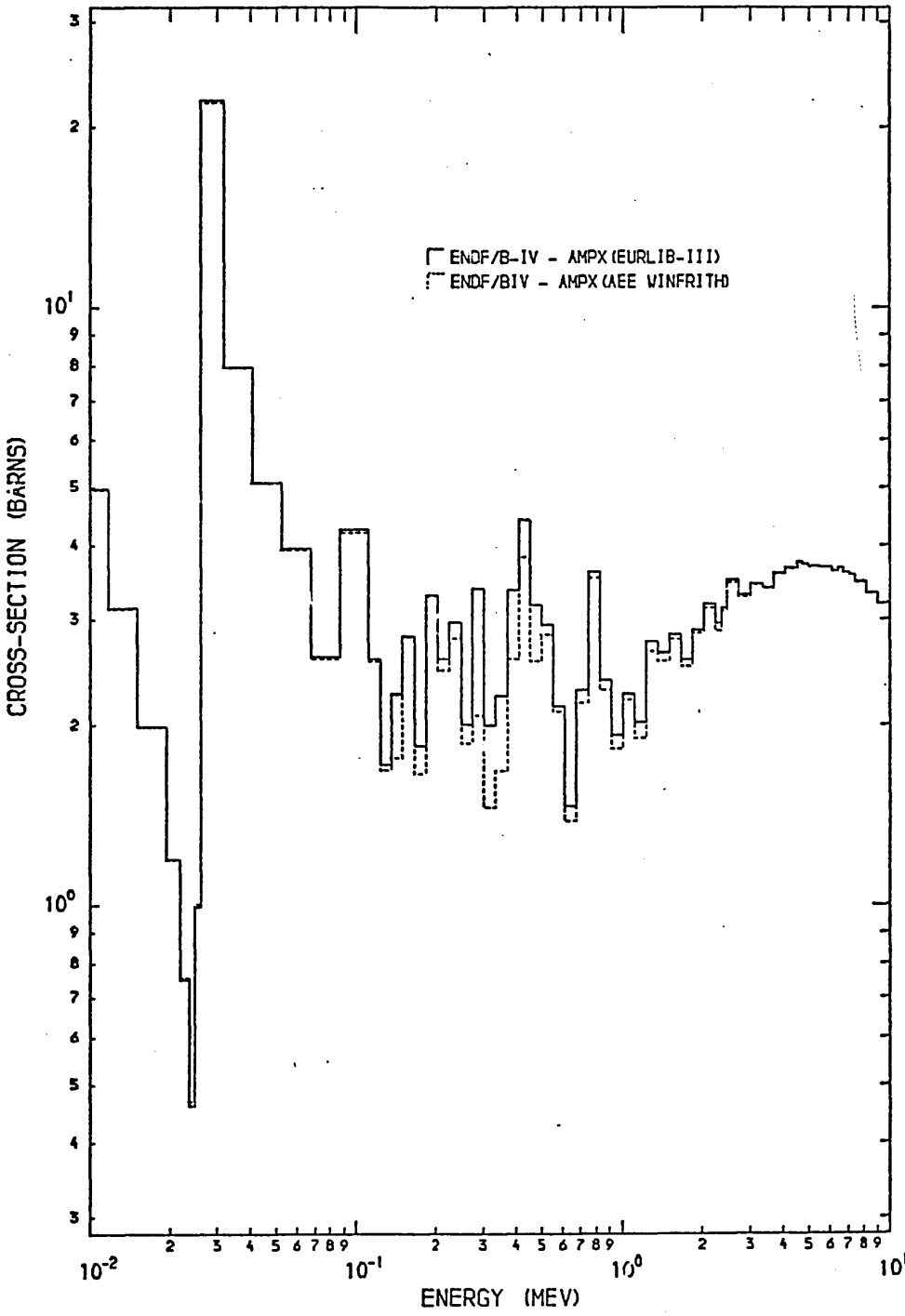


FIG. 9.32 COMPARISON OF MULTI-GROUP TOTAL CROSS-SECTIONS DERIVED FROM ENDF/B-IV USING AMPX AT DIFFERENT LABORATORIES.

The only way in which these scalar cross-section adjustments can be validated is by greater modelling resolution. The processes of elastic and inelastic scattering must be represented in greater detail in the statistical model. It is this very requirement that lead to the "Consistent Approach" of Gandini et al[88] and as mentioned previously Salvatores et al[31] have taken a subset of the ASPIS iron benchmark measurements and used the Consistent Method to adjust the secondary energy distribution for inelastic scattering in the continuum for ENDF/B-IV. Indeed the modifications to the scattering distribution predicted by Salvatores et al are such as to increase the number of neutrons being scattered to lower energies ($E \lesssim 1.5$ MeV) at the expense of those suffering less energy degradation. In the absence of any secondary parameters to adjust, the hybrid optimisation scheme has simulated this effect by increasing the proportion of inelastic scattering at higher energies thereby causing more neutrons to be injected into the lower energy groups and by reducing the proportion of inelastic scattering in the lower energy groups, thus lowering the rate of removal of neutrons from these groups. The cross-over is similarly at ~ 1.5 MeV.

In the analysis of the ORELA ring experiment for high energy neutron penetration in iron, similar results to those obtained in this study have been reported. Cramer et al[180] found that the inelastic scattering cross-section for the first three levels in ENDF/B-IV appeared to be too large by some 30 - 100% just above threshold. Moreover from 6 - 12 MeV they concluded that both the discrete and continuum inelastic data were too low by an unspecified amount. No low energy measurements were taken.

9.11 Summary

In this chapter the optimisation formalism of Chapters IV and V has been applied to the results of the ASPIS iron benchmark experiment. The PLATO suite has been shown to converge with iteration and to satisfy the χ^2 test. Adjustments have been evaluated for both the transmission and response data and the nature of these data inadequacies has been discussed. The status of the optimised parameter set has been assessed by both flux comparisons and calculated-to-observed response ratios. The information content of the detectors has been studied and the results of a single position adjustment exercise have been contrasted with the full multi-position optimisation calculation. Confirmation of the observed cross-section adjustments has been sought by comparisons with data sets derived from other libraries and from other studies of iron data cited in the literature. Finally the updated covariance matrices obtained from PLATO have been analysed and their utility in uncertainty analysis considered.

CHAPTER X

SUMMARY AND FURTHER DEVELOPMENTS

10.1 Summary

At the outset of this work the concepts of sensitivity and uncertainty analysis were introduced. It was shown that in the case of two reactor studies, the nuclear data for shielding materials were insufficiently well-known to meet the required target accuracies. Moreover widely varying estimates of the predicted target accuracy ensued from the use of different sources of cross-section error data. Consistency analysis was introduced as an expedient method for optimising the nuclear cross-section data and the associated error matrices, on the basis of comparison with observation, for subsequent use in reactor design uncertainty analysis.

During an examination of the methods of consistency analysis applied to core reactor physics, the rather different requirements of a shielding data optimisation scheme were identified. The method of solution of the transport equation and the representation of the detector response functions were considered to be a crucial part of the problem. A review of the differing philosophies adopted in the fast reactor physics domain lead to a discussion of the representation of cross-section errors; whilst the method of Mitani and Kuroi[78,81] was deemed to provide a good estimate, à priori, of the cross-section uncertainties and correlations, the technique could not be applied within the time-scale adopted for this work. The arguments for the feedback of data adjustments, derived from multi-group calculations, into basic nuclear data libraries have also been considered and this trend has been rejected because the observed adjustments usually have a multiplicity of sources of unknown magnitude, some of which may be problem dependent.

The two tier hybrid optimisation formalism developed in this work has attempted to meet the general requirements of a scheme for use in radiation shielding consistency analysis, but has kept close contact with the particular needs of the ASPIS iron benchmark analysis programme. The multi-channel detector distribution has been introduced as an efficient data reduction statistic which preserves the accuracy of the support function for the parameter set hypothesised to be appropriate to the statistical model. A methods' limitation to first order perturbation theory has made approximations to the support function necessary in order to obtain a soluble system of scores equations; an iterative solution scheme based on statistical tests has therefore been proposed. Solutions to the scores equations were derived and asymptotic theory has been used to demonstrate that physically reasonable solutions can be expected. The use of Fisher's information theory for rapid computation of the error

correlation matrices appropriate to the adjustment evaluators of a fully second order support function was noted but it was shown to be inadequate for the hybrid support function where recourse had to be made to expectation theory. Examples of the use of expectations for deriving error correlation data for various adjustment evaluators were given and the utility of the multi-channel adjoint source was again noted.

A detailed analysis of the modelling of the experiment used in the reference transport calculation has been given in an attempt to satisfy the criticisms of Goldstein[21]. Simple 1-D calculations were carried out with a view to optimising the choice of method parameters. Moreover methods of accounting for radial leakage were also examined since a methods' limitation and economic sense required a reduction to a 1-D working model for the optimisation scheme.

The survey of the detector response data included an examination of the proton recoil counter line-shapes and a comparison and assessment of the cross-section data for the activation foils. Consideration was also given to the processing of the observations into a convenient form for comparison with calculation and the integral form of the proton recoil data was used with a view to maintaining the quality of the experimental observations. The existence of an energy scale error on the unfolded flux spectrum derived using the conventional differential form of the response equation was noted and the RADAK code was used with integral response matrices to indicate the possibility of there being a method's problem near resonances.

The mathematical formalism of the hybrid optimisation scheme has been coded as the OPTOR program and implemented in the PLATO suite which interfaces the adjustment code with the cross-section group averaging program GALAXY, the DS_n code ANISN and the SWANLAKE sensitivity code.

The PLATO suite has been used to derive the data adjustments necessary to obtain consistency between neutron transport calculations based on the UKNDL DFN 908A iron data file and the measurements obtained from the ASPIS iron benchmark experiment. Comparison with other libraries showed that the adjustment trends were consistent with data contained in the ENDF/B-IV iron file and the FD5 UK adjusted fast reactor data set. Moreover the optimisation scheme provided evidence that the observations did not contain any significant energy scale calibration error affording further support for the adoption of an integral unfolding formalism.

10.2 à Posteriori Uncertainty Analysis

An important theme throughout this work has been the use of consistency analysis as an expedient for providing improved nuclear data for

uncertainty analysis. In Chapter II the results of two NEA theoretical benchmarks were reviewed and it is now appropriate to examine what reduction in the uncertainty arising from iron data can be obtained using the à posteriori covariance data compared with the rather artificial à priori independent group model used as a starting matrix for the optimisation scheme. Table 10.1 displays the components of the expected fractional uncertainty on the design parameters specified for the NEA PWR and FBR theoretical benchmarks as a result of optimising the iron cross-section data using consistency analysis. Only the changes arising from the use of the updated variance-covariance data have been considered. The largest contribution still appears to arise from the variances on the partial cross-section data; the effect of the negative correlations between cross-sections of the same type - the so-called 'self-correlation' - injected as a result of the constrained optimisation is to some extent off-set by the increase in the variances for a few group cross-sections which are considered inconsistent with the observations. The 'cross-correlation' data, representing the non-observational correlations injected between the independently measured cross-section parameters, contribute only a small amount to the total uncertainty.

The rather small changes in uncertainty for the PWR and FBR theoretical benchmark target quantities arise mainly from a lack of sensitivity to the energy regions where the PLATO suite has adjusted the data. Moreover the sensitivity to the changes around the 330 keV region has been mitigated by the lack of resolution of the EURLIB-42 group structure used by Lympany et al[22,50] for the sensitivity calculations.

Table 10.1

Comparison of NEA Theoretical Benchmark Design Parameter Uncertainties Derived from the Use of à Priori and à Posteriori Error Correlation Matrices

Matrix	Component	Fractional Uncertainty $\sigma(R)/R$		
		FBR Na Activation	FBR Damage	PWR Damage
Initial	Independent	4.45 -2	3.33 -2	2.08 -2
	Cross-Correlation	-	-	-
	Total	4.45 -2	3.33 -2	2.08 -2
Cycle 1	Independent	5.29 -2	3.86 -2	2.39 -2
	Cross-Correlation	2.09 -2	1.33 -2	9.64 -3
	Total	5.68 -2	3.62 -2	2.58 -2
Cycle 3	Independent	3.63 -2	3.30 -2	2.35 -2
	Cross-Correlation	4.93 -3	5.68 -3	2.13 -3
	Total	3.59 -2	3.25 -2	2.36 -2

The data of Table 10.1 should only be considered in relative terms as the regions where the sensitivity of a particular generic design parameter is greatest correspond to energy domains where the à posteriori error correlation matrix is largely dominated by the à priori variance data and as such will be dependent upon the propriety of the independent group cross-section model with variances taken from Schmidt[36]. Moreover continued iteration should reduce the uncertainties still further.

10.3 Further Improvements and Extensions

The primary achievement of this work has been the development of a method of data adjustment for radiation shielding. The coding of this method and subsequent application of the PLATO suite on the measurements obtained from the ASPIS iron benchmark experiment has served to validate the theoretical formalism. There remain however several areas where either further development could prove useful or further investigations should be conducted:

(i) A second order flux perturbation treatment should be developed and implemented in SWANLAKE so that the full second order support function could be exploited. This would relax the requirement for a scaling parameter in the AXSEC module of OPTOR and would lead to more rapid convergence. Moreover the exact second order method would allow the use of Fisher's information as a more direct method to evaluating the updated error data for the optimised parameter set.

(ii) The ASPIS iron benchmark data optimisation should be extended to cover the activation foil response data so that the quality of the S(n,p), In(n,n') and Rh(n,n') cross-sections can be assessed. The optimisation should also be continued until satisfactory convergence - no significant change in χ^2 say - is obtained.

(iii) The statistical model should be extended to admit the parameters of the secondary energy and angular distributions as adjustable variables. This would probably necessitate the inclusion of a code such as MC^2 in the PLATO suite.

(iv) The influence of different à priori cross-section error data should be assessed and a full optimisation of ENDF/B-V iron with the evaluated error correlation file should be undertaken to establish the adequacy of the new file.

(v) The PLATO code suite should be tested for theoretical consistency by the injection of small "mistakes" into the nuclear data; the code should be used to identify the position and magnitude of

these mistakes on the basis of a comparison with pseudo-measurements derived from the unaltered file.

(vi) The consistency of the results derived from the ASPIS iron benchmark experiment should be checked by use of other benchmark quality data taken either from the ENDF/B Benchmark Handbook[181] or other experiments within the NEA/OECD Collaborative Benchmark Programme.

(vii) Point energy Monte Carlo calculations should be included in the PLATO suite in order to assess the influence of the weighting function on the predicted data adjustments.

(viii) Since stainless steel is a major component in fast reactors, a small stainless steel benchmark experiment should be mounted with a view to determining whether the adjustments made to the iron data are sufficient to allow adequate prediction of target quantities in stainless steel. A laminated iron and stainless steel experiment might be used to assess the influence of decreasing iron content on the prediction of integral parameters. If the predictions are strongly dependent on the iron concentration, then the adjustment of the data for the pseudo-material, stainless steel, would be considered unwise because of the variations in stainless steel compositions used in different reactors.

The NEA/OECD Collaborative Benchmark Exercise for iron has been a testing ground for transport methods, experimental procedures, nuclear data files and adjustment philosophies. The importance attached to the investigation of iron has been considerable because of its dual rôle as a shielding medium and as a structural material; a knowledge of the cross-section data is important therefore both from the viewpoint of predicting the flux at a particular position in the reactor and for establishing the effectiveness of that flux in producing materials damage in components. The global data testing qualities of the iron benchmark arose mainly because no clear indication of the data requirements for iron in radiation shielding had been identified by the start of the benchmark programme; elucidation of some of the data requirements had to await the subsequent performance of rough generic design uncertainty calculations. It seems likely that the insight obtained from uncertainty analysis will severely moderate the scope of future benchmarks, which may well resemble the design situation mock-ups of old, testing methods and data only over very limited energy ranges.

Appendix A

The Diagnostic Fractional Energy Shift Evaluator for Neutron Spectrometers

A.1 Introduction

A discussion of the nature of the uncertainty in the energy scale assignment to the pulse height analyser distribution of recoil protons obtained for a neutron spectrometer and the way in which it can arise has been given in Chapter VII. Moreover it was emphasised that the energy scale calibration errors for these counters can often be misinterpreted as displaying inadequacies in the neutron transmission data. It is therefore important to be able to quantify, at least to an order of magnitude, the size of the likely energy scale error. If the energy scale error is small it may be neglected and omitted from further optimisation cycles; on the other hand if it is non-negligible, either some correction must be made to the model prior to optimisation or the data must be discarded as being inappropriate to the model.

A.2 Calculation of the Response Function Adjustment in the Bulk Matrix

Consider the matrix element a_{qij} which represents the probability of producing a recoil proton with energy between E_i and E_{i+i} per unit group j neutron flux where group j (E_j to E_{j+1}) is a region on the response plateau away from the threshold. The group boundaries chosen for the recoil protons are initially those assumed through the energy scale calibration to be appropriate to the bins into which the measured pulse height distribution has been grouped. The essence of the optimisation process is to assess the most likely value for the energy boundaries of the measurement channels and to calculate the appropriate adjustments for the elements of the response matrix. The energy calibration error is assumed to be a fractional error applicable to all the signal channels of a particular counter. In general it will be different for the various spectrometers. If $b_j(E)$ is the proton density distribution per unit neutron flux in group j, then by the trapezium rule:

$$a_{qij} = \frac{\left[b_j(E_i) + b_j(E_{i+1}) \right]}{2} (E_{i+1} - E_i) \qquad \text{A.2.1}$$

and

$$\delta a_{qij} = \frac{1}{2}\left[\left(\delta b_j(E_i) + \delta b_j(E_{i+1}) \right) \Delta E_i + \left(b_j(E_i) + b_j(E_{i+1}) \right) \delta \Delta E_i \right] \qquad \text{A.2.2}$$

Now

$$\delta b_j(E_i) = \left. \frac{\partial b_j(E)}{\partial E} \right|_{E_i} \cdot \delta E_i \qquad \text{A.2.3}$$

which in the finite difference approximation can be expressed as:

$$\left.\frac{\partial b_j(E)}{\partial E}\right|_{E_i} = \left\{\frac{a_{qij}}{\Delta E_i} - \frac{a_{qi-1j}}{\Delta E_{i-1}}\right\} \Big/ \left\{\frac{\Delta E_i + \Delta E_{i-1}}{2}\right\} \qquad \text{A.2.4}$$

Thus if the fractional energy scale calibration error is assumed to be g_q:

$$g_q = \frac{\delta E_i}{E_i} \qquad \text{for all } E_i \text{ and all } i \in q \qquad \text{A.2.5}$$

then:

$$\delta a_{qij} = \frac{\Delta E_i}{2}\left\{\frac{\left[\frac{a_{qi+1j}}{\Delta E_{i+1}} - \frac{a_{qij}}{\Delta E_i}\right]}{(\Delta E_{i+1} + \Delta E_i)/2} g_q E_{i+1} + \frac{\left[\frac{a_{qij}}{\Delta E_i} - \frac{a_{qi-1j}}{\Delta E_{i-1}}\right]}{(\Delta E_i + \Delta E_{i-1})/2} g_q E_i\right\} + \frac{a_{qij}}{\Delta E_i} g_q \Delta E_i$$

.....A.2.6

$$= \left\{\frac{(\Delta E_i a_{qi+1j} - \Delta E_{i+1} a_{qij}) E_{i+1}}{\Delta E_{i+1}(\Delta E_{i+1} + \Delta E_i)} + \frac{(\Delta E_{i-1} a_{qij} - \Delta E_i a_{qi-1j}) E_i}{\Delta E_{i-1}(\Delta E_i + \Delta E_{i-1})} + a_{qij}\right\} g_q$$

.....A.2.7

which for concision may be re-written as:

$$\delta a_{qij} = \}_{qij}\, g_q \qquad \text{A.2.8}$$

This treatment should be precise for the bulk matrix; near the threshold, where in a flat flux spectrum the reaction-rate would be greatest, corrections to this treatment may be necessary.

A.3 A Single Channel Detector Near Threshold

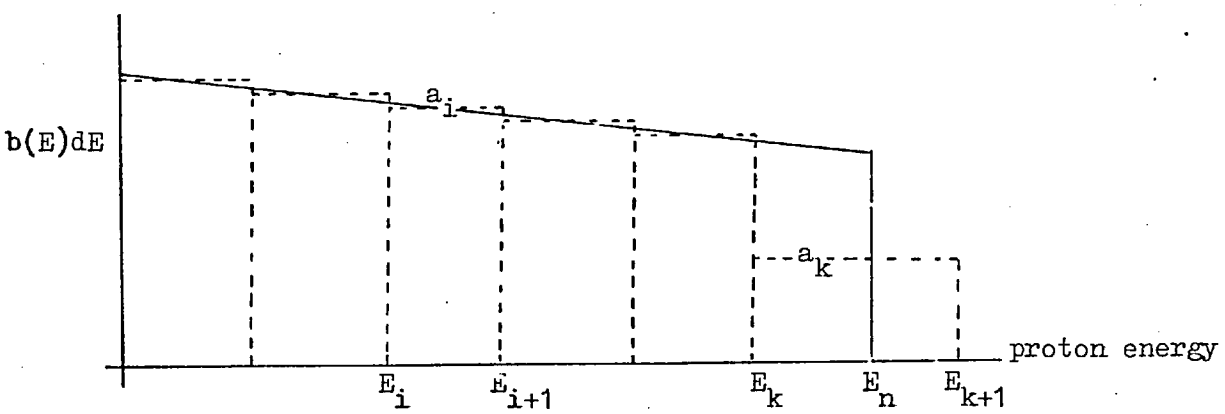


Figure A.1 Proton Recoil Detector Line-Shape for Neutron Energy E_n.

Consider the single channel E_k to E_{k+1} for a neutron energy E_n ($\simeq(E_k+E_{k+1})/2$). The recoil proton density per unit group flux in neutron group n is characterised by a_{qkn}. Now if $g_q < 0$:

$$a_{qkn} + \delta a_{qkn} = \int_{E'_k}^{E'_{k+1}} b_n(E)\,dE > a_{qkn} \qquad \text{A.3.1}$$

where E'_k and E'_{k+1} are the new boundary energies. The value of the integrand at $E'_{k+1} = E_n$ is fixed. Thus the change to only one boundary need be computed in $\mathfrak{Z}_{qij}$. The gradient across the boundary at E'_k cannot be explicitly computed without amending equation A.2.4 and so it is assumed to be the same as at E_{k-1}. It should be noticed that if the energy scale calibration uncertainty is so large that the proton energy scale is translated by more than half a group for any one group:

$$|g_q| = \frac{\Delta E_i}{(E_i + E_{i+1})} \qquad \text{A.3.2}$$

(about 5 - 14% for the EURLIB-100 group scheme) then the analysis is no longer accurate as the proton line-shape threshold will have moved into a contiguous group.

Appendix B

The Evaluates of the Linear Support Function

The analysis given here is essentially the same as that of Chestnutt and McCracken[106]. Consider the support function of a simplified statistical model in which adjustments to the source normalisation and the neutron spectrometer energy scale calibration have been neglected. Then:

$$\ln L(\underline{C}|\underline{M},\underline{\alpha},A\,\&\,\{\underline{x}^p\}) = -\sum_q\sum_{i\in q}\frac{(C_i-M_i+\delta C_i)^2}{2\sigma^2(M_i)} - \frac{1}{2}\sum_q\left\{\frac{\delta\alpha_q}{\sigma(\alpha_q)}\right\}^2 - \frac{1}{2}\sum_q\sum_{i\in q}\sum_j\left\{\frac{\delta a_{qij}}{\sigma(a_{qij})}\right\}^2 - \frac{1}{2}\sum_P\sum_k\left\{\frac{\delta x_k^p}{\sigma(x_k^p)}\right\}^2 \quad \text{.....B.1.1}$$

The adjustment to the predicted value of the integral response, δC_i, may be expanded to first order as:

$$\delta C_i = \frac{\delta\alpha_q}{\alpha_q}C_i + \alpha_q\sum_j\left(\delta a_{qij}\,\phi_j + a_{qij}\,\delta\phi_j\right) \qquad \text{B.1.2}$$

Substituting into the support expression and neglecting the second order term in δC_i:

$$\ln L(\underline{C}|\underline{M},\underline{\alpha},A\,\&\,\{\underline{x}^p\}) \simeq -\sum_q\sum_{i\in q}\left\{\frac{(C_i-M_i)^2}{2\sigma^2(M_i)} + \frac{(C_i-M_i)C_i\,\delta\alpha_q}{\sigma^2(M_i)\,\alpha_q} + \frac{(C_i-M_i)\alpha_q}{\sigma^2(M_i)}\sum_j\left(\delta a_{qij}\,\phi_j + a_{qij}\,\delta\phi_j\right)\right\} - \frac{1}{2}\sum_q\left\{\frac{\delta\alpha_q}{\sigma(\alpha_q)}\right\}^2 - \frac{1}{2}\sum_q\sum_{i\in q}\sum_j\left\{\frac{\delta a_{qij}}{\sigma(a_{qij})}\right\}^2 - \frac{1}{2}\sum_P\sum_k\left\{\frac{\delta x_k^p}{\sigma(x_k^p)}\right\}^2 \qquad \text{B.1.3}$$

Choosing the multi-channel detector distribution as:

$$H_j^+ = \sum_q\sum_{i\in q}\frac{(C_i-M_i)\alpha_q\,a_{qij}}{\sigma^2(M_i)} \qquad \text{B.1.4}$$

and expanding the term $\underline{\delta\phi}$ in a complete set of cross-section adjustment evaluates:

$$\ln L(\underline{c}|\underline{m},\underline{\alpha},A\,\&\,\{\underline{x}^p\}) = -\sum_q\sum_{i\epsilon q}\frac{(c_i-m_i)^2}{2\sigma^2(m_i)} - \sum_q\sum_{i\epsilon q}\sum_j\frac{(c_i-m_i)\,\delta a_{qij}\,\phi_j\,\alpha_q}{\sigma^2(m_i)}$$

$$-\sum_q\sum_{i\epsilon q}\frac{(c_i-m_i)\,c_i\,\delta\alpha_q}{\sigma^2(m_i)\,\alpha_q} - h\sum_p\sum_k\frac{\Gamma_k^{p,h}}{x_k^p}\delta x_k^p - \frac{1}{2}\sum_q\left\{\frac{\delta\alpha_q}{\sigma(\alpha_q)}\right\}^2 - \frac{1}{2}\sum_p\sum_k\left\{\frac{\delta x_k^p}{\sigma(x_k^p)}\right\}^2$$

$$-\frac{1}{2}\sum_q\sum_{i\epsilon q}\sum_j\left\{\frac{\delta a_{qij}}{\sigma(a_{qij})}\right\}^2 \qquad \text{B.1.5}$$

Differentiating to obtain the maximum likelihood evaluates for the partition coefficients, response cross-sections and transmission cross-sections respectively:

$$\delta\alpha_q = -\sum_{i\epsilon q}\frac{(c_i-m_i)\,c_i}{\sigma^2(m_i)\,\alpha_q}\,\sigma^2(\alpha_q) \qquad \text{B.1.6}$$

$$\delta a_{qij} = -\frac{(c_i-m_i)\,\alpha_q}{\sigma^2(m_i)}\,\sigma^2(a_{qij})\,\phi_j \quad \text{for } q\epsilon q_f\,,\ i=1 \qquad \text{B.1.7}$$

$$\delta x_k^p = -h\,\Gamma_k^{p,h}\,\frac{\sigma^2(x_k^p)}{x_k^p} \qquad \text{B.1.8}$$

It can be seen that these linear evaluators are unscaled for the magnitude of the adjustments they predict is entirely dependent upon the number of signal channels included in the optimisation, especially if the summation is extended to include multi-position data in which case it is clear that:

$$\delta\alpha_q = -\sum_\tau\sum_{i\epsilon q}\frac{(c_{i,\tau}-m_{i,\tau})\,c_{i,\tau}}{\sigma^2(m_{i,\tau})\,\alpha_q}\,\sigma^2(\alpha_q) \qquad \text{B.1.9}$$

$$\delta a_{qij} = -\sum_\tau\frac{(c_{i,\tau}-m_{i,\tau})\,\alpha_q}{\sigma^2(m_{i,\tau})}\,\phi_{j,\tau}\,\sigma^2(a_{qij}) \qquad \text{B.1.10}$$

$$\delta x_k^p = -h\,\Gamma_k^{p,h}\,\frac{\sigma^2(x_k^p)}{x_k^p} \qquad \text{B.1.11}$$

where h and $\Gamma_k^{p,h}$ are now appropriate to the detector distribution:

$$H_{j,\tau}^{+} = \sum_q\sum_{i\epsilon q}\frac{(c_{i,\tau}-m_{i,\tau})\,\alpha_q\,a_{qij}}{\sigma^2(m_{i,\tau})} \qquad \text{B.1.12}$$

Appendix C

Consideration of the Second Order Terms in the Support Function for the Transmission Cross-Section Adjustment Evaluators

To simply the analysis it will be assumed that the prior information about the detector response data is of very high quality and is supported by the experimental information. Thus $\sigma(\underline{\alpha}) \to 0$, $\sigma(g) \to 0$, $\sigma(a_{qij}) \to 0$ and $\sigma(S) \to 0$ such that $\delta\underline{\alpha}$, $\underline{g}$, δA and δS are null adjustment evaluates. For such a case the support equation 4.5.12 reduces to:

$$\ln L(\underline{c}|\underline{m},\underline{\alpha},A,\underline{g},S\,\&\,\{\underline{x}^{\rho}\}) = -\sum_{q}\sum_{i\epsilon q}\frac{1}{2\sigma^2(m_i)}\left\{(c_i-m_i)^2 + 2(c_i-m_i)S\alpha_q\sum_{j}a_{qij}\delta\phi_j + \left[S\alpha_q\sum_{j}a_{qij}\delta\phi_j\right]^2\right\} - \frac{1}{2}\sum_{K}\left\{\frac{\delta x_K^A}{\sigma(x_K^A)}\right\}^2 + \left\{\frac{\delta x_K^x}{\sigma(x_K^x)}\right\}^2 + \left\{\frac{\delta x_K^T}{\sigma(x_K^T)}\right\}^2 \qquad \text{C.1.1}$$

Then if in analogy with equation 4.5.8 adjoint sources are chosen as:

$$H_j^{+} = \sum_{q}\sum_{i\epsilon q}\frac{(c_i-m_i)}{\sigma^2(m_i)}S\alpha_q\,a_{qij} \qquad \text{C.1.2}$$

and

$$S_j^{+} = a_{qij} \qquad \text{C.1.3}$$

the support function can be written as:

$$\ln L(\underline{c}|\underline{m},\underline{\alpha},A,\underline{g},S\,\&\,\{\underline{x}^{\rho}\}) = -\sum_{q}\sum_{i\epsilon q}\frac{(c_i-m_i)^2}{2\sigma^2(m_i)} - \sum_{\rho}\left\{h\sum_{k}\Gamma_k^{\rho,h}\frac{\delta x_k^{\rho}}{x_k^{\rho}} + \sum_{q}\sum_{i\epsilon q}\frac{c_i^2}{2\sigma^2(m_i)}\sum_{l}\Gamma_l^{\rho,c_i}\frac{\delta x_l^{\rho}}{x_l^{\rho}}\sum_{m}\Gamma_m^{\rho,c_i}\frac{\delta x_m^{\rho}}{x_m^{\rho}} + \frac{1}{2}\sum_{k}\left[\frac{\delta x_k^{\rho}}{\sigma(x_k^{\rho})}\right]^2\right\} \qquad \text{.....C.1.4}$$

so that the support equation for δx_j^{ρ} is:

$$\frac{h\,\Gamma_j^{\rho,h}}{x_j^{\rho}} + \sum_{q}\sum_{i\epsilon q}\frac{c_i^2}{\sigma^2(m_i)}\sum_{l}\Gamma_l^{\rho,c_i}\frac{\delta x_l^{\rho}}{x_l^{\rho}}\cdot\frac{\Gamma_j^{\rho,c_i}}{x_j^{\rho}} + \frac{\delta x_j^{\rho}}{\sigma^2(x_j^{\rho})} = 0 \qquad \text{C.1.5}$$

and thus:

$$\sum_{l}\left\{\left[\sum_{q}\sum_{i\in q}\frac{c_i^2\,\Gamma_j^{\rho,c_i}}{\sigma^2(m_i)\,x_j^{\rho}}\right]\frac{\Gamma_l^{\rho,c_i}}{x_l^{\rho}}+\frac{\delta_{lj}}{\sigma^2(x_j^{\rho})}\right\}\delta x_l^{\rho}=-\frac{h\,\Gamma_j^{\rho,h}}{x_j^{\rho}} \qquad \text{C.1.6}$$

If the prior information on the cross-section is assumed to be of poor quality, corresponding to $\sigma(x_j^p)\to\infty$ and a simplified one group, one measurement situation is considered then:

$$\delta x^{\rho}=\frac{-h\,\Gamma^{\rho,h}/x^{\rho}}{\frac{c^2}{\sigma^2(m)}\,\frac{(\Gamma^{\rho,c})^2}{x^{\rho 2}}} \qquad \text{C.1.7}$$

$$\frac{\delta x^{\rho}}{x^{\rho}}=-\frac{(c-m)\,\Gamma^{\rho,h}}{c\,(\Gamma^{\rho,c})^2} \qquad \text{C.1.8}$$

and since $\Gamma^{\rho,h}=\Gamma^{\rho,c_i}$ for i = 1:

$$\frac{\delta x^{\rho}}{x^{\rho}}=-\frac{(c-m)}{c}\,\frac{1}{\Gamma^{\rho,c}} \qquad \text{C.1.9}$$

$$\frac{(c-m)}{c}=-\Gamma^{\rho,c}\,\frac{\delta x^{\rho}}{x^{\rho}} \qquad \text{C.1.10}$$

which is just the definition of the sensitivity function $\Gamma^{\rho,c}$. This is to be expected since although the original support function was truly second order, the terms in $\underline{\delta\phi}$ have been transformed using a first order expansion in the cross-section adjustment evaluators. For this reason the solution C.1.6 represents only pseudo-second order theory.

Appendix D

An Analysis of the Renormalisation Acceleration Techniques in DOT-III

D.1 Space Independent Scaling

The method of space independent renormalisation is based upon the observation that if the neutron density in the system is conserved between iterations, the rate of convergence is increased and the dominance ratio changes to the second largest eigenvalue of the transport within-group scattering operator[114]. In symbolic operator algebra the loss-rate for any iteration i and group j is:

$$\left[\hat{L}_j + \hat{\Sigma}_j^R \right] \phi_j^{(i)} \quad \neq \quad \left[\hat{L}_j + \hat{\Sigma}_j^R \right] \phi_j^{(i-1)} \qquad \text{D.1.1}$$

where $\hat{L}_j$ and $\hat{\Sigma}_j^R$ are the group leakage and removal operators respectively. For conservation of group neutron density, a scaling factor, f, must be introduced.

$$\left[\hat{L}_j + \hat{\Sigma}_j^R \right] f_j^{(i)} \phi_j^{(i)} \quad = \quad S_j \qquad \text{D.1.2}$$

and if the iterative algorithm is written as:

$$\left[\hat{L}_j + \hat{\Sigma}_j^R + \hat{\Sigma}_j^s \right] \phi_j^{(i)} \quad = \quad S_j + \hat{\Sigma}_j^s \phi_j^{(i-1)} \qquad \text{D.1.3}$$

then

$$f_j^{(i)} \quad = \quad \frac{S_j}{S_j + \hat{\Sigma}_j^s \left(\phi_j^{(i-1)} - \phi_j^{(i)} \right)} \qquad \text{D.1.4}$$

In problems involving large attenuation factors, the scale factor $f_j^{(i)}$ is dominated by the source since in that region the fluxes are generally largest:

$$\hat{\Sigma}_j^s \left(\phi_j^{(i-1)} - \phi_j^{(i)} \right) \quad = \quad \int_\tau \Sigma_j^s \left(\phi_{j(\underline{r})}^{(i-1)} - \phi_{j(\underline{r})}^{(i)} \right) d\underline{r} \qquad \text{D.1.5}$$

Moreover, the source flux tends to converge easily and after relatively few iterations, the scale factor approaches unity so that although the source fluxes have converged, the fluxes in the zone of interest, many mean free paths distant from the source will not, and the method offers

no further assistance to the calculation.

D.2 Space Dependent Scaling

The application of a single universal scaling factor quickly becomes useless in attenuation problems because of the dominance of the source. If, on the other hand, a seperate scaling factor $f_{l,m}$ exists for all mesh intervals l,m in a 2-D problem, then the method becomes decoupled from the source and the assistance to convergence for a particular interval then depends only on the convergent behaviour of that interval - that is on $(\phi_{lm}^{(i-1)} - \phi_{lm}^{(i)})$. The extension of the treatment of section D.1 for individual mesh intervals is obvious if the 2-D Boltzmann transport equation is written as:

$$\hat{L}I_{l-1,m}^{(i)} + \hat{L}I_{l+1,m}^{(i)} + \hat{L}I_{l,m-1}^{(i)} + \hat{L}I_{l,m+1}^{(i)} + \hat{L}O_{l,m}^{(i)} + \hat{\Sigma}^{R}\phi_{l,m}^{(i)} + \hat{\Sigma}^{S}\phi_{l,m}^{(i)} = S_{l,m} + \hat{\Sigma}^{S}\phi_{l,m}^{(i-1)} \quad \text{.....D.2.1}$$

where $\hat{L}I$ and $\hat{L}O$ represent the incoming and outgoing scalar leakage at the spatial phase space cell boundaries. The point dependent scaling factors are introduced logically so that:

$$f_{l-1,m}\hat{L}I_{l-1,m}^{(i)} + f_{l+1,m}\hat{L}I_{l+1,m}^{(i)} + f_{l,m+1}\hat{L}I_{l,m+1}^{(i)} + f_{l,m-1}\hat{L}I_{l,m-1}^{(i)}$$

$$+ f_{lm}\left(\hat{L}O_{lm}^{(i)} + \hat{\Sigma}^{R}\phi_{lm}^{(i)}\right) = S_{lm} \quad \text{D.2.2}$$

and can be determined from D.2.2 iteratively. The method of space dependent scaling was first introduced by Mynatt and Engle[126] and Mynatt[114] has cited studies where the method has reduced the computational effort by greater than a factor 5. The methods of space independent renormalisation and space dependent scaling have been investigated by the author for a simplified model of the iron benchmark. The model consisted of an iron cylinder 70 cm in axial length with a fission source at one end. Only the convergence rate of the first, high energy, group with dominance ratio equal to 0.58 was considered.

Table D.1

Maximum Flux Deviation for Group 1 after 20 Iterations

Convergence Test Used	Space Independent Renormalisation	Space Dependent Scaling
Integral Volume	2.8 -2	2.2 -2
Point Flux	3.0 -1	2.5 -1

The method of space dependent scaling can become numerically unstable. If the equations for solution for the set $\{f^j_{lm}\}$ are ill-conditioned, or unstable, the error in the resultant f^j_{lm} for a particular flux group j can be comparable to or greater than the error in the flux at l,m. A situation then arises where the flux vector is more discrepant after scaling than before re-normalisation and if the injected error is great enough, the process can become oscillatory. This behaviour results from the fact that scaling is performed after a fixed number of iterations (usually 3) and if the error injected is greater than can be handled by 3 inner iterations, divergent behaviour will ensue. It is possible to circumvent this instability by resorting to the less effective space independent renormalisation; however, in general, at the stage of the calculation at which the instability is met, the space dependent renormalising factor is usually very close to unity so that no acceleration is possible. The author has noticed that after a few cycles of normal power iteration, the equations determining the $\{f^j_{lm}\}$ can become properly conditioned and further acceleration using space dependent scaling can be used once the instability has been circumvented.

Appendix E

A Review of the Nuclear Data for the Threshold Dosimetry Reactions Used in the ASPIS Iron Benchmark Experimental Analysis

The ENDF/B-IV dosimetry file handbook[143] and the "Compilation of Threshold Reaction Neutron Cross-Sections for Neutron Dosimetry and Other Applications"[142] give some useful insight into the evaluation of the data contained in the primary libraries - the UKNDL and the ENDF/B-IV dosimetry file. In the following discussion some notes are provided on the status of the two files, apparent sources of energy-dependent correlation of the data and the adequacy of the error assignments by McElroy et al[37] for the threshold detectors utilised in the benchmark experiment. These notes reflect the critical assessments of a physicist, who is not an experienced evaluator, on his first perambulation through the world of data evaluation and should be considered in that light.

E.1 Sulphur (n,p)

The ENDF/B-IV dosimetry file contains the ENDF/B-III evaluation of Dudley and Kennerley[159] which placed substantial reliance on the data of Allen et al[160]. These data measured in 1957 relative to the $U^{238}(n,f)$ cross-section have been renormalised to the ENDF/B-III evaluation of U^{238}; this normalisation process must necessarily introduce a long range energy-dependent correlation and may indeed dominate all other sources of error for the plateau region of the cross-section. All other measured data chosen for use in the evaluation have been renormalised to agree with the Allen et al data. The paucity and dispersion of the measured data do little to substantiate the use of this cross-section as a standard for benchmark measurement.

For the UKNDL sulphur evaluation, DFN 97, the threshold is defined by the data of Klema (1948)[161] for which no errors are quoted. The errors given for the Allen data in the same region are 10% but these are exclusive of the Klema data and the dispersion of the measured data around the threshold region ($E_n < 2.2$ MeV) is such that it is hard to disagree with McElroy's estimate of a 100% uncertainty in the $S^{32}(n,p)$ threshold at the 68% confidence limit. Between 2.2 and 4.0 MeV the data of Hurlimann and Huber[162] are consistent with the evaluated file; the errors quoted on these data are about 12%, but compared with other sets of measured data the relative errors appear greater and the 20% error quoted by McElroy for this energy region does not appear to be unnecessarily conservative. Above 3.0 MeV the errors quoted on the measured data vary between 6 and

12%. However most of the measured data agree to within 10% so that the 8% error assignment of McElroy would appear acceptable.

E.2 Indium (n,n')

The ENDF/B-IV dosimetry file contains the 1972 ENDF/B-III evaluation of Sher[163]. From threshold (about 0.35 MeV) up to 1.8 MeV the evaluation follows the data of Ebel and Goodman (1954)[164] which was based on the detection of the 0.335 MeV γ-ray. They subsequently normalised their results at 0.88 MeV to the measurements of Martin et al[158](1954) which extended up to 4 MeV. The data of Menlove et al (1967)[165] and Menlove and Grench[166] cover the regions from 4 MeV to 8 MeV and from 12 MeV to 19.5 MeV respectively. They used a variety of techniques including γ-ray detection, measurements relative to the $U^{235}(n,f)$ cross-section and a few point measurements relative to the $Al^{27}(n,\alpha)$ cross-section and the $Au^{197}(n,\gamma)$ cross-section. Data measured by Butler and Santry (1967)[167] covering the range 0.8 MeV to 6.0 MeV and measured, at least at higher energies, relative to $S^{32}(n,p)$ cross-sections have also been used in the evaluation. At the time of evaluation no data were available covering the region from 8 MeV to 12 MeV.

The measurements from threshold up to 4 MeV will have an inherent long range energy-dependent correlation arising from uncertainties in the γ-ray internal conversion rate and the β^- branching ratio. The data of Menlove et al will have long range energy-dependent correlations arising from the re-normalisation of the data to agree with the ENDF/B-III evaluations for $U^{235}(n,f)$ and $Au^{197}(n,\gamma)$. The Butler and Santry data had not been fully published at the time of evaluation and no indication of which part of the $S^{32}(n,p)$ cross-section was used for the re-normalisation has been given. The evaluation of the file between 8 MeV and 12 MeV was simply based on a guessed line which smoothly joined the upper and lower regions of the measured data and the relative errors and correlations on this fit must be large.

The UKNDL file, DFN 239, follows the data of Ebel and Goodman from 0.35 MeV up to 1.8 MeV; no errors are quoted by the measurers but the general data suggest a scatter of some 50% or more up to 0.6 MeV and 20% up to 1.8 MeV. The overlap between the Ebel et al and the Martin et al data at 1.8 MeV would seem to be in accord with this assignment. From 1.8 MeV up to 5.0 MeV the data of Martin et al is followed very closely and their error assignment of 10% appears reasonably in agreement with the other measured data in this region. It seems that a calculation similar to that of Gardener et al has been used to interpolate the cross-

section up to the 13 MeV data, after fitting to the data of Martin et al at 4 MeV. The calculation does not fit the data of either Menlove et al or Butler and Santry. This file appears totally inadequate for benchmark experiments. The errors quoted by McElroy et al appear reasonable except below 0.6 MeV where 50% may be more appropriate and in the region between 5 and 12 MeV, where the UKNDL file appears to be 50% below the measured data, although reliance on the Butler and Santry measurements depends largely on the status of their $S^{32}(n,p)$ data.

E.3 Rhodium (n,n')

The UKNDL file, DFN 94, has been evaluated on the basis of the measurements of Butler and Santry (1968)[168]. The data of Kimura[169] deviate slightly from the data of the evaluated file but the quoted errors are not exclusive of the file. The data in the region 4.85 MeV to 14.8 MeV were measured relative to the $S^{32}(n,p)$ reaction. The lower energy data from 0.175 MeV to 5.93 MeV were measured using an absolutely calibrated counter; the cross-section cross-over region was checked at two points and agreed to within 1%. Indirectly this must provide a diagnostic check on the sulphur cross-section in this region. The higher energy data will have a long range energy-dependent correlation arising from the method of measurement.

The International Project to highlight inadequacies in threshold detector data, ILRR, appears to concentrate effort on the comparison of calculated and measured fission averaged cross-sections. Laudable as this is, the meaningfulness of such tests is open to question; in a LMFBR the spectrum may be quite soft due to the steel and sodium in the core and in the shielding domain, epithermal neutrons are often the most important contributors to the reaction-rate. The resonance integral would therefore appear to be a more critical test of the quality of the data for these detectors and for assessing their utility in these environments. An experimental measurement of the resonance integral for such detectors appears, however, to be impossible. Table E.1 displays the fission averaged cross-sections calculated for the different libraries and some measurements by Fabry et al[170] and also a comparison of some calculated resonance integrals.

Table E.1

Comparison of Fission Averaged and Resonance Integrals for Different Detector Cross-Section Libraries

Reaction	U^{235} Fission Average +		Watt-Cranberg		1/E Spectrum	
Detector	ENDF/B	Measured	SAND-II	ENDF/B(143)	SAND-II	ENDF/B(143)
S(n,p)	63.9	69 ± 2	60.9	65.0	-	-
In(n,n')	166.8	188 ± 4	185.0	170.0	21.5	18.0
Rh(n,n')	-	-	-	-	-	-
Au(n,γ)	84.9	88 ± 5	82.8	83.1	1.62×10^6	1.56×10^6

+ Spectrum appropriate to T = 1.32 MeV $\chi(E) = C.\sqrt{E}\,e^{-E/1.32}$

References

1. WRENDA 76/77 Ed. Lesseler, R.M.
"World Request List for Nuclear Data"
INDC (SEC)-55/URSF IAEA Vienna (1976)

2. Irving, D.C. and Straker, E.A.
"Evaluation of the Cross-Sections of Iron: ENDF/B MAT 1101".
ORNL-TM-2891 (ENDF-138) (1970)

3. Butler, J. and Nicks, R.
"Report of a Joint NEA/EURATOM Specialist Meeting on Shielding Benchmark Experiments".
NEACRP-L-1 Ispra (1974)

4. Carter, M.D. and Packwood, A.
"The Winfrith Benchmark Experiment in Iron - Experimental Results".
Paper B5. Proc. of the Specialists' Meeting on Sensitivity Studies and Shielding Benchmarks. Paris NEA/OECD (1975).

5. Grimstone, M.J. and McCracken, A.K.
"Preliminary Analysis of the Winfrith Iron Benchmark Experiment".
Paper C4. ibid(4).

6. Pope, A.L.
"The Current Edition of the Main Tape NDL-1 of the U.K. Nuclear Data Library - March (1973)".
AEEW-M1208 (1973)

7. Grimstone, M.J.
"The RADAK Users' Manual".
AEEW-M1455 (1976).

8. Herrnberger, V.
"Application of Sensitivity Theory to Energy Structure Definition".
Paper D2. ibid(4).

9. Ching, J. and Oblow, E.M.
"Selection of Group Energy Boundaries Using Sensitivity Theory".
Trans. Am. Nuc. Soc. 17 (1) (1973).

10. Engle, W.W. Jr.
"A Users' Manual for ANISN".
K-1693 (1967).

11. Mynatt, F.R. and Rhoades, W.A.
"The DOT-III Two-Dimensional Discrete Ordinates Code".
ORNL-TM-4280 (1973).

12. Straker, E.A., Cain, V.R., Irving, D.C. and Stevens, P.N.
"The MORSE Code - A Multi-group Neutron and Gamma-Ray Monte Carlo Transport Code".
ORNL-4585 (1970).

13. Stacey, W.M. Jr.
"Variational Estimates and Generalised Perturbation Theory for the Ratios of Linear and Bilinear Functionals".
J. Math. Phys. 13 (8) 1119 (1972).

14. Usachev, L.N.
"Perturbation Theory for the Breeding Ratio and for Other Number Ratios Pertaining to Various Reactor Processes".
J. Nuclear Energy Parts A/B 18 571 (1964).

15. Gandini, A.
"A Generalised Perturbation Method for Bi-Linear Functionals of the Real and Adjoint Neutron Fluxes".
J. Nuclear Energy 21 755 (1967).

16. Oblow, E.M.
"General Sensitivity Theory for Radiation Transport".
ORNL-TM-4110 (1973).

17. Gerstl, S.A.W. and Stacey, W.M. Jr.
"A Class of Second-Order Approximate Formulations of Deep Penetration Radiation Transport Problems".
Nucl. Sci. Eng. 51 339 (1973).

18. Gandini, A.
"Nuclear Data and Integral Measurements Correlation for Fast Reactors. Part 4: Second Order Adjustments and Systematic Errors".
RT/FI(78)10 (Revised Pre-print). (1978).

19. Childs, R.L., Bartine, D.E. and Engle, W.W. Jr.
"Perturbation Theory and Sensitivity Analysis for Two-Dimensional Shielding Calculations".
Trans. Am. Nuc. Soc. 21 543 (1975).

20. Rief, H.
"Three Dimensional Effects in Sensitivity Studies".
Paper B4. Proc. of the 5th Int. Conf. on Reactor Shielding.
Knoxville (1977).

21. Goldstein, H.
"A Survey of Cross-Section Sensitivity Analysis as Applied to Radiation Shielding".
Paper B1. ibid(20).

22. Germogenova, T.A., Suvorov, A.P. and Utkin, V.A.
"Evaluation of the Effect of Errors in Group Constants on Calculations of Neutron Fields in Shielding".
Paper E6. Proc. of a Specialists' Meeting on Differential and Integral Nuclear Data Requirements for Shielding Calculations.
IAEA/OECD(NEA) IAEA-207 Vienna (1976).

23. Lympany, S.D., McCracken, A.K. and Packwood, A.
"Contribution to the Exercise on Sensitivity Studies for the NEA Theoretical Fast Reactor Benchmark".
Paper C4. ibid(22).

24. Bartine, D.E., Oblow, E.M. and Mynatt, F.R.
"SWANLAKE - A Computer Code Utilising ANISN Radiation Transport Calculations for Cross-Section Sensitivity Analysis".
ORNL-TM-3809 (1973).

25. Perey, F.G.
"Covariance Matrices in Experimental Data".
Proc. of Int. Conf. on Neutron Physics and Nuclear Data for Reactor and Other Applied Purposes. OECD/NEA and UKAEA Harwell (1978).

26. Perey, F.G.
"Minutes of the Error Quantities Subcommittee of CSEWG".
S. Pearlstein, Editor, Brookhaven National Laboratory. December (1973).

27. Bendall, D.E.
"A Monte Carlo Programme for Calculating the Penetration of Neutrons in Systems with Cylindrical Geometry".
AEEW-R308 (1966).

28. Ching, J., Goldstein, H. and Oblow, E.M.
"Application of a Discrete-Energy Discrete Ordinates Technique to the Study of Neutron Transport in Iron".
ORNL-TM-4235 (1974).

29. Abagyan, L.P., Bazazyants, N.O., Bondarenko, I.I. and Nikolaev, M.N.
"Group Constants for the Design of Nuclear Reactors".
Atomizdat (1964).

30. O'Shea, D.M., Toppel, B.J. and Rago, A.L.
"The Automated Preparation of Multi-Group Cross-Sections for Fast Reactor Analysis using the MC^2 Code".
Session I. Proc. of the Int. Conf. on Fast Critical Experiments and their Analysis. Argonne ANL-7320 October 1966.

31. D'Angelo, A., Oliva, A., Palmiotti, G., Salvatores, M. and Zero, S.
"Consistent Utilisation of Shielding Benchmark Experiments".
Nucl. Sci. Eng. 65 477 (1978).

32. Butler, J.
"A Review of Progress in the NEA/IAEA Collaborative Programme of Sensitivity Studies and Shielding Benchmarks".
Paper A1. ibid(20).

33. Hehn, G.
"Conclusions from the Sensitivity Benchmark Results of a PWR Shield".
ibid(22).

34. Salvatores, M.
"Design Sensitivity and Uncertainty Analysis of Fast Breeder Reactor Shields".
ibid(22).

35. Campbell, C.G. and Rowlands, J.L.
"The Relationship of Microscopic and Integral Data".
Proc. IAEA Int. Conf. on Nuclear Data for Reactors. Helsinki.
IAEA-CN-26/116 (1970).

36. Schmidt, J.J.
"Neutron Cross-Sections for Fast Reactor Materials. Part I".
KFK-120 (1966).

37. Kellogg, L.S. and McElroy, W.N.
"Fuels and Materials Fast Reactor Dosimetry Data Development and Testing".
Nucl. Technol. 25 180 (1975).

38. Gerstl, S.A.W., Dudziak, D.J. and Muir, D.W.
"Application of Sensitivity Analysis to a Quantitative Assessment of Neutron Cross-Section Requirements for the TFTR".
LA-6118-MS Appendix A. (1975).

39. Canali, U., Gonano, G. and Nicks, R.
"Two NEA Sensitivity, 1-D Benchmark Calculations Part II: Sensitivity of the Secondary Sodium Activation in the FBR Configuration".
Paper B3 ibid(22).

40. Avery, A.F. and Lympany, S.D.
"Target Accuracies and Sensitivity Studies in the Assessment of Data Requirements for Practical Shield Design".
Paper A2 ibid(22).

41. Herrnberger, V., Hehn, G. and Nicks, R.
"Required Target Accuracies".
Paper D1 ibid(4).

42. Herrnberger, V., Hehn, G. and Nicks, R.
"Target Accuracies Required in Radiation Shielding".
Paper A1 ibid(22).

43. Chestnutt, M.M., and McCracken, A.K.
"The Use of Published Nuclear Data Covariance Matrices in Uncertainty Analysis of Shielding".
Proc. of a Specialists' Meeting on Integral Benchmarks and Data Adjustment. Paris (1977).

44. Chestnutt, M.M. and McCracken, A.K.
"Some Aspects of the Data Requirements for Fission and Fusion Reactor Shielding".
To be published.

45. Young, P.G.
LA-4780 (ENDF-174)

46. Chestnutt, M.M.
"MCOVE - An Approximate Method for Group Condensation of ENDF/B Error Correlation Files".
To be published.

47. Drischler, J.D. and Weisbin, C.R.
"Compilation of Multi-Group Cross-Section Covariance Matrices for Several Important Reactor Materials".
ORNL-5318 (ENDF-235) (1977).

48. Weisbin, C.R., Oblow, E.M., Ching, J., White, J.E., Wright, R.Q. and Drischler, J.D.
"Cross-Section and Method Uncertainties: The Application of Sensitivity Analysis to Study Their Relationship in Radiation Transport Benchmark Problems".
ORNL-TM-4847 (ENDF-218) (1975).

49. Hehn, G. and Koban, J.
"Reactor Shield Benchmark No. 2".
NEACRP-L-151.

50. Lympany, S.D., McCracken, A.K. and Packwood, A.
"Contribution to the Exercise on Sensitivities for the NEA Theoretical PWR Benchmark".
Paper B5. ibid(22).

51. McCracken, A.K.
"Correlated Uncertainties in Integral Data".
ibid(25).

52. Barré, J.Y.
"Fast Reactors: Definition of a Standard Configuration for the Comparison of Shielding Calculations".
REF/SPNR/76/350 Cadarache NEACRP-L-152 (1976)

53. Broomfield, A.M., George, C.F., Ingram, G., Jakeman, D. and Sanders, J.E.
"Measurements of k-infinity, Reaction-Rates and Spectra in ZEBRA Plutonium Lattices".
Paper 1.1 Proc. of BNES Int. Conf. on the Physics of Fast Reactor Operation and Design. (1969).

54. Butler, J., Carter, M.D., McCracken, A.K. and Packwood, A.
"The UK Programme of DATAM Experiments on Energy-Deposition and Radiation Penetration".
ibid(3).

55. Minsart, G. and Van Bosstraeten, C.
"Contribution to the Study of Reactor Shielding Benchmark No. 2 (PWR) Proposed by the NEA".
Paper B4. ibid(22).

56. Miyasaka, S., Minami, K., Kuroi, H. and Hirota, J.
"Sensitivity and Uncertainty Analysis for Iron Cross-Sections".
Paper C6. ibid(4).

57. An, S. et al.
"Iron Shielding Benchmark Experiments at YAYOI".
Paper B4. ibid(4).

58. Nicks, R. and Butler, J.
"Summary Report".
p10 ibid(4).

59. Carter, M.D. and Samways, J.
Private Communication. AEEW January (1978).

60. Perlini, G.
"First Measurements at EURACOS II".
ibid(43).

61. Hehn, G., Schriewer, J., Mattes, M., Canali, U. and Nicks, R.
"Calculations for Iron Benchmark Experiments with Californium and 14 MeV Neutron Sources".
Paper C1. ibid(4).

62. Furuta, Y., Sasamoto, N. and Tanaka, S.
"Preliminary Studies of Neutron Benchmark Experiments for One-Dimensional Transport Calculations with an Iron Sphere".
Paper B6. ibid(4).

63. Maerker, R.E., Muckenthaler, F.J., Childs, R.L. and Gritzner, M.L.
"Final Report on a Benchmark Experiment for Neutron Transport Through Thick Sodium".
ORNL-4880. (1974).

64. Oka, S. et al.
"Two-Dimensional Shielding Benchmarks of Sodium and Iron at YAYOI".
ibid(43).

65. Bouteau, R., Calamand, D., Oceraies, Y. and Vienot, R.
"Experiences Integrales de Propagation de Neutrons dans des Milieux Acier-Sodium".
Paper B1. ibid(4).

66. Estiot, J.C., Trapp, J.P., Salvatores, M. and Palmiotti, G.
"Interpretation des Experiences de Propagation de Neutrons dans des Melanges Fer-Sodium Avec Le Formulaire PROPANE-0".
Paper E2. ibid(22).

67. Palmiotti, G. and Salvatores, M.
"Towards PROPANE Preliminary Version 1 - Experimental Analysis, Sensitivity Studies and Related Problems".
RTJ/LTCR (76) 3 (1976).

68. Maerker, R.E. and Muckenthaler, F.J.
"Measurements and Calculations of Neutron Fluxes Through a Simulation of the CRBR Upper Axial Shielding".
Trans. Am. Nuc. Soc. 23 611 (1976).

69. Oblow, E.M. and Weisbin, C.R.
"Fast Reactor Shield Sensitivity Studies for Steel-Sodium-Iron Systems".
ibid(20).

70. Oblow, E.M. and Weisbin, C.R.
"Recent Progress at ORNL in Determining Nuclear Data Requirements for Fast Reactor Shield Design using Advanced Sensitivity Techniques".
Paper C2. ibid(22).

71. Weisbin, C.R., Oblow, E.M., Marable, J.H., Peelle, R.W. and Lucius, J.L.
"Application of Sensitivity and Uncertainty Methodology to Fast Reactor Integral Experiment Analysis".
Nucl. Sci. Eng. 66 307 (1978).

72. Hemment, P.C.E. and Pendlebury, E.D.
"The Optimisation of Neutron Cross-Section Data Adjustments to give Agreement with Experimental Critical Sizes".
ibid(30)

73. Ballance, B.M.O., Pendlebury, E.D., Price, J.A. and West, P.H.
"The Optimisation of Neutron Cross-Section Adjustments to Give Agreement with Spectrum Measurements at the Centre of Critical Systems".
Paper 1.13 ibid(53).

74. Macdougall, J.D. and Rowlands, J.L.
"The Use of Integral Measurements to Adjust Cross-Sections and Predict Reactor Properties".
Paper 1.16 ibid(53).

75. Gandini, A.
"Nuclear Data and Integral Measurements Correlation for Fast Reactors. Part 1: Statistical Formulation".
CNEN Report RT/FI(73)5 (1973).

76. Barré, J.Y. and Ravier, J.
"Imprécisions des Paramêtres Charateristiques d'un Reactuer Rapide de Puissance dues aux Incertitudes Actuelles Concernant les Données Neutroniques".
Proc. of a Symp. on Fast Reactor Physics Vol. I SM-101/58 Karlsruhe (1968).

77. Pazy, A., Rakavy, G., Reiss, Y. and Yeivin, Y.
"Integral Measurements as Supplementary Data in Neutron Cross-Section Evaluation".
Proc. of IAEA Conf. on Nuclear Data for Reactors. Vol. II CN-23/15 Paris (1966).

78. Mitani, H. and Kuroi, H.
"Adjustment of Group Cross-Sections by Means of Integral Data - (I) Theoretical Study".
J. Nucl. Sci. and Technol. 9 (7) (1972).

79. Cecchini, G., Farinelli, U., Gandini, A. and Salvatores, M.
"Analysis of Integral Data for Few-Group Parameter Evaluation of Fast Reactors".
A/Conf. 28/P/627 Vol. 2 388 Geneva (1964).

80. Gandini, A.
"Nuclear Data and Integral Measurements Correlation for Fast Reactors. Part 2: Review of Methods".
CNEN Report RT/FI(73)22 (1973).

81. Mitani, H. and Kuroi, H.
"Adjustment to Cross-Section Data to Fit Integral Experiments by Least Squares Method".
J. Nucl. Sci. and Technol. 12 (11) (1975).

82. Linnik, Y.V.
"Method of Least Squares and Principles of the Theory of Observation".
Pergamon (1961).

83. Peelle, R.W.
"Uncertainties and Correlations in Evaluated Data Sets Induced by Use of Standard Cross-Sections".
Paper CB4 Proc. of Conf. on Nuclear Cross-Sections and Technology NBS-425 Vol. I Washington D.C. (1975).

84. Mitani, H. and Kuroi, H.
"Adjustment to Group Cross-Sections by Means of Integral Data - (II) Numerical Study".
J. Nucl. Sci. and Technol. 9 (11) (1972).

85. Pearlstein, S.
"Neutron Cross-Sections and their Uncertainties Obtained from Nuclear Systematics".
p332 ibid(83).

86. Perey, F.G.
"Estimated Uncertainties in Nuclear Data - An Approach".
Paper IA3 ibid(83).

87. Pazy, A., Ravaky, G., Reiss, I., Wagshal, J.J., Ya'ari, A. and Yeivin, Y.
"The Role of Integral Data in Neutron Cross-Section Evaluation".
Nucl. Sci. Eng. 55 280 (1974).

88. Gandini, A. and Salvatores, M.
"Nuclear Data and Integral Measurements Correlation for Fast Reactors. Part 3: The Consistent Method".
CNEN Report RT/FI(74)3 (1974).

89. Gandini, A., Petilli, M. and Salvatores, M.
"Nuclear Data and Integral Measurements Correlation for Fast Reactors. Statistical Formulation and Analysis of Method. The Consistent Approach".
Paper B2. Proc. of Int. Symp. on Physics of Fast Reactors. Vol. II. Tokyo (1973).

90. Toppel, B.J., Rago, A.L. and O'Shea, D.M.
"MC^2, A Code to Calculate Multi-Group Cross-Sections".
ANL-7318 (1967).

91. Butler, J.
Private Communication. AEEW Februrary (1978).

92. "Panel Discussion on Adjustments to Differential Data to Fit Integral Experiments".
p277 ibid(53).

93. Rowlands, J.L.
Private Communication. AEEW November (1978).

94. Fisher, R.A.
"Contributions to Mathematical Statistics".
Wiley N.Y. (1950).

95. Laplace, Marquis de.
"A Philosophical Essay on Probabilities".
Dover N.Y. (1951).

96. Jeffreys, H.
"Further Significance Tests".
Proc. Camb. Phil. Soc. 32 416 (1936).

97. Jánossy, L.
"Theory and Practice of the Evaluation of Measurements".
Clarendon Press. (1965).

98. Shannon, C.E.
"A Mathematical Theory of Communication".
Bell Syst. Tech. J. 27 379 (1948).

99. Meyer, P.L.
"Introductory Probability and Statistical Applications".
World Student Series. Addison-Wesley 2nd Edition (1977).

100. Williams, M.L. and Engle, W.W. Jr.
"The Concept of Spatial Channel Theory Applied to Reactor Shielding Analysis".
Nucl. Sci. Eng. 62 92 (1977).

101. Price, J.A.
"A Guide to GALAXY 6 Part 1".
AWRE O 13/75 (1975).

102. Chestnutt, M.M.
"The PRCM Users' Manual".
To be published.

103. Lewins, J.
"Importance: The Adjoint Function".
Pergamon Press (1965).

104. Goodfellow, M.R.
"The Maximum Likelihood Solution of Integral Equations Applied to Problems in Nuclear Spectrometry".
Ph.D. Thesis. Imperial College, University of London. (1974)

105. McCracken, A.K.
"The Application of Sensitivity Analysis to the Identification of Data Requirements for Shielding".
NEACRP-A-298. (1977).

106. Chestnutt, M.M. and McCracken, A.K.
"Method of Analysis of the Winfrith Iron Benchmark Experiment".
ibid(43).

107. Matthes, W.
"Cross-Section Adjustment in the Analysis of Benchmark Experiments".
ESIS Newsletter. No. 26. (1978).

108. Cramér, H.
"Mathematical Methods of Statistics".
Princeton University Press. (1946).

109. Chestnutt, M.M. and McCracken, A.K.
"An Error Estimation for the DOT-III Reference Calculation Performed for the Winfrith Iron Benchmark".
ibid(43).

110. Packwood, A. and Carter, M.D.
Private Communication. AEEW August (1977).

111. Davison, B. and Sykes, J.B.
"Neutron Transport Theory".
Oxford University Press. (1957).

112. Carlson, B.G.
"The Numerical Theory of Neutron Transport".
Methods in Computational Physics. Academic Press (1961).

113. Lathrop, K.D. and Carlson, B.G.
"Numerical Solution of the Boltzmann Transport Equation".
J. Comp. Phys. Vol. I No. 2. (1966).

114. Mynatt, F.R.
"Development of a 2-D Discrete Ordinates Transport Theory of Radiation Shielding".
Ph.D. Thesis. University of Tennessee. (1969).

115. Lathrop, K.D.
"Discrete Ordinates Methods for Numerical Solution of the Boltzmann Transport Equation for Neutrons".
Reactor Technol. 15 No.2 (1972).

116. Mynatt, F.R.
"The Discrete Ordinates Method Involving Deep Penetration".
ORNL-RSIC-19 (1967).

117. Jeffreys, H. and Jeffreys, B.S.
"Methods of Mathematical Physics".
Cambridge University Press. (1972).

118. "Synthesis of Calculational Methods for the Design and Analysis of Radiation Shields for Nuclear Rockets".
WANL-PR(LL) - 010 Vol. 6 June (1967)

119. Disney, R.K. and Soltesz, R.G.
"Mesh Spacing in Transport Codes".
RA-3611. (1966).

120. ESIS Newsletter No. 12 January (1975).

121. Soltesz, R.G., Disney, R.K. and Collier, G.
"Manual for DOT-IIW".
WANL-TONE-1982.

122. Greenspan, H., Kelber, C.N. and Okrent, D.
"Computing Methods in Reactor Physics".
Gorden and Breach. N.Y. (1968).

123. Madsen, N.K.
"Convergence of the Weighted Diamond Difference Approximation in Discrete Ordinate Equations".
Proc. of Conf. on New Developments in Reactor Maths. and Applications.
USAEC Report CONF-710302 Vol. II 565 (1971).

124. Salvatores, M.
Private Communication. CNEN (1977).

125. Varga, R.S.
"Matrix Iterative Analysis".
Prentice-Hall. N.J. (1966).

126. Mynatt, F.R. and Engle, W.W. Jr.
"A Comparison of Methods of Inner Iteration Convergence in Discrete Ordinates Codes".
Trans. Am. Nucl. Soc. 11 (1) Vol. II June (1968).

127. Nicks, R., Canali, U. and Burn, K.
"100-Group 2-D Calculation of the Winfrith Iron Benchmark Experiment".
Paper E4. ibid(22).

128. "A Calculation Model of the ASPIS Iron Benchmark Experiment". Circulated to Participants at the Specialists' Meeting on Sensitivity Studies and Shielding Benchmarks. Paris (1975).

129. Farinelli, U.
Letter to Members of the NEA/EURATOM Collaborative Benchmark Programme.

130. Oka, Y. et al.
"Integral Experiments for the Layers of Iron and Sodium Shields at YAYOI".
ibid(43).
(See also ref. (64)).

131. Benjamin, P.W., Kemshall, C.D. and Redfearn, J.
"The Use of a Gas-Filled Spherical Proportional Counter for Neutron Spectrum Measurements in a Zero Energy Fast Reactor".
AWRE R NR2/64 (1964).

132. Snidow, N.L. and Warren, H.D.
"Wall Effect Corrections in Proportional Counter Spectrometers".
Nucl. Instr. and Methods 51 109 (1967).

133. Kemshall, C.D.
"The Use of Spherical Proportional Counters for Neutron Spectrum Measurements".
AWRE O 31/73 (1973).

134. Nuclear Enterprises Scintillator Catalogue.
7 (1973).

135. Grundl, J.A. and Eisenhauer, C.
"Fission-Rate Measurements for Materials Neutron Dosimetry in Reactor Experiments".
1st ASTM-EURATOM Symp. on Reactor Dosimetry. Petten (1975).

136. Grundl, J.A. and Eisenhauer, C.
"Fission Spectrum Neutrons for Cross-Section Validation and Flux Transfer".
ibid(83).

137. Farinelli, U. and McCracken, A.K.
"List of Activation Reactions and Cross-Sections Suggested for Use in Benchmark Shielding Experiments".
Appendix C. ibid(3).

138. Farinelli, U.
"Tables on Suppressed Gold Cross-Section Data".
Distributed by JRC (Ispra). (1975).

139. Oster, C.A., McElroy, W.N., Lippincott, E.P. and Simmons, R.L.
"Solution Weighting for the SAND-II Monte Carlo Code".
BNWL-SA-5736. (1976).

140. Vlasov, M.F., Dunford, C.L., Schmidt, J.J. and Lemmel, H.D.
"Status of Neutron Cross-Section Data for Reactor Radiation Measurements".
INDC (NDS) 47/L IAEA (1972).

141. Zijp, W.L.
"Review of Activation Methods for the Determination of Neutron Flux Density Spectra".
RMG Note 75/19 (1975).

142. Liskien, H. and Paulsen, A.
"Compilation of Cross-Sections for Some Neutron Induced Threshold Reactions".
EUR 119.e.

143. Magurno, B.A. (Editor).
"Handbook for the ENDF/B-IV Dosimetry File".
NEACRP-L-145 (1975).

144. Packwood, A.
Private Communication. AEEW January (1978).

145. Dean, C.J.
Private Communication. AEEW February (1978).

146. Chestnutt, M.M.
"The SUPPRES Code for Calculating Energy-Dependent Foil Suppression Factors".
To be published.

147. McCracken, A.K. and Packwood, A.
Private Communication. AEEW February (1978).

148. Fabry, A., McElroy, W.N., Kellogg, L.S., Lippincott, E.P., Grundl, J.A., Gilliam, D.M. and Hansen, G.E.
"Review of Microscopic Integral Cross-Section Data in Fundamental Reactor Dosimetry Benchmark Neutron Fields".
HEDL-SA 1148 (1976).

149. Carter, M.D.
Internal Document. AEEW (1976).

150. Bennett, E.F. and Yule, T.J.
"Techniques and Analyses of Fast Reactor Neutron Spectroscopy with Proton Recoil Counters".
ANL-7763.

151. Werle, H.
"Spectrum Measurements of Radioactive Neutron Sources in the 10 keV - 10 MeV Energy Region with Proton Recoil Proportional Counters".
ORNL-TR-2415.

152. Ferguson, A.T.G.
Private Communication. AERE Harwell (1977).

153. Brierley, C.
Private Communication. University of Birmingham, England. (1977).

154. Benjamin, P.W., Kemshall, C.D. and Brickstock, A.
"The Analysis of Recoil Proton Spectra".
AWRE O 9/68 (1968).

155. Price, W.G. Jr.
"A Revised Version of the ANISN Code".
MATT-1035 (1974).

156. Chestnutt, M.M.
"PLATO - An Interfaced Suite of Codes for Cross-Section Data Optimisation".
To be published.

157. Birmingham, J.A.
"Notes on Fortran Programme Optimisation".
Internal Document. AERE Harwell (1976).

158. Martin, H.C., Diven, B.C. and Taschek, R.F.
"Cross-Sections for Production of In-115 (Metast) and Au-197 (Metast) by Inelastic Scattering of Neutrons".
Phys. Rev. 93 199 (1954).

159. Dudley, N.P. and Kennerley, R.
"Evaluation of the $S^{32}(n,p)P^{32}$ Reaction".
ibid(143).

160. Allen, J. Jr., Biggers, W.A., Prestwood, R.J. and Smith, R.K.
"Cross-Sections for the $S^{32}(n,p)P^{32}$ and the $S^{34}(n,\alpha)Si^{31}$ Reactions".
Phys. Rev. 107 (5) 1363 (1957).

161. Klema, E.D. and Hanson, A.O.
"A Determination of the $S^{32}(n,p)P^{32}$ Cross-Section for Neutrons Having Energies of 1.6 to 5.8 MeV".
Phys. Rev. 73 (2) 106 (1948).

162. Hurlimann, T. and Huber, P.
"Cross-Sections of S(n,alpha)Si and S(n,proton)P for Neutron Energies for 2.2 to 4.0 MeV".
Helvetica Physica Acta 28 33 (1950).

163. Sher, R.
"The $In^{115}(n,n')In^{115m}$ Reaction for ENDF/B-III".
ibid(143).

164. Ebel, A.A. and Goodman, C.
"Inelastic Scattering of Neutrons by In^{115} and Au^{197}".
Phys. Rev. 93 197 (1954).

165. Menlove, H.O., Coop, K.L., Grench, H.A. and Sher, R.
"$Na^{23}(n,2n)Na^{22}$, $Mn^{55}(n,2n)Mn^{54}$, $In^{115}(n,2n)In^{114m}$, $Ho^{165}(n,2n)Ho^{164m}$, $In^{115}(n,n')In^{115m}$ and $Al^{27}(n,\alpha)Na^{24}$ Reactions".

166. Menlove, H.O. and Grench, H.A.
"$In^{113}(n,\gamma)In^{114m}$, In^{114G}, $In^{113}(n,n')In^{113m}$, $In^{115}(n,\gamma)In^{116m}$, In^{116G}, and $In^{115}(n,n')In^{115m}$ Activation Cross-Sections Between 0.36 and 1.02 MeV".
Phys. Rev. 165 1298 (1968).

167. Butler, J.P. and Santry, D.C.
"Cross-Sections for the Production of In-115 (Metast.) by Neutron Inelastic Scattering".
Bull. Am. Phys. Soc. 12 547 (1967).

168. Butler, J.P. and Santry, D.C.
"The Neutron Inelastic Cross-Section for the Production of Rh-103 (Metastable)".
2nd Conf. on Nuclear Cross-Sections and Technology. Washington D.C.
Vol. II. 803 (1968).

169. Kimura, W., Kobayashi, K. and Shibata, T.
"Measurement of Cross-Section for the $Rh^{103}(n,n')Rh^{103}$ (metastable) Reaction and its Application to Fast Neutron Flux Measurements".
J. Nucl. Sci. Technol. 6 485 (1969).

170. Fabry, A.
"Evaluation of Microscopic Integral Cross-Sections Averaged in a U^{235} Thermal Fission Neutron Spectrum (for 29 Nuclear Reactions Relevant to Neutron Dosimetry and Fast Reactor Technology)".
BLG-465 (1972).

171. Carter, M.D. and Samways, J.
Private Communication. AEEW January (1978).

172. Arcipiani, B. and Chestnutt, M.M.
"The Interpretation of the Special High Energy Measurement Data from the ASPIS Iron Benchmark Experiment".
To be published.

173. Cameron, J.
"MISSIONARY - A Computer Program to Convert Data in the ENDF Format to the UKAEA Nuclear Data Library Format".
AWRE O 17/76.

174. Pope, A.L. and Story, J.
Private Communication. AEEW October (1977).

175. Martini, M., Palmiotti, G. and Salvatores, M.
"A Benchmark Experiment of Neutron Propagation in Iron Used to Test ENDF/B Cross-Section Data".
Nucl. Sci. Eng. 56 427 (1975).

176. Rowlands, J.L., Dean, C.J., James, M.F., Macdougall, J.D. and Smith, R.W.
Internal Document. AEEW (1973).

177. Wright, R.Q., Lucius, J.L., Greene, N.M. and Craven, C.W. Jr.
"SUPERTOG: A Program to Generate Fine Group Constants and P_n Scattering Matrices from ENDF/B".
ORNL-TM-2679 (1969).

178. Greene, N.M., Lucius, J.L., Petrie, L.M., Ford, W.E. III, White, J.E. and Wright, R.Q.
"AMPX: A Modular Code System for Generating Coupled Multi-Group Neutron-Gamma Libraries from ENDF/B".
ORNL-TM-3706 (1974).

179. Parker, K.
"The Format and Conventions of the UKAEA Nuclear Data Library as at June 1965".
Draft Report.

180. Cramer, S.N. and Oblow, E.M.
"Analysis of a Neutron Scattering Integral Experiment on Iron for Neutron Energies from 1 to 15 MeV".
ORNL-TM-5548 (1976).

181. "A Compilation of Integral Benchmarks".
ENDF-202.